University of Ioannina
Department of Physics

Self-assembly and Dynamics of Liquid Crystals

A Thesis presented

By

MAHDY MOHAMMED ELMAHDY

To

The Department of Physiscs

in partial fulfillment of the requirements for the degree of

Doctor of Philosophy

in the subject of

Physics

ΙΩΑΝΝΙΝΑ 2008

Self-assembly and Dynamics of Liquid Crystals

Ph.D. Dissertation

Mehdy Mohammad Elbahily
Department of Physics
University of Ioannina

Anagnostopoulos
Assistant Prof., Dept. of Materials

...Bakas
Associate Prof., Dep...

Evangelou
Professor, Dept. of Physics...

...kos
...er, Dept. of Physics...

...Dept. of Physics...

K...

...

Vlachos
Assistant Prof., Dept. of Chemistry...

Dedicated to my wife AMAL and my son KAREEM

«Self-assembly and Dynamics of Liquid Crystals»

Ph.D. Dissertation

Mahdy Mohammed Elmahdy
Department of Physics
University of Ioannina

INQUIRY COMMISION

A. Avgeropoulos
Assistant Prof., Dept. of Materials Science and Engineering, UoI

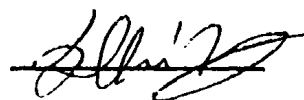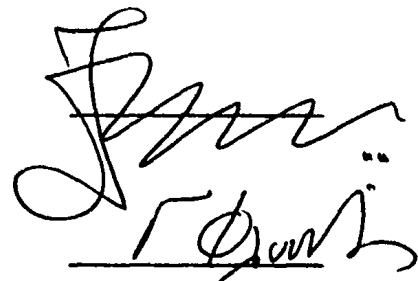Th. Bakas
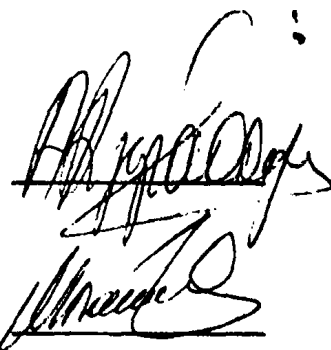Associate Prof., Dept. of Physics, UoI

S. Evangelou
Professor, Dept. of Physics, UoI

G. Floudas
Professor, Dept. of Physics, UoI

S. Foulias
Assistant Prof. Dept. of Physics, UoI

M. Kosmas
Professor, Dept. of Chemisty, UoI

K. Vlachos
Assistant Prof. Dept. of Chemistry, UoI

ΠΕΡΙΛΗΨΗ

Στην εργασία αυτή μελετήθηκε η αυτο-οργάνωση και η δυναμική μιας σειράς δισκόμορφων και ραβδόμορφων υγρών κρυστάλλων, με εφαρμογές στα ηλεκτρονικά και σε εύκαμπτες οθόνες, με σκοπό να απαντηθούν ορισμένα ανοικτά επιστημονικά ερωτήματα. Για το σκοπό αυτό έγινε η σύνθεση μιας σειράς κατάλληλα τροποποιημένων (Mr. X. Dou/Prof. Müllen) με ηλεκτρικά δίπολα δισκόμορφων υγρών κρυστάλλων και μελετήθηκαν ως προς τη δομή (με χρήση σκέδασης ακτίνων Χ, πυρηνικού μαγνητικού συντονισμού, διαφορικής θερμιδομετρίας σάρωσης, πολωτικής οπτικής μικροσκοπίας) και τη δυναμική (με χρήση διηλεκτρικής φασματοσκοπίας και πυρηνικού μαγνητικού συντονισμού). Τα ερωτήματα που απαντήθηκαν στην παρούσα εργασία είναι: (i) η επίδραση του διπόλου στη θερμοδυναμική σταθερότητα της κρυσταλλικής φάσης, (ii) η δυναμική των δίσκων στην κιονική φάση, (iii) το θερμοδυναμικό διάγραμμα ισορροπίας φάσεων καθώς και (iv) η κινητική της δημιουργίας της κρυσταλλικής φάσης μέσα από συγκεκριμένα «μονοπάτια» του διαγράμματος ισορροπίας φάσεων. Ειδικότερα, η πλήρης εξήγηση της «αργής» και «γρήγορης» δυναμικής στην κιονική φάση, το διάγραμμα ισορροπίας φάσεων και η κινητική της δημιουργίας και ανάπτυξης της κρυσταλλικής φάσης έγιναν για πρώτη φορά.

Πιο αναλυτικά, στους μη τροποποιημένους (Dr. M. Kastler /Prof. Müllen) δισκόμορφους υγρούς κρυστάλλους (HBC) βρέθηκε ένας ασθενής μηχανισμός κίνησης που «παγώνει» στους 215 Κ. Οι τεχνικές της διηλεκτρικής φασματοσκοπίας και του πυρηνικού μαγνητικού συντονισμού (Dr. M. Mondeshki/Prof. Spiess) απέδειξαν ότι η κίνηση αυτή οφείλεται στην αξονική περιστροφή των δίσκων μέσα στους κίονες η οποία παγώνει σε μία θερμοκρασία γνωστή σαν σημείο υάλου (T_g). Έγινε η σύνθεση τροποποιημένων δισκόμορφων υγρών κρυστάλλων με ισχυρά (CN, Br) καθώς και με λιγότερο ισχυρά δίπολα (OCH₃, C≡H). Το αποτέλεσμα της τροποποίησης με τα ισχυρά δίπολα ήταν η αποσταθεροποίηση της κρυσταλλικής φάσης. Αντίθετα η κρυσταλλική φάση επανεμφανίζεται όταν η τροποποίηση γίνεται με ασθενέστερα δίπολα. Επίσης αποδείχθηκε ότι η προέλευση του μηχανισμού κίνησης, με την ισχυρή εξάρτηση από τη θερμοκρασία, οφείλεται στην περιστροφική κίνηση των δίσκων στην κιονική φάση. Το σημείο υάλου βρέθηκε στους 236 Κ για την υγρο-κρυσταλλική φάση και στους 253 Κ για την κρυσταλλική φάση. Ένα σημαντικό συμπέρασμα από αυτή τη μελέτη ήταν ότι το είδος της φάσης (κρυσταλλική ή υγροκρυσταλλική) ελέγχει απόλυτα τη δυναμική των δίσκων εντός των κιόνων.

Μια άλλη παρατήρηση είναι ότι οι χαρακτηριστικοί χρόνοι ηρέμησης καθώς και η κατανομή των χρόνων ηρέμησης παρουσιάζουν πολύ διαφορετική θερμοκρασιακή εξάρτηση εντός των υγροκρυσταλλικών και των κρυσταλλικών φάσεων. Αυτή η παρατήρηση βοήθησε

στην κατασκευή του πρώτου διαγράμματος ισορροπίας φάσεων δισκόμορφων υγρών κρυστάλλων του τύπου HBC. Αποτέλεσμα του διαγράμματος ήταν η παρατήρηση ότι η κρυσταλλική φάση παρουσιάζει μεγαλύτερη σταθερότητα σε υψηλές πιέσεις. Στη συνέχεια μελετήθηκε η κινητική του σχηματισμού της κρυσταλλικής φάσης σαν συνέπεια της απότομης μεταβολής της πίεσης, με σκοπό τη μελέτη: (i) ενδιάμεσων φάσεων, (ii) των σημείων εμφάνισης πυρήνων της νέας φάσης, καθώς και (iii) της ύπαρξης μετασταθών καταστάσεων. Τα αποτέλεσμα της μελέτης κατέδειξαν την απουσία ενδιάμεσων φάσεων αλλά έδειξαν την ύπαρξη μεταστάθειας με μεγάλο χρόνο ζωής καθώς και κλασματικούς εκθέτες με ισχυρή εξάρτηση από τη θερμοκρασία και την πίεση της τελικής κατάστασης. Παρότι τα περισσότερα από αυτά τα δεδομένα βρίσκονται σε συμφωνία με ένα μηχανισμό γέννησης και ανάπτυξης των πυρήνων (nucleation and growth) η εξάρτηση των χαρακτηριστικών χρόνων οργάνωσης από την ενεργό δύναμη, υπεύθυνη για τη δημιουργία της κρυσταλλικής φάσης, δεν έχει την αναμενόμενη εξάρτηση.

Σε σχέση με τους ραβδόμορφους υγρούς κρυστάλλους έγινε η σύνθεση μίας σειράς ολιγο-ινδενιοφλουορενίων καθώς και του αντίστοιχου πολυμερούς και μελετήθηκαν ως προς τη δομή και τη δυναμική. Τα ολιγομερή αυτά μπορούν να θεωρηθούν σαν μοντέλα συστήματα ραβρόμορφων υγρών κρυστάλλων με εφαρμογές σε οργανικές διόδους εκπομπής φωτός (OLEDs). Μελετήθηκαν (i) η παρουσία/απουσία δομικών σφαλμάτων (κετόνες) υπεύθυνων για τη μεταβολή της χρωματικής εκπομπής, (ii) το είδος και η σταθερότητα των φάσεων καθώς και (iii) η προέλευση της δυναμικής υπεύθυνης για τη δημιουργία υάλου. Τα αποτελέσματα ως προς την καθαρότητα, το είδος των φάσεων καθώς και τη δυναμική έδειξαν πολλές ομοιότητες με τα αντίστοιχα ολιγο-φλουορένια. Για παράδειγμα, και τα δύο συστήματα έχουν χαμηλή διηλεκτρική ένταση και χαμηλή αγωγιμότητα που αποδεικνύει την απουσία ατελειών και οδηγεί σε σταθερή εκπομπή μπλε φωτός. Παρόλα αυτά βρέθηκαν και μερικές σημαντικές διαφορές. Τα ολιγο-ινδενιοφλουορένια έχουν μεγαλύτερη οργάνωση σε μικροσκοπικό επίπεδο και δημιουργούν σμηκτικές φάσεις σε αντίθεση με τα ολιγο-φλουορένια που σχηματίζουν νηματικές φάσεις. Οι σμηκτικές φάσεις έχουν ιδιαίτερη σημασία σε ηλεκτρονικές εφαρμογές διότι είναι περισσότερο οργανωμένες. Τα πολυμερή των ινδενιοφλουορενίων έχουν επίσης χαμηλότερο σημείο υάλου από τα αντίστοιχα πολυμερή των φλουορενίων και επομένως παρουσιάζουν μεγαλύτερη ευκαμψία σε ένα εύρος θερμοκρασιών. Τα παραπάνω πλεονεκτήματα των ινδενιοφλουορενίων είναι κρίσιμα για εφαρμογές σε εύκαμπτες οθόνες από οργανικές διόδους εκπομπής φωτός (OLEDs).

ABSTRACT

In the present Thesis the self-assembly and dynamics of a series of discotic and calamitic liquid crystals with applications in electronics and in flexible displays is studied aiming at providing answers to some open literature questions. With respect to the discotic liquid crystals, a series of un-functionalized (Dr. M. Kastler/Prof. Müllen) and dipole functionalized (Mr. X. Dou/Prof. Müllen) HBCs are synthesized and examined by structural (X-ray, NMR, DSC, POM) and dynamic (DS, NMR) probes. Pertinent issues investigated include the effect of dipole substitution on the stability of the liquid crystalline phases, the core dynamics within the columns, the thermodynamic phase diagram and the evolution of structure formation (i.e., kinetics) following distinct paths in the thermodynamic phase diagram. The complete assignment of the "fast" and "slow" dynamics, the thermodynamic phase diagram and the evolution of structure formation following a jump from the liquid crystalline to the crystalline state is made here for the first time.

The un-functionalized hexa-*peri*-hexabenzocoronenes (HBCs), despite their symmetric shape display a very weak dipolar relaxation with a non-Arrhenius temperature dependence that freezes at ~215 K. Dielectric spectroscopy together with NMR (Dr. M. Mondeshki/Prof. Spiess) reveal that the origin of this process is the freezing of the disc axial motion at the respective glass temperature (T_g). For the dipole substituted HBCs, four dipole functionalized HBC derivatives are studied bearing strong (mono-cyano and mono-bromo HBCs) to moderate (dimethoxy and mono-ethynyl HBCs) dipole moments. The effect of dipole substitution with strong dipoles is to destabilize the columnar crystalline phase at low temperatures. On the other hand, substitution with weaker dipoles gives rise to a crystalline phase on cooling. It is shown that the strongly temperature-dependent α-process reflects the collective axial disc rotational dynamics. The freezing of the axial disc motion occurs at about 236 K for the discotics within the liquid crystalline phase (bearing stronger dipoles) and at 253 K for the discotics within the crystalline phase (bearing moderate dipoles). The important conclusion from this study is that the phase state completely controls the dynamic response.

Another pertinent finding is that the relaxation times and breadth of α-process have distinctly different temperature- and pressure-dependencies on entering the crystalline state. These features enable the construction of the first phase diagram (T-P) for HBCs. The main outcome from this study is the increased stability of the crystalline phase at elevated pressures. Subsequently, the transformation of the liquid crystalline to the crystalline phase is studied by pressure jumps aiming at identifying possible intermediate states, nucleation sites and the
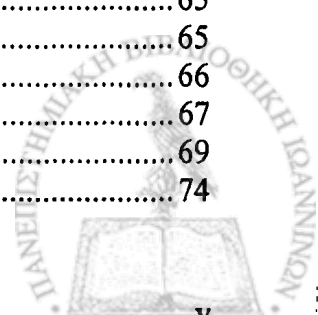
existence of long-lived metastability. The results of the kinetic investigation reveal the absence of intermediate states but show long-lived metastability and fractional exponents that strongly depend on the quench depth. Although most of these finding support nucleation and growth, as the main mechanism of formation of the crystalline phase, the dependence of the kinetic times on the driving force is not typical for a nucleation and growth process.

With respect to the calamitic liquid crystals a series of model oligoindenofluorenes up to the polymer are synthesized (Dr. L. Oldridge, Dr. A. C. Grimsdale/Prof. Müllen) and studied with structural (X-ray, photoluminescence, POM, DSC) and dynamic (DS) probes. These oligomers can be considered as model systems of calamitic liquid crystals with applications as OLEDs. Pertinent issues investigated are the presence or the absence of keton defects, which are responsible for the color instability, the type of mesophases and the origin of the intrinsic molecular dynamics associated with the liquid-to-glass transition. This study facilitated the comparison of oligoindenofluorenes with the more popular oligofluorenes. The results on the purity, the self-assembly and the associated dynamics of the oligoindenofluorenes reveal several similarities with the corresponding oligofluorenes. For instance, both classes of materials show low dielectric loss and low ionic conductivity, that facilitates stable blue emission in both. However, there are some important differences too. The oligoindenofluorenes are more highly ordered and form smectic mesophases rather than nematic mesophases. Smectic mesophases are more amenable to device applications because they are more ordered. The polyindenofluorenes also have a lower glass transition temperature than their fluorene counterparts and so can be switched between the ordered and disordered phases more easily. These are major advantages of oligoindenofluorenes (and PIF) as compared to oligofluorenes (and PF) that are critical for device fabrication.
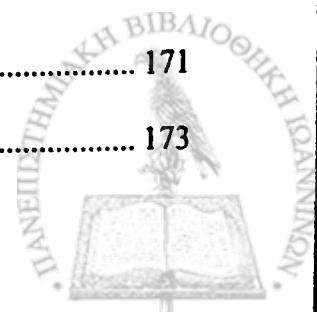
Table of contents

Acknowledgements

I would like to take this opportunity to thank the people that have helped me during my study at the University of Ioannina. This Thesis would not have been possible without the help, guidance and supervision of my advisor Prof. George Floudas. I would like to thank him for giving me the opportunity to work in his group, which exposed me to a variety of interesting scientific projects. His simple approach towards solving complex problems is something I have tried my best to imbibe. I have learned a lot from him and his enthusiasm and support have made working in his lab a wonderful learning experience. In addition, I would like to thank Prof. Marios Kosmas and Assistant Prof. A. Avgeropoulos for scientific discussions durning our group seminars and for serving as a members of the 3-member committee. I am also thankful to Prof. S. Evangelou, Associate Prof. Th. Bakas, Assistant Prof. S. Foulias and Assistant Prof. C. Vlachos for serving in the 7-member committee.

I would like to thank Prof. Dr. K. Müllen and in particular, Mr. X. Dou and Dr. M. Kastler at the Max-Planck Institute for Polymer Research (MPI-P) for the synthesis of the discotic liquid crystals and Dr. Grimsdale and Dr. L. Oldridge for the synthesis of the oligoindenofluorenes. I would also like to thank Prof. Dr. H. W. Spiess and Dr. M. Mondeshki (MPI-P) for the advanced NMR measurements and discussions on the discotic liquid crystals.

I am grateful to my colleagues, Kostas Mpoukouvalas, Perikles Papadopoulos and Antonios Gitsas, for the mentoring that I had received as a new graduate student. I have enjoyed interacting with and learning from all the members of the group. I would also like to thank Mr. George Tsoumanis for technical support and the continued friendly disposition. I would like also to thank Associate Prof. Perikles Tsekeris not only for teaching me quantum mechanics but also for his help and kindness during my PhD study.

I acknowledge IKY for a 4-year fellowship and the University of Mansoura at Egypt for giving me the opportunity to complete my PhD study in Greece.

Outside the realm of physics, I would like to acknowledge the support and encouragement of my parents, and my brothers and sisters. I am truly fortunate to have their blessing and good wishes. Their support and encouragement are the strongest motivation for me to reach this accomplishment. Special thanks go to my wife, Amal, for her continuous encouragement and firm emotional support.

Chapter 1

Introduction

1.1 What is a liquid crystal?

During our years in primary education, we have all been taught that matter exists only in three states: solid, liquid, and gas. However, this is not quite correct: in particular, certain organic materials do not show a single transition from solid to liquid, but rather a cascade of transitions involving new phases; the mechanical and symmetry properties of these phases are intermediate between those of a liquid and of a crystal. For this reason, they have often been called liquid crystals [1-5]. A more proper name is "mesomorphic phases" (i.e., of intermediate form) (Figure 1-1).

crystal   liquid crystal   liquid
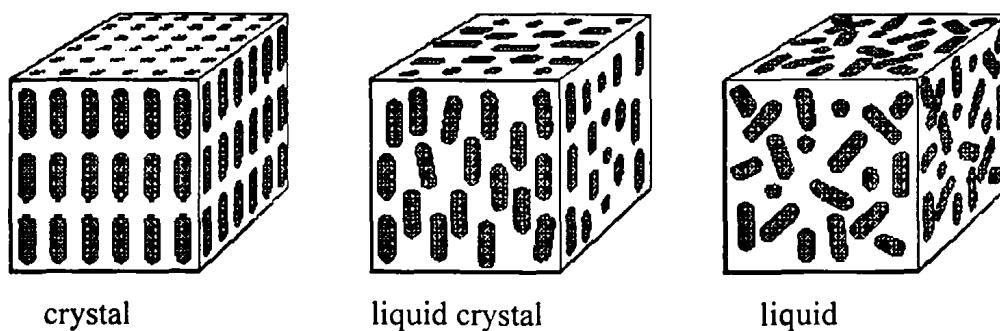
Figure 1-1: *Illustration of crystal, liquid crystal, and liquid phases.*

The study of liquid crystals began in 1888 when an Austrian botanist named Friedrich Reinitzer [6] observed that a material known as cholesteryl benzoate had two distinct "melting points". In his experiments (Figure 1-2), Reinitzer increased the temperature of a solid sample and watched the crystal change into a hazy liquid at 145.5 °C. As he increased the temperature further, the material changed again into a clear, transparent liquid at 178.5 °C. This strange phenomenon of the existence of two "melting points" was explained by the German physicist Otto Lehmann and the term "fluid crystals" or "liquid crystals" (LCs) was introduced. Because

of this early discovery, Reinitzer marks an important milestone in the history of scientific discoveries and immense efforts in research and development have pushed this field to where it now stands.

Liquid crystalline materials are divided into two categories: thermotropic and lyotropic [3]. When a substance passes from the solid, to the liquid crystal and liquid states, as a function of temperature and in the absence of the solvent, the liquid crystalline phases are classified as thermotropic (Figure 1-2), while lyotropic phases form in the presence of a suitable solvent. Thus lyotropic mesophases, found abundantly in biological systems, are always mixtures, whereas thermotropic LCs could be single component or a mixture of many compounds. In the present Thesis, we shall be concerned only with thermotropic LCs.

crystalline solid   liquid crystal   liquid
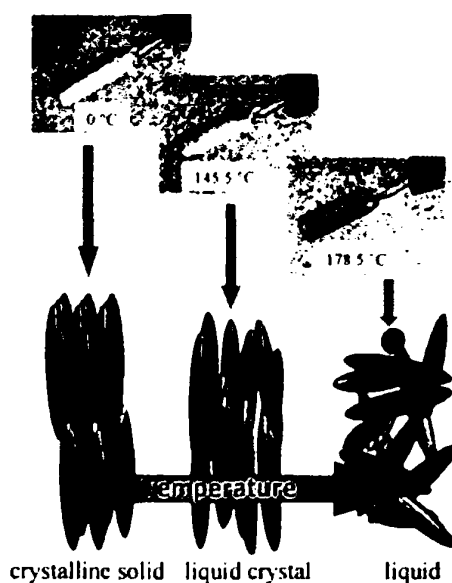
Figure 1-2: *Melting behavior of the thermotropic LCs. Translational order is lost while the orientational order is partially retained. After ref. [7].*

The properties of liquid crystalline materials can be investigated with a wide range of techniques. To investigate phase transitions, usually differential scanning calorimetry (DSC) is used. This technique gives information about the temperatures and enthalpies accompanying these phase transitions, as a function of thermal history. For the identification of the liquid crystalline mesophases, very often the texture observed by polarizing optical microscopy (POM) is analyzed. The defects of a phase give rise to the characteristic textures that are visible between two crossed polarizers. It must be stressed that phase characterization by POM alone is not always sufficient, since in some cases textures of different phases are similar (various columnar phases) or are undistinguishable (e.g. the three nematic phases for disc-shaped mesogenes). Furthermore, POM is bound by its resolution ($\sim 1\mu m$). On the contrary, X-

ray diffraction (XRD) measurements can give detailed information about the molecular organization within a given phase at certain temperature. Solid-state NMR spectroscopy is a powerful tool for investigating the aromatic packing and type of mesophase as well as the geometry of molecular motions in liquid crystals. Using these techniques, the bulk properties and the solid state characteristics of a material can be studied. Dielectric spectroscopy (DS) on the other hand, is capable of measuring the dipolar and ionic relaxations as a function of frequency, temperature and pressure. Thus DS is a very sensitive probe of the molecular processes as well as of phase transformations that affect both the molecular and ionic relaxation. An introduction into the basics of the DS technique and the methods of analysis are discussed in Chapter 2. It is important to mention that other experimental techniques, namely, rheology, neutron and light scattering, not employed in this Thesis, can also provide information on the liquid crystal mesophases.

1.2 Different classes of thermotropic liquid crystals

Thermotropic LCs are generally further distinguished with respect to the molecular shape of the constituent molecules. Based on their appearance they are divided into two different classes: (i) *calamitic mesogens* (mesogen is the fundamental unit of a liquid crystal that induces structural order), which are rod-like molecules (prolate), and (ii) *discotic mesogenes*, which are characterized by a disc-like core (oblate) of the molecule. These rod- and disc-like structures are formed not only by covalent bonds, but also by non-covalent interactions, such as hydrogen bonds, ionic interactions, and metal coordination. Examples of these two classes of liquid crystals are illustrated in Figure 1-3 for indenofluorene monomer (IF-monomer) [8] and branched hexaalkyl hexa-*peri*-hexabenzocoronenes (HBC) [9]. These are the main structural motifs that will be employed in the present study.

(a)

R R

R = C₈H₁₇   R   R

Rigid rode-like part = mesogen

(b)

R=C₁₀.₆

Rigid disc-like part= mesogen
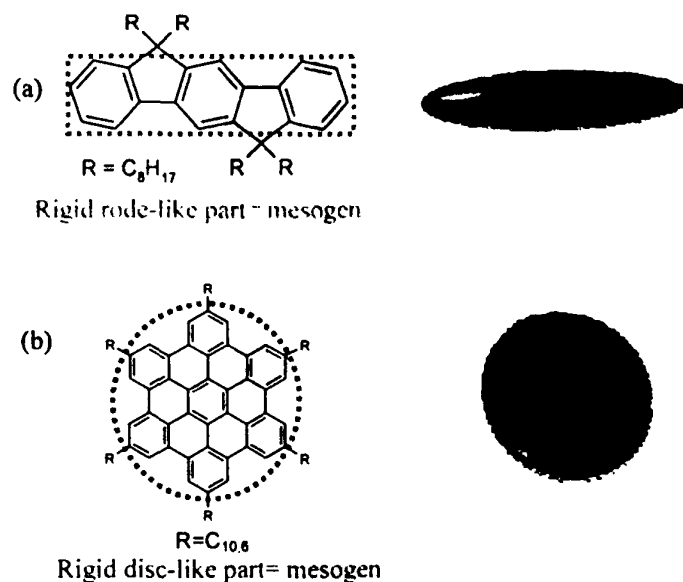
Figure 1-3: *Examples of mesogenic structure: (a) Indenofluorene monomer (IF-monomer) composed of calamitic mesogen and flexible alkyl chains (After ref. [8]). (b) Branched hexaalkyl hexa-peri-hexabenzocoronenes (HBC) comprises a discotic mesogen and several flexible alkyl chains forming the corona (After ref. [9]).*

1.3 Calamitic liquid crystals
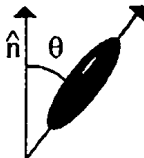
The rod-like configuration of a typical calamitic mesogen such as the IF-monomer (Figure 1-3a) is usually represented by an elongated uniaxial ellipsoid or cylinder, and the structure of its liquid crystalline phase is described as a packing of these ellipsoids or cylinders. While ellipsoids represent rather anisometric molecular shapes, the principal axis of the calamitic mesogen is given by the long axis of the ellipsoid. The self-organization of calamitic mesogenic molecules into various liquid-crystalline phases (that is, spontaneously anisotropic ordered fluids) is driven by the anisotropy in the intermolecular interactions (mainly steric and dispersion interactions) between the molecules.

1.3.1 Ordering of calamitic liquid crystals

Calamitic liquid crystals possess three types of order that give rise to different liquid crystalline phases. These types are [3]:

(i) Orientational order (OO): This type of order is possible when the symmetry axes of the ordering objects are on average parallel to a well-defined spatial direction, $\hat{n}$, known as the director. To quantify just how much orientational order is present in a material consisting of rod-like molecules, a static orientational order parameter (S) is defined. The orientational order parameter is defined as [1,10]:
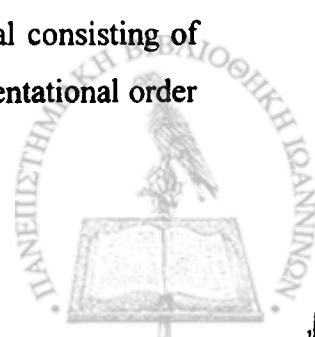
4

$$S = \frac{1}{2}\left\langle\left(3\cos^2\theta - 1\right)\right\rangle$$

(1.1)

where θ is the angle between the director $\hat{n}$ and the long axis of each molecule. In an isotropic liquid (random orientation), $<cos^2\theta>=1/3$, and therefore the order parameter $S=0$. For a perfect crystal (parallel alignment), $\theta=0$ or π, $cos\theta=\pm1$, and the order parameter $S=1$ (the directions $\hat{n}$ and $-\hat{n}$ are equivalent). On the other hand, if the orientational order is such that molecules on average are perpendicular to $\hat{n}$, then S is negative and its values range from 0 to -1/2. For a typical liquid crystal, S is on the order of 0.3 to 0.9, and generally decreases as temperature is raised. In particular, a sharp drop of the order parameter to 0 is observed when the system undergoes a phase transition from a LC phase to the isotropic phase, as illustrated below in Figure 1-4 for a nematic liquid crystal material.
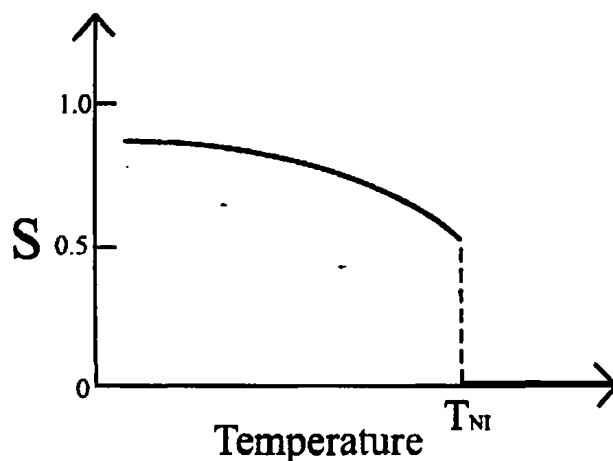
Figure 1-4: *Schematic illustration of the order parameter versus temperature for a nematic liquid crystal. Notice the drop of S to zero when the system undergoes a phase transition from a LC phase to the isotropic phase. After ref. [11].*

(ii) Positional or translational order (PO): When PO is present the system remains invariant under translation by an integer number of lattice translation vectors. The arrangement of the basic units (e.g., molecules) and the mass density (and consequently, electron density) exhibit periodicity. In the simplest case, this periodicity is one dimensional, and may be conveniently represented by a density function of the form [3]:

$$\rho(r) = \langle\rho\rangle + \text{Re}\left[\psi \exp(ik.r)\right]$$

(1.2)

where $<\rho>$ is the average electron density, ψ is the complex amplitude, and k is the wavevector. It is important to note that a liquid crystal system does not have to possess translational order in all three directions. In particular, for the "fluid" smectic (A and C) phases, which possess

5

positional order only in one dimension, the smectic order parameter representing the density variation is written as [3]

$$\left|\psi(r)\right| = \text{Re}\left[\rho_1 \exp\left(\frac{i2\pi z}{d}\right)\right] \qquad (1.3)$$

where d is the thickness of smectic layers which are assumed to be perpendicular to the z-direction.

(iii) Bond orientational order (BOO): A bond, in the present context, is not a chemical bond but a line in space joining two adjacent molecules. If the orientation of these bonds is preserved over a long range, then a system possesses bond orientational order. It is encountered in a category of smectic phases called *hexatic* smectics. In these phases, the molecules within a smectic plane possess BOO and, since the molecules can best pack in a hexagonal fashion, the orientation of bonds possess six-fold symmetry. A complex order parameter, ψ_6, similar to the smectic density wave is used to account for BOO [3];

$$\psi_6 = \text{Re}\left[I_6 \exp(6i\Phi)\right] \qquad (1.4)$$

where I_6 is a complex amplitude, and Φ is the azimuthal angle with respect to the layer normal. The BOO and PO can be either short-range (SR), as is observed in liquids, or long-range as observed in crystals. It is possible for PO to become short-range due to the presence of dislocations and disclinations which can leave the BOO unperturbed. The three types of order discussed above are shown in two dimensions in Figure 1-5.
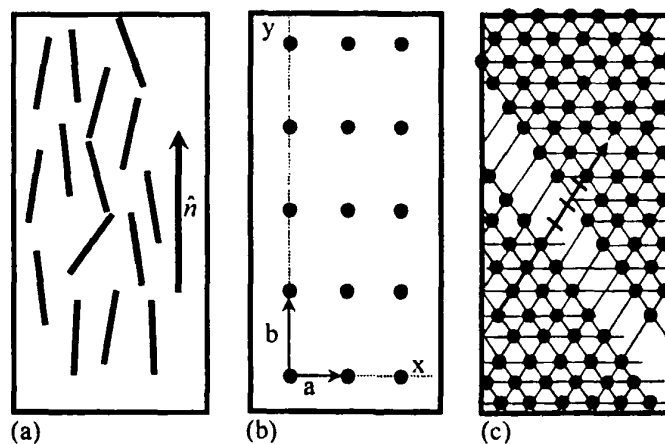
Figure 1-5: *Schematic representation of the three basic types of order: (a) orientational order parallel to the director $\hat{n}$, (b) positional order in two dimensions with lattice vectors a and b, and (c) bond orientational order. In the last case, translation from one lattice site along the arrow by an integer multiple of lattice spacing shows a lack of translation symmetry. After ref. [3].*

All types of ordering in calamitic liquid crystals can be measured experimentally in a number of ways (diamagnetism, birefringence, Raman scattering, NMR and EPR can also be used to determine S [1]).

1.3.2 Mesophases formed by calamitic liquid crystals

The different mesophases formed by rod-like molecules are [3]:

1.3.2.1 Smectic meosophases

The name "smectic" was given by G. Friedel to describe certain mesophases that feel slippery like soap when touched, and was originally associated with what is now known as the smectic-A phase. The important feature which distinguishes smectic phases is that they have a layered structure. In fact, as mentioned above, PO and BOO have all been observed among molecules lying in a smectic plane resulting in over 20 smectic liquid crystalline phases. A smectic phase has at least two unique directions, the director $\hat{n}$ and the layer normal. Smectic mesophases can be classified into two types:

(A) Non-tilted smectic phases: This is a sub-class of thermotropic liquid crystalline phases which are free from chirality and molecular tilt. The different classes of the non-tilted smectic phases are:

(i) The smectic-A phase (SmA): The SmA phase made of non-chiral and non-polar molecules and characterized by a one-dimensional layered structure (or PO) as shown in Figure 1-6 along with the corresponding optical microscopy (POM) image. This phase is uniaxial, the layers are essentially incompressible, and the long axes of molecules within the layer, on the average, are perpendicular to the layers. The SmA is characterized by short-range PO and short-range BOO in the layers, and quasi long-range PO perpendicular to the planes.

(ii) The hexatic-B or hexatic smectic-B phase (HexB): In the HexB phase, the molecules are locally hexagonally packed, and the resulting six-fold BOO is maintained for macroscopic distances. The HexB is a uniaxial phase characterized by quasi long-range PO in the direction perpendicular to the layers, short-range PO within the smectic layers, and most importantly BOO.

(iii) The crystal-B phase (CrB): There are several crystalline smectic phases; that is, smectics which are very close to three-dimensional crystals. They differ from true crystal phases in one important aspect: the molecules have rotational freedom about their long axis, i.e., their thermal motion is not completely frozen. Such phases, in which the position of the molecules is fixed but their motion is not arrested, should more correctly be classified as plastic crystalline
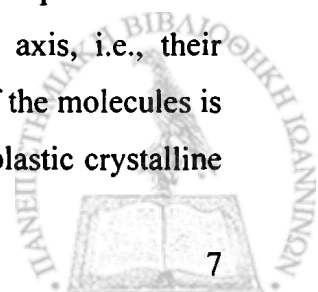
phases. The common feature of these phases is that the average molecular orientation is normal to smectic layers and within each layer the molecules are ordered in a triangular lattice and possess long-range PO and, of course, BOO. The stacking of these triangular arrays varies from material to material and restacking transitions have been observed.

(iv) The crystal-E phase (CrE): As in the crystal-B phase, the molecules within a smectic-E plane are arranged on a triangular (or hexagonal) lattice and are perpendicular to the smectic layers. This phase differs from the crystal-B phase in the rotational motion of molecules. In the crystal-E phase, the thermal motion of molecules is reduced to the extent that they arrange themselves in a *herringbone* pattern within a smectic layer. With this type of packing their continuous rotational freedom is hindered.

(B) Tilted smectic phases: There is a complete set of smectic phases in which the long axis of molecules (or the director) is not perpendicular to the layer normal, but makes a relatively large angle. The different types of these tilted phases are:

(a) The smectic-C phase (SmC): The SmC phase is similar to the SmA phase in that it is a layered structure and each layer may be thought of as a two-dimensional liquid film with no BOO or PO. However, in this case the molecules are on the average tilted with respect to the layer normal, subsequently, $\hat{n}$ and the smectic layer normal are not collinear, as shown in Figure 1-6 along with the corresponding optical microscopy image.
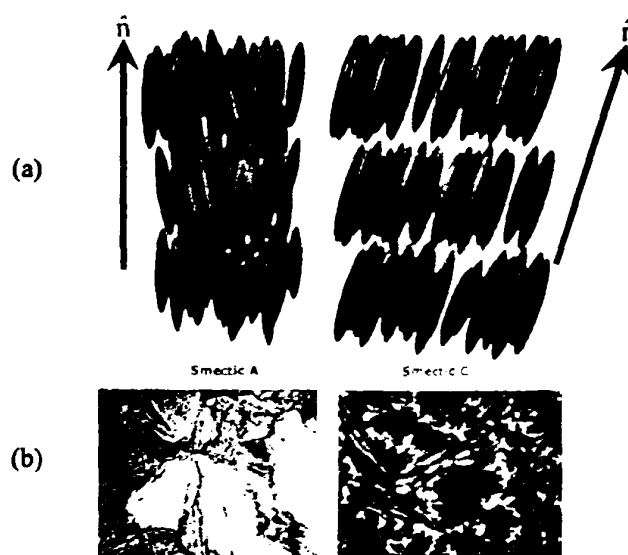
Figure 1-6: *(a) Schematic illustration of the arrangement of molecules in a smectic-A and smectic-C mesophase (After ref. [12]). (b) POM images of smectic-A phase (fan-shaped texture) (After ref.[8]) and smectic-C phase (broken fan texture) (After ref. [13]).*

Furthermore, the tilt angle is a strong function of temperature. The angle a, which is an order parameter for this phase, can range from zero to as high as 45-50° deep in the SmC phase. The

temperature dependence of molecular tilt in the smectic phases of terephthal-bis-(4n)-butylaniline (TBBA) is shown in Figure 1-7.
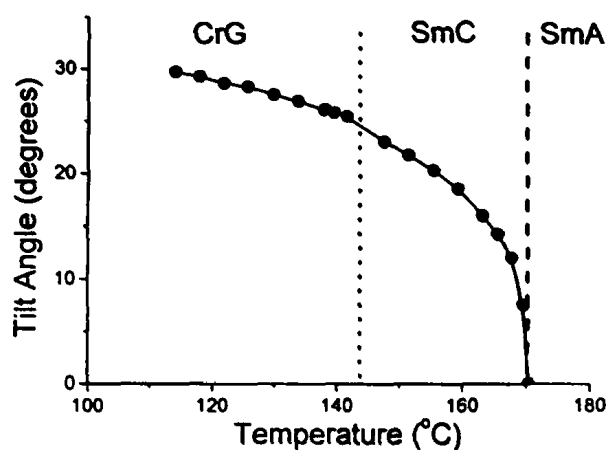
Figure 1-7: *Temperature dependence of molecular tilt in the SmC phase of TBBA determined by high-resolution X-ray diffraction. After ref. [3].*

(b) The smectic-F (HexF) and smectic-I (HexI) phases: In the HexF phase, the tilt is in a direction perpendicular to the sides of the hexagon. If molecules tilt towards a corner, it is known as the HexI phase. When both phases are formed by the same material, the HexI is always the higher temperature phase.

(c) The crystal-G (CrG) and crystal-J (CrJ) phases: The CrG and CrJ phases are the phases normally obtained at temperatures lower than the HexF and HexI phases. The molecular arrangement within a smectic plane possess long-range PO and BOO. In both these phases and their higher temperature hexatic versions, the molecules are tilted with respect to the layer normals by approximately 25 to 30°. The local order is hexagonal which is distorted due to molecular tilt, with molecules having rotational freedom comparable to the untilted crystal-B phase.

(d) The crystal-H (CrH) and crystal-K (CrK) phases: The CrH and CrK phases are tilted versions of the CrE phase. The molecules in the CrH (K) phase are tilted in a manner similar to the CrG (J) and HexF (HexI) phases, i.e., along the direction perpendicular to a side (towards a corner) of the underlying hexagonal structure. The general sequence of tilted phases with decreasing temperature is shown in Figure 1-8.

9

```
                              Smectic-C
                          ↙               ↘
              Smectic-F                         Smectic-I
                 ⬇                                 ⬇
              Crystal-G                         Crystal-J
                 ⬇                                 ⬇
              Crystal-H                         Crystal-K
```
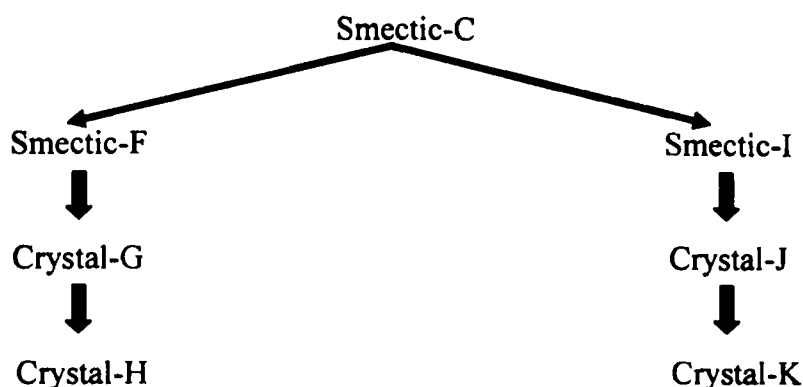
Figure 1-8: *A typical phase sequence for tilted phases of rod-like molecules. After ref. [3].*

1.3.2.2 Nematic mesophases

The nematic mesophases are non-tilted phases which have long-range orientational order, OO, but lack PO and BOO [3]. Thus, the molecules *flow* and their center of mass positions are randomly distributed as in a liquid, but they all point in the same direction (within each domain). The two primary types of nematic LCs are uniaxial and biaxial (Figure 1-9) [14].
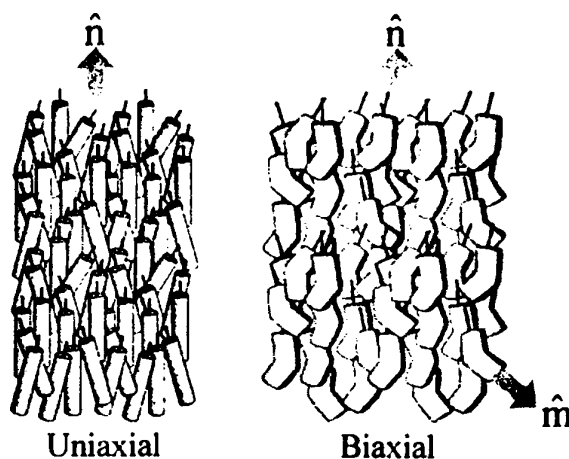
Uniaxial   Biaxial

Figure 1-9: *Schematic illustration of nematic phases with major* $\hat{n}$ *and minor* $\hat{m}$ *directors: (left) uniaxial nematic comprised of cylindrically symmetric (calamitic) mesogenes; (right) biaxial nematic phase of nonlinear (bent-core) mesogenes. After ref. [14].*

Both are characterized by the following features : (a) absence of PO and BOO; (b) OO parallel to the director $\hat{n}$; (c) the direction of $\hat{n}$ in space is arbitrary, and typically imposed by outside forces such as electric/magnetic fields; (d) $\hat{n}$ and -$\hat{n}$ are equivalent, and (e) molecules which form nematics are either achiral (identical to their mirror images) or racemic (contain equal numbers of left- and right-handed molecules). However, biaxial nematics do not possess cylindrical symmetry about $\hat{n}$ but have two unique directions rendering it biaxial. It should be pointed out, that despite some reports, there are no known thermotropic biaxial nematic phases.

The X-ray scattering pattern of nematic compounds is diffuse and liquid-like due to the absence of long-range PO.

In a nematic liquid the director field is not uniform unless an external field of electric, magnetic or mechanical nature is applied. The director may vary in a smooth continuous way around certain points, or more abruptly as in domain walls. In the case of heterogeneous planar orientation of nematics, the director $\hat{n}$ is parallel to substrates but points in different directions. Such a structure appears as a schlieren texture between crossed polarizers in a POM (Figure 1-10b). This texture exists also in SmC, SmI, SmF, and biaxial SmA phases.
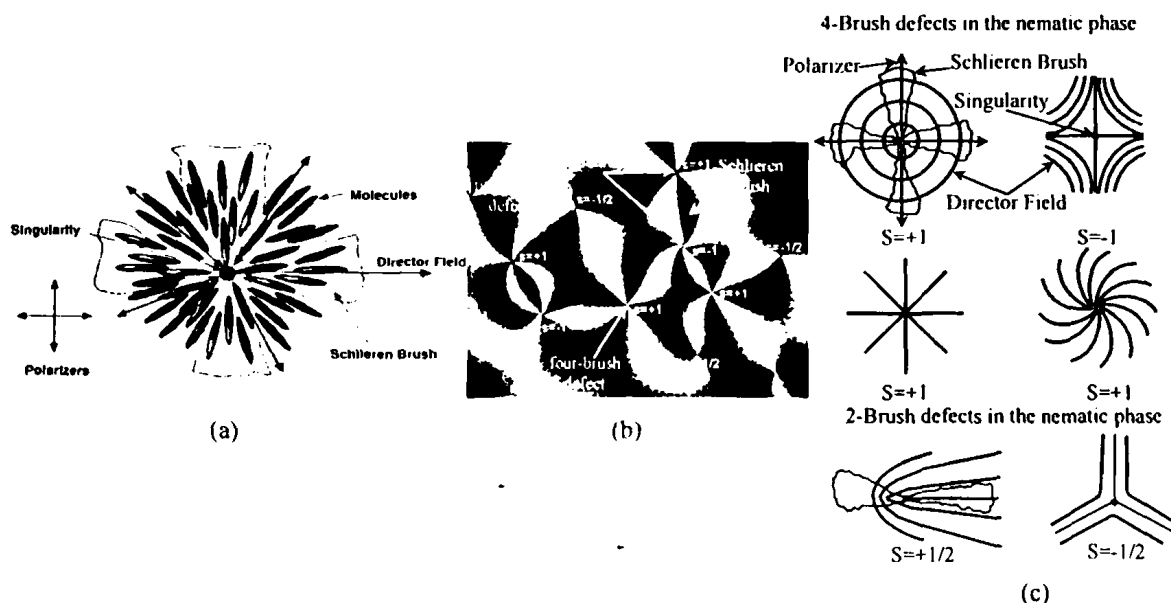
Figure 1-10: *(a) Schematic illustration of the origin of schlieren brushes in a nematic liquid crystal mesophase (After ref. [15]). (b) POM image of the nematic schlieren defect texture (After ref. [16]). (c) Schematic illustration of disclinations of strengths S=±1 and ±1/2 in liquid crystals with the local directors indicated by the lines. Each type of disclination has a central singularity (After ref. [10,17]).*

As shown in Figure 1-10b, the schlieren texture shows dark brushes, which indicate that the local molecular director of the optically anisotropic region is parallel to the polarizer or to the analyzer, or that region is optically isotropic. The points, where two or four brushes meet, correspond to the director singularities and are called *disclinations*. Disclinations are "defects", which break rotational symmetries in liquid crystals and can be associated with a certain extra volume, enthalpy and entropy. The molecular director "rotates" about a disclination (point) line. The disclination is characterized by its strength S, which shows how much the director rotates in each point on the closed curve around the singularity point. The points where four brushes meet (Figure 1-10b) correspond to the disclinations with $S=\pm 1$, and the molecular director is rotating by 360° about the center of the disclination (Figure 1-10c). The points where two brushes meet correspond to the disclinations with $S=\pm 1/2$, and the director is

11

rotating by $180°$ about the center of the disclination (Figure 1-10c). In fact, disclinations of $S=\pm1/2$ appear only in nematics. The strength of the disclination is given by [10]:

$$|\text{strength}| = \frac{\text{number of bands}}{4} = \frac{\sum \text{angular change of director}}{360°} \quad (1.5)$$

To distinguish between the disclinations of different sign, one can rotate the sample possessing schlieren texture between the crossed polarizers. When the LC sample is rotated, the black brushes move continuously indicating a continuous change of the director $\hat{n}$. At points with positive sign, the brushes rotate in the same sense as the sample, but at the points with negative sign of the strength brushes move in the opposite direction. Two disclinations with the same strength but with different signs may combine and annihilate one another. A uniform director field is then created in this area.

The general sequence of the non-tilted calamitic liquid crystal phases with decreasing temperature is shown in Figure 1-11 [3].

Non-tilted calamitic liquid crystal phases			
Temperature	**Phase**	**Type of order**	**Abbreviation**
	Isotropic	disordered	I
	Nematic	OO	N
	Smectic-A	PO; $\hat{n}\perp$ to layers	SmA
	Hexatic-B	In-plane: LR-BOO, SR-PO	HexB
	Crystal-B	In-plane: LR-PO and BOO (Molecular rotation allowed)	CrB
	Crystal-E	In-plane: LR-PO and BOO (Molecular rotation restricted)	CrE

Figure 1-11: *An illustration of a possible phase progression in the non-tilted calamitic liquid crystal phases. The most symmetric and least ordered phase is at the top, and the most ordered and least symmetric phase is at the bottom. The abbreviations SR=short-range and LR=long-range. After ref. [3].*

Smectic, nematic and crystal phases of rod-like molecules with long- and short-range order are compiled in Figure 1-12 [15].
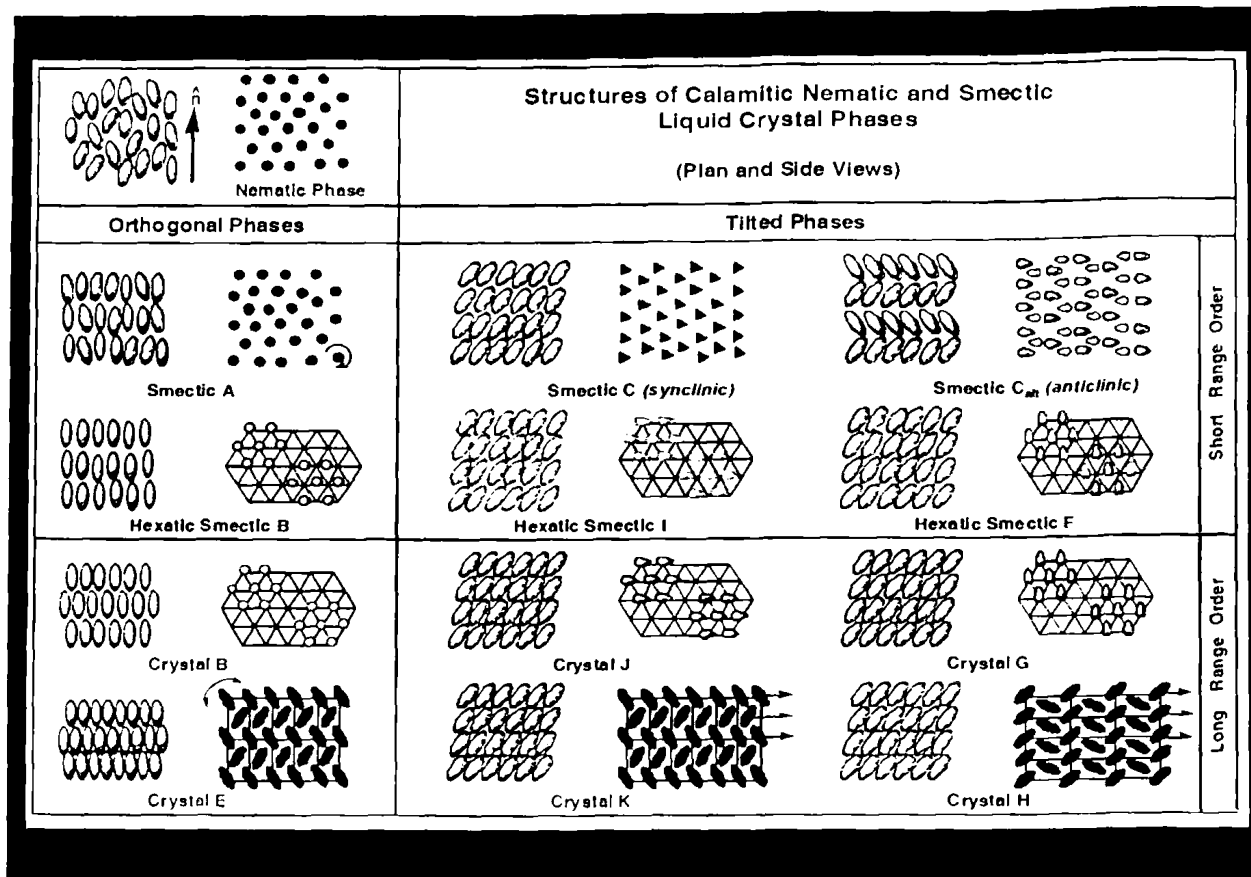
Figure 1-12: *Schematic illustration of the arrangement of the rod-like molecules in the smectic, nematic and crystal phases. After ref. [15].*

1.3.2.3 Chiral tilted mesophases

Molecules which are not identical to their mirror image are said to be chiral. Molecular chirality has profound influence on liquid crystal properties. Chiral tilted mesophases are classified into the following types [3]:

(i) Cholesteric or chiral nematic mesophase: The phase which, in most regards, is similar to the nematic phase but with chiral structure is known as the cholesteric phase. The name is based on the fact that derivatives of the infamous cholesterol were initially found to exhibit this phase. This phase forms if the molecules are either intrinsically chiral or if chiral dopants are added to a non-chiral (regular) nematic. The chirality of the system leads to a helical distortion, in which the director $\hat{n}$ rotates continuously in space along, say, the z-direction, with a spatial period of π/p (Figure 1-13). Here p is the pitch, which is defined as the distance it takes for the director to rotate one full turn of $360°$ in the helix as illustrated in Figure 1-14. The pitch typically changes when the temperature is altered or when other molecules are added to the LC host, allowing the pitch of a given material to be tuned accordingly. In some liquid crystal systems, the pitch is of the same order as the wavelength of visible light. This causes these

systems to exhibit unique optical properties, such as selective reflection, and these properties are exploited in a number of optical applications.
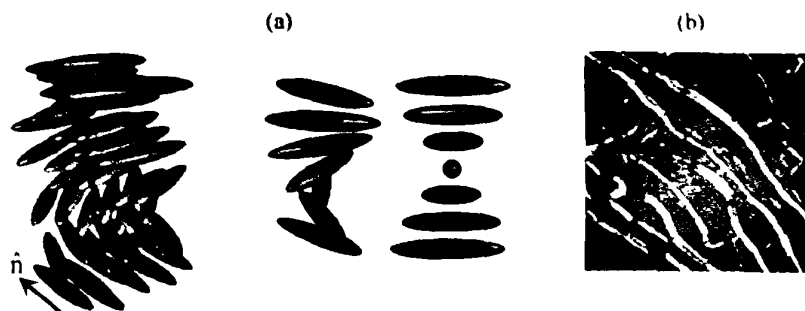
Figure 1-13: *(a) Schematic illustration of the arrangement of molecules in the cholesteric liquid crystal mesophase (After ref. [12]). (b) POM image of the cholesteric liquid crystal mesophase (oily streak texture) (After ref. [13]).*
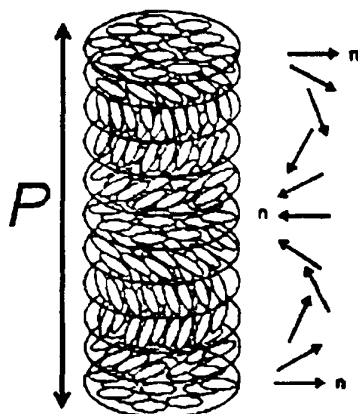
Figure 1-14: *Schematic illustration of the arrangement of molecules in the cholesteric liquid crystal phase to complete rotation of 360 degrees in the helix. After ref. [18].*

(ii) Chiral smectic mesophases: The smectic mesophases formed by chiral molecules are designated with an asterisk over the letter specifying the analogous non-chiral phase. For example, the chiral smectic-A is abbreviated as SmA* (many of the physical properties of a chiral phase, e.g., the linear electro-optical effect of the SmA* phase, are not present in the SmA phase). Tilted phases occur for chiral molecules. The simplest is called the fluid smectic-C*, SmC*, phase. This extra degree of freedom obtained from chirality causes a distortion in the SmC structure, and the direction of tilt processes around the layer normal as one moves from layer to layer. A schematic picture of the SmC* is shown in Figure 1-15. This phase is ferroelectric in nature as the molecules have a transverse permanent dipole moment (this property has been the basis of many new technologies and the subject of intense study in its own right). The precession of tilt angle from layer to layer is also seen in other chiral smectic and crystalline phases. Because the molecules are chiral in analogy with the SmC* all of these phases are also labeled with a star (HexF*, HexI*, CrG*, CrJ*, CrH* and CrK*).
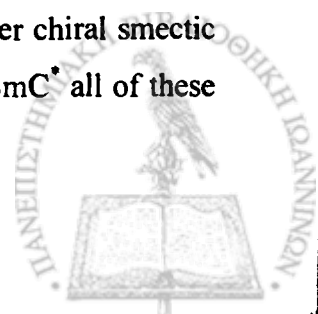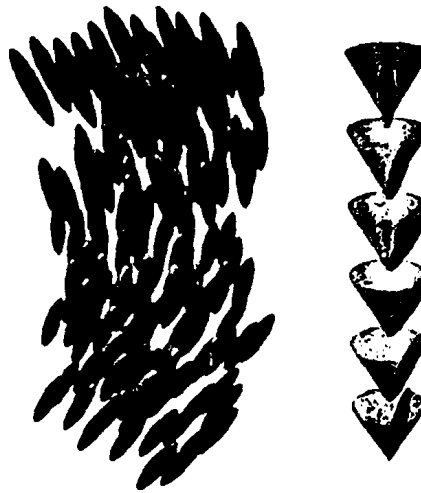
Figure 1.15: *A schematic diagram of the SmC* phase showing the precession of the tilt angle as one moves along the layer normal. After ref. [12].*

1.3.3 Orientation of calamitic liquid crystals on substrates

Almost any surface causes the director, $\hat{n}$, to orient in a specific direction near the surface. The molecules alignment at surfaces propagates over macroscopic distances. There are three main types of the LC director $\hat{n}$ alignment near solid walls or at the free surface: homeotropic, planar, and tilted orientations (Figure 1-16a,b). The surface, which is in a contact with the mesophase is usually considered to be flat on the microscopic scale, and the position of the director near it is determined by the polar, θ, and azimuthal, φ, angles (Figure 1-16c).
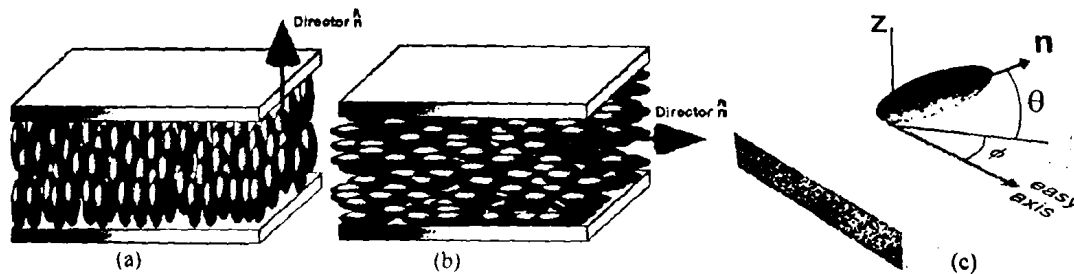
Figure 1-16: *Types of calamitic liquid crystals orientation near surface: (a) homeotropic orientation, (b) planar orientation (homogeneous), and (c) position of director $\hat{n}$ near surface is determined by polar θ and azimuthal φ angles (a,b after ref. [15] while c modified after ref. [16]).*

When the director $\hat{n}$ is oriented homeotropically, the polar angle $\theta = 90°$. The director within the planar orientation lies in the plane of the surface or phase separation border. In the later case two possible orientations exist: (i) homogeneous planar orientation, when the director is oriented uniformly over the surface and φ is fixed and (ii) heterogeneous planar orientation, when the orientation of the director is not uniform over the surface and φ has different fixed values in different points of the surface. In case of a tilted orientation, θ, is fixed and, φ, is

arbitrary. The preferred direction of the director $\hat{n}$ at the surfaces set by alignment is called "easy axis".

1.4 Thermodynamic properties of liquid crystals

1.4.1 Classification of phase transitions

Phase transition or phase change is the transformation of a thermodynamic system from one phase to another. The distinguishing characteristic of a phase transition is an abrupt change in one or more physical properties. According to Ehrenfest [19], a first-order transition is one for which the free energy as a function of any given state variable (V, P, T) is continuous, but the first partial derivatives of the free energy with respect to the relevant state variables are discontinuous. Thus, if the Gibbs free energy, G, at the transition temperature is continuous, but $(\partial G/\partial T)_P$ and $(\partial G/\partial P)_T$ are discontinuous, we have a first-order transition. At a typical first-order transition point, such as fusion or vaporization, there is a discontinuity in entropy S, volume V and enthalpy H, since [19]

$$G = U - TS + PV = H - TS$$

$$\left[\frac{\partial G}{\partial T}\right]_P = -S, \quad \left[\frac{\partial G}{\partial P}\right]_T = V, \quad \left[\frac{\partial(G/T)}{\partial(1/T)}\right]_P = H \tag{1.6}$$

Similarly, a second-order transition is characterized by a discontinuity in the second partial derivatives of the free energy function with respect to the relevant state variables, but by continuity in both the free energy and its first partial derivatives. Thus, there is no discontinuity in S, V or H at the transition temperature but there is in the heat capacity, C_p, the isothermal compressibility, κ_T, and the coefficient of thermal expansion, α, since [19]

$$-\left[\frac{\partial^2 G}{\partial T}\right]_P = \left[\frac{\partial S}{\partial T}\right]_P = \frac{C_p}{T}, \quad \left[\frac{\partial^2 G}{\partial P^2}\right]_T = \left[\frac{\partial V}{\partial P}\right]_T = -\kappa_T V$$

$$\frac{\partial}{\partial T}\left[\left[\frac{\partial(G/T)}{\partial(1/T)}\right]_P\right]_P = \left[\frac{\partial H}{\partial T}\right]_P = C_p, \quad \left[\frac{\partial}{\partial T}\left[\frac{\partial G}{\partial P}\right]_T\right]_P = \left[\frac{\partial V}{\partial T}\right]_P = \alpha V \tag{1.7}$$

In Figure 1-17 are depicted schematically the behaviors of the first and second derivatives of the Gibbs free energy function for first-order, second-order, first-order with pretransition, and infinite-order.
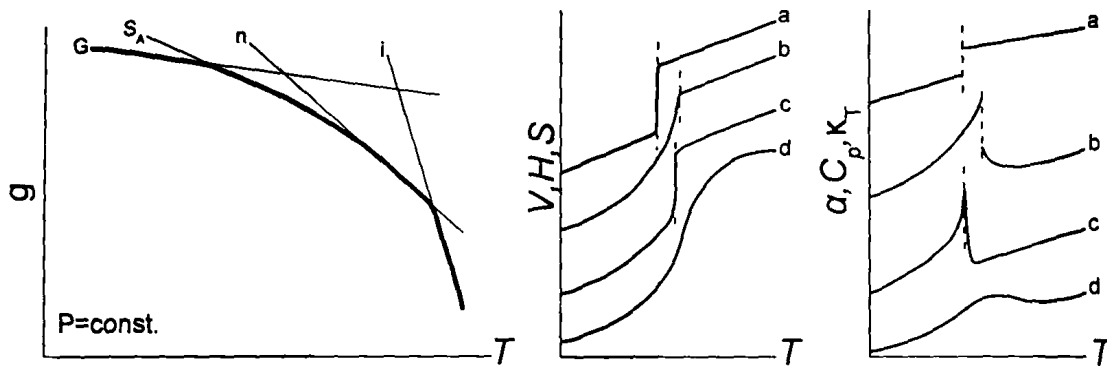
Figure 1-17: *Schematic representation of changes with temperature of the free energy (left) and its first (middle) and second (right) derivatives for: (a) first order, (b) second order, (c) first order with pretransition, and (d) infinite order. The vertical dashed-line indicates the transition temperature T_{tr}. After ref. [5].*

Transitions of the types shown by Figure 1-17a,b,c occur only if condensed phases are involved. These transitions are characterized by a discontinuity in the first and/or the second partial derivatives of the free energy function. Figure 1-17d, on the other hand, illustrates a completely continuous transition between two states with different characteristics, as with a homogenous gas or solution equilibrium.

Phase transitions between the smectic, nematic and isotropic phases of liquid crystals are all of first order and thus the free energy changes slope at the respective temperatures (Figure 1-17). Pressure exerts a strong influence at the transition temperatures through the well-known Clausius-Clapeyron relation [19]

$$\frac{dP}{dT} = \frac{\Delta H}{T \Delta V}$$ (1.8)

where ΔH is the heat of fusion associated with the phase transformation, T is the transition temperature at atmospheric pressure and ΔV is the associated change of specific volume. Transitions between the different liquid crystalline phases can be identified by thermal, i.e., differential scanning calorimetry (DSC) and thermodynamic (pressure-volume-temperature, *PVT*) measurements. Figure 1-18 displays the DSC trace and *PVT* measurements of a side-chain polymer liquid crystal with a poly(methyl acrylate) backbone and a (*p*-alkoxy-phenyl)-benzoate mesogenic group [20]. From DSC, two first-order transitions can be seen at 370 and 397 K, associated with the smectic-to-nematic and nematic-to-isotropic transitions, respectively. In addition, a glass temperature (is the temperature at which the material goes from a rubber-like state to a hard, glass-like state) exists at lower temperatures (T_g=300 K).
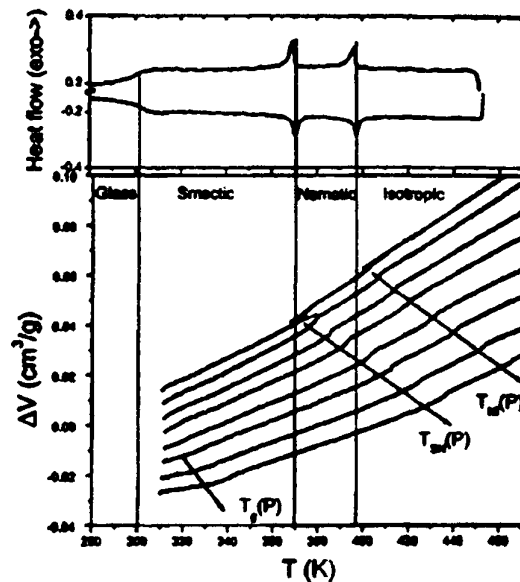
Figure 1-18: *(Top) DSC trace of the polymer taken on cooling and subsequent heating (with a rate of 10 K/min) indicating a glass transition at 300 K, a smectic-to-nematic transition at about 370 K and a nematic-to-isotropic transition at 397 K. Vertical lines indicate the transition temperatures. (Bottom) Relative change in the specific volume (ΔV) as a function of temperature for different pressures in the range from 10 to 200 MPa. The data were obtained under "isothermal" conditions. The lines through the 10 MPa data points are guides to the eye. The arrows indicate the pressure dependence of the glass temperature (T_g), of the smectic-to-nematic transition (T_{SN}), and of the nematic-to-isotropic transition (T_{NI}). Notice the steeper dependencies of the first order transitions as opposed to the glass temperature. After ref. [20].*

In the *PVT* measurements, we notice the change of slope associated with the glass temperature and, at higher temperatures, the two first- order transitions accompanied by a stepwise increase in specific volume. The effect of compression on the three temperatures is very distinct. Pressure affects the glass temperature to a lesser extent as compared to the first-order transitions at higher temperatures. Thus, DSC and *PVT* results can reveal the existence of considerable mesoscopic order as well as transitions between the different liquid crystalline phases. From the *PVT* data in particular, the phase diagram (i.e., *T* vs. *P*) can be constructed.

1.4.2 Theory of phase transitions

Landau considered the free energy, $G=G(T,P)$, as a function of pressure, temperature, and the degree of order, ζ, and developed it as an exponential series of ζ (Eq. (1.9)) [5]

$$G = G_0 + \alpha\zeta + \beta\zeta^2 + \frac{1}{3}\gamma\zeta^3 + 0\left(\zeta^4\right) \qquad (1.9)$$

where P, T, and ζ are considered as independent variables determining the free energy and α, β, and γ are functions of pressure and temperature. Higher terms in Eq. (1.9) are supposed to vanish with higher order. ζ has been conceived in the sense of an occupational probability of
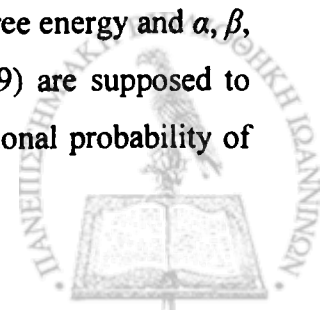
lattice positions, such that when it is equal to zero, then there is a completely random distribution, corresponding to the entropy maximum. In a more sophisticated way and in direct relation to the nematic order, de Gennes replaced ζ by the tensor order parameter, Q_{ik}, which gives a much more translucent picture, because Q is well defined [5]:

$$G = G_0 + \frac{1}{2} A(T) Q_{\alpha\beta} Q_{\beta\alpha} + \frac{1}{3} B(T) Q_{\alpha\beta} Q_{\beta\alpha} Q_{\beta\gamma} + 0 \left(Q^4 \right) \qquad (1.10)$$

To fit Eq. (1.10) with experimental results the coefficient must be chosen adequately, regarding their temperature dependence, and, as the most essential problem, stability criteria have to be introduced. Special cases of stability conditions are demonstrated in Figure 1-19, the curves being selected quit arbitrarily.
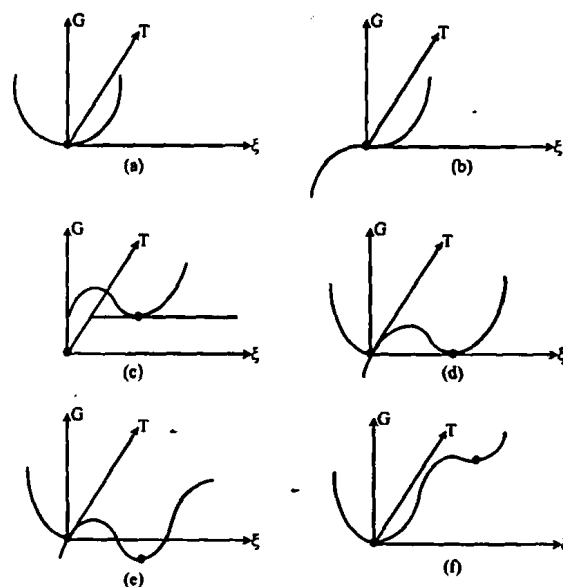
Figure 1-19: *Some arbitrary chosen curves showing the Gibbs free energy, G, as a function of temperature and the degree of order, ζ. (a) stable disordered phase, (b) critical point, (c) stable ordered phase, (d) equilibrium order-disorder transition, (e) stable ordered phase and metastable disordered phase, and (f) stable disordered phase and metastable ordered phase. Modified after ref. [5].*

Thermodynamically stable and metastable states are represented by the minima $\partial G/\partial\zeta = 0$ and the isotropic state is defined by $\zeta = 0$. The explanations of the stability conditions demonstrated in Figure 1-19 are: (i) curve a represents a stable disordered phase ($\partial G/\partial\zeta = 0$ and $\zeta = 0$). (ii) curve b represents a "critical point" which is defined by the first, second and third derivative of Eq. (1.9):

$$\frac{\partial G}{\partial \xi} = \alpha + 2\beta\xi + \gamma\xi^2 = 0 \Rightarrow \alpha = \beta = 0; \xi = 0$$

$$\frac{\partial^2 G}{\partial \xi^2} = 2\beta + 2\gamma\xi = 0 \Rightarrow \beta = 0; \gamma \neq 0; \xi = 0 \qquad (1.11)$$

$$\frac{\partial^3 G}{\partial \xi^3} = 2\gamma > 0 \Rightarrow \gamma \neq 0$$

In such case the critical point is necessarily characterized by the conditions $\alpha=\beta=0$, $\xi=0$, whilst $\gamma\neq0$. (iii) curve c represents a stable ordered phase ($\partial G/\partial\xi=0$ and $\xi\neq0$), (iv) curve d represents a stable equilibrium between disordered ($\xi=0$) and ordered ($\xi\neq0$) phases, (v) curve e represents a stable ordered phase at $\xi\neq0$ and metastable disordered phase at $\xi=0$, (vi) curve f represents a stable disordered phase at $\xi=0$ and metastable disordered phase at $\xi\neq0$. Theory of higher order phase transitions is discussed in Appendix 1.

1.4.3 High-pressure investigations

There exist only few studies on the pressure dependence of the transition temperatures of mesophases. For example, the P-T phase diagrams of the calamitic liquid crystals p,p'-bis(heptyloxy)azoxybenzene [5] and cholesteryl myristate [21] are shown in Figure 1-20.
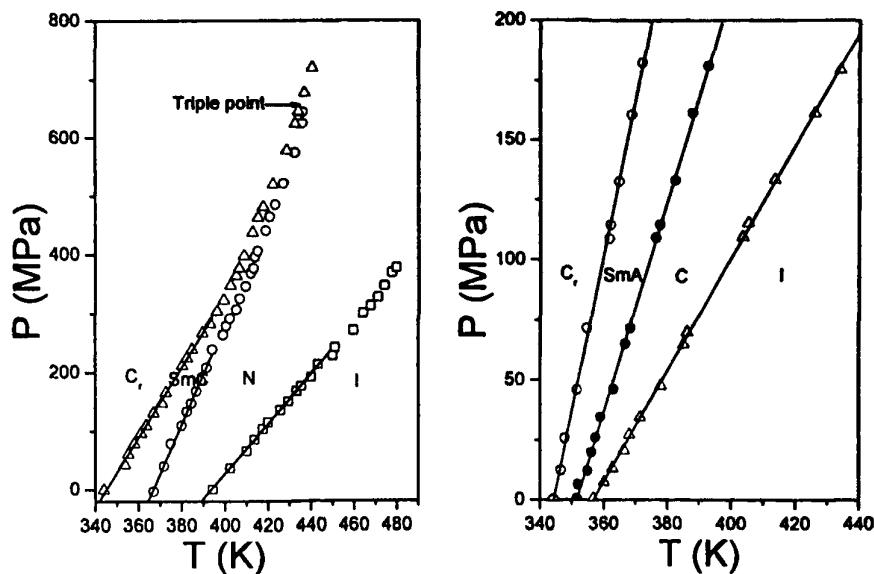
Figure 1-20: *Phase diagrams (pressure, P, vs. temperature, T) for the p,p'-bis(heptyloxy)azoxybenzene (left) (After ref. [5]) and the cholesteryl myristate (right) (After ref. [21]). The C, SmC, SmA, N, C, and I correspond to the crystal, smectic C, smectic A, nematic, cholesteric, and isotropic phases, respectively.*

The first compound (p,p'-bis(heptyloxy)azoxybenzene), exhibits four phases: crystal (C_r), SmC, nematic (N), and isotropic (I) phases. With increasing pressure, the nematic phase, N, has greater temperature range stability whereas the SmC, range narrows. At 660 MPa and 435 K the N-SmC boundary intersects the melting curve at a N-C_r-SmC triple point above which the transition is second order. The latent heat of the transition vanishes as the tricritical point is approached from below. The slopes (dT/dP) at P=1 atmosphere (1 atm.=0.1 MPa) for the C_r-SmC, SmC-N, and N-I transitions will be discussed later in Chapter 4 with respect to the present investigation. The second compound (cholesteryl myristate) shows four phases: crystal (C_r), smectic A (SmA), cholesteric (C), and isotropic phases. The tricritical behavior is not observed here indicating that the smectic A-cholesteric transition is of first order. The dT/dP values for the C_r-SmA, SmA-C, and C-I transitions are discussed later with respect to the present investigation.

For discotic liquid crystals, the phase behavior is relatively unexplored. Some pressure studies have been carried out on the hexa-alkanoyloxybenzenes (Figure 1-21) [22].
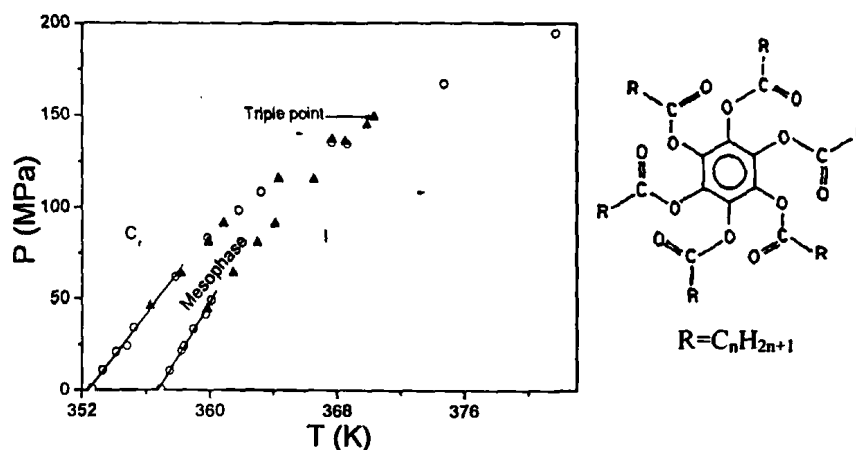
Figure 1-21: *Pressure-temperature phase diagram (left) of benzene hexa-n-octanoate (right). The circles and triangles represent two independent sets of measurement. After ref. [22].*

From the homologues (n=6,7 and 8) only three were mesomorphic at atmospheric pressure, the last (n=8) being monotropic. For all three compounds, the temperature range of the mesophase decreased with increasing pressure, and finally disappeared. The crystal-mesophase-isotropic triple points occurred at 296 MPa and 389.65 K, 143 MPa and 370.55 K, and 130 MPa and 347.15 K for n=6,7 and 8, respectively. On the other hand, the n=5 homologue, which is non-mesomorphic at atmospheric pressure, showed pressure-induced mesomorphism. The dT/dP

values obtained at $P=1$ atmosphere for the C_r-mesophase and mesophase-I transitions will be compared later (see Chapter 4) with the results of the present study.

In a second study, the effect of high pressure on the columnar density modulation of the hexa-octylether of rufigallol (rufigallol-HOE), resulting from the incommensurability of the aromatic and aliphatic packing, was studied by 1D and 2D ^{2}H-NMR spectroscopy [23].
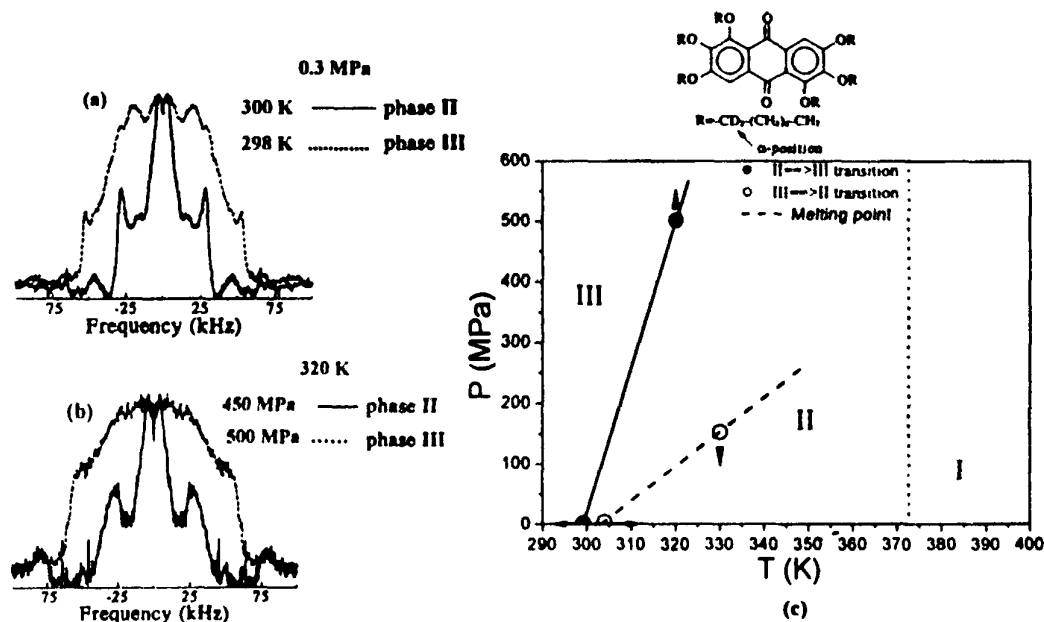
Figure 1-22: *The II→III "phase" transition is indicated by the broadening of the quadrupole echo spectra, caused by a discontinuous decrease in the molecular reorientation rate. (a) The transition at 298 K and 0.3 MPa. (b) The transition at 320 K and 500 MPa. (c) The P-T "phase" diagram with approximate II→III transition lines. As can be seen, the transition has a rather large hysteresis. The arrows indicate the paths taken during transitions. After ref. [23].*

Figure 1-22 depicts three "phases" indicated as I (isotropic phase), II and III. The later "phases" (II and III) have the same hexagonal columnar packing with molecules reorienting at different rates about the columnar axis. Therefore, the "phases" involved are not the usual stable thermodynamic phases. It was thought that "phase" II associates with the density modulations along the columns predicted by de Gennes (see Figure 1-33 below) and therefore the stability of this "phase" was investigated by pressure.

The ^{2}H-quadrupole echo spectra were measured and on cooling from 310 K (phase II), at 0.3 MPa, a discontinuous broadening in the quadrupole echo spectra was observed, between 300 and 298 K (Figure 1-22a), associated with the II→III phase transition. The broadening was attributed to the discontinuous decrease in the rate of reorientation of the molecules about the molecular axis. On applying pressure, the II→III phase transition was found at 320 K and 500 MPa (Figure 1-22b), that gave a rough indication of the II→III transition line in the *P-T*

diagram (Figure 1-22c). The dT/dP values for the II→III and III→II transitions are compared later (see Chapter 4) with the results of the present work.

1.5 Discotic liquid crystals

With the discovery of liquid crystals from disc-shaped molecules, or discotic liquid crystals, in 1977 by Chandrasekhar [24], a demanding and challenging door was opened for many research groups [25]. Discotic liquid crystalline materials have attracted considerable interest because of their unique self-organization behavior into columnar superstructure, leading to high charge carrier mobilities along the columnar stacks [26]. This feature resulted in a successful application of such materials in one-dimensional conductors, photoconductors, light emitting diodes, photovoltaic solar cell, gas sensors and field-effect transistors (FETs) [27]. Discotic liquid crystals are flat and round molecules of varying size. They always have a rigid mesogenic core and flexible corona laterally attached to the core. The flexible corona can have four, six, or eight alkyl chains.

In Figure 1-23 some of the most prominent discotic liquid crystals are displayed. These range from the benzene 1 [28], hexa-alkanoyloxybenzenes 2 [29], hexa-octylether of rufigallol 3 [23], triphenylenes 4 [30], carboxyldiimido-perylenes 5 [31], dibenzopyrenes 6 [32], hexa-n-alkanoates of truxene 7 [29], porphyrins 8 [33], phthalocyanines 9 [34], and hexa-*peri*-hexabenzocoronenes (HBCs) 10 [35]. All consist of a planar core which is substituted by flexible substituents in the periphery, ensuring solubility. The structure, phase state and dynamics of HBCs is a central point of this work.
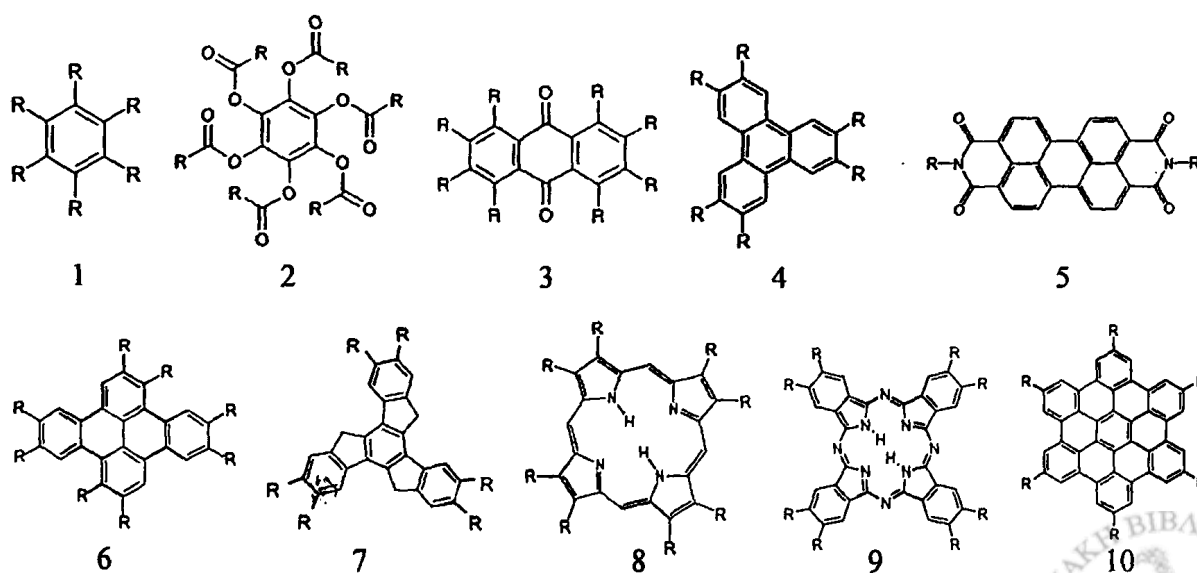
R = flexible substituents, which guarantee solubility and phase forming properties

Figure 1-23: *Variety of some of the most prominent discotic liquid crystals.*

1.5.1 Supramolecular organization of discotic liquid crystals

Discotic liquid crystals belong to a group of molecules, which reveal a pronounced tendency to self-assemble both in solution and in the bulk. Supramolecular structures emerge from spontaneous association because of noncovalent interactions. Interactions such as hydrogen bonds [36] or aromatic π-stacking [37] are the driving forces responsible for the supramolecular organization. Notably, the properties of these aggregates differ distinctly from those of the single molecule.

1.5.1.1 Self-assembly

Self-assembly is the autonomous organization of components into ordered patterns or structures.
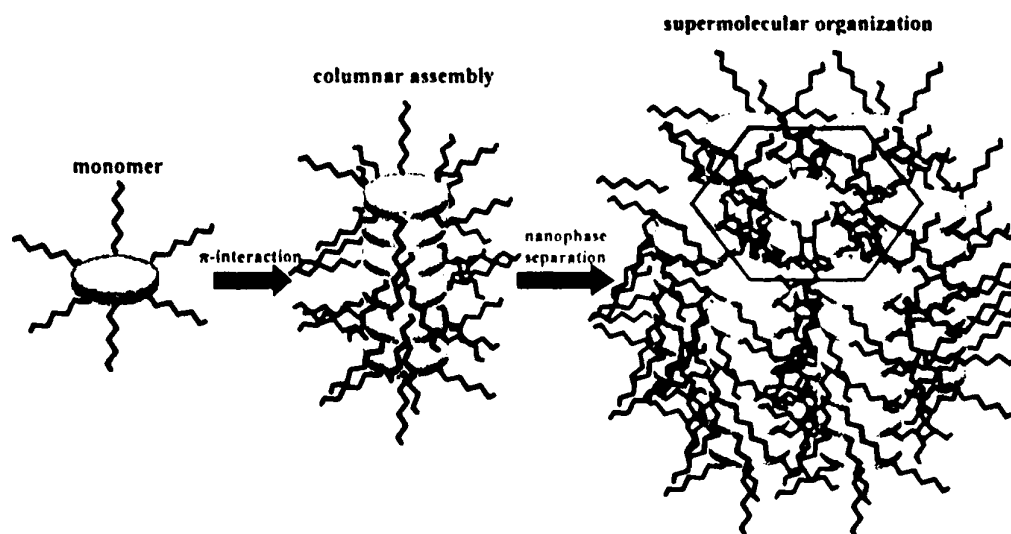
Figure 1-24: *Schematic illustration of the self-assembly organization process taking place during solidification of discotic liquid crystals from the solution or isotropic phase.*

In solution, or in the melt, monomeric species assemble into columns due to the overlapping of the π^*-π^* LUMOs (lowest-unoccupied molecular orbitals), which would lead to a conduction band for charge transport along the column axis (Figure 1-24). With higher concentration and/or with decreasing temperature, the size of the columnar aggregates in solution increase, resulting ultimately in the solidification of the material. During this final organization process, *nanophase separation* takes place between the highly ordered, rigid aromatic cores and the disordered aliphatic chains. The overall superstructure contains a columnar organization of disc-shaped molecules, the so-called discotics, which in turn arrange into a two-dimensional array [38] and the alkyl side chains fill the intercolumnar space.

1.5.1.2 Orientation on substrates

In thin-film devices, the bulk charge transport is usually limited due to the disorder of the active material deposited between the electrodes, grain boundaries (defects), and metal-interface resistance. Therefore, the control of the molecular arrangement on the surface is an important issue during processing of the discotic materials [39].
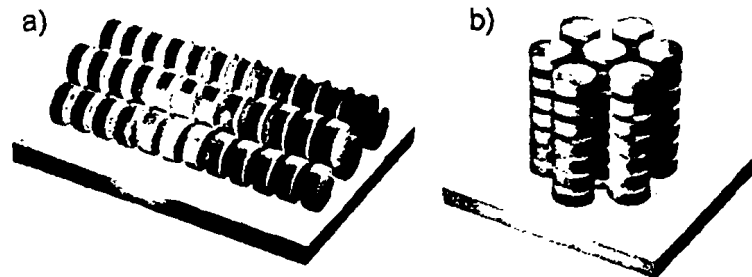
Figure 1-25: *Schematic representation of the different types of supramolecular arrangements on surfaces with (a) edge-on orientation of the molecules, where the columnar axis is oriented parallel to the substrate, and (b) face-on arrangement resulting in homeotropical order. After ref. [40].*
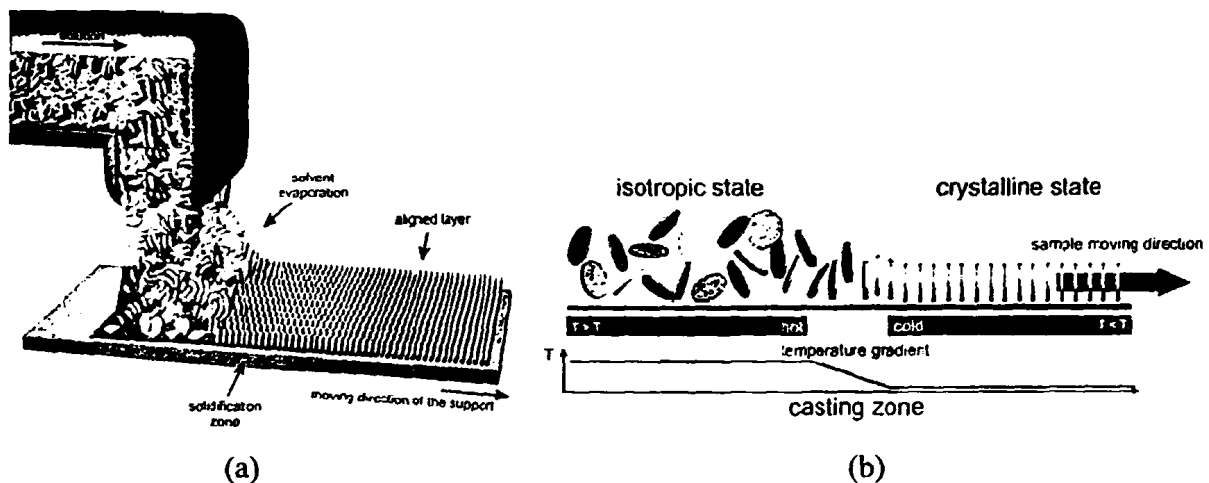
Figure 1-26: *Schematic illustration of the zone-casting (a) and the zone-crystallization (b) techniques used in the processing of the discotic materials. After ref. [41].*

In field-effect transistors (FETs), the charges migrate between source and drain parallel to the substrate, which requires an edge-on arrangement of molecules (Figure 1-25a) [42]. On the other hand, a molecular face-on orientation (Figure 1-25b), which leads to the formation of a homeotropic phase, is thought to improve the efficiency of photovoltaic cells [43,44] or could be interesting as hole-injection layers for organic light emitting diodes (LEDs) [45]. The control of the molecular orientation and therefore the alignment of the charge carrier pathways constitute a task of major importance for material scientists, because it sensitively determines the performance of the electronic device. The "edge on" arrangement with respect to the substrate (Figure 1-25a) is obtained by zone-casting and the zone-crystallization techniques

(Figure 1-26) [40,41], while the face-on arrangement was obtained when processed from the melt [46]. In the zone-casting technique (Figure 1-26a), a solution of organic material is deposited by a nozzle onto a moving support . In this arrangement, a concentration gradient is formed between the nozzle and the support. At the critical concentration, the material is nucleated from the solution onto the moving support as an aligned thin layer. In the zone-crystallization technique (Figure 1-26b), the sample is moved at a defined velocity from a hot plate with a temperature above the isotropic phase to a cold plate with a temperature lower than the isotropic phase transition temperature (T_i). Between these two plates, the material crystallizes along a temperature gradient as an aligned film.

1.5.1.3 The organization within the phases

Three are the major phases found in most discotic liquid crystals: crystalline (C_r), liquid crystalline (LC) and isotropic (Figure 1-27) [40,47].
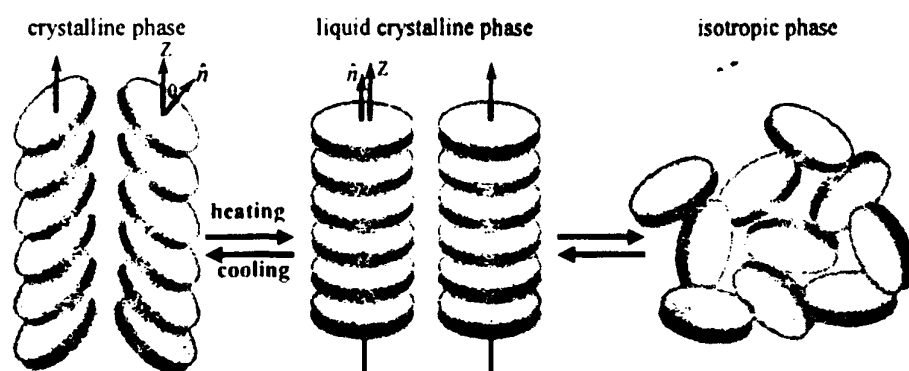
Figure 1-27: *Schematic representation of the organization within the three major phases of discotic liquid crystals.*

In the crystalline state, the disc-shaped molecules organize into columns that further assemble into a two-dimensional lattice composed of nanophase separated and tilted aromatic cores and more flexible alkyl chains. Within the crystalline state, the director $\hat{n}$ makes an angle θ with the columnar z-axis. In the columnar liquid crystalline phase, the discs undergo reorientation from the tilted to a planar arrangement. In this case the angle between the director $\hat{n}$ and the columnar axis is zero. In the isotropic phase, the columnar structures break into monomeric species, leading to an amorphous melt.

1.5.2 Mesophases formed by discotic liquid crystals

Mesophases formed by disc-shaped molecules fall into three different categories: nematic, columnar and lamellar mesophases [31,48].

1.5.2.1 Nematic mesophases

The nematic mesophases of disc-shaped molecules can be subdivided into three types: discotic nematic (N_d), chiral nematic (N_d^*) and nematic columnar (N_{Col}).
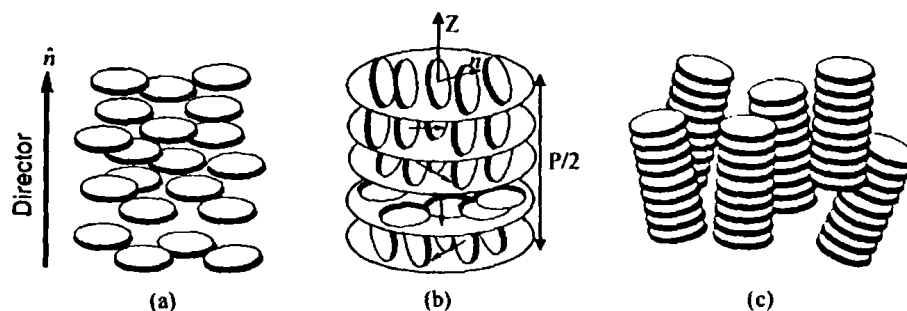
Figure 1-28: *Schematic representation of (a) discotic nematic, (b) helical structure of chiral nematic mesophase and (c) nematic columnar mesophase. After ref. [48].*

In the discotic nematic mesophase (N_d), the molecules stay more or less parallel, having orientational order but no long-range positional order (Figure 1-28a). The N_d mesophase typically shows the Schlieren textures (Figure 1-29), similar to that of a nematic mesophase of calamitic molecules. However, the discotic nematic mesophase is optically negative, which clearly contrasts with the optically positive nematic mesophase of calamitic liquid crystals.
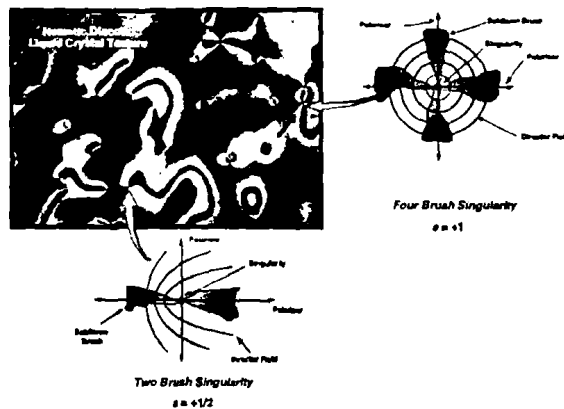
Figure 1-29: *POM image of the nematic schlieren defect texture of the N_d mesophase along with schematic illustration of disclinations of strengths S=+1 and +1/2. After ref. [15].*

When the molecules are chiral, the resulting chiral discotic nematic mesophase (N_d^*), shows a modulated structure (twisted nematic mesophase) which is illustrated in Figure 1-28b. The director $\hat{n}$ is continuously twisted along the z-axis with a pitch p (equal to one complete turn of the local director by 2π). Similar to the textures of cholesteric mesophases of calamitic molecules, oily streaks, fingerprint, and polygonal textures can be observed for N_d^* mesophases. The nematic columnar (N_{Col}) mesophase is characterized by a columnar stacking of the molecules. However, these columns do not form two-dimensional lattice structures.

They display a positional short-range order and an orientational long-range order (Figure 1-28c). The N_{Col} mesophase shows Schlieren textures like N_d and N_d^* but with deep colors (Figure 1-30) because of the formation of charge-transfer complexes [49].

Figure 1-30: *Schlieren texture of the nematic columnar (N_{Col}) phase of an equimolar charge transfer complex obtained by doping the nonyloxypentayne with 2,4,7-trinitrofluorenone at 174°C on heating. The deep red color is thought as indicating the formation of electron donor acceptor complexes. After ref. [49].*

1.5.2.2 Columnar mesophases

In columnar mesophases, molecules assemble one on top of the other in columns, which are packed parallel on a two-dimensional lattice. These columns may be arranged upright or tilted as illustrated in Figure 1-31.
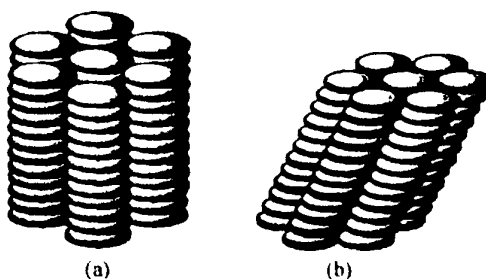
Figure 1-31: *Schematic representation of columnar structures of discotic mesogenes: (a) upright columns, (b) tilted columns. After ref. [50].*

Depending on the order of molecular stacking within the columns and the two-dimensional lattice symmetry of the columnar packing, mesophases are classified in five classes: columnar hexagonal (Col_h), columnar rectangular (Col_r), columnar oblique (Col_{ob}), columnar plastic (Col_p), and columnar helical (Col_H) mesophases.

(i) The columnar hexagonal mesophase (Col_h)

The columnar hexagonal mesophase (Col_h) is characterized by a hexagonal packing of the molecular columns as illustrated in Figure 1-32 [31].
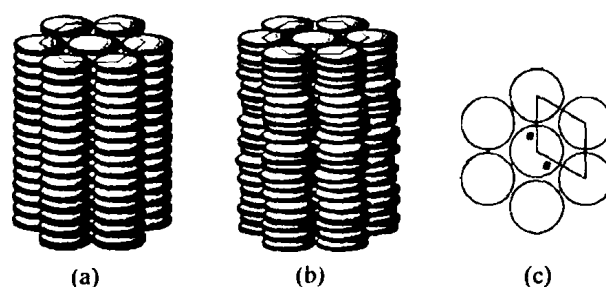
Figure 1-32: *Two-dimensional hexagonal packing within the columnar hexagonal mesophase (Col$_h$). (a) ordered hexagonal columnar phase (Col$_{ho}$); (b) disordered columnar hexagonal phase (Col$_{hd}$); and (c) plan view of the two-dimensional hexagonal lattice (P6/mmm). After refs. [15,31].*

The Col$_h$ mesophases are often denoted as Col$_{ho}$ or Col$_{hd}$ where h stands for hexagonal and o and d for ordered or disordered stacking of the molecules within the columns. In the Col$_{ho}$ (Figure 1-32a), the cores are stacked in a regular ordered (equidistant) fashion while the flexible tails are still disordered. In the Col$_{hd}$ mesophase (Figure 1-32b), structural disorder such as non-parallel arrangement of the discs and longitudinal and lateral displacements occur. The 2D hexagonal unit cell (Figure 1-32c) can be calculated from the X-ray diffraction patterns, and the d_{hk}-spacings are related to the lattice constant a according to Eq. (1.12) [31]

$$\frac{1}{d_{hk}^2} = \frac{4}{3}\frac{h^2 + k^2 + hk}{a^2}$$

(1.12)

where h and k are the Miller indices of the associated reflection and a is the lattice constant. For example, the small-angle X-ray diffraction (SAXS) profiles of an unorientated (powder) sample within the Col$_h$ mesophase are shown in Figure 1-33 [31].
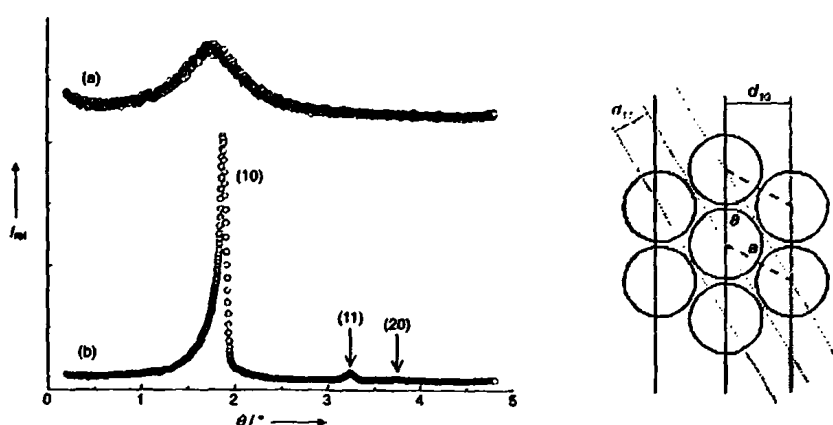
Figure 1-33: *(left) Small-angle X-ray scattering profiles of tetraphenylene. (a) Isotropic melt, (b) Col$_h$ mesophase: the reflections (10),(11), and (20) are due to the long-range intercolumnar ordering. (right) In a hexagonal lattice, the d-spacings of the (10) and (11) reflections show the characteristic ratio 1:1/√3 . After ref. [31].*

29

The d-spacing of the (10) and (11) reflections show the ratio $1:1/\sqrt{3}$. More geometric considerations result in the characteristic ratios of $1:1/\sqrt{3}:1/\sqrt{4}:1/\sqrt{7}:1/\sqrt{9}:1/\sqrt{12}:1/\sqrt{13}$ for the d-spacings of the (10), (11), (20), (21), (30), (22), and (31) reflections of a 2D hexagonal lattice.

It has been pointed out that the columnar mesophase, as realized by rigid aromatic molecules having six to eight flexible aliphatic chains, poses packing problem because of the incommensurability of the packing of the aliphatic and the aromatic moieties (Figure 1-34).
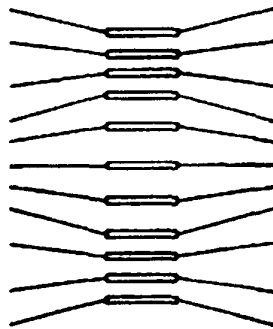
Figure 1-34: *Density waves along the columns as proposed by de Gennes.* After ref. [51].

One of the possible ways to overcome this problem is by the creation of density modulations along the columns as proposed by de Gennes [51], giving rise to the Col_{hd} phase. The proposed quasi-disorder packing of discs within the column, relief the side-chain packing frustration.

Col_h mesophases, are characterized by conic fan-shaped (pseudofocal conic) and focal conic textures (Figure 1-35a and b, respectively) [31].
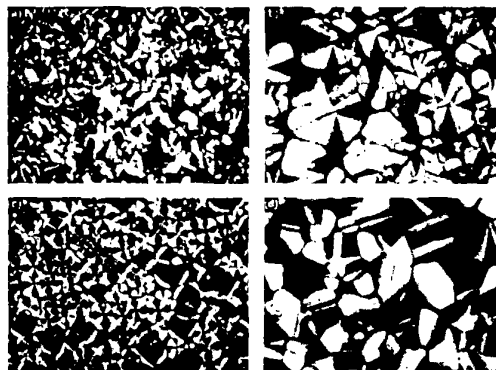
Figure 1-35: *Textures of Col_h mesophases. a) Fan-shaped focal conic texture, b) focal conic texture, c) spherulitic-like texture with maltese crosses, and d) The straight linear defects are characteristic for ordered columnar mesophases. After ref. [31].*

Mosaic and dendritic textures are not as common. When dendritic textures grow in all directions from one point, "flowerlike" texture are formed. Furthermore, relatively rare spherulitic-like (Figure 1-35c) and fingerprint textures are known. Textures of an ordered

hexagonal columnar mesophase typically exhibit straight linear defects (Figure 1-35d). However, the problem often occurs that only small domains are formed that could not be attributed to a typical texture.

(ii) The columnar rectangular mesophase (Col$_r$)

Three different columnar rectangular mesophases Col$_r$ have been identified (Figure 1-36b–d) [31,48].

(a)   (b)   (c)   (d)

Figure 1-36: *(a) General view of the stacking of the mesogen cores in the columns. (b-d) Plan views of the 2D lattices in rectangular mesophases: (b) rectangular (P2₁/a); (c) rectangular (P2/a); and (d) rectangular (C2/m). After refs. [31,48].*

In general, in the columnar rectangular mesophase (Col$_r$), molecules are tilted with respect to the column axis, whereby the cross section, orthogonal to the long axis of a column, is elliptic. The symmetries of the 2D lattices (Figure 1-36b-d) are specified by three different planar space groups $P2_1/a$, $P2/a$, and $C2/m$, belonging to the subset of space groups without any transitional periods in the direction of the principal symmetry axis (that is, the direction of the columns). As a result of the elliptical projection of the molecules in the plane, the symmetry of the Col$_r$ phases deviates from a proper hexagonal arrangement. Thus rectangular phases sometimes are also called pseudohexagonal. However, stronger core–core interactions are needed for the formation of Col$_r$ mesophases rather than for the formation of hexagonal phases, because the cores of one column have to "know" how they must be tilted with respect to the cores of the neighboring columns. Therefore, a crossover from columnar rectangular to hexagonal mesophases with increasing side-chain lengths has often been observed.[52,53]. However, a closer look to the SAXS profiles of a hexagonal and rectangular columnar mesophases reveal certain differences (Figure 1-37). The (10) peak of the Col$_h$ mesophase splits in the (20) and (11) reflection of the Col$_r$ phase. This observation is explained in Figure 1-37.
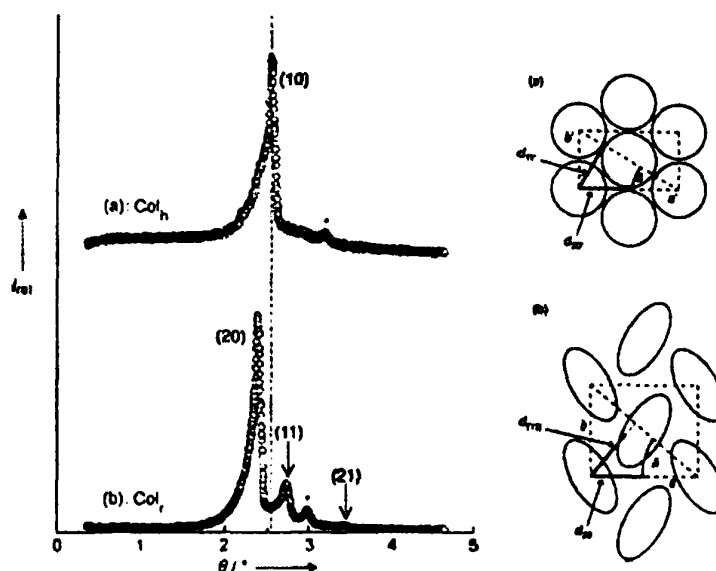
Figure 1-37: *SAXS profiles of a hexagonal (a) and a rectangular columnar mesophase (b) of tetraphenylene. The (10) reflection of the Col$_h$ phase divides into two peaks of the Col$_r$ phase (the scattering maximum (*) is a satellite peak of the strong (10) and (20) reflections,respectively,and originates from parasitic radiation). Symmetry breakdown at the transition from a hexagonal (a) to a rectangular columnar phase (b). For better clarification the rectangle in (b) is shown in a disproportionate way. Normally the lattice of a rectangular mesophase is closer to that of a hexagonal columnar phase. After ref. [31].*

In a hexagonal lattice a rectangular unit cell with the lattice constants a' and b' is shown (Figure 1-37a). Since $\delta=30°$ in a hexagonal arrangement, $b'=a'/\sqrt{3}$, leading to $d_{11}=d_{20}$. For a rectangular lattice, Eq. (1.13) is valid [31]

$$\frac{1}{d_{hk}^2} = \frac{h^2}{a^2} + \frac{k^2}{b^2}$$

(1.13)

where a and b are the lattice constants. As soon as the lattice deviates from perfect hexagonal symmetry, that is $\delta\neq30°$ (Figure 1-37b), the degeneracy of d_{11} and d_{20} is broken and two separate reflections appear. As a result of the minor differences in the structures, textures known for Col$_h$ phases (Figure 1-35) can also be observed for Col$_r$ phases. However, broken fan-shaped and mosaic textures are more common for columnar rectangular mesophases than for columnar hexagonal ones.

(iii) The columnar oblique mesophase (Col$_{ob}$)

Figure 1-38 shows the arrangement of the columns in a columnar oblique mesophase, in which the tilted columns are represented by elliptic cross sections. The symmetry of this 2D lattice corresponds to the space group P_1 [31].
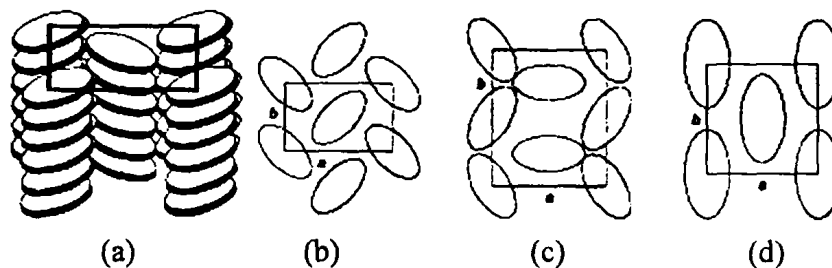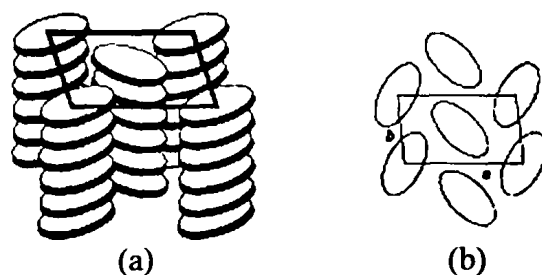
Figure 1-38: *(a) General view of the stacking of the mesogen cores in the columns; (b) Plan view of the 2D lattice in a columnar oblique (P₁) mesophase . After refs. [31,48].*

Examples for columnar oblique mesophases are rare because strong core-core interactions are required. Since P_1 is a primitive planar space group, there are no reflection conditions and therefore all peaks (hk) are allowed. Besides fan-shaped textures spiral textures are characteristic for Col_{ob} phases [31].

(iv) The columnar plastic (Col$_p$) and the columnar helical (Col$_H$) mesophases

. Recently, a columnar plastic mesophase (Col$_p$) has been identified in discotic liquid crystals [54]. The mesophase is characterized by three-dimensional crystal-like order in a hexagonal lattice, while the discs within the columns are able to rotate about the column axis (Figure 1-39a). In addition, they show a plastic deformation at room temperature in comparison to crystalline materials [55].
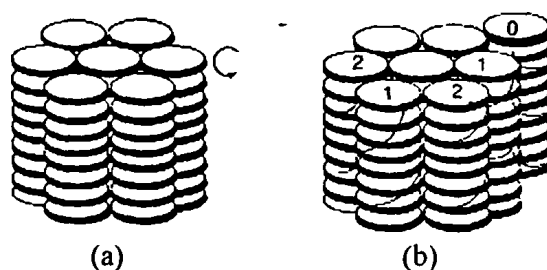
Figure 1-39: *General view of the columnar plastic mesophase, Col$_p$, (a) and of the columnar helical mesophase (b). After ref. [48].*

Mesophase structure with *helical order* has been demonstrated for a triphenylene derivative namely hexahexylthiotriphenylene (HHTT) [56]. In this columnar mesophase (Col$_H$), helical molecular orientational order develops within the columns (Figure 1-39b). Additionally, a three-column superlattice was reported, associated with both the helical phase and the vertical displacement of three columns.

Columnar mesophases of "non-discotic" molecules: Columnar type phases have also been observed for substances that do not possess a disc-like core. In these columnar phases, the mesogen can have different shapes such as conical, pyramidal-, macrocyclic, and polycatenar

(phasmids) mesogenes [4,29]. Figure 1-40 shows two examples, one for a conical core (Figure 1-40a) and the other for pyramidal shaped one (Figure 1-40b).

R = $C_9H_{19}COO-$
R = $C_9H_{23}COO-$
R = $C_{12}H_{25}O-$⟨⟩$-COO-$

(a)

R=C_nH_{2n+1}—O
R=C_nH_{2n+1}—CO-O

(b)
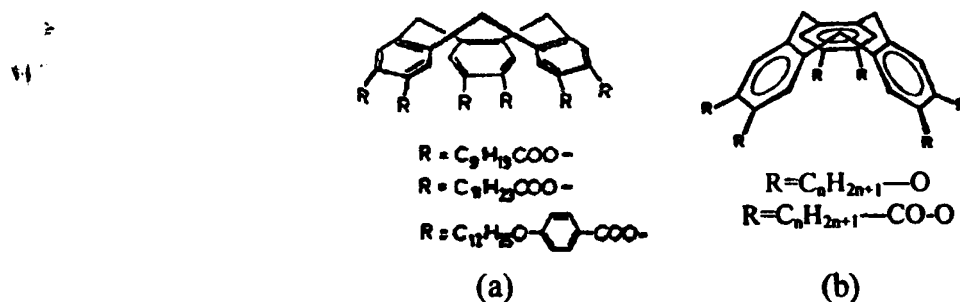
Figure 1-40: *Structure of the mesogenic conical molecule (a) and the pyramidal shaped one (b). Both molecules show columnar mesophases. After ref. [4].*

Malthete and coworkers [4,29] have prepared a series of mesogens, which they call "phasmids". These are molecules consisting of a central rod-like rigid core with a half-disc-like feature at either end (Figure 1-41a). The structure proposed for the columnar hexagonal mesophase is shown schematically in Figure 1-41b.

(a)

(b)
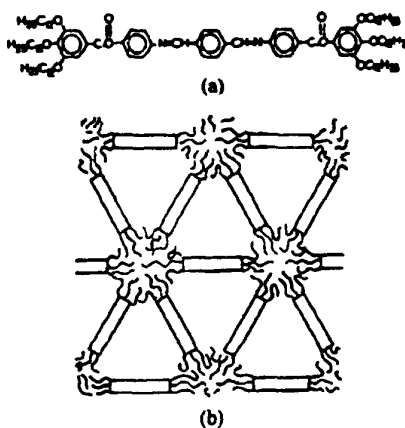
Figure 1-41: *(a) Hexa-n-alkoxy terepthal-bis-[4-benzoyloxyaniline] and (b) the structure of the hexagonal columnar mesophase formed by this compound. The mesophase has been described as "phasmidic". After ref. [29].*

Macrocyclic molecules, are composed of hollow cores at the center and of columns that are in the form of tubes (Figure 1-42), therefore the name "tubular" [4,29,57].

Defects in the columnar mesophases are discussed in Appendix 2.
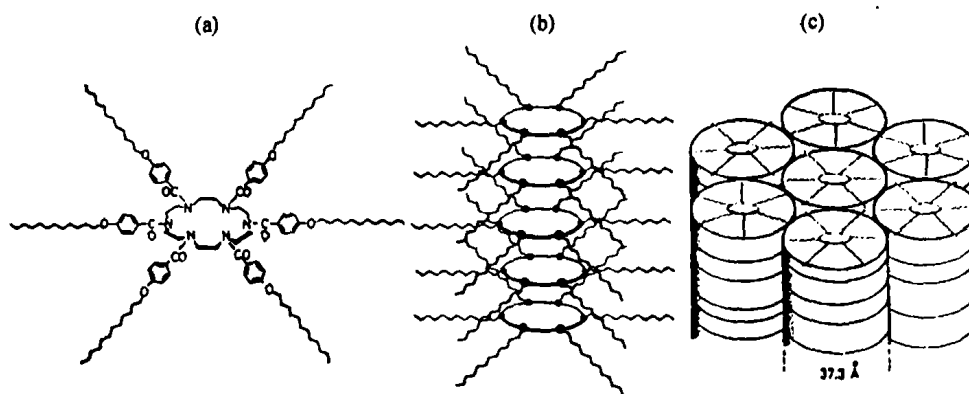
Figure 1-42: *Structure of the mesogenic macrocyclic molecule (a); schematic representation of the stacking of macrocycles in the mesomorphic phase (b, for clarity, the molecules are arbitrarily drawn with the same orientation); and of the tubular mesophase thus formed (c). After ref. [57].*

1.5.2.3 Lamellar mesophase

In a lamellar mesophase the molecules are arranged in layers similar to calamitic mesogens in smectic phases. Thus is not surprising that, the textures of the lamellar mesophases are similar to the textures of calamitic smectic phases. Typically, broken fanlike textures with large domains (Figure 1-43) can be observed for the lamellar phases.
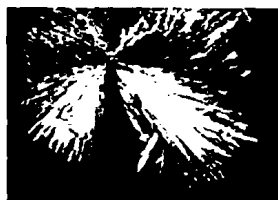
Figure 1-43: *Broken fanlike texture of a lamellar mesophase of tetraphenylene. After ref. [31].*

The molecular arrangement within the lamellar mesophase has not yet been completely clarified. A suggestion by Sakashita et al. [58] is shown in Figure 1-44. In a 2D diffraction pattern of an orientated sample, Sakashita et al. observed only one diffraction maximum and its corresponding higher order peaks in the equatorial direction; Figure 1-44 shows this behavior for the crown ether [59]. This observation indicated a layer structure, with interlayer spacing that is comparable to the molecule length. It was further deduced that the molecular plane is. tilted against the layer normal by about $5°$ (Figure 1-44). Furthermore, no columnar structure in a lamellar mesophase was observed, and the molecules possessed a liquid-like order in the layers. Thus the structure of the lamellar mesophase deduced by Sakashita et al. is very similar to that of a SmC phase of calamitic mesogens.
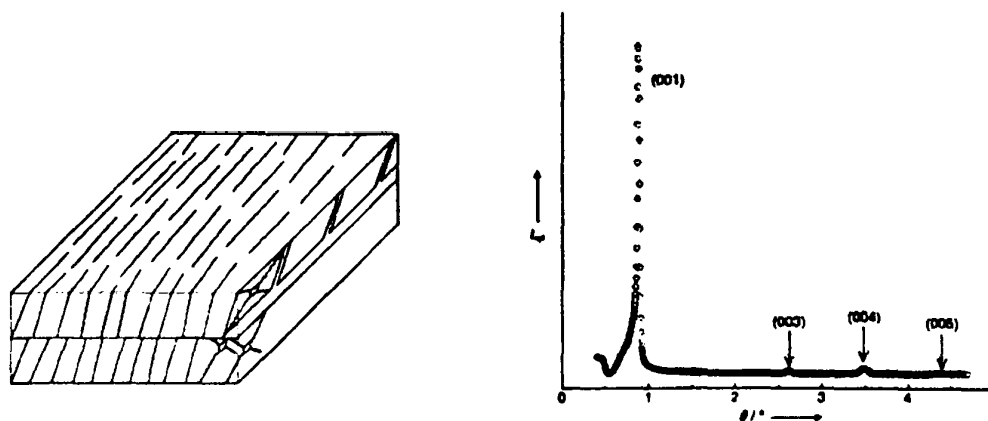
Figure 1-44: *(Left) Structure of the lamellar mesophase proposed by Sakashita et al. (right) X-ray scattering profile of a lamellar (smectic) mesophase of the ortho-terphenyl crown ether. Only one diffraction maximum and its corresponding higher order peaks are observed, related to pure 1D translational order. After ref. [31].*

Méry et al. presented a further lamellar columnar mesophase, in which the molecules of [1]benzothieno[3,2-b][1]benzothiophene-2,7-dicarboxylate were proposed to assemble in microcolumns made of alternatively crossed molecules within the smectic layers [60].

1.5.3 Electrical properties of discotic liquid crystals

The assembly of discotic aromatic mesogenes into columnar stacks, with typical intercore distances of about 3.5 Å, gives rise to an overlap of the π^*-π^* lowest-unoccupied molecular orbitals, that could lead to the formation of charge carrier pathways for organic electronics (Figure 1-45) [61].
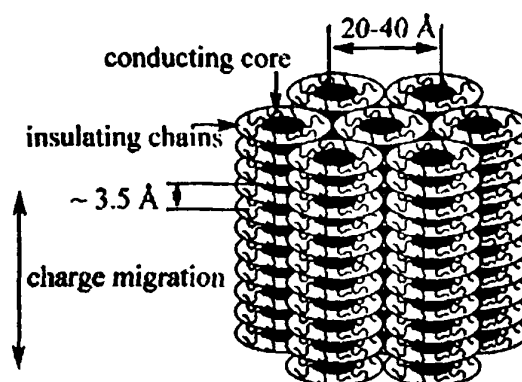
Figure 1-45: *Schematic view of charge migration in columnar phase. After ref. [48].*

As long flexible aliphatic chains surround the core, the intercolumnar distance is usually 2-4 nm, depending on the lateral chain length. Therefore, interactions between neighbouring molecules within the same column would be much stronger than interactions between neighbouring columns [48]. Consequently, charge migration in these materials is expected to

36

be quasi-one-dimensional [62]. Very high intrinsic charge carrier mobilities have been determined for these discotics, which are about one order of magnitude higher than the one found for conjugated polymers (Figure 1-46) [63].
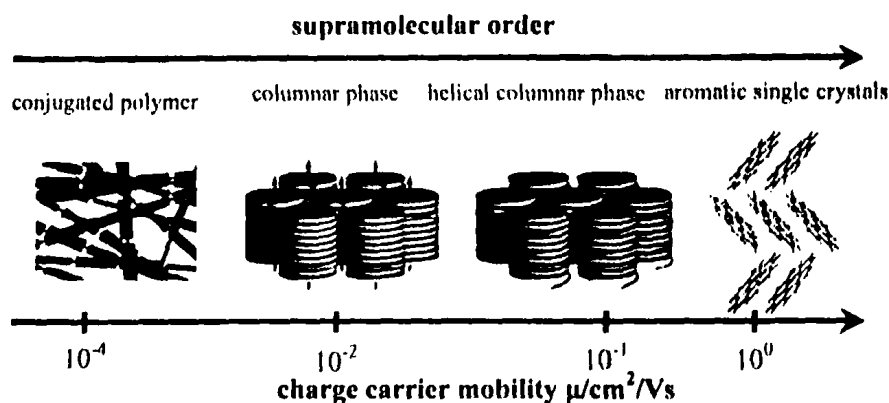
Figure 1-46: *Illustration of the relation between supramolecular order and charge carrier mobility. After ref. [41].*

¯ One would therefore expect the electrical conductivity along the columnar axis, $\sigma_{\parallel}$, to be high, but in fact these compounds are good insulators. The reason for this is that their intrinsic charge carrier concentration is low because of the large energy gap (of about 4 eV). However, one can induce conductivity, by injecting charge carriers using (i) chemical dopants, (ii) photo-injection, (iii) radiation and (iv) application of an electric field across metal electrodes.

The increase in conductivity with the addition of dopants, electron acceptors or donors been demonstrated in a number of cases: hexahexylthiotriphenylene (HHTT) doped with I_3 [64], hexahexyloxytriphenylene (HAT6) doped with $AlCl_3$ [65], HATn, $n = 4, 6, 9$ and 11, doped with $NOBF_4$ [66], HAT6 doped with C_{60} [67] and HHTT doped with trinitrofluorenone [62]. Herein we briefly describe the a.c. conductivity measurements carried out on aligned samples of HAT6 doped with a small quantity (mole fraction $x=0.005$) of $AlCl_3$ [65]. The measurements were made within the crystalline (K), hexagonal discotic liquid crystal (D_{hd}) and isotropic liquid (I) phases (Figure 1-47). The most interesting findings were: (i) HAT6 when doped with small quantities of $AlCl_3$ was converted from an insulator to a quasi-one-dimensional semiconductor. The conductivity along the column axes, $\sigma_{\parallel}$, was some 3 orders of magnitude greater than that in the perpendicular direction, $\sigma_{\perp}$, (ii) the frequency dependence of the conductivity, as measured along the direction of the columns in aligned phases could be described in terms of a single charge transport process in which the charge carriers hop between localized sites (radical cations) associated with $AlCl_4^-$ counterions linearly distributed off-axis along the columns. Thus, highly directional charge transport over large distances (~

100 nm) took place, and (iii) charge transport proceeded stochastically, by phonon-assisted tunnelling between neighbouring states/coulombic wells.
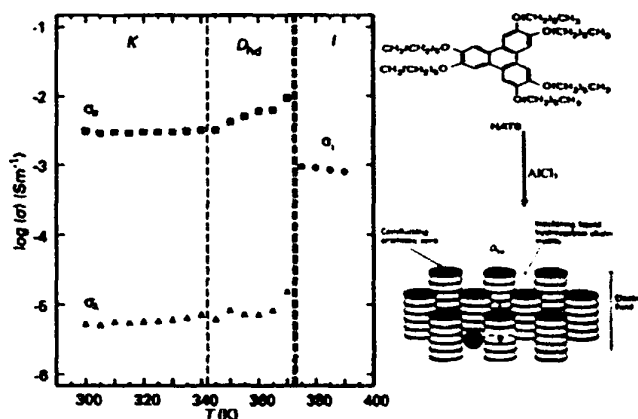
Figure 1-47: *The low frequency limiting conductivity (f= 100 Hz) of HAT6/AlCl₃ (x = 0.005) as a function of temperature. After ref. [65].*

Record intrinsic charge carrier mobility, μ, in excess of 1 $cm^2V^{-1}s^{-1}$, was determined for a substituted hexa-*peri*-hexabenzocoronenes (HBC) derivative (Figure 1-23 (10)), which qualifies such materials for the implementation in organic electronic devices [55,68]. The size of the aromatic cores is thought to have a close relation with the intracolumnar charge transport, which increases from 0.1 $cm^2V^{-1}s^{-1}$ for triphenylenes (Figure 1-23 (4)) [63,69] over 0.7 $cm^2V^{-1}s^{-1}$ for phthalocyanines (Figure 1-23 (9)) [70-73] and up to 1.0 $cm^2V^{-1}s^{-1}$ for HBCs (Figure 1-23 (10)) [55,68,73,74]. These mobility values are already in the range of amorphous silicon [75]. A comparison of some electrical properties of HAT6 with those of the organic metal TTF/TCNQ (Tetrathiafulvalene/Tetracyanoquinodimethan) and pure silicon is given in Table 1.1. In addition, a schematic illustration of the energy band formation from a single molecule to a columnar stack is shown in Figure 1-48 [31].
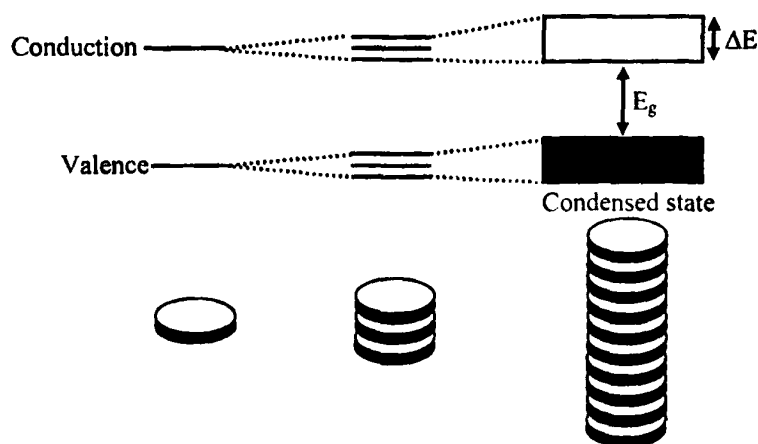
Figure 1-48: *Energy band formation from a single molecule (left) to the column (right). After ref. [31].*

Table 1.1. Comparison of some electrical properties of HAT6 with the organic metal TTF/TCNQ and pure silicon at 300 K. (Compiled from refs. [4,76]).

Compound	σ (Ω^{-1} cm^{-1})	μ (cm^{2}V^{-1}s^{-1})	n (cm^{-3})	E_g (eV)	ΔE (eV)
HAT6	10^{-13}	4×10^{-4}	10^{10}	4	0.2
TTF/TCNQ	500	1	10^{21}	2	0.2-0.5
Amorphous silicon	-	0.1-1	-	-	-
Single-crystalline silicon	4.3×10^{-6}	1500	1.45×10^{10}	1.12	-

σ: dc-conductivity - μ: mobility - n: intrinsic carrier concentration - E_g: energy gap - ΔE: bandwidth

Two mechanisms have been proposed for the charge carrier transfer for this group of molecules. The hopping mechanism describes a "hopping" of the charge carriers between localized states [77]. The high mobilities found require hopping rates in excess of 10^{12} Hz. Since discotic liquid crystals contain imperfections [78], the hopping rate will be probably much higher than this. The second more probable mechanism involve the formation of conduction bands across several molecules, where the charge is delocalized. This explains better the measured high charge carrier mobilities [79].

For studying charge transport in discotic liquid crystals, the Pulse Radiolysis Time-Resolved Microwave Conductivity (PR-TRMC) [80] and the Time-of-Flight (TOF) [31,81,82] techniques are most widely used. The two techniques are described in Appendix 3.

A comparative study of results obtained using PR-TRMC with TOF measurements on the classic discotic compound hexakis (hexylthio)-triphenylene (HHTT) is shown in Figure 1-49 [69,80].
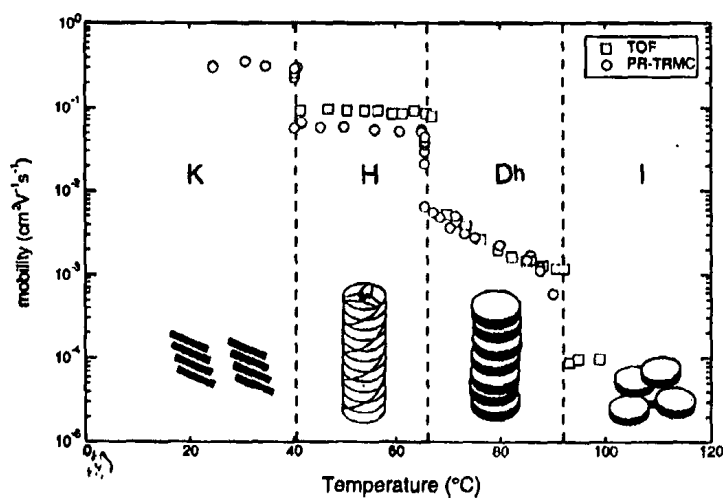
Figure 1-49: *A comparison of the temperature dependence of the charge mobility determined by PR-TRMC with the hole mobility determined by TOF on cooling hexakis(hexylthio)-triphenylene from the isotropic liquid phase. The phase transition temperatures are indicated by the vertical dashed lines. After ref. [80].*

As can be seen, on cooling from the isotropic liquid (I), a hexagonal disordered columnar liquid crystalline phase (D_h) first forms at 93 °C. On further cooling this transforms at 68 °C to an ordered, helical columnar phase (H), which converts to a (poly)crystalline solid (K) at close to 40 °C. The agreement between the two techniques was found to be extremely good for both the helical and the columnar hexagonal phases. By combining the results obtained using both techniques, a complete description of the change in the mobility by more than three orders of magnitude in going from the I phase (1×10^{-4} cm^{2}V^{-1}s^{-1}) via the D_h (1×10^{-3} cm^{2}V^{-1}s^{-1}) and H (5×10^{-3} cm^{2}V^{-1}s^{-1}) mesophases to the K phase (0.3 cm^{2}V^{-1}s^{-1}) could be made.

The good agreement confirmed the proposition that the mobility determined by PR-TRMC corresponds to that in well-organised, columnar domains within the bulk material. This study has shown the importance of the low temperature crystalline phase with respect to the higher charge carrier mobilises. It is therefore of importance to control the appearance of this phase also in other discotics. Below we review the most important structural findings.

1.5.4 Structure investigations of discotic liquid crystals

The structure of discotic liquid crystals has been studied with a combination of techniques such as differential scanning calorimetry (DSC), polarized optical microscope (POM), X-ray diffraction [53,56,83,84], solid-state NMR spectroscopy [85-88] and recently with computer simulation [89].

1.5.4.1 X-rays and POM studies

High resolution X-ray studies have yielded important information about the columnar structure. The first examples of thermotropic mesomorphism in discotic compounds were observed in the hexa-alkanoyloxy benzenes [24] and the hexa-alkoxy and hexa-alkanoyloxytriphenylenes [4], and it was established by X-ray studies that the mesophases of these compounds have a columnar structure.

Hexahexylthiotriphenylene (HHTT) exhibited a transition from a hexagonal ordered phase (D_{ho}) to a hexagonal disordered one (D_{hd}). X-ray studies revealed a helicoidal stacking of the cores within each column, the helical spacing being incommensurate with the intermolecular spacing [56]. In addition, a three-column superlattice developed as a result of the frustration caused by molecular interdigitation in a triangular symmetry (Figure 1-50). The supramolecular structure that was proposed for this triphenylene derivative is depicted in Figure 1-50c.
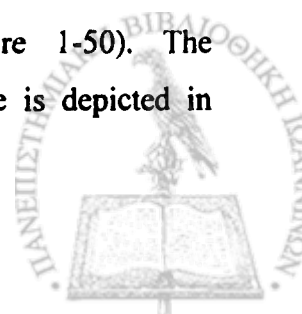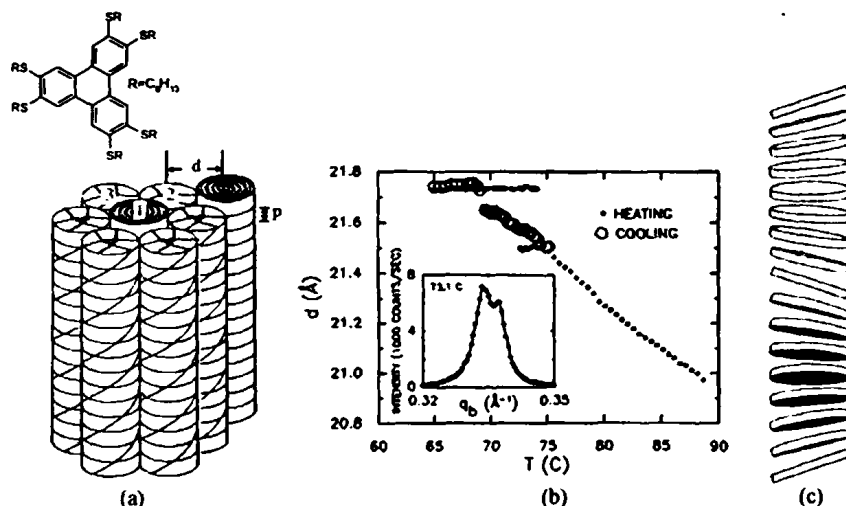
Figure 1-50: *(a) Structure of the D_{ho} phase of the HHTT: the diagram represents a three-column superlattice, with column 1 displaced by p/2 relative to columns 2 and 3, neighbouring columns having correlated helical phases. (b) the intercolumn separation d plotted versus temperature, showing a negative coefficient of thermal expansion (●) Heating mode; (○) cooling mode. (c) schematic representation of the possible helical arrangement proposed for this triphenylene derivative. After refs. [34,56].*

In this case adjacent molecules along a column minimize steric hindrance via a relative out-of-plane rotation of roughly 45° [56]. From this, the helical pitch p was determined to be $p = 7.92$, (i.e., after approximately 8 molecules the helical motif is repeated [56]). This helical arrangement of the discotic molecules enhances the packing and resulted in higher charge carrier mobility along the columnar assemblies [90]. An unusual feature observed in the D_{hd} phase of this compound was the negative coefficient of thermal expansion (Figure 1-50b). This was attributed to the stiffening of the hydrocarbon tails, which become longer with decreasing temperature.

The structure and physical properties of an optically active, metal-free phthalocyanine derivative were investigated by van Nostrum and co-workers [34]. X-ray diffraction and circular dichroism studies indicated that the molecules were stacked in columns with a hexagonal arrangement and a left-handed helical superstructure. This structure is, according to van Nostrum and coworkers, best represented by column c in Figure 1-50.

X-ray investigations by Möller et al. on the temperature dependence of the linear expansion coefficients along the columnar axis and perpendicular to this axis revealed that the glass transition leads to a stepwise change of the expansion coefficient along the columnar axis and to a continuous variation for the corresponding coefficient perpendicular to this direction (Figure 1-51) [91]. Based on this finding it has been proposed that the glass transition in such columnar hexagonal ordered phase is highly anisotropic.
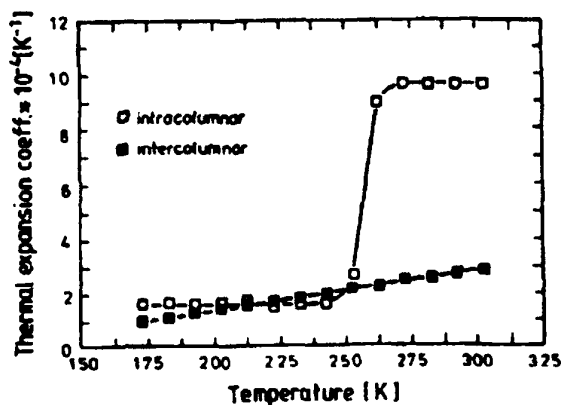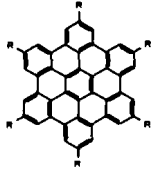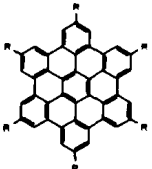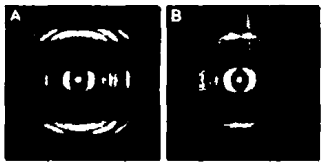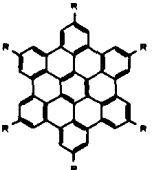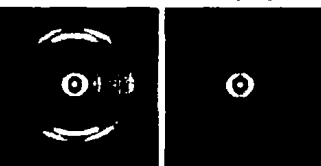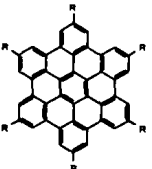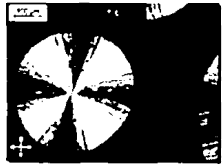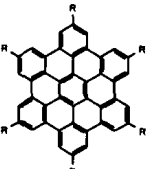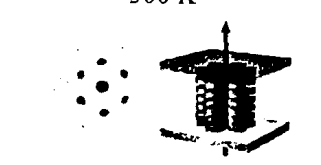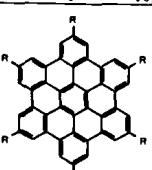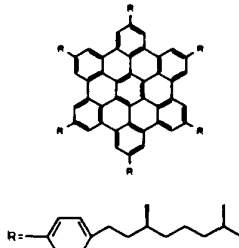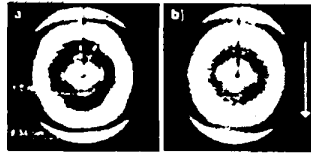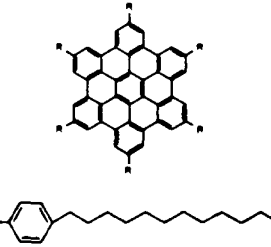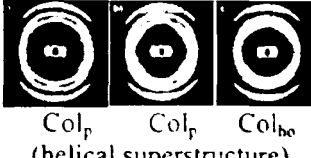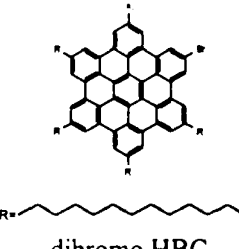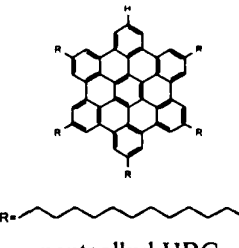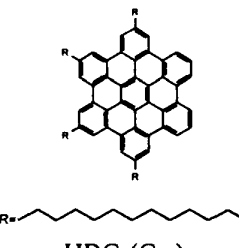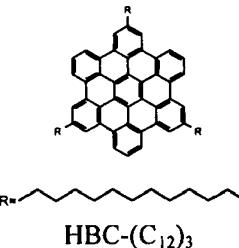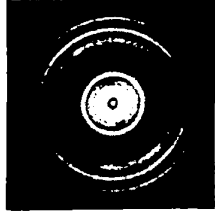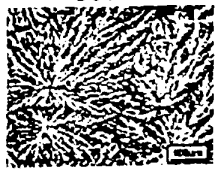
Figure 1-51: *Thermal expansion coefficients characteristic of the intracolumnar and intercolumnar order versus temperature. After ref. [91].*

Extensive studies on the structure of HBCs including X-ray, polarizing optical microscopy (POM), and differential scanning calorimetry (DSC) have been made in view of their high intrinsic charge carrier mobility and potential applications. These studies are compiled in Table 1.2.

Table 1.2. Molecular structure, X-ray images (2D-WAXS), POM images, transition temperature and the phase transition (transition temperatures are obtained from DSC and POM).

Molecular structure	2D-WAXS image	POM image	Transition temperature/phase transition
HBC-C$_{10}$	LC phase (Col$_{ho}$)		$C_r \xrightarrow{397\,K} Col_{ho}$ $Col_{ho} \xrightarrow{\sim 693\,K} I$
HBC-C$_{12}$	300 K 400 K Col$_r$ Col$_h$		$C_r \xrightarrow{380\,K} Col_{ho}$ $Col_{ho} \xrightarrow{\sim 693\,K} I$
HBC-C$_{14}$		613 K Fan-type texture	$C_r \xrightarrow{387\,K} Col_{ho}$ $Col_{ho} \xrightarrow{\sim 693\,K} I$

 R= HBC-C$_{16,4}$		528 K Fan-shaped texture	Col$_p$ $\xrightarrow{237\,K}$ Col$_{ho}$ Col$_{ho}$ $\xrightarrow{504\,K}$ I
 R= HBC-C$_{6,2}$	300 K 333 K C$_r$ Col$_d$	653 K Pseudo focal conic fan-shapes	C$_r$ $\xrightarrow{370\,K}$ Col$_d$ Col$_d$ $\xrightarrow{693\,K}$ I
 R= HBC-C$_{10,6}$	300 K 333 K Col$_p$ Col$_d$	300 K Cyclic clusters	Col$_p$ $\xrightarrow{297\,K}$ Col$_d$ Col$_d$ $\xrightarrow{366\,K}$ I
 R= HBC-C$_{14,10}$	300 K 333 K Col$_p$ Col$_d$	308 K Spherulitic morphology	Col$_p$ $\xrightarrow{319\,K}$ I
 R= HBC-C$_3$-O-C$_{10,6}$	300 K Col$_h$ phase	 Dendritic-like texture	Col$_p$ $\xrightarrow{272\,K}$ Col$_{hd}$ Col$_{hd}$ $\xrightarrow{435\,K}$ I
 R= HBC-C$_{8,2}$*	333 K 403 K C$_r$ Col*$_{ho}$ (helical superstructure)	 Col$_h$ mesophase texture	C$_r$ $\xrightarrow{369\,K}$ Col*$_{ho}$ Col*$_{ho}$ $\xrightarrow{703\,K}$ I

HBC-PhC$_{8,2}$*	303 K 403 K Col$_p$ Col$_{ho}$ (helical superstructure)		$Col_p \xrightarrow{<173\,K} Col^{\bullet}_{ho}$ $Col^{\bullet}_{ho} \xrightarrow{>673\,K} I$
HBC-PhC$_{12}$	173 K 303 K 403 K Col$_p$ Col$_p$ Col$_{ho}$ (helical superstructure)		$Col_p \xrightarrow{353\,K} Col_{ho}$ $Col_{ho} \xrightarrow{>673\,K} I$
dibromo HBC	300 K		$C_r \xrightarrow{332\,K} Col_{ho}$ $Col_{ho} \xrightarrow{>693\,K} I$
pentaalkyl HBC		681 K Pseudofocal conical fan shapes	$C_r \xrightarrow{397\,K} Col_{ho}$ $Col_{ho} \xrightarrow{685\,K} I$
HBC-(C$_{12}$)$_4$	Col$_p$ Col$_{ho}$		$Col_p \xrightarrow{419\,K} Col_{ho}$
HBC-(C$_{12}$)$_3$	300 K Hexagonal and orthorhombic	300 K Spherulitic morphology	$C_r \xrightarrow{444\,K} I$

	300 K	300 K	
  HBC-(C$_{12}$)$_2$	 Hexagonal and orthorhombic	 LC-like texture	C$_r$ $\xrightarrow{494\ K}$ I
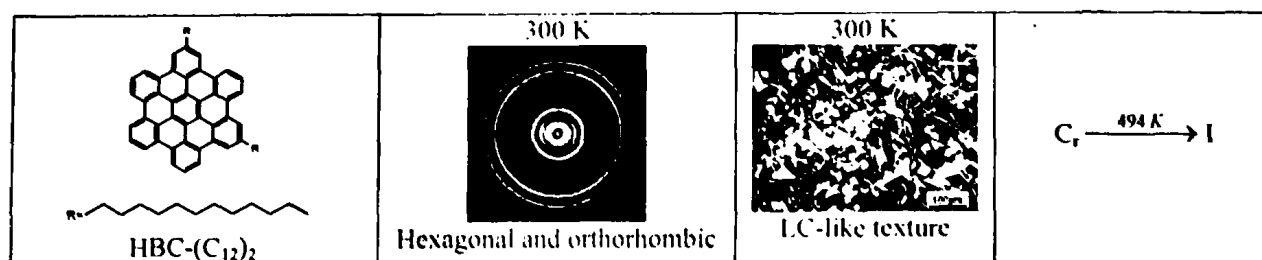
Among the above worth mentioning is an investigation of the effect of the length of the side chains on the structure of HBCs. The azimuthally averaged scattered intensity distributions shown in Figure 1-52 illustrate a strong relation between the length of the side chain and the parameters of the lateral packing of columns for the different 6-fold substituted HBC derivatives (Table 1.2, HBC-C$_{10}$, HBC-C$_{12}$, HBC-C$_{14}$, and HBC-C$_{16,4}$) [92].
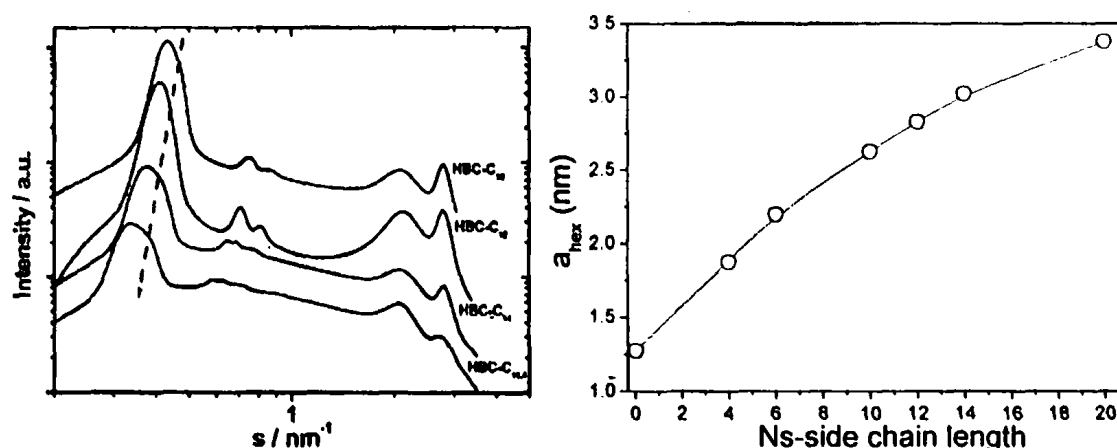
Figure 1-52: *(Left) Scattering intensity distributions as a function of the scattering vector for HBC derivatives substituted by side chains of different length. (right) Hexagonal unit cell dimensions as a function of the side chain length for HBC-C$_n$. After ref. [92].*

The results reveal a shift of the reflections to lower s values ($s=2\sin\theta/\lambda$, where 2θ is the scattering angle) with increasing side chain length. This shift is correlated to increasing unit cell parameters (a_{hex} is calculated from Eq. (1.12)) which expanded from 2.69 nm determined for HBC-C$_{10}$ to 3.37 nm found for HBC-C$_{16,4}$ (Figure 1-52 right). Note that while the lateral organization of columns is strongly dependent on the substituents, the intracolumnar period in the mesophase remained in the typical range between 0.34 and 0.37 nm for the investigated HBC derivatives, whereby the value increases slightly with increasing side chains length. This difference of the intracolumnar dimensions is correlated with the increase of the steric requirements of longer side chains, which hinder a closer approach of the aromatic cores.

In another study the supramolecular organization of HBC-C_{12} was investigated by two-dimensional wide-angle X-ray diffraction (2D-WAXD) experiments at different temperatures [47,93].
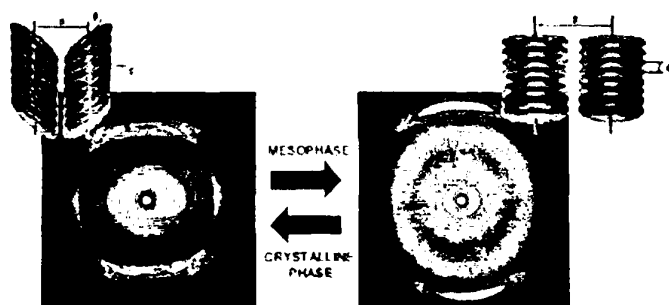
Figure 1-53: *Example of 2D-WAXS patterns and schematic illustrations of the herringbone order in the crystalline phase and the nontilted arrangement in the mesophase for hexadecyl-substituted HBC. After ref. [40].*

A "herringbone" order, was observed in the crystalline phase whereas a non-tilted packing of the aromatic cores was observed in the LC phase (Figure 1-53). It has been found that derivatives with linear side chains, such as HBC-C_{12}, possess a lower solubility and a higher isotropization temperature (above 673 K) in comparison to those of derivatives carrying the bulky branched alkyl chains (Table 1.2, HBC-$C_{16,4}$, HBC-$C_{6,2}$, HBC-$C_{10,6}$ and HBC-$C_{14,10}$) [46,55,92]. The isotropization temperature values for the HBC-$C_{16,4}$, HBC-$C_{10,6}$ and HBC-$C_{14,10}$ dropped to 504, 366 and 319 K, respectively. It has been shown that the increased side chain length results in the formation of larger ordered domains. For example, spherulitic domains of HBC-$C_{14,10}$ in which the columnar structures were oriented radially were found indicating a high degree of organization over long ranges (Table 1.2) [61], whereby the columnar growth of HBC-$C_{10,6}$ takes place around the nucleation center [61]. A fan-shaped texture appeared at 528 K for the HBC-$C_{16,4}$ (Table 1.2) which was characteristic for a hexagonal columnar mesophase [94].

By introducing a long alkyl chain with four branching points it was possible to reduce the $Col_p \rightarrow Col_{ho}$ transition temperature to such an extent, that a columnar mesophase was observed even below room temperature for HBC-C_{16}. Furthermore, it was possible to reach the thermodynamically stable isotropic phase. Both facts suggested a stable columnar mesophase width of over 540 K in HBC-C_{16}.

The relation between molecular structure and supramolecular organization has been investigated by temperature dependent two-dimensional wide-angle X-ray scattering (2D-WAXS) for the HBC-$C_{6,2}$, HBC-$C_{10,6}$ and HBC-$C_{14,10}$ (Table 1.2). A "herringbone" structure was observed in the crystalline phase with an intracolumnar period of 0.48 nm [55]. This phase

was assigned to a plastic-crystalline phase for the HBC-$C_{10,6}$ and HBC-$C_{14,10}$. On the other hand, a direct transition from the columnar plastic crystalline phase (Col_p) to the isotropic phase, without an intermediate LC phase, was observed in HBC-$C_{14,10}$.

In another study, HBCs were substituted by long branched side chains with ether linkages (Table 1.2, HBC-C_3-O-$C_{10,6}$) [95]. A dendritic morphology was obtained by cooling the sample from the isotropic phase between two surfaces which appeared black via POM, which is characteristic for homeotropic alignment [95]. On the other hand, the hexagonal pattern was confirmed by the 2D-WAXS.

The effect of chirality on the mesophase behavior and structure were studied for HBCs carrying six chiral branched chains (Table 1.2, HBC-$C_{8,2}$*) [35]. It was found that the chirality shifts the thermal $C_r \rightarrow Col*_{ho}$ transitions to lower temperatures, relative to analogous HBCs carrying n-alkyl chains. On the other hand, X-ray investigations revealed that the discs of HBC-$C_{8,2}$* were arranged in a helical fashion as depicted in Figure 1-50c.

Investigation of the supramolecular organization of two hexaphenyl-substituted HBC derivatives, differing only in the chiral/achiral nature of the attached alkyl side chains (Table 1.2, HBC-Ph$C_{8,2}$* and HBC-PhC_{12}) revealed that both compounds self-assemble into identical helical columnar structures [96,97]. It was shown that the steric requirements of the bulky phenyl rings attached directly to the aromatic core induce helicity. This steric effect was caused by rotation of the phenyl rings out-of-plane of the aromatic core. The experimental results were supported by applying a theoretical model based on quantum chemical calculation, confirming the molecular geometry and twisting of the discotic molecules within the columnar stacks.

The effect of dipole substitution on the mesophase behavior as well as the packing of the HBCs were studied [98,99]. It was found that, the introduction of a bromo function at the aromatic core (Table 1.2, dibromo HBC) destabilized the low temperature crystalline phase and increased the disordering temperature [99]. For example, the $C_r \rightarrow Col_{ho}$ transition temperature dropped from 380 K for the HBC-C_{12} to 332 K for the dibromo HBC while the $Col_{ho} \rightarrow I$ transition temperature increased above 693 K for the dibromo HBC (see Table 1.2).

The effect of a reduced number of side chains on the supramolecular organization of the HBC discotic cores (Table 1.2, HBC-$(C_{12})_4$), has been investigated [92]. It was found that, the HBC-$(C_{12})_4$ exhibited the same hexagonal packing like the HBC-C_{12}. On the other hand, the reduced number of the alkyl chains increased the $C_r \rightarrow Col_{ho}$ transition temperature from 380 K for the HBC-C_{12} to 419 K for HBC-$(C_{12})_4$. In a subsequent study, it was found that the isotropization temperatures (T_i) values of a D_3 symmetric HBC (HBC-$(C_{12})_3$) and a C_2

symmetric HBC (HBC-$(C_{12})_2$) with three and two dodecyl chains, respectively, have been dramatically reduced by approximately 523 and 473 K with respect to the D_{6h} symmetric hexadodecyl HBC (HBC-C_{12}) (Table 1.2) [100]. The dramatic T_i drop was explained in terms of a decrease of the molecular symmetry.

These studies have shed light into the self-assembly of HBCs nevertheless many structural aspects are still unexplored. For example the exact packing within the C_r phase, the metastability of phases, with respect to T- and P-variations and the kinetics of phase transformations remain largely unexplored.

1.5.4.2 Solid-state NMR

Solid-state NMR spectroscopy is a powerful tool for the investigation of aromatic packing behavior in liquid crystals [85-88]. Fast magic-angle spinning (MAS) and double-quantum ^1H solid-state NMR spectroscopy have been used to further investigate the π-π packing in the columnar structures formed by hexabenzocoronenes and triphenylenes [87]. In the crystalline phase of the α-deuterated HBC-C_{12}, three distinct aromatic signals (Figure 1-54a) were found in the single-quantum MAS spectrum at 8.3, 6.9, and 5.7 ppm. This observation was, at first, sight, surprising since the symmetry of the isolated molecule would predict equivalence of all aromatic protons. Further insight was provided by the aromatic region of a two-dimensional ^1H DQ MAS spectrum of HBC-C_{12} as shown in Figure 1-54b. In such a spectrum, a peak is only observed if the two protons have a close proximity; for HBC-C_{12}, the arrangement of the aromatic protons into well-isolated "bay" proton pairs means that the observed DQ peaks can only arise from such pairs. Of the six possible DQ peaks, only AB cross-peaks and a CC diagonal peak were observed. This implied the existence of only two different types of bay proton pairs: one (AB) where two neighboring aromatic protons have different chemical shifts, namely, 8.3 and 6.9 ppm, and the other (CC) where the two protons both have the same chemical shift of 5.7 ppm. These three distinguishable peaks are explained in terms of different ring current influences of adjacent layers which the aromatic core protons experience within the columnar-rectangular herringbone-type structure as demonstrated in Figure 1-54c, d.

These observation are in agreement with the crystal structures obtained from substituted [87,101] and unsubstituted [102] HBCs. On heating the samples into the mesophase (383 K), the HBC molecules underwent a reorientation from the tilted to a planar arrangement. In the ^1H MAS spectra, this transition manifested itself in the narrowing of the resonance lines.
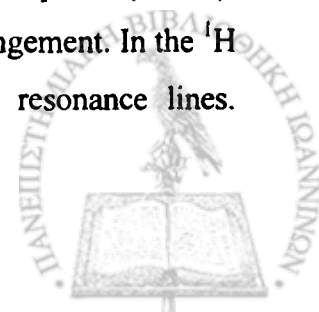
Moreover, the three distinct aromatic peaks observed earlier in the solid state, merged into a single aromatic ^1H resonance.
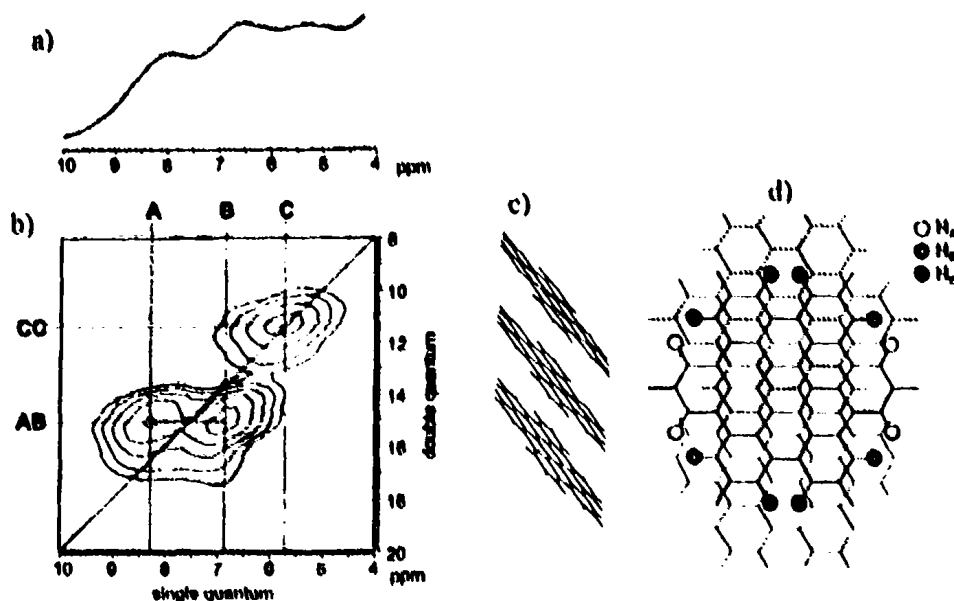
Figure 1-54: (a) One-dimensional ^1H NMR spectra of a-deuterated HBC'-C$_{12}$ in the crystalline phase at 333 K. (b) Tow-dimensional solid-state ^1H-^1H DQ MAS NMR spectrum. (c) The packing of the aromatic cores of HBC'-C$_{12}$ in the so-called "herring-bone" arrangement, according to the known X-ray single crystal structure of unsubstituted HBC. In (d), the staggered arrangement of the cores, viewed along a direction perpendicular to each layer, is shown, with the molecules above and below the central HBC'-C$_{12}$ molecules being indicated by dashed and dotted lines, respectively. The circles representing the aromatic bay protons are shaded according to the extent to which each proton experiences the ring current of the next aromatic layer. After refs. [87,88].

Recently, the comparison of quantum chemical ab initio calculations with experimental ^1H solid-state NMR spectra allowed the assignment of the specific molecular packing [86]. Thus NMR spectroscopy can be used as a means of structural technique in differentiating between the crystalline "herringbone" and the planar LC structure. We will employ this technique in the course of our studies.

1.5.4.3 Computer simulations

Molecular dynamics (MD) simulations with atomistic force fields are powerful tools for calculating local properties such as order parameters and molecular arrangements. The atomistic simulation study of columnar HBC derivatives provided information about the arrangement of the molecules in the planes parallel (along the z-axis) and perpendicular (in the xy plane) to the director $\hat{n}$, and the ordering of the side chain [89]. Below we summarize the main findings from a recent simulation study on HBCs.
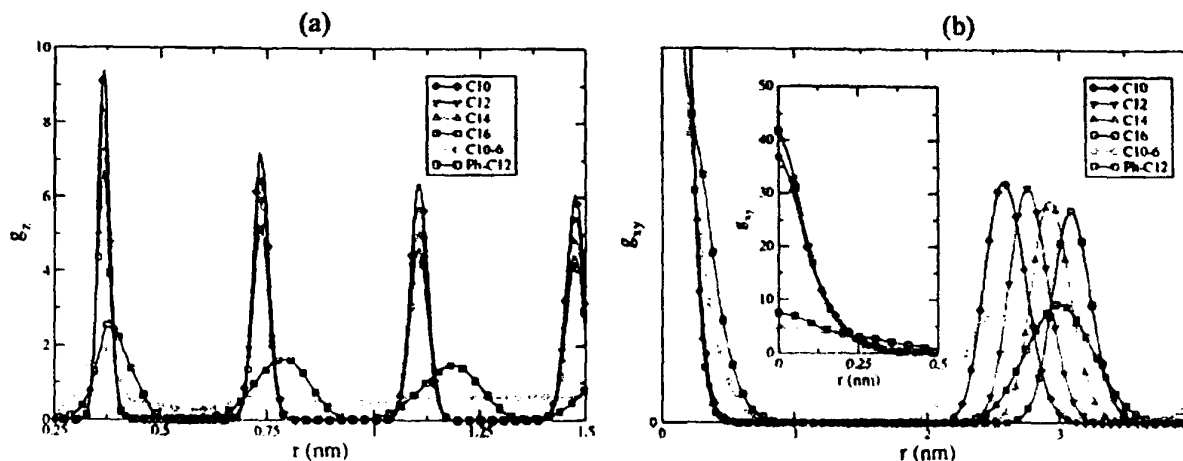
Figure 1-55: *(a) Intra-columnar probability to find another molecule of the same column at a distance r from the reference molecule; T=400 K. (b) inter-columnar probability of finding the center of mass of another molecule at a distance r from the reference molecule (two-dimensional radial distribution function). The inset shows the large peak around r=0; T=400 K. After ref. [89].*

The probability, $g_z(r)$, to find a molecule at a distance r from a reference molecule at 400 K for HBCs bearing a variety of different side chains was calculated (Figure 1-55a). $g_z(r)$ had a series of narrow peaks, that indicated the ordered stacking of the molecules in the columns. For linear side chains, the peaks were sharp with a constant intra-columnar distance that was independent of the chain length. When a phenyl ring was added, or branched side chains, the peaks were broadened and shifted, indicating a greater disorder of the mesophase. The second distribution function, g_{xy}, provided information on the lateral arrangement of molecules in planes perpendicular to the director $\hat{n}$ (in the xy plane, i.e., inter-columnar organization) as shown in Figure 1-55b. The two-dimensional radial distribution, apart from the peak around $r=0$, exhibited a peak reflecting in-plane nearest neighbor correlations and the underlying lattice constants of the hexagonal (or square) unit cell formed by the columns. The spacing between the in-plane (along the z-axis) nearest neighbors increased almost constantly with increasing length of the linear side chains. In the case of branched chains, the position of the peak was nearly identical to the C_{10} case, but the peak was broader due to disorder. For PhC_{12} side chains, the peak position was between C_{14} and C_{16}.

In addition to this information on the self-assembly, some dynamical information was also extracted, from the mean-square displacement of the molecular center of mass along the column direction. For long times it was shown that $<r^2>\sim t^1$ suggesting that the columns could diffuse as a whole. Despite these very important results, the disc dynamics within the columns (time-scale and geometry of motion) have not been investigated in detail. There exist only some preliminary molecular simulations in triphenylene discotic molecules (HAT6) that

revealed separate in-plane disc dynamics at 0.2 *ps* and softer out-of-plane motions at ~7 *ps* [109]. However, these simulations were made only on four discs and this limited size may have a strong effect on the dynamics.

1.5.5 Molecular dynamics of discotic liquid crystals

For applications as advanced electronic materials, the intrinsic disc mobility can influence the charge carrier mobility and thus needs to be explored in detail. In this respect, recent efforts through solid-state NMR spectroscopy [23,47,51,103-107], neutron scattering [108,109], computer simulations [89,109,110] and dielectric spectroscopy (DS) [91,106,107,111-115] have shed some light on the dynamics of the aromatic core as well as of the hydrocarbon side chains. Below we review the most important results from theses studies as well as the open questions and controversies.

1.5.5.1 NMR studies

Solid-state NMR spectroscopy has contributed a wealth of information about the dynamic properties of liquid crystals [116-121]. In particular, solid-state NMR can reveal information about the degree of dynamic order and mobility in the hexagonally arranged columns formed by discotic materials [93]. A dynamic order parameter S, can now be defined by Eq. (1.14) [122]

$$S_{CH} = \left\langle \frac{1}{2}\left(3\cos^2\theta_{CH}(t)-1\right)\right\rangle_t = \frac{\langle D_{CH}(t)\rangle_t}{D_{CH,static}} \tag{1.14}$$

which is different from the static order parameter introduced earlier in Eq. (1.1). The former is given in the form of the second order Legendre polynomial and is obtained experimentally as the ratio of the measured effective dipolar coupling constant to that of a static pair. Thus $S=1$ corresponds to a perfectly immobile disc (i.e., glassy) whereas $S = 0$ corresponds to a totally random motion of discs in the isotropic state. As an example, the triphenylene ((2S,3S)-2-chloro-3-methylpentanoyloxypentakis (pentoxy)triphenylene) has an order parameter of $S = 0.95$ [105]. In the case of the alkyl substituted HBC-C$_{12}$, S was found to be 0.84, which is substantially lower than the one reported for discotic forming triphenylenes suggesting increased disc mobility in the latter.

Herwig and co-workers [105] attributed this to the fact that the area of the core of hexabenzocoronene is approximately three times the size of triphenylene (Figure 1-56) and

therefore the overlap of the aromatic core can be very well sustained even without "perfect" π-π overlap.
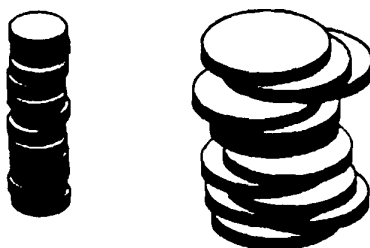
Figure 1-56: *Stacks of triphenylenes (left) and hexabenzocoronenes (right). To obtain strong π-π interactions, the stacking of small discs requires substantial overlap of discs. After ref. [105].*

This further suggests that both in-plane and out-of-plane disc dynamics could be present in HBCs but only the former in triphenylenes. However this point has not been clarified yet.

The molecular dynamics and phase transitions of a columnar liquid crystal based on the hexaether-substituted rufigallol mesogen were studied by 1D and 2D solid-state NMR spectroscopy [51]. 2D-exchange NMR spectra revealed a "slow" process involving the side chains, which was attributed to changes in the packing density of the molecules along the column. In this study the packing problem of columnar liquid crystals, resulting, from the incommensurability of the aromatic core moieties and the aliphatic side chains was solved by the model proposed by de Gennes [51] (see Section 1.5.2.1).

The molecular dynamics of the aromatic core as well as of the hydrocarbon side chains have been studied by using 2D-exchange NMR in a glass-forming discotic liquid crystal, with a triphenylene core [103]. Slow dynamics with non-Arrhenius temperature dependence (α process) reflecting the axial motion of the discs along the columnar axes was observed. The geometry of this motion was found to be neither a simple threefold jump, as suggested by the pseudo threefold symmetry of the substituted triphenylene core, nor did it correspond to small-step rotational diffusion. A simple model combining small-step diffusion and rotational jumps was presented that could quantitatively account for the observed angular displacements.

Deuterium NMR spectroscopy was also employed in studying the core and tail order parameters within the columnar phase of hexa-n-hexyloxy triphenylene [29]. Spectra were recorded on selectively deuterated isotopic species, that brought out considerable differences between the order parameters of the cores and the tails. As an example, Figure 1-57 gives the quadrupole splittings of the aromatic and α-aliphatic deuterons versus temperature in the mesophase region. It can be seen that the cores were highly ordered, with an orientational order
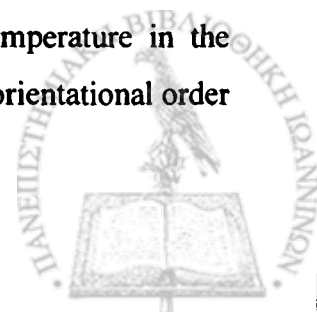
parameter, S, in the range from 0.95-0.90, whereas the a-aliphatic chains were in the disordered state.
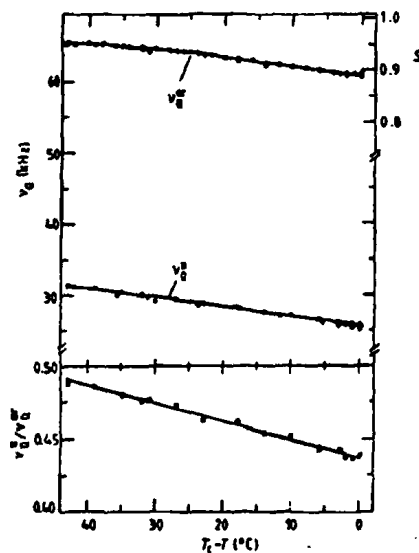
Figure 1-57: *Quadrupole splittings for the aromatic v_Q^{ar} and a-aliphatic v_Q^α deuterons of deuterated hexa-n-hexyloxytriphenylene (THE6) as functions of temperature $(T_c- T)$ in the mesophase region, where T_c is the mesophase-isotropic transition point. The open circles correspond to measurements on neat THE6-ar-d_6 and THE6-a-d_{12} separately; while the filled circles correspond to a 2: 1 mixture of the two isotopic species. The scale on the upper right hand side gives the orientational order parameter of the aromatic part. The curve at the bottom gives the ratio of the quadrupole splittings for the a-aliphatic and aromatic deuterons. After ref. [29].*

This study emphasized the fact that molecules forming the discs cannot be treated as completely rigid, but one has to take into account the conformational degrees of freedom of the hydrocarbon chains.

1.5.5.2 Neutron scattering studies

The quasi-elastic neutron scattering (QENS) is a powerful tool to probe the microscopic dynamical properties of liquid crystals within the time scale of 10^{-9} to 10^{-12} s [5].

The incoherent quasi-elastic neutron scattering (QENS) from the heptyl and octyl derivatives of the acta-alkylphthalocyanines, CnPcH2, in their crystalline and liquid crystalline (discotic columnar) phases was studied aiming at probing the mobility of the alkyl chains [123]. A diffusive motion was observed on the 10^{-10} to 10^{-12} s time scale that was attributed to alkyl chain dynamics. A major finding in this study was the small discontinuity in the elastic fraction of the quasi-elastic scattering, consistent with a change in the molecular tilt at the transition between the two D_{hd} phases.

A combination of QENS with molecular dynamics simulations on the discotic molecule hexakis(n-hexyloxy)triphenylene (HAT6) revealed a strong correlation of the dynamics of the cores and tails [109]. The system being characterized by overall in-plane motion, on a time scale of 0.2 *ps*, and softer out-of-plane motions at 7 *ps*. Small-amplitude in-plane motions where the discs move over each other were almost entirely determined by tail/tail interactions, these also playing an important role in the out-of-plane motion. Interestingly, the QENS results revealed that these motions were little affected in passing from the columnar to the isotropic phase.

QENS on hexakismethoxytriphenylene (HMT) revealed molecular motions at time scales of 0.1 and 7.3 *ps* at 370 K [108]. Deuteration of the methoxy tails, suppressed the signal for the slower motion, whereas the signal from the more rapid motion of the triphenylene cores was still present. persists. A molecular dynamics simulation on an isolated model of 4 HMT molecule revealed the slower methoxy motion to be a torsion of the whole methyl group around the core to oxygen bond. The faster motion was attributed to lateral sliding of the cores with respect to each other.

1.5.5.3 Dielectric spectroscopy studies

Broadband dielectric spectroscopy (DS) is a versatile tool in studying the dynamics of discotic liquid crystals [91,106,107,111-115]. The main advantage of DS is that it provides vital information on the disc dynamics (time scale) that is not easily accessible by other methods. It has, however, one requirement: a dipole is needed preferably in the vicinity of the core.

In fact, few dielectric studies have been carried out mainly on triphenylene discotic materials. In a first such study, DS was employed in studying the dynamics of two HAT6 derivatives; one having a dipole close to the core [91,103,106] and another where the dipole was located away from the core [114]. The molecular structures of the two derivatives are shown in Figures 1-58 and 1-59 as well as the corresponding relaxation map.

The fast β-process, with an activation energy of 37±3 kJ/mol, was attributed to a local librational motion of the chiral side chains involving the carbonyl group of the ester linkage and the adjacent chloro-substituent, and the "slower" α-process was attributed to the hindered disc rotation around the column axis, thus directly related to the glass temperature (T_g=228 K). ^{2}H NMR was employed to show that the α-process is due to the disc axial motion.
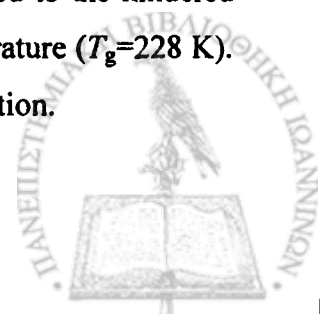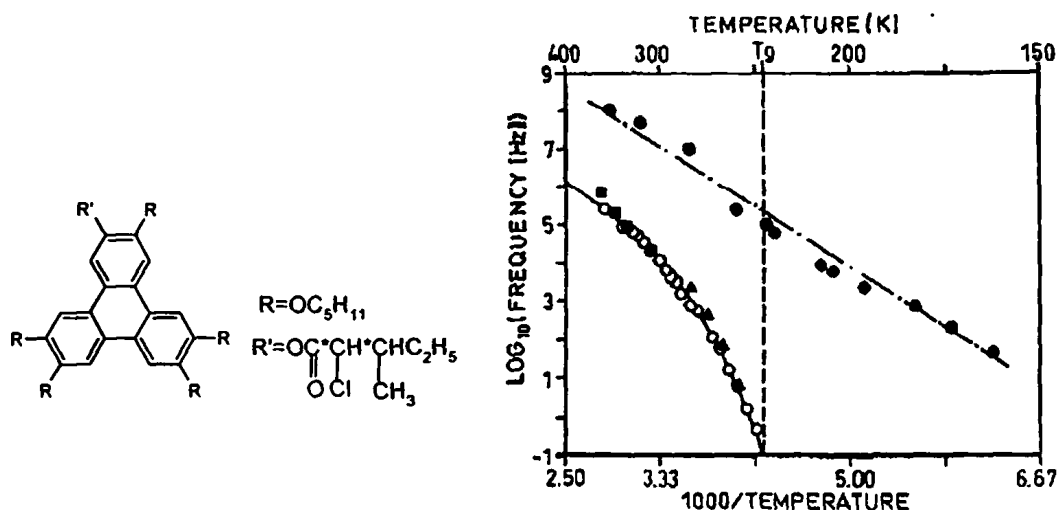
Figure 1-58: *Mean relaxation rate v_t measured by dielectric spectroscopy ($\bullet$,$\bigcirc$) versus inverse temperature of (2S,3S)-2-chloro-3-methyl-penta-noyloxypentakis(pentyloxy)-triphenylene. The dashed line represents the glass temperature as determined by DSC. Displayed on the same plot are the jump rates for a threefold jump determined by one-dimensional solid-echo spectra ($\blacksquare$) and 2D-exchange spectra ($\blacktriangle$) of the core deuterated molecule. Note the good agreement of all methods for the curved solid line, which is fitted to the WLF equation. After ref. [103].*

A recent DS study reported on the dynamics of the asymmetrically substituted triphenylene HAT6-C_{10}Br (where the dipole is located far from the core) in comparison to its symmetrically substituted HAT6 as shown in Figure 1-59 [114].
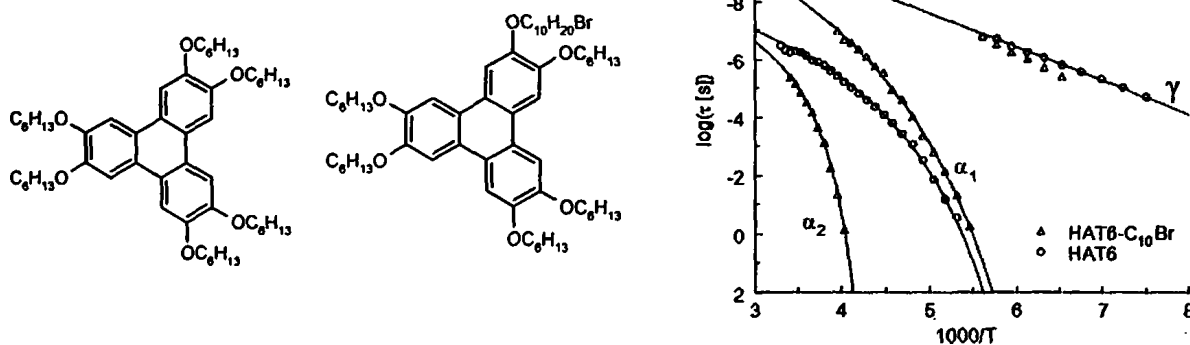
Figure 1-59: *Temperature dependence of the relaxation times for all dielectrically active processes in the HAT6 and HAT6-C_{10}Br. Full lines represent fit curves assuming Arrhenius (γ-process) and VFT-behavior (α-process). After ref. [114].*

Two α-processes (α_1 and α_2) and one local process (γ-process) were resolved for the dipole substituted compound. The γ-process, with an activation energy of 23 kJ/mol, was very similar in the HAT6 and HAT6-C_{10}Br. The faster α_1-process obeyed the VFT-dependence and assumed a T_g value around 176 K for both compounds. The slower α_2-process was only found in the HAT6-C_{10}Br and assumed a T_g value of 242 K. The faster α_1-process was attributed to a hindered polyethylene-like dynamic glass "transition". It is surprising that a PE-like process

was associated with a non-Arrhenius T-dependence. Nevertheless, our results, despite on a different system (HBC), will be compared with the results of this investigation.

The influence of the chirality and inclination of molecules on the dynamics has been investigated on three chiral metallorganic discotic mesogenes (chiral oxovanadium (IV), copper (II) and palladium (II) β-diketonates) that showed tilted columnar phases [124]. A new "slow" relaxation process (c-mode) appeared and was attributed to a Goldstone-like mode, similar to that present in SmC* phases, whose existence requires a helical arrangement. In addition to the Goldstone-like mode, two fast processes were found. The first process (h-mode), showed a non-Arrhenius behavior and was attributed to small-angle motions of the side groups that contain an ester linkage and a branch. The second fast process (l-mode), with Arrhenius dependence, it was attributed to the glass "transition".

In another DS study, the molecular dynamics of various triphenylene and benzene derivatives in their isotropic and liquid crystalline phases were investigated [28]. Two relaxation processes were detected within the columnar mesophases: the β-process with an Arrhenius temperature dependence and with activation energies between 37 and 40 kJ/mol was assigned to a librational motion of the ester groups in the side chains. The slower a-process followed a Williams-Landel-Ferry (WLF) (see Chapter 5, Eq. (5.1)) T-dependence and was assigned to the hindered rotation of the molecular discs around the columnar axis. The non-symmetrically substituted triphenylene derivative had the same two relaxation processes (a and β) like in the liquid crystal phase, whereas the symmetrically substituted triphenylene derivative revealed only the β-process due to fast conformational rearrangements. However, the claim that the hindered disc rotation is related to the glass transition was not proved by an independent NMR study.

The main result from the DS studies above is the observation of glass "transition" dynamics in the highly ordered columnar discotic liquid crystals. This finding is spectacular because glass formation, i.e., the dynamic freezing of supercooled liquids by circumvention of crystallization, is generally attributed to disordered matter. It is only recently, that a glass transition was found in shape persistent molecules [125]. Independent NMR studies together with DS have shown that this process associates with the axial disc motion around the columnar axis [103].

What is still missing, however, is the assignment of the slower dynamics pertinent to the long range organization on surfaces, the presence of multiple glass temperatures, as well as of the complete phase state and the stability (and metastability) of such compounds.
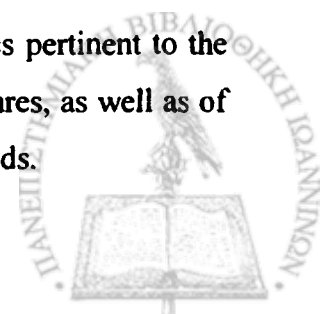
1.6 Motivation and objective

The aim of the Thesis is to understand the interplay between self-assembly and dynamics in a series of discotic and calamitic liquid crystals with applications as advanced electronic materials. The first part deals with hexa-*peri*-hexabenzocoronenes (HBCs) discotic liquid crystals. Studies of charge carrier mobilities in the crystalline phase of HBCs, revealed record high intrinsic mobilities that are about an order of magnitude higher than the one found in conjugated polymers. However, for applications as advanced electronic materials, the intrinsic disc mobility (both time-scale and geometry of motion) within the columns that can influence the charge carrier mobility needs to be explored in detail. The aim of this work is to provide a systematic investigation of HBC discotic liquid crystals with respect to the nanoscale self-assembly, the molecular dynamics, the thermodynamic phase state and the pathways of structure formation with the identification of possible metastable states. All these aspects are pertinent to the intrinsic charge carrier mobility. This requires a combination of model systems bearing dipoles directly attached to the cores and different microscopic techniques that are sensitive probes of the time-scale and geometry of motion. Furthermore, additional thermodynamic variables are needed (i.e., pressure) for constructing the complete phase diagram. For this purpose we employ a series of un-functionalized (Chapter 3) and dipole functionalized (Chapter 4) HBCs recently synthesized by Dr. Kastler and Mr. Dou at the MPI-P (Synthetic chemistry group of Prof. Dr. K. Müllen) especially for this study. First, we study the effect of dipole substitution on the stability of the crystalline and liquid crystalline phases. Second, we investigate the core dynamics within the columns by combining dielectric spectroscopy with site-specific NMR techniques. These probes provide unambiguously the rate and geometry of motion. Third, we employ pressure and investigate for the first time, the stability of the liquid crystalline and crystalline phases by providing the thermodynamic phase diagram for dimethoxy substituted HBC. This study delineates the pressure and temperature stability limits of the crystalline phase associated with the highest charge carrier mobility. Lastly, we monitor for the first time, the evolution of structure formation by dielectric means, following a distinct path within the *T-P* phase diagram. In that study we are interested in the presence or absence of intermediate states, the possible nucleation sites and the existence of long-lived metastability. The latter study provides glimpses of the exact mechanism for structural re-organization and growth.

The second part deals with calamitic liquid crystals that exhibit blue-light emission. So far, researchers have focused on phenylene-based polymers, such as polyfluorenes, ladder-type

polyphenylenes and more recently to polyindenofluorenes, because of their photoluminescence emission maximum being at around 2.9 *eV*, making them potential blue-emitting materials. Several challenges, however, remain before their use becomes widespread mainly because of color instability. The aim of this work is to understand the self-assembly and intrinsic dynamics of oligoindenofluorenes, because they can act as model systems for the polymers that can be prepared free of defects. For this purpose a series of model oligoindenofluorenes up to the polymer were synthesized recently by Dr. Grimsdale (Synthetic chemistry group of Prof. Dr. K. Müllen) and their self-assembly, the optical and dynamic properties are studied by employing, X-ray scattering, photoluminescence, polarizing optical microscopy, differential scanning calorimetry and dielectric spectroscopy.

The methodology consists of three steps. First, we probe the presence of keton defects that are held responsible for the color instability. For this purpose an indenofluorene monoketon was also synthesized for comparison with those of the defect-free IF oligomers. Second, we identify the type of mesophase (nematic/smectic) and third we follow the intrinsic molecular dynamics associated with the liquid-to-glass transition. Finally, these results are compared to the corresponding properties of oligofluorene samples. We find that oligoindenofluorenes have several similarities to the corresponding oligofluorenes, but also some distinct differences with respect to the mesoscopic order and glass temperatures that make them attractive materials for electronic applications.

1.7 References

[1] de Gennes, P. G., *The Physics of Liquid Crystals*, 1st Ed., Clarendon Press, Oxford, (1974).

[2] de Gennes, P. G.; Prost, J., *The Physics of Liquid Crystals: International Series of Monographs on Physics*, 2nd Ed., Clarendon Press, Oxford, (1995).

[3] Kumar, S., *Liquid Crystals: Experimental Study of Physical Properties and Phase Transitions*, Cambridge University Press, Cambridge, (2001).

[4] Demus, D.; Goodby, J.; Gray, G. W.; Spiess, H. W.; Vill, V., *Handbook of Liquid Crystals, Vol. 2B: Low Molecular Weight Liquid Crystals II*, Wiley-VCH, (1998).

[5] Kelker, H.; Hatz, R., *Handbook of Liquid Crystals*, Verlag Chemie GmbH, D-6940 Weinheim, (1980).

[6] Reinitzer, F. *Monatsh. Chem.* **9**, 421 (1888); for English translation see *Liq. Cryst.* **5**, 7 (1989).

[7] http://olla.ichf.edu.pl/lect/SS2005/Binnemans_lecture1.pdf
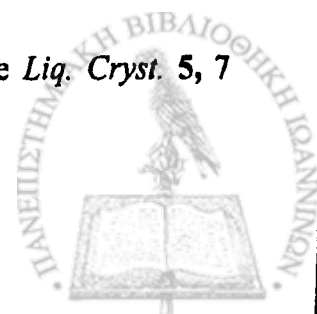
[8] Elmahdy, M. M.; Floudas, G.; Oldridge, L.; Grimsdale, A. C.; Müllen, K. *ChemPhysChem* **7**, 1431 (2006).

[9] Elmahdy, M. M.; Floudas, G.; Kastler, M.; Müllen, K. *J. Phys C* (submitted).

[10] Gedde, U. W., *Polymer Physics*, Chapman & Hall, London, (1995).

[11] http://web.media.mit.edu/~stefan/liquid-crystals/node2.html

[12] http://barrett-group.mcgill.ca/teaching/liquid_crystal/LC02.htm

[13] http://www.lci.kent.edu/lcphotosneubert.html

[14] Madsen, L. A.; Dingemans, T. J.; Nakata, M.; Samulski, E. T., *Phys. Rev. Lett.* **92**, 145505 (2004).

[15] http://www.yorklc.com/docs/pdf/LCM.pdf

[16] http://dept.kent.edu/spie/liquidcrystals/textures1.html

[17] Barón, M. *Pure Appl. Chem.* **73**, 845 (2001).

[18] http://www.fyslab.hut.fi/kurssit/Tfy-3.363/lectures/lecture09a.pdf

[19] McKenna, G. B. in *Polymer Properties, Vol. 2 of Comprehensive Polymer Science*, edited by C. Booth and C. Price, Ch. 10, P. 311, Pergamon, Oxford, (1989).

[20] Floudas, G.; Mierzwa, M.; Schönhals, A. *Phys. Rev. E* **67**, 031705 (2003).

[21] Shashidhar, R. *Mol. Cryst. Liq. Cryst.* **43**, 71 (1977).

[22] Chandrasekhar, S.; Sadashiva, B. K.; Suresh, K. A.; Madhusudana, N. V.; Kumar, S.; Shashidhar, R.; Venkatesh, G. *J. Phys. Colloques*, **40**, C3-120 (1979).

[23] Hollander, A.; Hommels, J.; Prins, K.O.; Spiess, H.W.; Werth, M. *J. Phys. II France* **6**, 1727 (1996).

[24] Chandrasekhar, S. ; Sadashiva, B. K.; Suresh, K. A. *Pramana* **7**, 471 (1977).

[25] Chandrasekhar, S.; Prasad, S. K. *Contemop. Phys.* **40**, 237 (1999).

[26] Boden, N.; Bushby, R. J.; Clements, J.; Movaghar, B.; Donovan, K. J.; Kreouzis, T. *Phys. Rev. B* **52**, 13274 (1995).

[27] Pisula, W.; Menon, A.; Stepputat, M.; Lieberwirth, I.; Kolb, U.; Tracz, A.; Sirringhaus, H.; Pakula, T.; Müllen, K. *Adv. Mater.* **17**, 684 (2005).

[28] Groothues, H.; Kremer, F.; Collard, D. M.; Lillya, C. P. *Liq. Cryst.* **18**, 117 (1995).

[29] Chandrasekhar, S.; Ranganath, G. S. *Rep. Prog. Phys.* **53**, 57 (1990).

[30] Frampton, C. S.; MacNicol, D. D.; Rowan, S. J. *J. Mol. Struct.* **405**, 169 (1997).

[31] Laschat, S.; Baro, A.; Steinke, N.; Giesselmann, F.; Hägele, C.; Scalia, G.; Judele, R.; Kapastina, E.; Sauer, S.; Schreivogel, A.; Tosoni, M. *Angew. Chem. Int. Ed.* **46**, 4832 (2007).

[32] Uznanski, P.; Marguet, S.; Markovitsi, D.; Schumacher, P.; Ringsdor, H. *Mol. Cryst. Liq. Cryst.* **293**, 123 (1997).

[33] Rothemund, P. *J. Am. Chem. Soc.*, **58**, 625 (1936).

[34] van Nostrum, C. F.; Bosman, A. W.; Gelinck, G. H.; Schouten, P. G.; Warman, J. M.; Kentgens, A. P. M.; Devillers, M. A. C.; Meijerink, A.; Picken, S. J.; Sohling, U.; Schouten, A. J.; Nolte, R. J. M. *Chem. Eur. J.* **1**, 171 (1995).

[35] Fechtenkötter, A.; Tchebotareva, N.; Watson, M. D.; Müllen, K. *Tetrahedron* **57**, 3769 (2001).

[36] Pak, C.; Lee, H. M.; Kim, J. C.; Kim, D.; Kim, K. S. *Struct. Chem.* **16**, 187 (2005).

[37] Hoeben, F. J. M.; Jonkheijm, P.; Meijer, E. W.; Schenning, A. *Chem. Rev.* **105**, 1491 (2005).

[38] Pisula, W.; Tomović, Ž.; Simpson, C. D.; Kastler, M.; Pakula, T.; Müllen, K. *Chem. Mater.* **17**, 4296 (2005).

[39] Pisula, W.; Tomović, Ž.; El Hamaoui, B.; Watson, M. D.; Pakula, T.; Müllen, K. *Adv. Funct. Mater.* **15**, 893 (2005).

[40] Wu, J.; Pisula, W.; Müllen, K. *Chem. Rev.* **107**, 718 (2007).

[41] Kastler, M., *Discotic Materials for Organic Electronics*, PhD thesis, Max-Planck Institute for Polymer Research, Mainz (2006).

[42] Dimitrakopoulos, C. D.; Malenfant, P. R. L. *Adv. Mater.* **14**, 99 (2002).

[43] Schmidt-Mende, L.; Fechtenkötter, A.; Müllen, K.; Friend, R. H.; MacKenzie, J. D. *Physica E* **14**, 263 (2002).

[44] Schmidt-Mende, L.; Watson, M.; Müllen, K.; Friend, R. H. *Mol. Cryst. Liq. Cryst.* **396**, 73 (2003).

[45] Stapff, I. H.; Stumpflen, V.; Wendorff, J. H.; Spohn, D. B.; Mobius, D. *Liq. Cryst.* **23**, 613 (1997).

[46] Kastler, M.; Pisula, W.; Wasserfallen, D.; Pakula, T.; Müllen, K. *J. Am. Chem. Soc.* **127**, 4286 (2005).

[47] Fischbach, I.; Pakula, T.; Minkin, P.; Fechtenkötter, A.; Müllen, K.; Spiess, H. W.; Saalwachter, K. *J. Phys. Chem. B* **106** 6408 (2002).

[48] Kumar, S. *Chem. Soc. Rev.* **35**, 83 (2006).

[49] Praefcke, K.; Singer, D.; Kohne, B.; Ebert, M.; Liebmann, A.; Wendorff, J. H. *Liq. Cryst.* **10**, 147 (1991).

[50] Chandrasekhar, S.; Prasad, S. K. *Contemop. Phys.* **40**, 237 (1999).

[51] Werth, M.; Leisen, J.; Boeffel, C.; Dong, R. Y.; Spiess, H. W. *J. Phys. II France* **3**, 53 (1993).

[52] Zheng, H.; Lai, C. K.; Swager, T. M. *Chem. Mater.* **7**, 2067 (1995).

[53] Safinya, C. R.; Liang, K. S.; Varady, W. A.; Clark, N. A.; Anderson, G. *Phys. Rev. Lett.* **53**, 1172 (1984).

[54] Glüsen, B.; Heitz, W.; Kettner, A.; Wendorff, J. H. *Liq. Cryst.* **20**, 627 (1996).

[55] Pisula, W.; Kastler, M.; Wasserfallen, D.; Mondeshki, M.; Piris, J.; Schnell, I.; Müllen, K. *Chem. Mater.* **18**, 3634 (2006).

[56] Fontes, E. ; Heiney, P. A. ; De Jeu, W.H. *Phys. Rev. Lett.* **61**, 1202 (1988).

[57] Lehn, J. M.; Malthête, J.; Levelut, A. M. *J. Chem. Soc. Chem. Commun.* 1794 (1985).

[58] Sakashita, H.; Nishitani, A.; Sumiya, Y.; Terauchi, H.; Otha, K.; Yamamoto, I. *Mol. Cryst. Liq. Cryst.* **163**, 211 (1988).

[59] Steinke, N.; Frey, W.; Baro, A.; Laschat, S.; Drees, C.; Nimtz, M.; Hägele, C.; Giesselmann, F. *Chem. Eur. J.* **12**, 1026 (2006).

[60] Méry, S.; Haristoy, D.; Nicoud, J.-F.; Guillon, D.; Diele, S.; Monobe, H.; Shimizu, Y. *J. Mater. Chem.* **12**, 37 (2002).

[61] Kastler, M.; Pisula, W.; Laquai, F.; Kumar, A.; Davies, R. J.; Baluschev, S.; García-Gutiérrez, M. C.; Wasserfallen, D.; Butt, H. J.; Riekel, C.; Wegner, G.; Müllen, K. *Adv. Mater.* **18**, 2255 (2006).

[62] Chandrasekhar, S.; Balagurusamy, V. S. K. *Proc. R. Soc. Lond. A* **458**, 1783 (2002).

[63] Warman, J. M.; de Haas, M. P.; Dicker, G.; Grozema, F. C.; Piris, J.; Debije, M.G. *Chem. Mater.* **16**, 4600 (2004).

[64] Vaughan, G. B. M.; Heiney, P. A.; McCauley Jr, J. P.; Smith III, A. B. *Phys. Rev. B*, **46**, 2787 (1992).

[65] Boden, N.; Bushby, R. J.; Clements, J. *J. Mater. Sci. Mater. Electron.* **5**, 83 (1994).

[66] Arikainen, E. O.; Boden, N.; Bushby, R. J.; Clements, J.; Movaghar, B.; Wood, A. *J. Mat. Chem.* **5**, 2161 (1995).

[67] Yoshino, K.; Nakayama, H.; Ozaki, M.; Onoda, M.; Hamaguchi, M. *Jpn. J. Appl. Phys.* **36**, 5183 (1997).

[68] van de Craats, A. M.; Warman, J. M.; Fechtenkötter, A.; Brand, J. D.; Harbison, M. A.; Müllen, K. *Adv. Mater.* **11**, 1469 (1999).

[69] van de Craats, A. M.; Warman, J. M.; deHaas, M. P.; Adam, D.; Simmerer, J.; Haarer, D.; Schuhmacher, P. *Adv. Mater.* **8**, 823 (1996).

[70] Ohta, K.; Hatsusaka, K.; Sugibayashi, M.; Ariyoshi, M.; Ban, K.; Maeda, F.;Naito, R.; Nishizawa, K.; van de Craats, A. M.; Warman, J. M. *Mol. Cryst. Liq. Cryst.* **397**, 325 (2003).

[71] Schouten, P. G.; Chen, W. M.; Warman, J. M.; Dehaas, M. P.; Vanderpol, J. F.; Zwikker, J. W. *Synth. Met.* **42**, 2665 (1991).

[72] Ban, K.; Nishizawa, K.; Ohta, K.; van de Craats, A. M.; Warman, J. M.; Yamamoto, I.; Shirai, H. *J. Mater. Chem.* **11**, 321 (2001).

[73] van de Craats, A. M.; Warman, J. M. *Adv. Mater.* **13**, 130 (2001).

[74] Debije, M. G.; Piris, J.; de Haas, M. P.; Warman, J. M.; Tomović, Ž.; Simpson, C. D.; Watson, M. D.; Müllen, K. *J. Am. Chem. Soc.* **126**, 4641 (2004).

[75] Kraft, A. *ChemPhysChem* **2**, 163 (2001).

[76] Sze, S. M. *Physics of Semiconductor Devices*, John Wiley, New York, (1981).

[77] Lino, H.; Hanna, J.; Bushby, R. J.; Movaghar, B.; Whitaker, B. J. *J. Appl. Phys.* **100**, 043716 (2006).

[78] Pecchia, A.; Lozman, O. R.; Movaghar, B.; Boden, N.; Bushby, R. J.; Donovan, K. J.; Kreouzis, T. *Phys. Rev. B* **65**, 104204 (2002).

[79] Lever, L. J.; Kelsall, R. W.; Bushby, R. J. *Phys. Rev. B* **72**, 035130 (2005).

[80] Warman, J. M.; van de Craats, A. M. *Mol. Cryst. Liq. Cryst.* **396**, 41 (2003).

[81] Müller-Horsche, E.; Haarer, D.; Scher, H. *Phys. Rev. B* **35**, 1273 (1987).

[82] Kepler, R. G. *Phys. Rev.* **119**, 1226 (1960).

[83] Van Winkle, D. H.; Clark, N. A. *Phys. Rev. Lett.* **48**, 1407 (1982).

[84] Safinya, C. R.; Clark, N. A.; Liang, K. S.; Varady, W. A.; Chiang, L. Y. *Mol. Cryst. Liq. Cryst.* **123**, 205 (1985).

[85] Brown, S. P.; Schnell, I.; Brand, J. D.; Müllen, K.; Spiess, H. W. *J. Am. Chem. Soc.* **121**, 6712 (1999).

[86] Ochsenfeld, C. *Phys. Chem. Chem. Phys.* **2**, 2153 (2000).

[87] Brown, S. P.; Schnell, I.; Brand, J. D.; Müllen, K.; Spiess, H. W. *J. Mol. Struct.* **521**, 179 (2000).

[88] Ochsenfeld, C.; Brown, S. P.; Schnell, I.; Gauss, J.; Spiess, H. W. *J. Am. Chem. Soc.* **123**, 2597 (2001).

[89] Andrienko, D.; Marcon, V.; Kremer, K. *J. Chem. Phys.* **125**, 124902 (2006).

[90] van de Craats, A. M.; Siebbeles, L. D. A.; Bleyl, I.; Haarer, D.; Berlin, Y. A.; Zharikov, A. A.; Warman, J. M. *J. Phys. Chem. B* **102**, 9625 (1998).

[91] Möller, M.; Wendorff, J. H.; Werth, M.; Spiess, H. W. *J. Non-Cryst. Solids* **170**, 295 (1994).

[92] Pisula, W.; Tomović, Ž.; Simpson, C. D.; Kastler, M.; Pakula, T.; Müllen, K. *Chem. Mater.* **17**, 4296 (2005).

[93] Fischbach, I.; Ebert, F.; Spiess, H. W.; Schnell, I. *Chem. Phys. Chem.* **5**, 895 (2004).

[94] Fechtenkötter, A., *Liquid Crystalline Hexabenzocoronenes as Organic Molecular Materials-Synthesis, Characterization and Application*, PhD thesis, Max-Planck Institute for Polymer Research, Mainz (2001).

[95] Pisula, W.; Tomović, Ž.; El Hamaoui, B.; Watson, M. D.; Pakula, T.; Müllen, K. *Adv. Funct. Mater.* **15**, 893 (2005).

[96] Samorí, P.; Fechtenkötter, A.; Jäckel, F.; Böhme, T.; Müllen, K.; Rabe, J. P. *J. Am. Chem. Soc.* **123**, 11462 (2001).

[97] Pisula, W.; Tomović, Ž.; Watson, M. D.; Müllen, K.; Kussmann, J.; Ochsenfeld, C.; Metzroth, T.; Gauss, J. *J. Phys. Chem. B* **111**, 7481 (2007).

[98] Ito, S.; Wehmeier, M.; Brand, J. D.; Kübel, C.; Epsch, R.; Rabe, J. P.; Müllen, K. *Chem. Eur. J.* **6**, 4327 (2000).

[99] Fechtenkötter, A.; Tchebotareva, N.; Watson, M. D.; Müllen, K. *Tetrahedron* **57**, 3769 (2001).

[100] Feng, X.; Pisula, W.; Ai, M.; Gröper, S.; Rabe, J. P.; Müllen, K. *Chem. Mater.* **20**, 1191 (2008).

[101] Herwig, P. T.; Enkelmann, V.; Schmelz, O.; Müllen, K. *Chem. Eur. J.* **6**, 1834 (2000).

[102] Goddard, R.; Haenel, M.; Herndon, W. C.; Kröger, C.; Zander, M. *J. Am. Chem. Soc.* **117**, 30 (1995).

[103] Leisen, J.; Werthg, M.; Boeffel, C.; Spiess, H.W. *J. Chem. Phys.* **97**, 3749 (1992).

[104] Werth, M.; Leisen, J.; Boeffel, C.; Dong, R.Y.; Spiess, H.W. *J. Phys. II France* **3**, 53 (1993).

[105] Herwig, P.; Kayser, C.W.; Müllen, K.; Spiess, H.W. *Adv. Mater.* **8**, 510 (1996).

[106] Vallerien, S. U.; Werth, M.; Kremer, F.; Spiess, H. W. *Liq. Cryst.* **8**, 889 (1990).

[107] Wasserfallen, D. et al., *Adv. Funct. Mater.* **15**, 1585 (2005).

[108] Kearley, G.J.; Mulder, F.M.; Picken, S.J.; Kouwer, P.H.J.; Stride, J. *Chem. Phys.* **292**, 185 (2003).

[109] Mulder, F.M.; Stride, J.; Picken, S.J.; Kouwer, P.H.J.; de Haas, M.P.; L.D.A. Siebbeles, L.D.A.; Kearley, G.J. *J. Am. Chem. Soc.* **125**, 3860 (2003).

[110] Kirkpatrick, J.; Marcon, V.; Nelson, J.; Kremer, K.; Andrienko, D. *Phys. Rev. Lett.* **98**, 227402 (2007).

[111] Möller, M.; Wendorff, J. H.; Werth, M.; Spiess, H. W.; Bengs, H.; Karthaus, O.; Ringsdorf, H. *Liq. Cryst.* **17**, 381 (1994).

[112] Ngai, K. L. *J. Non-Cryst. Solids* **197**, 1 (1996).

[113] Glüsen, B.; Kettner, A.; Kopitzke, J.; Wendorff, J. H. *J. Non-Cryst. Solids* **241**, 113 (1998).

[114] Yildirim, Z.; Wübbenhorst, M.; Mendes, E.; Picken, S.J.; Paraschiv, I.; Marcelis, A.T.M.; Zuilhof, H.; Sudhölter, E.J.R. *J. Non-Cryst. Solids* **351**, 2622 (2005).

[115] Kruglova, O.; Mendes, E.; Yildirim, Z.; Wübbenhorst, M.; Mulder, F.M.; Stride, J.A.; Picken, S.J.; Kearley, G.J. *ChemPhysChem* **8**, 1338 (2007).

[116] Feike, M.; Demco, D. E.; Graf, R.; Gottwald, J.; Hafner, S.; Spiess, H. W. *J. Magn. Reson.* A **122**, 214, (1996).

[117] Schnell, I.; Spiess, H. W. *J. Magn. Res.* **151**, 153, (2001).

[118] Saalwächter, K.; Schnell, I. *Solid State Nucl.Magn. Res.* **22**, 154 (2002).

[119] Saalwächter, K.; Spiess, H. W. *J. Phys. Chem.* **114**, 5707 (2001).

[120] Langer, B.; Schnell, I.; Spiess, H. W.;Grimmer, A.-R. *J. Magn. Res.* **138**, 182 (1999).

[121] Dong, R. Y. *Prog. NMR Spectrosc.* **41**, 115 (2002).

[122] Elmahdy, M. M.; Floudas, G.; Mondeshki, M. ; Spiess, H. W.; Dou, X.; Müllen, K. *Phys. Rev. Lett.* **100**, 107801 (2008).

[123] Belushkin, A. V.; Cook, M. J.; Frezzato, D.; Haslam, S. D.; Ferrarini, A.; Martin, D.; McMurdo, J.; Nordio, P. L.; Richardson, R. M.; Stafford, A. *Molec. Phys.* **93**, 593 (1998).

[124] Palacios, B.; De La Fuente, M. R. ; Pérez-Jubindo, M. A. ; Iglesias, R. ; Serrano, J. L. ; Sierra, T. *Liq. Cryst.* **25**, 481 (1998).

[125] Floudas, G. *Prog. Polym. Sci.* **29**, 1143 (2004).

Chapter 2

Experimental Techniques and Methods of Analysis

2.1 Introduction

In the present work, the following techniques were employed: Differential scanning calorimetery (DSC), Polarizing optical microscopy (POM), X-ray diffraction (XRD), Nuclear magnetic resonance (NMR), and Dielectric spectroscopy (DS). Below we briefly report on the technical characteristics of these techniques and describe, in more detail, the latter technique.

2.2 Experimental techniques

2.2.1 Differential scanning calorimetry (DSC)

DSC is a thermoanalytical technique in which the difference in the amount of heat required to increase the temperature of a sample and reference are measured as a function of temperature. Using this technique it is possible to observe melting and crystallization temperatures as well as the glass "transition" temperatures (T_g). Glass "transition" appears as a step in the baseline of the recorded DSC signal. This is due to the sample undergoing a change in heat capacity. The apparent melting ($T_{m'}$) (cold crystallization, T_c) temperatures appear as endothermic (exothermic) peaks in the DSC curve (Figure 2-1).
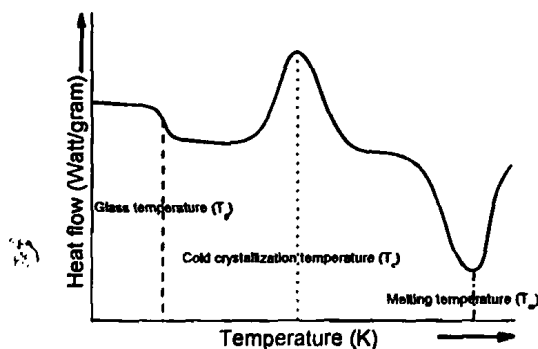
Figure 2-1: *Schematic DSC curve demonstrating the appearance of several common features: Glass temperature (T_g) followed by cold crystallization (T_c) and by the apparent melting temperature ($T_{m'}$).*

In our measurements a Mettler Toledo Star DSC was used with heating and cooling rates of 10 K/min in the range from 150-523 K. The transition temperatures of the second heating and cooling cycle were used that exclude influences from thermal history.

2.2.2 Polarizing optical microscopy (POM)

Polarizing optical microscopy is very sensitive to the birefringence and to changes in birefringence as a result of phase transitions. As such, it can be used to identify transition temperatures. POM is equipped with two-crossed polarizers (Figure 2-2). The first, the polarizer, is located in front of the specimen stage and the second, the analyser, is located behind the objective. The light entering the specimen is linearly polarized. When the light passes through an optically isotropic sample, then there is no change of polarization and the crossed analyser extinguishes the light. However, after passing through a birefringent sample and the analyser the outgoing light is elliptically polarized. The analyser reduces the intensity of the outgoing light but an appreciable fraction of the incoming light is transmitted.
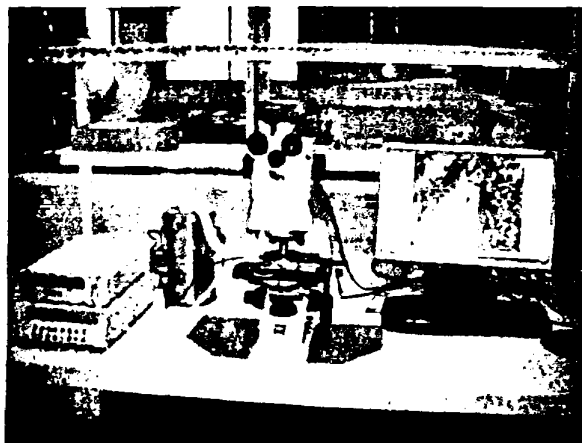
Figure 2-2: *Polarizing optical microscopy set-up used at the UoI.*

For the measurements, a Zeiss Axioskop 40 POM (Figure 2-2) with a Linkam THMS600 heating/cooling stage was used to identify the different phases. The Linkam THMS600 stage had a temperature range of 77 K to 873 K with a temperature stability of 0.1 K. Sample preparation involved placing a small amount between two glass slides then mounted on a highly polished silver heating element that ensured high heat transfer. A platinum resistor sensor, accurate to 0.01 K, provided an accurate and stable temperature signal. LNP94/2 liquid nitrogen pump cooling system enabled controlled cooling rates. The samples were heated to the isotropic phase, then slowly cooled with different cooling rates in the range from 0.01 to 0.1
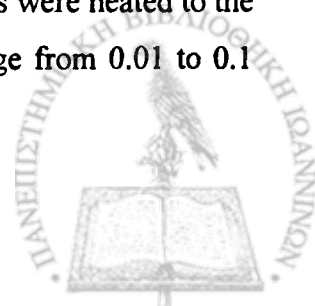
K/min. Representative POM images of the branched hexaalkyl hexa-*peri*-hexabenzocoronenes HBC-$C_{10,6}$ and HBC-$C_{14,10}$ at 313 K are shown in Figure 2-3.

Figure 2-3: *POM images of the HBC-$C_{10,6}$ (left) and HBC-$C_{14,10}$ (right) at 313 K with a cooling rate of 0.1 K/min. The HBC-$C_{10,6}$ suggests a smectic mesophase while the HBC-$C_{14,10}$ shows a spherulitic structure. After ref. [1].*

2.2.3 X-ray diffraction (XRD)

The samples were prepared by filament extrusion using a homebuilt mini extruder according to ref. [2], which is presented schematically in Figure 2-4. The extruder is practically a copy of the one designed and used at the Max-Planck Institute for Polymer Research (MPI-P) by T. Pakula [2].
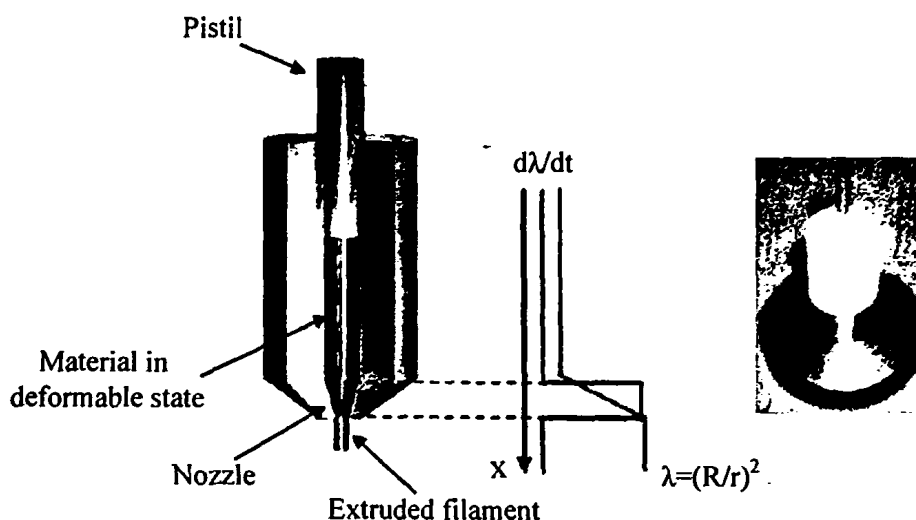
Figure 2-4: *(left) Schematic illustration of the filament alignment by extrusion using a mini extruder first designed by Prof. T. Pakula at the MPI-P. Profiles of the drawing rate and the draw ratio along the extruder axis are schematically plotted on the right-hand side. (right) picture of the extruder. Schematic after ref. [2].*

Therein, the material is heated to a phase at which it becomes plastically deformable and is extruded as a thin filament by a constant-rate motion of the piston along the cylinder. A number of parameters control this mechanical processing: the velocity of the piston, diameters of cylinder and orifice, and the die shape as well as specimen dependent parameters (temperature, shear modulus, etc.). The ratio of the cylinder to orifice diameters defines the

macroscopic draw ratio $(\lambda=(R/r)^2)$ and the shape of the die defines the drawing rate profile. In the case of the conical die, as in the example shown in Figure 2-4, the drawing rate is constant within the die and is zero within the cylinder and at the die orifice. In the extruder used, the cylinder had an inner diameter of 2.0 mm and the orifice diameter was 0.7 mm. In this way, 0.7 mm thick filaments drawn to $\lambda \sim 8$ were obtained. The piston has been moved typically with the rate of 5 mm/s, which resulted in a high drawing rate within the die. The X-ray diffraction experiments revealed that under such conditions the polymer chains and the columns in discotic liquid crystals are in most cases well oriented in the extrusion direction. The structure investigation was performed using a 2D wide-angle X-ray scattering (WAXS) setup at MPI-P, which is shown schematically in Figure 2-5.
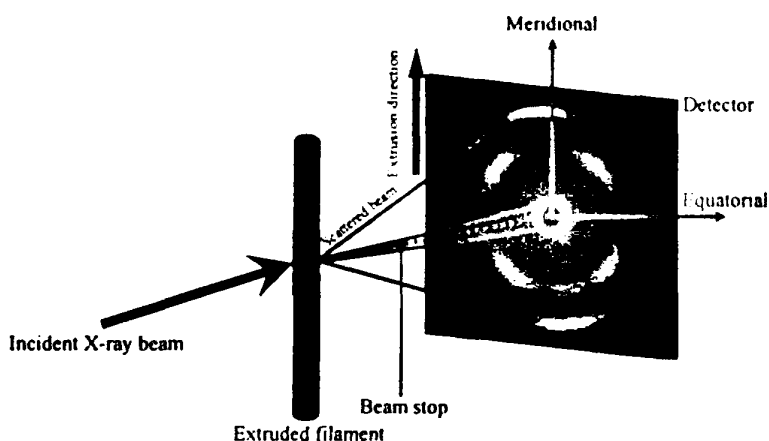
Figure 2-5: *Schematic illustration of the experimental setup of the 2D-WAXS scattering of an extruded filament of the mono-bromo HBC at 403 K.*

WAXS patterns were obtained from the studied materials using the X-ray beam with pinhole collimation and a two-dimensional detector (Siemens A102647) with 1024x1024 pixels. A double graphite monochromator for the CuKα radiation (λ=0.154 nm) was used. The sample-to-detector distance was in the range from 7.2 to 8 cm. Measurements were made at different temperatures on heating and subsequent cooling runs. The scattered intensity distributions were integrated along the equatorial and meridional axis, and the resulting intensities are presented as a function of the scattering wave vector $q(=(4\pi/\lambda)\sin\theta$, 2θ is the scattering angle). The sample was positioned vertically with respect to the incident X-ray beam. From the reflection positions in the 2D WAXS pattern, it is possible to obtain information about the intra- and intermolecular correlations. Since the fibres are placed vertically with respect to the incident X-ray beam, the meridional reflections correspond to the correlations resulting from the intramolecular organization and the equatorial reflections provides information about the intermolecular order.
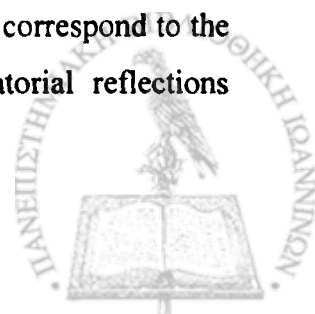
2.2.4 Solid-state NMR spectroscopy

Solid-state NMR spectroscopy can provide valuable information about molecular and supra-molecular structures, packing arrangements, as well as molecular dynamics [3-7]. In the solid state, anisotropic spin interactions such as the chemical shift anisotropy or dipolar couplings contain unique spatial and dynamic information. However, these interactions lead to broad and overlapping spectral lines, which obscure the isotropic chemical information known from solution-state NMR spectroscopy. In order to obtain high resolution, it is necessary to remove the broadening due to this anisotropic interactions. The most convenient way to achieve this goal is by rapid sample rotation at the so-called "magic" angle (MAS) relative to the static magnetic field (B_0) (Figure 2-6). At spinning speeds up to 35 kHz the anisotropic spin interactions are mostly refocused and the isotropic chemical shift information is regained.
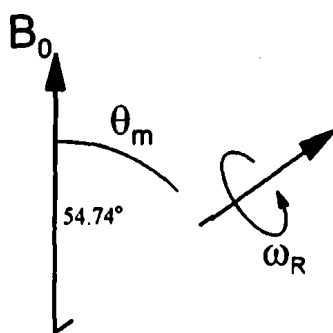
Figure 2-6: *Schematic illustration of the sample rotor at magic angle of 54.74^o and rotation frequency ω_R with respect to the static magnetic field B_0.*

Magic-angle spinning introduces artificial motion by placing the axis of the sample rotor at the magic angle of 54.74^o with respect to B_0. At this angle the dipolar and chemical shift interactions term vanish (i.e., $3\cos^2\theta - 1 = 0$). Samples are finely powdered and packed tightly into rotors, which are then spun at rates from 1 to 35 kHz, depending on the rotor size and type of experiment being conducted. If the sample is spun at a rate less than the magnitude of the anisotropic interaction, a manifold of spinning sidebands becomes visible, which are separated by the rate of spinning (in Hz).

Referring to the effect of MAS on anisotropic broadenings, Maricq and Waugh. distinguished between "homogeneous" and "inhomogeneous" interactions [8]: under MAS, an inhomogeneously broadened line splits spontaneously into a pattern of sharp spinning sidebands, while homogeneously broadened lines successively narrow with increasing MAS frequencies, allowing the observation of the underlying spinning-sideband pattern.

The MAS NMR experiments considered herein employed sequences of strong radio-frequency (RF) pulses separated by delays, during which the spin system evolved under the

internal interactions. These pulse sequences are often referred to as "laboratory frame" sequences, because the quantization axis is given by the static magnetic field B_0 along the laboratory z-axis [9]. The principle of laboratory-frame recoupling pulse sequences can be understood by considering the rotor modulations which are introduced by the sample rotation [10]. The spatial parts of the interaction Hamiltonians are modulated by the MAS frequency ω_R and twice the MAS frequency $2\omega_R$. For illustration, the respective oscillations are depicted in Figure 2-7.
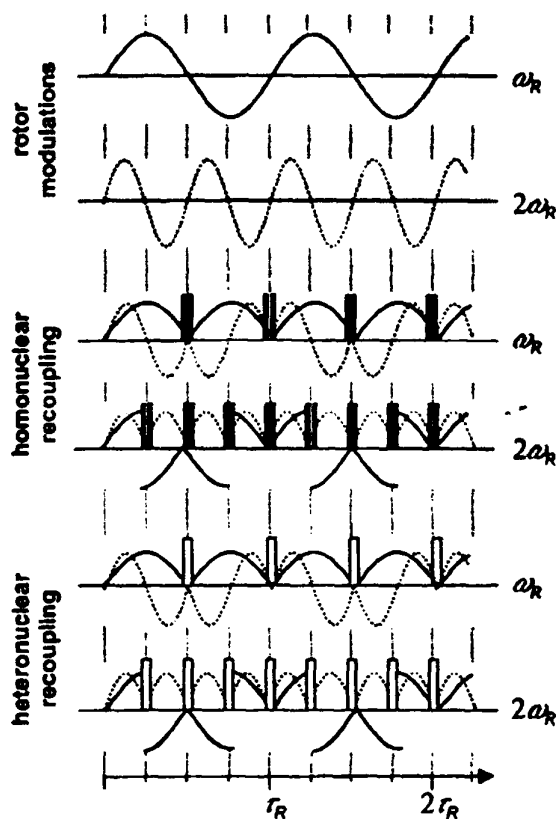
Figure 2-7: *Modulations of an anisotropic interaction Hamiltonian under MAS (top) and pulse sequences for recoupling interactions which depend on the nuclear spin in a bilinear (middle) or linear fashion (bottom). The pairs of $90°$ pulses (middle) recouple homonuclear dipole-dipole couplings and (weak) quadrupole couplings, whereas the $180°$ pulses (bottom) recouple heteronuclear dipole-dipole couplings or chemical shift anisotropies. After ref. [9].*

As there are two modulation frequencies, ω_R and $2\omega_R$, the sign change in the spin part can be performed at intervals of either $\tau_R/2$ or $\tau_R/4$, respectively (τ_R is the recoupling time). The type of RF pulses required for this sign inversion depend on the nature of the spin part of the interaction. For interactions that depend linearly on a spin (that is, chemical shift anisotropy (CSA) and heteronuclear dipole-dipole couplings), the sign inversion is achieved by π-pulses which was first realized in the REDOR (rotational-echo double-resonance) experiment with pulse spacings of $\tau_R/2$ [11]. Interactions with a bilinear spin dependence (that is, homonuclear
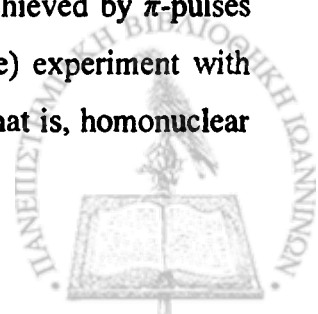
dipole-dipole and quadrupole couplings) can be recoupled in an analogous fashion by the so-called back-to-back (BABA) pulse sequence [3]. In this sequence, each π-pulses of REDOR-type recoupling is replaced by a pair of $\pi/2$-pulses with orthogonal phases. Effectively, these pairs of $\pi/2$-pulses invert the sign of the spin part of the homonuclear dipole-dipole and quadrupole couplings. In Figure 2-7, the principles of BABA and REDOR recoupling are illustrated. Clearly, pulse trains with pulse spacings of $\tau_R/2$ recouple only the ω_R-modulated terms, whereas pulse trains with pulse spacings of $\tau_R/4$ recouple only the $2\omega_R$-modulated terms. Henceforth, these two types of recoupling are referred to as "ω_R-recoupling" and "$2\omega_R$-recoupling".

An efficient and sensitive way to measure anisotropic interactions is the generation of spinning sideband patterns via rotor encoding (RE) of the recoupled interactions [9]. Such rotor encoding is accomplished by combining two recoupling blocks with different initial rotor phases, meaning that the second block is shifted with respect to the first by a time t_1 which is incremented in steps $\Delta t_1 < \tau_R$ (Figure 2-8).
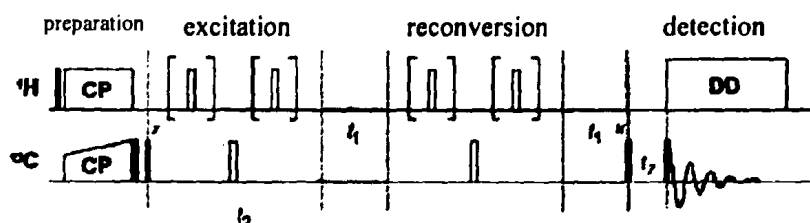
Figure 2-8: *Pulse sequences used for heteronuclear ^1H-^{13}C dipolar recoupling (REDOR) based on simple π-pulse trains that are separated into two blocks by t_1 intervals which are incremented in steps $\Delta t_1 < \tau_R$ to introduce rotor encoding. ω_R- or $2\omega_R$-recoupling is realized by separating π-pulses by $\tau_R/2$ or $\tau_R/4$, respectively. After ref. [9].*

The generation of these multi-quantum (MQ) sideband patterns has been found to be due to several effects [12]: (1) "rotor encoding" of the dipolar or first-order quadrupolar interaction due to the change in rotor phase (and, hence, in the Hamiltonian) between the multiple-quantum excitation and reconversion periods; (2) rotor modulation of non-total MQ coherences due to dipolar or quadrupolar evolution during the t_1 period; and (3) rotor modulation of all MQ coherences due to evolution under the chemical-shielding anisotropy (CSA) interaction during the t_1 period.

In cases where the spinning frequency exceeds the magnitudes of the anisotropic internuclear interactions, narrow spectral lines can often be obtained. However, it is frequently useful to acquire spectra in the so-called "slow-spinning" regime, where the MAS frequency is less than the static powder line-width. If the line-shapes are dominated by inhomogeneous

interactions (e.g., the chemical-shielding or the heteronuclear dipolar interaction), slow magic-angle spinning will split the spectrum into a pattern of narrow spinning sidebands spaced by integer multiples of the rotation frequency [12]. The relative intensities of these sidebands contain information about the nature of the dominant anisotropic interactions, and the envelope of the sideband pattern at slow speeds generally resembles the shape of the static powder spectrum [12].

Magic angle spinning can be used to average the dipolar coupling and to simplify the interaction. If the magic angle spinning frequency (ω_R) is on the order of the dipolar coupling constants (D_{ij}), spinning sideband patterns resulting from the rotor modulation of the dipolar couplings are observed during unsynchronized detection of NMR signals [12]. These patterns can be analyzed and the effective dipolar coupling can be estimated. Following this idea, a magic angle spinning separate local field experiment has been designed, recording spinning sideband patterns due to the heteronuclear dipolar couplings between a ^{13}C nucleus and the surrounding protons while refocusing all chemical shift anisotropy contributions. The method provides qualitative information about the dynamics of the different segments.

The possibility to study site-specific, different dipolar couplings with various known orientations with respect to the molecular frame renders the high resolution multiple-quantum techniques under fast magic angle spinning a powerful tool for the investigation of complex dynamics in solids. The dipolar coupling constant for two nuclear spins i and j spaced by an internuclear distance, r_{ij}, is given by [13]

$$D_{ij} \propto \frac{1}{r_{ij}^3} \cdot \frac{1}{2}\left(3\cos^2\theta_{ij} - 1\right)$$ (2.1)

where, θ_{ij}, denotes the angle of the internuclear vector between i and j with respect to the external magnetic field, B_0, as illustrated in Figure 2-9.
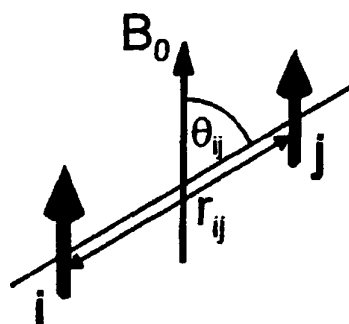
Figure 2-9: Dipole-dipole coupling between unlike spins, where θ_{ij} denotes the angle between r_{ij} and the magnetic field B_0.
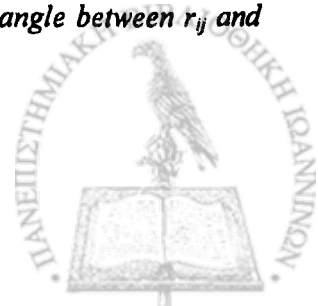
Dynamic averaging of the dipolar coupling takes place if θ_{ij} and/or r_{ij} are affected by the molecular motion and therefore become time-dependent [$\theta_{ij}=\theta_{ij}(t)$ and/or $r_{ij}=r_{ij}(t)$]. Significant changes of the couplings are observed in the fast limit, when the molecular dynamics characterized by a correlation time t_c become substantially faster than the effective dipolar coupling strength ($D_{ij} \ll 1$). In cases where the internuclear distance, r_{ij} , between the coupled spins is not affected by the molecular dynamics, e.g., CH bonds, the observed reduced dipolar coupling, $<D_{ij}(t)>_t$, can be directly interpreted as a measure of the anisotropy of the motion. To facilitate the comparison of residual dipolar couplings independent of the internuclear distances of the coupled spins, a local order parameter, S_{ij}, can be defined as [13]

$$S_{ij} = \left\langle \frac{1}{2}\left(3\cos^2\theta_{ij}(t)-1\right) \right\rangle_t = \frac{\langle D_{ij}(t) \rangle_t}{D_{ij,stat}} \tag{2.2}$$

For isotropic reorientations the effective dipolar coupling, $<D_{ij}(t)>_t$, vanishes and so does the order parameter ($S_{ij}=0$), whereas for uniaxial rotation the effective residual coupling depends on the angle between the internuclear vector and the rotation axis according to the second Legendre polynomial [14]. Therefore, it is the ratio of the dipolar coupling, D_{ij}, to the magic angle spinning frequency, ω_R, that determines the number and the relative intensities of the observed spinning sidebands. A qualitative interpretation of sideband patterns recorded under comparable experimental conditions uses the following rule of thumb: "the stronger the intensity of higher order sidebands in comparison to the centerband or the first order sidebands the higher the ratio D_{ij}/ω_R. Based on this rule, qualitative information can be obtained just by inspection of the measured sideband patterns.

For the systems investigated herein, the two-dimensional rotor-synchronized double quantum (DQ) magic-angle spinning (MAS) spectra were recorded on a Bruker Avance 700 spectrometer using a standard double-resonance probe supporting rotor of 2.5 mm outer diameter. The ^{1}H-^{1}H back-to-back (BABA) [3] recoupling technique for the excitation and reconversion of double-quantum coherences (DQCs) was applied for one cycle at 25 kHz MAS. Details on the methods as well as on the interpretation of the DQ MAS spectra are given elsewhere [4]. The molecular dynamics investigations were performed by recording ^{13}C-^{1}H REREDOR spinning sideband patterns [5,6], at 80 μs recoupling time and 25 kHz magic angle spinning (MAS) on a Bruker Avance 500 spectrometer using a Bruker double-resonance probe supporting rotors of 2.5 mm outer diameter. All experimental temperatures were corrected for the frictional heating effects arising from the fast rotor spinning [7].

2.2.5 Dielectric spectroscopy (DS)

The interaction of electromagnetic radiation with molecular systems gives rise to quantized transitions between the electronic, vibrational and rotational molecular energy states which may be observed by UV/visible and infra-red absorption spectroscopies at frequencies above about 1 THz (10^{12} Hz) (Figure 2-10). The interaction of electromagnetic waves with matter in the frequency regime between 10^{-6} and 10^{12} Hz is the domain of broadband dielectric spectroscopy [15]. In this extraordinarily extended dynamic range, molecular and collective dipolar fluctuations, charge transport and polarization effects at inner and outer boundaries take place, and determine the dielectric properties of the material under study. Hence broadband dielectric spectroscopy enables us to gain a wealth of information on: (i) dipole relaxation arising from the reorientational motions of molecular dipoles and (ii) electrical conduction arising from the translational motions of electric charges (ions, electrons).
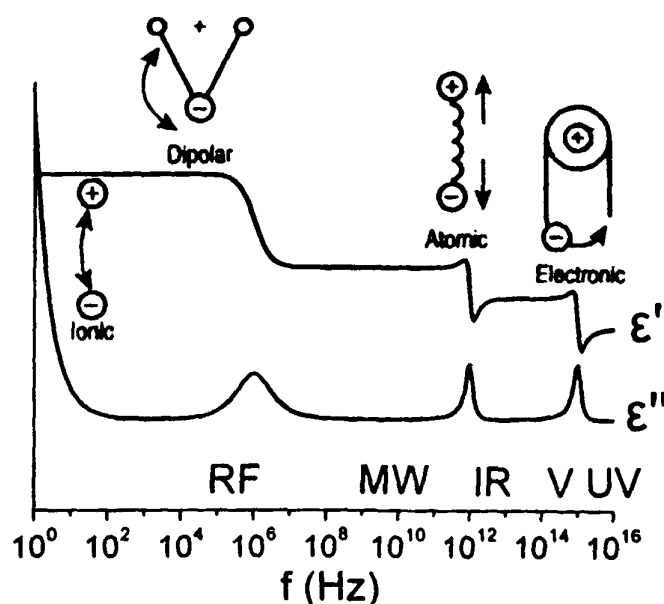
Figure 2-10: *A schematic of dielectric permittivity over a wide range of frequencies. The real, ε', and imaginary, ε'', parts of permittivity are shown and various processes are depicted: ionic and dipolar relaxation, followed by atomic and electronic resonances at higher frequencies.*

In general, dielectric mechanisms can be divided into relaxation and resonance processes. The most common, starting from high frequencies (Figure 2-10), are [16]:

(i) Electronic polarization: This resonant process arises when an isolated neutral atom is placed in an electric field. The electrons will be displaced in a direction opposite to that of the field. Therefore a dipole moment is formed due to displacement and the atom is said to be polarized. The electronic polarization appear, however, at very high frequencies of about 10^{15} Hz, corresponding to the ultraviolet range.
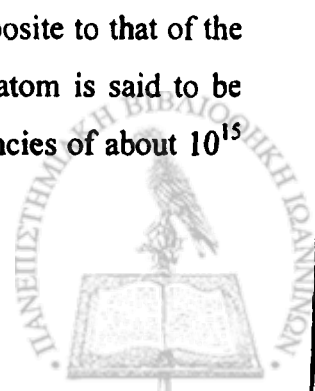
(ii) Atomic polarization: It is a resonant process which is found in ionic substances (such as sodium chloride) whose molecules are formed of atoms having excess charges of opposite polarities. An electric field will tend to shift the relative position of the positive and negative ions of a molecule, thus inducing a dipole moment other than that induced by the distortion of the electronic charges around individual atoms. The movement of heavy ions is more sluggish than electrons so that atomic polarization cannot occur at such high frequencies as electronic polarization. It is occures at a frequency of $\sim 10^{13}$ Hz, which correspondes to the infrared range.

(iii) Dipolar relaxation: This is associated with dipolar substances. The molecules or association of ions possess dipole moments even in the absence of an applied field. Such moments are not normally observed macroscopically, because the thermal agitation orient the molecules randomly, therefore average moment over a physically small volume is zero. In the presence of an external field, the dipoles experience a torque tending to orient them in the direction of the field so that the average moment is no longer zero. The relaxation times of these dipoles range from several picoseconds, in low-viscosity liquids, to hours in glasses. The corresponding measurement frequencies range from 10^{-6} Hz to 10^{12} Hz, which requires a series of instruments for complete coverage. Relaxation mechanisms are relatively slow compared to resonant electronic transitions or molecular vibrations, which usually have frequencies above 10^{12} Hz.

(iv) Ionic relaxation: Ionic relaxation comprises ionic conductivity, interfacial or space-charge polarization. Ionic conductivity dominates at low frequencies and high temperatures and introduces only losses to the system. Interfacial polarization occurs when charge carriers are trapped at interfaces in heterogeneous systems.

2.2.5.1 Static electric field

The polarization, $\vec{P}$, is defined as the difference between the electric displacement, D, due to bound charges and the electric field strength, $\vec{E}$, due to free charges [17]

$$\vec{P} = \frac{D - \vec{E}}{4\pi} \qquad (2.3)$$

Many molecules have a permanent dipole moment $\vec{\mu}$ which can be oriented by an external electric field $\vec{E}$. Hence for a system containing only one kind of dipoles, a macroscopic polarization $\vec{P}$ of the molecules within a volume V becomes [15]
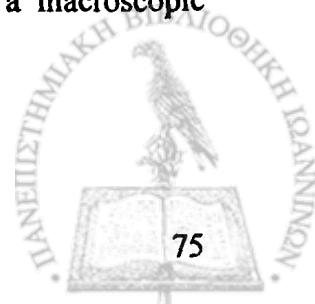
$$\vec{P} = \frac{1}{V}\sum \vec{\mu}_i + \vec{P}_\infty = \frac{N}{V}\langle \vec{\mu}\rangle + \vec{P}_\infty \qquad (2.4)$$

where N denotes the total number of dipoles in the system, $\langle \vec{\mu}\rangle$ is the mean dipole moment and $\vec{P}_\infty$ is an induced polarization (electronic and atomic polarization). The dielectric permittivity, $\varepsilon^*(\omega) = \varepsilon'(\omega) - i\varepsilon''(\omega)$, is related to the macroscopic polarization $\vec{P}$ by

$$\vec{P} = (\varepsilon^* - 1)\varepsilon_0 \vec{E} \qquad (2.5)$$

where ε_0 ($=8.854\times10^{-12}$ A s V^{-1} m^{-1}) is the dielectric permittivity of vacuum, the real part $\varepsilon'(\omega)$ is proportional to the energy stored reversibly in the system per period and the imaginary part $\varepsilon''(\omega)$ is proportional to the energy which dissipated per period. Assuming non-interacting dipoles and that the electric field E_{Loc} at the location of the dipole is equal to the outer electrical field $\vec{E}$ (i.e., no local field corrections), the mean value of the dipole moment is given only by the counterbalance of the thermal energy and the interaction energy U of a dipole with the electric field given by $U = -\vec{\mu}\cdot\vec{E}$. According to Boltzmann statistics one gets

$$\langle \vec{\mu}\rangle = \frac{\displaystyle\int_{4\pi} \vec{\mu}\exp\left(\frac{\vec{\mu}\cdot\vec{E}}{k_B T}\right)d\Omega}{\displaystyle\int_{4\pi}\exp\left(\frac{\vec{\mu}\cdot\vec{E}}{k_B T}\right)d\Omega} \qquad (2.6)$$

where T is the temperature, k_B is the Boltzmann constant and $d\Omega$ the differential space angle. The factor $\exp\left(\dfrac{\vec{\mu}.\vec{E}}{k_B T}\right)d\Omega$, gives the probability that the dipole moment vector has an orientation between Ω and $\Omega + d\Omega$. Only the dipole moment component which is parallel to the direction of the outer electric field contributes to the polarization. Therefore the interaction energy is given by $U = -\mu E\cos\theta$ where θ is the angle between the orientation of the dipole moment $\vec{\mu}$ and the electric field $\vec{E}$. So Eq. (2.6) simplifies to

$$\langle \mu\rangle = \frac{\displaystyle\int_0^\pi \mu\cos\theta\exp\left(\frac{\mu E\cos\theta}{k_B T}\right)\frac{1}{2}\sin\theta d\theta}{\displaystyle\int_0^\pi\exp\left(\frac{\mu E\cos\theta}{k_B T}\right)\frac{1}{2}\sin\theta d\theta} \qquad (2.7)$$

The term $\frac{1}{2}\sin\theta$ corresponds to components of the space-angle in θ direction. With $x=\mu E\cos\theta/k_B T$ and $a=\mu E/k_B T$ it results $\langle \mu\rangle = \mu\langle\cos\theta\rangle$ and Eq. (2.7) can be written as
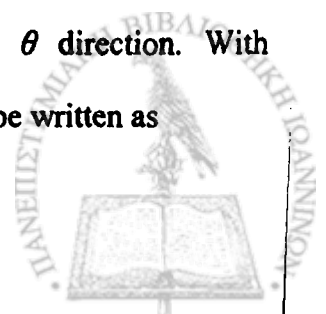
$$\langle\cos\theta\rangle = \frac{1}{a}\frac{\int_{-a}^{a} x\exp(x)dx}{\int_{-a}^{a}\exp(x)dx} = \frac{\exp(a)+\exp(-a)}{\exp(a)-\exp(-a)} - \frac{1}{a} = \Lambda(a) \qquad (2.8)$$

where $\Lambda(a)$ is the Langevin function that has Taylor series $\Lambda(a) = \frac{1}{3}a - \frac{1}{45}a^3 + \frac{2}{945}a^5 - \dots$.

The dependence of Λ on a is given in Figure 2-11. For small values of the electric field (i.e. $E<0.1k_BT/\mu$ or $a=\mu E/k_BT<0.1$) the dipole moment will obey a linear dependence with the electric field, therefore Eq. (2.6) reduces to

$$\langle\vec{\mu}\rangle \cong \frac{\mu^2}{3k_BT}\vec{E} \qquad (2.9)$$

The intensity of electric field that was applied in the experiments of this work was $\sim 10^4$ V/m (the sample thickness ~ 50 μm and the applied voltage ~ 1 Volt) that is inside the linear region.
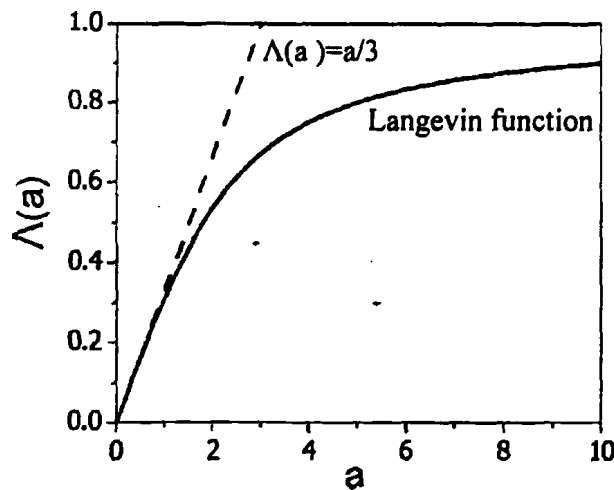
Figure 2-11: *Dependence of the Langevin function $\Lambda(a)$ versus a (solid line) together with the linear approximation (dashed line). The linear approximation $\Lambda(a)=a/3$ holds for $a<<1$. After ref. [15].*

Inserting Eq. (2.9) into Eq. (2.4) and with the aid of Eq. (2.5) the contribution of the orientational polarization to the dielectric function can be calculated as

$$\varepsilon_S - \varepsilon_\infty = \frac{1}{3\varepsilon_0}\frac{\mu^2}{k_BT}\frac{N}{V}, \quad \varepsilon_\infty = 1+\frac{P_\infty}{\varepsilon_0 E} \qquad (2.10)$$

where $\varepsilon_S = \lim_{\omega\to 0}\varepsilon'(\omega)$ and $\varepsilon_\infty = \lim_{\omega\to\infty}\varepsilon'(\omega)$ are the limits of the dielectric constant, ε', at low- and high-frequencies, respectively. The ε_∞ covers all contributions to the dielectric function which are due to electronic and atomic polarization P_∞ in the optical frequency range.

As mentioned earlier, Eq. (2.10) enables one to estimate the mean molecular dipole moment, $\langle \mu^2 \rangle^{1/2}$, from dielectric spectra with two assumptions: (i) the dipoles should not interact with each other which is true only for much diluted systems and (ii) local field effects (shielding of the outer electric field) are negligible. Onsager treated the problem of the local field effects for polar molecules by the theory of the reaction field which considers the enhancement of the permanent dipole moment of a molecule, $\bar{\mu}$, by the polarization of the environment (reaction field) [18]. The detailed calculation gives

$$\varepsilon_S - \varepsilon_\infty = \frac{1}{3\varepsilon_0} F \frac{\mu^2}{k_B T} \frac{N}{V}, \quad F = \frac{\varepsilon_S (\varepsilon_\infty + 2)^2}{3(2\varepsilon_S + \varepsilon_\infty)} \tag{2.11}$$

where F is the factor of local field. Eq. (2.11) can be used to estimate dipole moments for non-associating organic liquids and failed for polar associating liquids. The reason for the failure is static orientation correlations between molecules which are not considered in the derivation of the Onsager equation. Therefore Kirkwood and Fröhlich [17] introduced the correlation factor g to model the interaction between dipoles with respect to the ideal case of non-interacting dipoles. In general the Kirkwood/Fröhlich correlation factor is defined by

$$g = \frac{\left\langle \sum_i \mu_i \sum_j \mu_j \right\rangle}{N \mu^2} = \frac{\mu_{interact}^2}{\mu^2} \tag{2.12}$$

where μ^2 is the mean square dipole moment for non-interacting isolated dipoles which can be measured. The g-factor can be smaller or greater than one depending on the case if the molecules have the tendency to orient anti-parallel or parallel. The contribution of the Kirkwood/Fröhlich correlation factor g to the dielectric function can be calculated as

$$\varepsilon_S - \varepsilon_\infty = \frac{1}{3\varepsilon_0} g F \frac{\mu^2}{k_B T} \frac{N}{V} \tag{2.13}$$

with

$$g = 1 + z \langle \cos\psi \rangle \tag{2.14}$$

where z is the coordination number and ψ is the angle between the test dipole and a neighbor. Usually the g-factor is difficult to be measured and the effective dipole moment μ_{eff} can only measured

$$\mu_{eff} = (g\mu^2)^{1/2} \tag{2.15}$$

2.2.5.2 Alternating electric field

The polarisation that is created by alternating electric field, $E(t)$, in the framework of linear response theory (i.e., small electric field), is given by

$$\vec{P}(t) = \vec{P}_\infty + \varepsilon_0 \int_{-\infty}^{t} \varepsilon(t-t') \frac{dE(t')}{dt'} dt' \qquad (2.16)$$

where $\varepsilon(t)$ is the time-dependent dielectric function and $\vec{P}_\infty$ covers all contributions arising from induced polarization. Eq. (2.16) is based only on linearity (the response of the system on two disturbances is the sum of the two single reactions) and causality (only disturbances in the past contribute to the response at the time t). $P(t)$ can be measured directly as the time dependent response caused by a step-like change of the outer electrical field $(dE(t)/dt=E_0\delta(t)$; $P(t)=P_\infty+E\varepsilon_0\varepsilon(t))$. The relationship between the time dependence of the polarization is sketched in Figure 2-12 for a step-like change of the electric field.
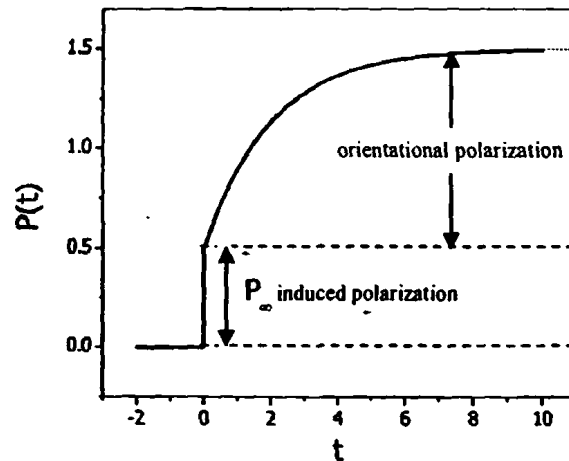
Figure 2-12: *Schematic illustration of the time dependence of the polarization. At t=0 the time-dependence polarization, $\vec{P}(t)$, is equal to the induced polarization, $\vec{P}_\infty$, while at t>0 it is equal to the orientational polarization [15].*

If a stationary periodic electric field $E(\omega,t)=E_0 exp(-i\omega t)$, where $\omega(=2\pi f)$ is the angular frequency, is applied to the system, Eq. (2.16) is transformed to

$$P(\omega,t) = \varepsilon_0 \left[\varepsilon^*(\omega) - 1 \right] E(\omega,t) \qquad (2.17)$$

The relationship of $\varepsilon^*(\omega)$ to the time dependent dielectric function $\varepsilon(t)$ is given by

$$\varepsilon^*(\omega) = \varepsilon'(\omega) - i\varepsilon''(\omega) = \varepsilon_\infty - \int_0^\infty \frac{d\varepsilon(t)}{dt} \exp(-i\omega t) dt \qquad (2.18)$$

Eq. (2.18) is a one-sided Fourier transformation. Like for all one-sided Fourier transformations of a causal function the real and the imaginary part of $\varepsilon^*(\omega)$ are related to each other by the Kramers-Kronig relations [15],

$$\varepsilon'(\omega) - \varepsilon_\infty = \frac{2}{\pi} \int_0^\infty \frac{\xi \varepsilon''(\xi)}{\xi^2 - \omega^2} d\xi$$

$$\varepsilon''(\omega) = \frac{2}{\pi} \int_0^\infty \frac{\xi [\varepsilon'(\xi) - \varepsilon_\infty]}{\xi^2 - \omega^2} d\xi + \frac{\sigma}{\varepsilon_0 \omega}$$

(2.19)

where ξ is a complex quantity. From an experimental point of view Eq. (2.19) means that both $\varepsilon'(\omega)$ and $\varepsilon''(\omega)$ carry the same information. In addition, the second equation contains a conductivity term, $\sigma/\varepsilon_0\omega$, which has no contribution in the $\varepsilon'(\omega)$ part. However, because of the limited frequency range and conductivity contributions including Maxwell/Wagner or electrode polarization the practical applicability of the Kramers/Kronig transformations is limited for dielectric experiments. Recalling that $\varepsilon_S = \varepsilon'(0)$ one finds for $\omega \rightarrow 0$

$$\varepsilon_s - \varepsilon_\infty = \Delta\varepsilon = \frac{2}{\pi} \int_0^\infty \varepsilon''(\xi) \frac{d\xi}{\xi} = \frac{2}{\pi} \int_0^\infty \varepsilon''(\xi) d\ln\xi$$

(2.20)

where $\Delta\varepsilon = \varepsilon_S - \varepsilon_\infty$, is the dielectric strength which can be obtained by integrating the imaginary part of the complex dielectric function $\varepsilon^*(\omega)$.

The fluctuation-dissipation theorem (FDT) of Callen and Welton [15] states a general relationship between the response of a given system to an external disturbance and the internal fluctuation of the system in the absence of the disturbance. Such a response is characterized by a response function or equivalently by an admittance, or an impedance. The internal fluctuation is characterized by a correlation function of relevant physical quantities of the system fluctuating in thermal equilibrium, or equivalently by their fluctuation spectra. For dielectric relaxation, the complex dielectric function, $\varepsilon^*(\omega)$, is related to the dipole moment correlation function $\Phi(t)$ (Eq. (2.21)) via Fourier transformation (Eq. (2.22)):

$$\Phi(t) = \frac{\langle \vec{\mu}(t) \cdot \vec{\mu}(0) \rangle}{\langle \vec{\mu}^2 \rangle}$$

(2.21)

where t denotes the time variable. It is obvious that $\Phi(0)=1$ and $\Phi(t \rightarrow \infty)=0$ hold.

The $\varepsilon(t)$ and $\varepsilon^*(\omega)$ are related to the correlation function $\Phi(t)$ of the dipolar fluctuations by

$$\Phi(t) = \frac{\varepsilon(t) - \varepsilon(\infty)}{\varepsilon(0) - \varepsilon(\infty)}$$

$$\frac{\varepsilon^{*}(\omega) - \varepsilon_{\infty}}{\varepsilon_{S} - \varepsilon_{\infty}} = 1 - i\omega \int_{0}^{\infty} \Phi(t) \exp(-i\omega t) dt \qquad (2.22)$$

The real, $\varepsilon'(\omega)$, and imaginary, $\varepsilon''(\omega)$, parts of the complex dielectric function can be calculated from the correlation function following Eqs. (2.23) and (2.24):

$$\frac{\varepsilon'(\omega) - \varepsilon_{\infty}}{\varepsilon_{S} - \varepsilon_{\infty}} = 1 - \omega \int_{0}^{\infty} \Phi(t) \sin(\omega t) dt \qquad (2.23)$$

$$\frac{\varepsilon''(\omega)}{\varepsilon_{S} - \varepsilon_{\infty}} = \omega \int_{0}^{\infty} \Phi(t) \cos(\omega t) dt \qquad (2.24)$$

2.2.5.3 The distribution functions of the relaxation times

The decreasing of the polarization in the absence of an electric field, due to the occurrence of a field in the past, is independent of the history of the dielectric, and depends only on the value of the orientation polarization at the instant, with which it is proportional. Denoting the proportionality constant by $1/\tau_D$, since it has the dimension of a reciprocal time, one thus obtains the following differential equation for the orientation polarization in the absence of an electric field:

$$\frac{d\vec{P}(t)}{dt} = -\frac{1}{\tau_D} \vec{P}(t) \qquad (2.25)$$

where τ_D is a characteristic relaxation time. The solution of the first order differential Eq. (2.25) leads to an exponential decay for the correlation function $\Phi(\tau)$

$$\Phi(t) = \exp\left[-\frac{t}{\tau_D}\right] \qquad (2.26)$$

Inserting Eq. (2.26) into Eq. (2.22) one gets for the complex dielectric function $\varepsilon^{*}(\omega)$

$$\varepsilon^{*}(\omega) = \varepsilon_{\infty} + (\varepsilon_{S} - \varepsilon_{\infty})\left[1 - i\omega \int_{0}^{\infty} \exp(-t/\tau_D) \exp(-i\omega t) dt\right]$$

$$= \varepsilon_{\infty} + (\varepsilon_{S} - \varepsilon_{\infty})\left(1 - \frac{i\omega\tau_D}{1 + i\omega\tau_D}\right) = \varepsilon_{\infty} + (\varepsilon_{S} - \varepsilon_{\infty})\frac{1}{1 + i\omega\tau_D} \qquad (2.27)$$

$$\varepsilon^{*}(\omega) = \varepsilon_{\infty} + \frac{\Delta\varepsilon}{1 + i\omega\tau_D} \text{ with } \varepsilon'(\omega) = \varepsilon_{\infty} + \Delta\varepsilon\frac{1}{1 + \omega^{2}\tau_D^{2}} \text{ and } \varepsilon''(\omega) = \Delta\varepsilon\frac{\omega\tau_D}{1 + \omega^{2}\tau_D^{2}}$$

These relationships are known as the Debye formulas. The Debye process has a relaxation time distribution, which is symmetrical around $f_{max}=\omega_{max}/2\pi=1/(2\pi\tau)$ and with a full-width at half-maximum of ~1.14 decades in frequency for the dielectric loss. In most cases, the half width of measured loss peaks is much broader than the predicted by Eq. (2.27) (up to six decades) and in addition, their shapes are asymmetric and with a high frequency tail. This is called non-Debye (or non-ideal) relaxation behavior. In the literature, several empirical model functions, mostly generalization of the Debye function, have been developed and tested which are able to describe broadened and/or asymmetric loss peaks. Among these empirical model functions, the most important are the Kohlrausch-Williams-Watts (KWW), Cole-Cole (CC), Cole-Davidson (CD) and the Havriliak-Negami function (HN). HN-function is most commonly used in the frequency domain as will discuss in detail later in the analysis of dielectric spectra section.

The non-exponential [stretched] relaxation behavior can be characterized by the Kohlrausch-Williams-Watts (KWW) function in the time-domain [19]:

$$\Phi(t)=\Phi(0)\exp\left[-\left(\frac{t}{\tau_{KWW}}\right)^{\beta_{KWW}}\right].\tag{2.28}$$

The quantities $\Phi(t)$ and $\Phi(0)$ are the dynamic response at time t and 0, respectively, after a perturbation, while τ_{KWW} is a characteristic time (usually different from τ_{HN}). β_{KWW} is the stretching exponential parameter and is generally in the range of 0 to 1. For a simple Debye relaxation behavior, the response is an exponential function with $\beta_{KWW}=1$. The broadening of the dielectric function can be described by the Cole-Cole function [20]

$$\varepsilon_{CC}^{*}(\omega)=\varepsilon_{\infty}+\frac{\Delta\varepsilon}{1+\left(i\omega\tau_{CC}\right)^{\beta}}\tag{2.29}$$

where $0<\beta\leq1$ leads to a symmetrical broadening for the relaxation function compared to Eq. (2.27). For $\beta=1$ the Debye-function is obtained. The Cole-Cole relaxation time, τ_{CC}, gives the position of maximal loss by $\omega_{p}=2\pi\nu_{p}=1/\tau_{CC}$. Many experimental results, especially on liquids or low molecular glass forming materials, show that the complex dielectric function can have also an asymmetric broadening which can be described by Cole-Davidson function which reads [21]

$$\varepsilon_{CD}^{*}(\omega)=\varepsilon_{\infty}+\frac{\Delta\varepsilon}{\left(1+i\omega\tau_{CD}\right)^{\gamma}}\tag{2.30}$$

The parameter γ ($0<\gamma\leq1$) describes an asymmetric broadening of the relaxation function for frequencies $\omega>1/\tau_{CD}$ is the Cole-Davidson relaxation time. For $\gamma=1$ the Debye-function is
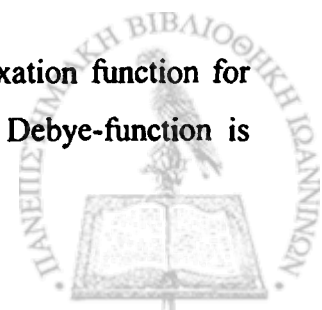
recovered again. It should be noted that for an asymmetric model function, like the Cole-Davidson function, the characteristic relaxation time of the model function does not coincide with the relaxation time which is related to the position of maximal loss. The relationship of both quantities depends on the shape parameters. For the Cole-Davidson Eq. (2.30) one obtains

$$\omega_p = \frac{1}{\tau_{CD}}\tan\left[\frac{\pi}{2\gamma+2}\right] \tag{2.31}$$

In the frequency domain, the complex dielectric function $\varepsilon^*(\omega)$ is related to the complex electric modulus $M^*(\omega)$ through Eq. (2.32)

$$M^*(\omega) = M' + iM'' = \frac{1}{\varepsilon^*(\omega)} \Rightarrow M' = \frac{\varepsilon'}{\varepsilon'^2 + \varepsilon''^2}, \ M'' = \frac{\varepsilon''}{\varepsilon'^2 + \varepsilon''^2} \tag{2.32}$$

where M' and M'' denote real and imaginary parts of the complex electric modulus.

For the Debye case (Eq. 2.27), the relation between the modulus relaxation time constant, τ_M, and the permittivity retardation time constant, τ_ε, can result from

$$M^*(\omega) = \frac{1}{\varepsilon^*(\omega)} = \frac{1}{\varepsilon_\infty + \frac{\varepsilon_S - \varepsilon_\infty}{1+i\omega\tau}} = \frac{1+i\omega\tau}{\varepsilon_\infty(1+i\omega\tau)+\varepsilon_S-\varepsilon_\infty} = \frac{1+i\omega\tau}{\varepsilon_\infty i\omega\tau + \varepsilon_S} =$$

$$= \frac{1}{\varepsilon_\infty} + \frac{1+i\omega\tau - \frac{1}{\varepsilon_\infty}(\varepsilon_\infty i\omega\tau + \varepsilon_S)}{\varepsilon_\infty i\omega\tau + \varepsilon_S} = \frac{1}{\varepsilon_\infty} + \frac{1+i\omega\tau - i\omega\tau - \frac{\varepsilon_S}{\varepsilon_\infty}}{\varepsilon_S + \varepsilon_\infty i\omega\tau} = \frac{1}{\varepsilon_\infty} + \frac{\frac{1}{\varepsilon_S} - \frac{1}{\varepsilon_\infty}}{1 + \frac{\varepsilon_\infty}{\varepsilon_S}i\omega\tau} =$$

$$= M_\infty + \frac{M_S - M_\infty}{1+i\omega\left(\frac{\varepsilon_\infty}{\varepsilon_S}\tau\right)} = M_\infty + \frac{M_S - M_\infty}{1+i\omega\tau_M}, \ \text{with} \ \tau_M = \frac{\varepsilon_\infty}{\varepsilon_S}\tau$$

where $M_S=1/\varepsilon_s$ and $M_\infty=1/\varepsilon_\infty$, denote the electric modulus in the limits $t\rightarrow\infty$ and $t\rightarrow0$, respectively. Including the d.c. conductivity, $\varepsilon^*(\omega)$ and $M^*(\omega)$ for the Debye process become

$$\varepsilon^*(\omega) = \varepsilon_\infty + \frac{\varepsilon_S - \varepsilon_\infty}{1+i\omega\tau} + \frac{\sigma_{dc}}{i\omega\varepsilon_0}$$

$$M^*(\omega) = \frac{1}{\varepsilon^*(\omega)} = M_\infty + \frac{M_S - M_\infty}{1+i\omega\tau_M} + \frac{i\omega\varepsilon_0}{\sigma_{dc}}, \ \text{with} \ \tau_M = \frac{\varepsilon_\infty}{\varepsilon_S}\tau \tag{2.33}$$

Time/frequency domanis representations of the permittivity, ε, electric modulus, M, and the probability densities, $g_\varepsilon(\tau)$ and $g_M(\tau)$, are compiled in Figure 2-13.

$$\begin{array}{|c|c|}
\hline
\text{Complex dielectric function } \varepsilon^*(\omega) & \text{Complex electric modulus } M^*(\omega) \\
\varepsilon^*(\omega) = i\omega \int_0^\infty \varepsilon(t)\exp(-i\omega t)dt & M^*(\omega) = i\omega \int_0^\infty M(t)\exp(-i\omega t)dt \\
\hline
\end{array}$$

$$\boxed{\{\varepsilon^*(\omega) \times M^*(\omega) = 1\}}$$

Retardation function $\varepsilon(t)$	Relaxation function $M(t)$
$\varepsilon(t) = \dfrac{1}{2\pi}\int_0^\infty \dfrac{\varepsilon^*(\omega)}{i\omega}\exp(i\omega t)d\omega$	$M(t) = \dfrac{1}{2\pi}\int_0^\infty \dfrac{M^*(\omega)}{i\omega}\exp(i\omega t)d\omega$

$$\varepsilon(t) = \varepsilon_\infty + (\varepsilon_s - \varepsilon_\infty)\int_0^\infty g_\varepsilon(\tau)[1-\exp(-t/\tau)]d\tau \qquad M(t) = M_s + (M_\infty - M_s)\int_0^\infty g_M(\tau)[\exp(-t/\tau)]d\tau$$

$$\boxed{\left\{\int_0^t M(\tau)\cdot\varepsilon(t-\tau) = \int_0^t \varepsilon(\tau)\cdot M(t-\tau) = t\theta(t)\right\}}$$

Probability density $g_\varepsilon(\tau)d\tau$	Probability density $g_M(\tau)d\tau$
$\varepsilon^*(\omega) = \varepsilon_\infty + (\varepsilon_s - \varepsilon_\infty)\int_0^\infty \dfrac{g_\varepsilon(\tau)}{1+i\omega\tau}d\tau$	$M^*(\omega) = M_s + (M_\infty - M_s)\int_0^\infty \dfrac{g_M(\tau)i\omega\tau}{1+i\omega\tau}d\tau$

Figure 2-13: *Different representations for time/frequency domains of the permittivity, ε, electric modulus, M, and the probability densities, $g_\varepsilon(\tau)d\tau$ and $g_M(\tau)d\tau$.*

Time-scale relations for the Debye and non-Debye processes [22,23] are compiled in Figure 2-14.

$$\underline{\textbf{\textit{Debye}}}$$

$$\varepsilon^*(\omega) = \varepsilon_\infty + \frac{\varepsilon_s - \varepsilon_\infty}{1+i\omega\tau}; \quad \tau_M \approx \tau_\varepsilon \times \left(\frac{\varepsilon_\infty}{\varepsilon_s}\right)$$

$$\underline{\textit{Cole - Cole (CC)}}$$

$$\varepsilon^*(\omega) = \varepsilon_\infty + (\varepsilon_s - \varepsilon_\infty)\frac{1}{1+(i\omega\tau)^\alpha}; \quad \tau_M = \tau_\varepsilon \times \left(\frac{\varepsilon_\infty}{\varepsilon_s}\right)^{\frac{1}{\alpha}}$$

$$\underline{\textit{Cole - Davidson (CD)}}$$

$$\varepsilon^*(\omega) = \varepsilon_\infty + (\varepsilon_s - \varepsilon_\infty)\frac{1}{[1+i\omega\tau]^\gamma}; \quad \tau_M \approx \tau_\varepsilon \times \left(\frac{\varepsilon_\infty}{\varepsilon_s}\right)^{\frac{1}{\gamma}}$$

$$\underline{\textit{Kohlrausch - Williams - Watts }(KWW)}$$

$$\varepsilon(t) = \varepsilon_\infty + (\varepsilon_s - \varepsilon_\infty)\times\left[1-\exp\left[-\left(\frac{t}{\tau}\right)^\beta\right]\right]; \quad \tau_M \approx \tau_\varepsilon \times \left(\frac{\varepsilon_\infty}{\varepsilon_s}\right)^{\frac{1}{\beta}}$$

Figure 2-14: *Time-scale relations of the dielectric permittivity, ε^*, and electric modulus, M^*, for the Debye and non-Debye processes.*

From Figure 2-14 one concludes that, relaxation-time dispersions are capable of shifting the relaxation or modulus time scales much more towards fast responses relative to the Debye
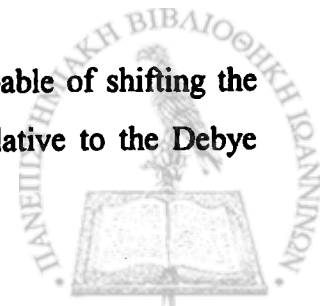
case. As an example, a polar liquid with $\varepsilon_s/\varepsilon_\infty=10$ will have $\tau_e/\tau_M=10$ in the Debye approximation, but a ratio as high as $\tau_e/\tau_M=100$ for a realistic CC exponent of $\alpha=0.5$.

2.2.5.4 The conductivity contribution

The fluctuation-dissipation theorem (FDT) relates the response of a system onto an outer disturbance to the spontaneous fluctuations within the system. The FDT expresses the dc-conductivity, σ_{dc}, in terms of the current density, j, autocorrelation function as [24]

$$\sigma_{dc} = \frac{1}{k_B T}\int_0^\infty \langle j(0)\cdot j(t)\rangle dt \qquad (2.34)$$

The σ_{dc} is related to the diffusion constant, D_i, and the ion mobility, μ_i, by the generalized Nernst-Einstein relation [25]

$$D_i = \frac{\sigma_{dc} k_B T}{Ne^2} = \frac{\mu_i k_B T}{e}$$
$$\mu_i = \frac{\sigma_{dc}}{Ne} \qquad (2.35)$$

For spherical particles of radius r, Stokes' law gives

$$\gamma = 6\pi\eta r = \frac{1}{\mu} \qquad (2.36)$$

where γ, η and μ are the drag coefficient, the shear viscosity and the mobility, respectively. The fundamental Stokes-Einstein equation states that a diffusion coefficient D of a Brownian particle has to be proportional to a factor T/η [26], thus the Stokes-Einstein relations for the translational self-diffusion and rotational self-diffusion are

$$D_{transl} = \frac{k_B T}{6\pi\eta r}$$
$$D_{rotational} = \frac{k_B T}{8\pi\eta r^3} \qquad (2.37)$$

Considering ions like spheres having translational and rotational diffusion (Eq. (2.37)), a simple relationships between the d.c.-conductivity, σ_{dc}, and viscosity, η, can be calculated as

$$\sigma_{dc} = \frac{Ne^2}{6\pi\eta r}, \rightarrow \sigma_{dc} \sim \eta^{-1} \qquad (2.38)$$

In addition, the diffusion coefficient is related to the mean-square displacement of a particle, $\langle r^2\rangle$, by the Einstein-Smoluchowski relation

$$D_t = \frac{\langle r^2 \rangle}{6\tau} \tag{2.39}$$

where τ is the characteristic time. From Eqs. (2.33) and (2.37) the relation between the d.c.-conductivity and the mean-squared displacement of ions is given by [24]

$$\sigma_{dc} = \frac{Ne^2}{6k_B T} \frac{\langle r^2 \rangle}{\tau} \tag{2.40}$$

As a microscopic approach, hopping conduction has to be considered. A variety of different models exist. The simplest is the random free-energy barrier model as developed by Dyre [24]. This model assumes that conduction takes place by hopping of charge carriers which are subject to spatially randomly varying energy barriers. It is solved within the Continuous-Time-Random Walk (CTRW) approximation with the result [15]

$$\sigma^*(\omega) = \sigma_{dc} \frac{i\omega\tau_e}{\ln(1 + i\omega\tau_e)} \tag{2.41}$$

where τ_e is the attempt frequency to overcome the largest barrier determining the d.c.-conductivity. Splitting Eq. (2.41) into real, σ', and imaginary, σ'', parts delivers

$$\sigma'(\omega) = \frac{\sigma_{dc}\omega\tau_e \arctan(\omega\tau_e)}{\frac{1}{4}\ln^2(1 + \omega^2\tau_e^2) + (\arctan\omega\tau_e)^2}$$

$$\sigma''(\omega) = \frac{\sigma_{dc}\omega\tau_e \ln(1 + \omega^2\tau_e^2)}{\frac{1}{2}\ln^2(1 + \omega^2\tau_e^2) + 2(\arctan\omega\tau_e)^2} \tag{2.42}$$

The complex dielectric function, $\varepsilon^*(\omega)$, is related to the complex electric conductivity, $\sigma^*(\omega)$, through Eq. (2.43) [15]

$$\sigma^*(\omega) = \sigma' + i\sigma'' = i\omega\varepsilon_0\varepsilon^*(\omega) \Rightarrow \sigma' = \omega\varepsilon_0\varepsilon'', \sigma'' = \omega\varepsilon_0\varepsilon' \tag{2.43}$$

For pure electronic conduction no contribution arises to ε' while $\varepsilon''(\omega) = \sigma_{dc}/\varepsilon_0\omega$ increases linearly with decreasing frequency. The frequency- and temperature-dependence of the real part of the conductivity, σ', is characterized by a plateau at lower frequencies and elevated temperatures (σ_{dc}) and becomes strongly frequency dependent at higher frequencies ($\sigma'(\omega)\propto\omega^s$). This behavior can be further expressed by the following equation [24,27]

$$\sigma'(\omega,T) = \sigma_{dc} + A\omega^s \tag{2.44}$$

where $0 < s \le 1$ is a frequency exponent that depends on temperature and A is a constant that depends on temperature as well. However, as we will see below with respect to Figure 2-22,
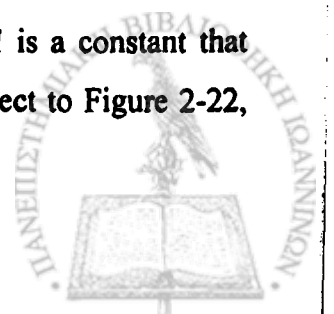
the exponent s is not unique since in this range, there is interference from molecular processes as well.

2.2.5.5 Measuring systems

Two types of experiments were performed: "isobaric" as a function of temperature and "isothermal" as a function of pressure. The "isobaric" measurements were performed at different temperatures in the range 123–473 K, at atmospheric pressure, and for frequencies in the range from 10^{-2} to 10^6 Hz using a Novocontrol broadband dielectric spectrometer (BDS) system (Figure 2-15) composed of a frequency response analyzer (Solartron Schlumberger FRA 1260) and a broadband dielectric converter (BDC) (Figure 2-17). The sample cell consisted of two electrodes 20 mm in diameter and the sample with a thickness of 50 μm. The dielectric relaxation spectra $\varepsilon^*(T, P, \omega)$ were collected isothermally in the frequency domain from high to low frequency. Temperature was controlled by a NOVOCONTROL Quatro Cryosystem, having a stability of ±0.1 °C. The samples were cooled and heated in the presence of N_2 during measurement. The P-dependent (i.e. "isothermal") measurements were made using a setup (Figure 2-16) consisting of a temperature-controlled high-pressure cell, a pump for hydrostatic pressure and a closing press with pump. Pressure was applied using silicone oil as the transducing medium. The sample cell again consisted of two metal electrodes 20 mm in diameter with a 50 μm thick sample the spacing maintained by Teflon spacers, which was sealed and placed inside a Teflon ring to prevent contact with oil. The same BDS system as with the T-dependent measurements was used for the P-dependent measurements. "Isothermal" measurements were made for temperatures in the range 293-403 K and for pressures in the range 0.1-300.0 MPa. Temperature was controlled by Fluid circulator FP40 of JULABO.

The dielectric converter (Figure 2-17) uses a broadband electrometer amplifier with variable gain in order to match the huge impedance range required for dielectric measurements which typically covers about 13 orders of magnitude over the frequency range from 1 mHz to 10 MHz. If Z_x is a variable impedance which can be changed in resistance R_x, and capacitance C_x, the sample impedance $Z^*(\omega)$ of a direct measurements is given by

$$Z^*(\omega) = Z' - iZ'' = \frac{U_1}{I_s} = -\frac{U_1}{U_2}Z_x \qquad (2.45)$$

where the voltage U_1 applied from the generator to the sample and the sample current I_S are directly measured by the analyzer. The complex dielectric function $\varepsilon^*(\omega)$ is related to the sample impedance $Z^*(\omega)$ by

$$\varepsilon^*(\omega) = \varepsilon' - i\varepsilon'' = \frac{1}{i\omega C_0 Z^*(\omega)} \Rightarrow \varepsilon' = \frac{Z''}{\omega C_0 |Z|^2}, \quad \varepsilon'' = \frac{Z'}{\omega C_0 |Z|^2} \tag{2.46}$$

where C_0 is the capacity of the empty sample capacitor. At $\varepsilon'=0$, the sample impedance Z will represents a resistor R i.e. $Z=R$ therefore $\varepsilon''=1/\omega R C_0$ which reflects that the ionic conductivity is presented only in the imaginary part.
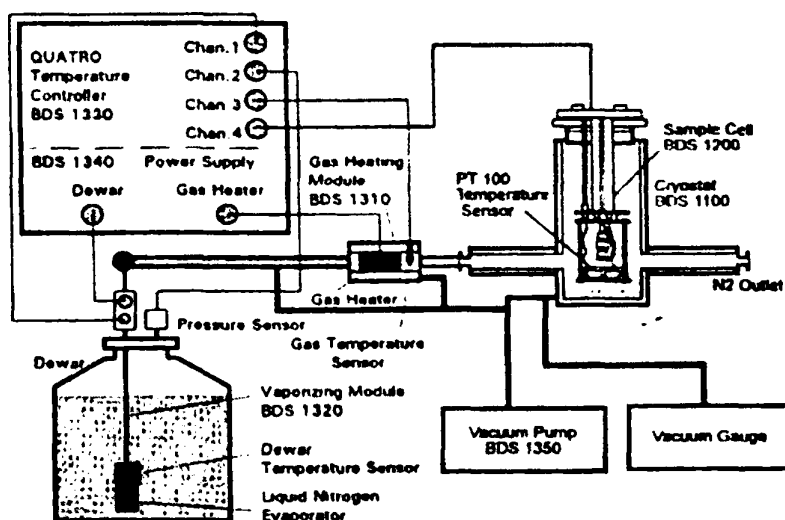
Figure 2-15: *Schematic diagram of temperature dependence dielectric measurements set-up.*
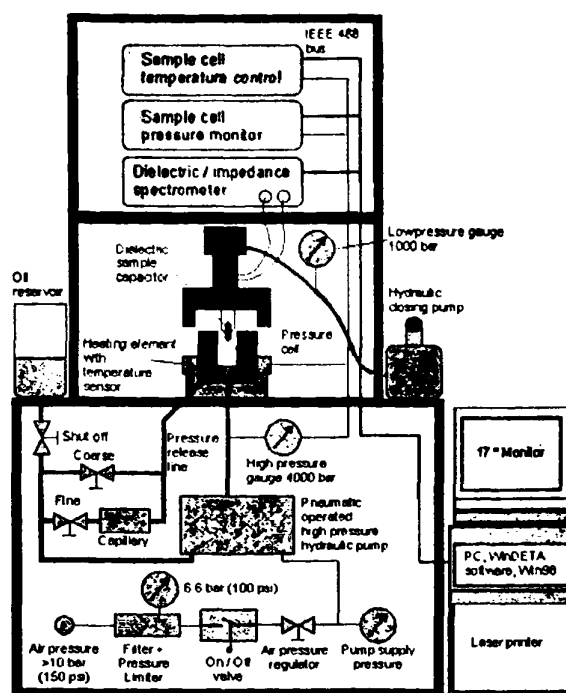
Figure 2-16: *Schematic diagram of pressure dependence dielectric measurements set-up.*
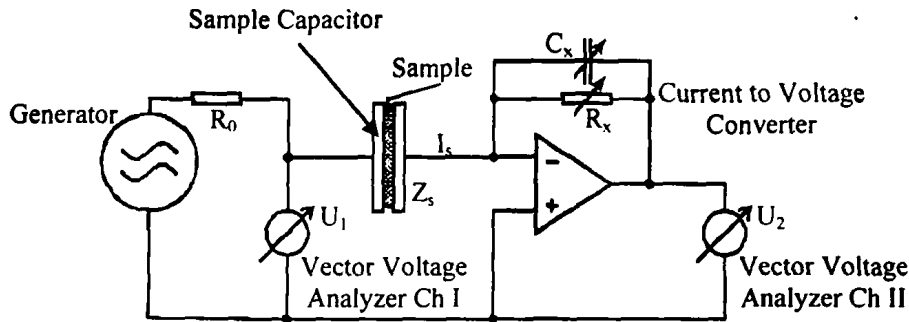
Figure 2-17: *Schematic diagram of the broadband dielectric converter (BDC) for the impedance measurements in the low-frequency range (<100 kHz) with electrometer amplifier and variable reference capacitor. The A.C. voltage from the generator is applied to the sample and measured in amplitude and phase as U_I. The resistor R_0 protects the BDC electronics from damage if the sample impedance becomes too low. The sample current I_S feeds in the inverting input of an operational amplifier which has the variable capacity C_X and resistor R_X in its feed back loop. C_X can be switched between 200 pF and 2200 pF. R_X can be switched between 10 Ω and 1 TΩ in logarithmic intervals of a factor 10. The BDC selects a combination of R_X and C_X in such a way that the output voltage U_2 of the operational amplifier is in a good measurable range of the analyzer (200 mV-5mV). The BDC uses at high frequencies (10^5-10^7 Hz) another principle of current to voltage conversion. In contrast to the low-frequency range, the active current to voltage converter is replaced by a passive parallel combination of the resistor R_X and capacitor C_X. C_X is fixed at 1000 pF and R_X can be switched between 10 Ω and 100 KΩ in logarithmic steps of a factor 10.*

2.2.5.6 Analysis of dielectric spectra

The isothermal dielectric loss spectra ε'' were used to determine the relaxation times and their distributions at each temperature, by fitting them with the Havriliak and Negami (HN) equation, which is in fact a combination of the Cole-Cole and the Cole-Davidson function [28]:

$$\frac{\varepsilon^*(T,P,\omega) - \varepsilon_\infty(T,P)}{\Delta\varepsilon(T,P)} = \frac{1}{\left[1 + \left(i\omega\tau_{HN}(T,P)\right)^\alpha\right]^\gamma}$$ (2.47)

where $\tau_{HN}(T,P)$ is the characteristic relaxation time in this equation, $\Delta\varepsilon(T,P)=\varepsilon_0(T,P)-\varepsilon_\infty(T,P)$ is the relaxation strength of the process under investigation and α and γ (with limits $0<\alpha$, $\alpha\gamma\leq1$) describe the symmetrical and asymmetrical broadening of the distribution of relaxation times, respectively. The linear rise of the ε'' at lower frequencies is caused by the conductivity ($\varepsilon''\approx(\sigma_{dc}/\varepsilon_f)\omega^{-1}$, where σ_{dc} is the dc-conductivity and ε_f is the permittivity of free space) which has been included in the fitting procedure. From τ_{HN}, the relaxation time at maximum loss, τ_{max}, is obtained analytically following Eq. (2.48)

$$\tau_{max} = \tau_{HN}\left[\frac{\sin\left(\dfrac{\alpha\gamma\pi}{2+2\gamma}\right)}{\sin\left(\dfrac{\alpha\pi}{2+2\gamma}\right)}\right]^{1/\alpha}$$ (2.48)

τ_{max}, instead of τ_{HN}, is used to compare and calculate activation energies because the latter is a function of the shape parameters α and γ. Sometimes, two or a more HN functions, plus the dc contribution if necessary, were used to fit the experimental loss curves when different relaxation processes contribute to the observed spectra. In this case some of the shape parameters were fixed (this requires measurements over a broad T-range). The fitting was done with the OriginLab program. The real and imaginary components of the HN-equation are then calculated using [15]:

$$\varepsilon'_{HN} = \Delta\varepsilon \frac{\cos\theta}{\left[1+2(\omega\tau)^{\alpha}\cos(\alpha\pi/2)+(\omega\tau)^{2\alpha}\right]^{\gamma/2}} \tag{2.49}$$

$$\varepsilon''_{HN} = \Delta\varepsilon \frac{\sin\theta}{\left[1+2(\omega\tau)^{\alpha}\cos(\alpha\pi/2)+(\omega\tau)^{2\alpha}\right]^{\gamma/2}} \tag{2.50}$$

in which:

$$\theta = \gamma \, \text{atan}\left[\frac{(\omega\tau)^{\alpha}\sin(\alpha\pi/2)}{1+(\omega\tau)^{\alpha}\cos(\alpha\pi/2)}\right] \tag{2.51}$$

The interrelation between the HN- shape parameters (α and γ) in the frequency domain and the KWW parameter (β_{KWW}) in the time domain is $\alpha\gamma=\beta_{KWW}^{1.23}$ [29].

In some cases, the peak at lower frequencies was covered by the strong conductivity contribution making the direct analysis of the dielectric loss data, ε'', a formidable task. In this case, we have made use of the first derivative method of ε' to derive the ε'' as [30,31]

$$\varepsilon''_{der} = -\left(\frac{\pi}{2}\right)\left(\frac{\partial\varepsilon'}{\partial\ln\omega}\right), \quad \omega=2\pi f \tag{2.52}$$

which provides a conduction-free dielectric loss peak but a somewhat narrower peak [32]. For the HN-function the first derivative of ε' is given by [31]

$$\varepsilon''_{der} = -\left(\frac{\pi}{2}\right)\Delta\varepsilon \frac{\alpha\gamma(\omega\tau)^{\alpha}\left[\cos(\theta-\alpha\pi/2)+\cos\theta(\omega\tau)^{\alpha}\right]}{\left[1+2(\omega\tau)^{\alpha}\cos(\alpha\pi/2)+(\omega\tau)^{2\alpha}\right]^{(1+\gamma)/2}} \tag{2.53}$$

where θ is given by Eq. (2.51).

We have used also the electric modulus representation (Eq. (2.32)) for the data analysis. This representation enables extracting the characteristic times for the ion motion in addition to the molecular dynamics. The ionic conductivity contribution can be observed as a maximum, where the M' and M'' curves cross. For the HN-formula (Eq. (2.47)), the corresponding
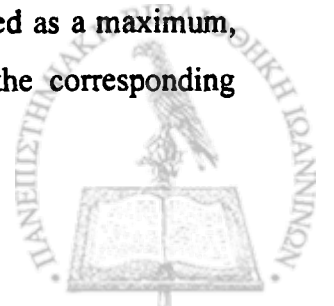
modulus $M^*_{HN}(\omega)$ cannot be calculated exactly but in a good approximation a proper model function is given by [15]

$$\frac{M^*_{HN}(T,P,\omega) - M_\infty(T,P)}{\Delta M(T,P)} = \frac{1}{\left[1 + \left(-i\left(\omega\tau_{HN-M}(T,P)\right)^{-1}\right)^\alpha\right]^\gamma} \qquad (2.54)$$

where mainly the frequency is changed to its reciprocal value and $\Delta M(=M_S-M_\infty)$ is the relaxation strength of the electric modulus. The relaxation times obtained from the imaginary part of the electric modulus ($\tau_{M''}$) and the ones obtained from the imaginary part of the dielectric function ($\tau_{\varepsilon''}$) (Figure 2-18) are related through [33]

$$\tau_{M''} \sim \tau_{\varepsilon''}\left(1 + \frac{\Delta\varepsilon}{\varepsilon_\infty}\right)^{-1/\alpha} \qquad (2.55)$$

in the case of symmetric ($\gamma_{HN}=1$) process, where α parameter is the HN parameter that describes the symmetric broadening of relaxation time distribution. Notice that for weak processes ($\Delta\varepsilon \ll \varepsilon_\infty$) the two representations give identical times.
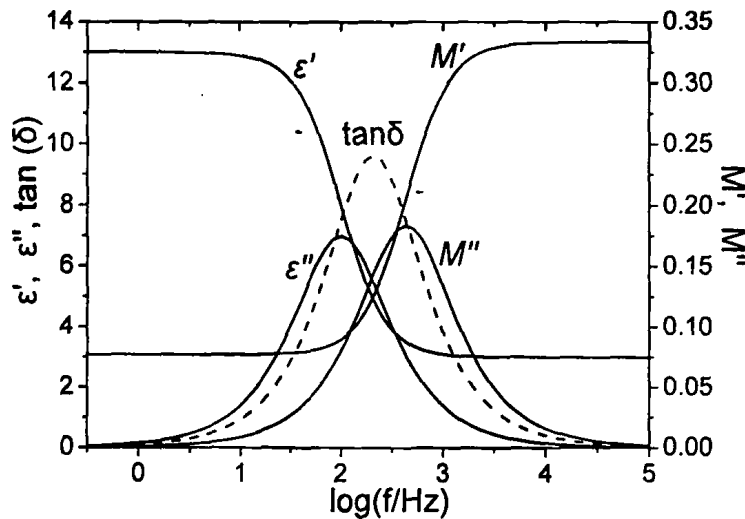
Figure 2-18: *Schematic illustration of the real and imaginary parts of the complex dielectric permittivity $\varepsilon^*(\omega)$, complex electric modulus $M^*(\omega)$ and the loss $\tan\delta=\varepsilon''/\varepsilon'$. The relation between the relaxation times derived from ε'' and M'' was mentioned above in Figure 2-14 for the Debye and non-Debye processes.*

As demonstrated in Figure 2-18, the relaxation process appears in the modulus representation at a higher frequency than for the corresponding permittivity $\varepsilon^*(\omega)$. This means that in the modulus representation high frequencies have greater weight. Figure 2-19 gives the dielectric data of an indenofluorene monoketon (IFK) at T=318.15 K in the dielectric function (Figure 2-19a) and the electric modulus (Figure 2-19b) representations.
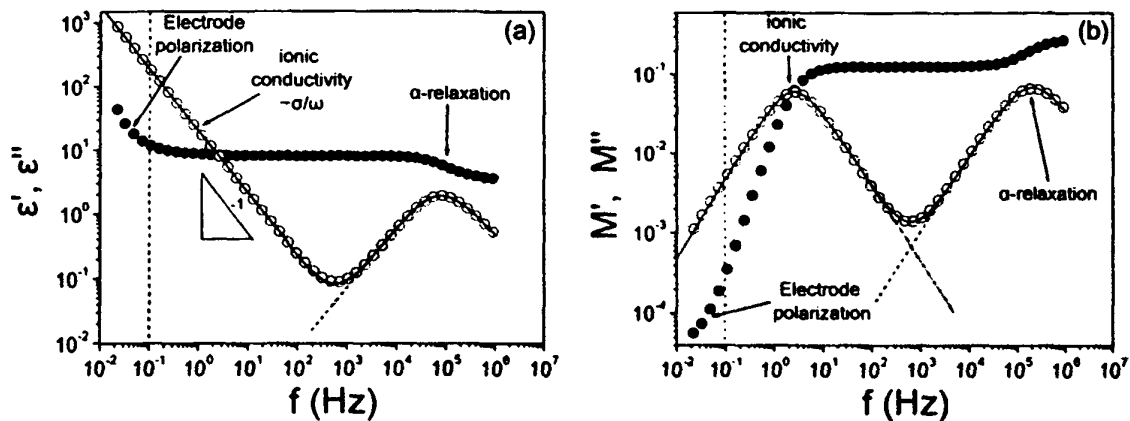
Figure 2-19: *(a) real (ε', ●) and imaginary (ε", ○) parts of the complex dielectric function ε*(ω) for an indenofluorene monoketon (IFK) at T=318.15 K. In the high frequency side, the α-relaxation (dynamic glass transition) due to rotational fluctuations of molecular dipoles exhibits a maximum in ε" and a step-like increase in ε' with decreasing frequency. In contrast, the ionic conductivity (~σ/ω) shows an increase of ε" with decreasing frequency. The solid line is the sum of the α-relaxation (dashed line) and a conductivity contribution (dotted line) fitting of one HN-function. (b) corresponding plot for the real (M', ●) and imaginary (M", ○) parts of the complex electric modulus M*(ω). The α-process is characterized by a peak in M" and a step-like decrease of M' with decreasing frequency. It is demonstrated that the increase in ε" with decreasing frequency is transformed into a peak in M" which is related to the ionic conductivity. Two HN-functions were used, one for the α-relaxation (dashed line) and the other for extracting the ionic mobility (dotted line).*

Only one HN-function in addition to the conductivity contribution is able to describe the data of the imaginary part of the dielectric function in the whole frequency range (Figure 2-19a). This means that for a complete description of an isolated relaxation region at least a set of four parameters is needed. For the α-relaxation these parameters are α=0.94, γ=0.85, $\Delta\varepsilon$=4.54 and τ_{HN}=1×10^{-5} s. The shape of the loss peak deviates from a single Debye process (α=$\alpha\gamma$=1). Two HN-functions are fitted to the imaginary part of the electric modulus. One describes the α-relaxation with fitting parameters α=0.94, $\alpha\gamma$=0.85, ΔM=0.16 and τ_{HN-M}=6×10^{-6}s and the other describes the ionic conductivity relaxation with fitting parameters α=1.0, γ=0.93, ΔM=0.13 and τ_{HN-M}=0.41 s. The α-relaxation has the same shape parameters like the dielectric function (α and $\alpha\gamma$) with different dielectric strengths ΔM and some what different relaxation times. According to Eq. (2.55) the relaxation times obtained from the imaginary part of the electric modulus ($\tau_{M"}$) and those from the imaginary part of the complex permittivity may differ as $\tau_{M"}/\tau_{\varepsilon"}$ ~0.5. The shape parameters of the ionic conductivity relaxation are symmetric while for the α-relaxation are asymmetric. The relaxation times extracting from the electric modulus representation for the ion motion in addition to the molecular dynamics was addressed by several authors [33-35].

Figure 2-20 shows representative plot of the imaginary part of the complex dielectric function as a function of frequency for the mono-cyano HBC at T=318.15 K [36]. Three dynamic processes exist associated with the Cyano dipole relaxation and one process associated with the ionic conductivity relaxation.
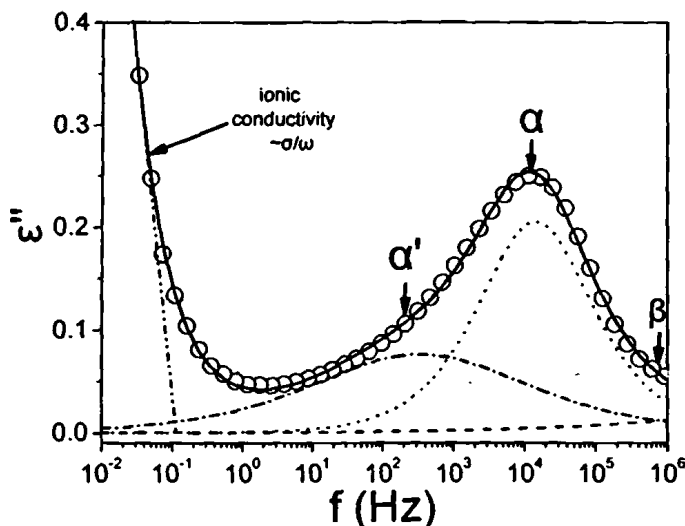
Figure 2-20: *Imaginary part* $(\varepsilon'', \bigcirc)$ *of the complex dielectric function* $\varepsilon^*(\omega)$ *versus frequency for the mono-cyano HBC at T=318.15 K. In the high frequency side, the* β *(dashed-line),* α *(dotted-line) and the* α' *(dash-dotted-line) processes appear. In addition, the ionic conductivity* $(\sim\sigma/\omega)$ *appears in the low frequency side. The solid line is the sum of the* β, α, α' *and a conductivity contribution. Three HN-functions in addition to a conductivity contribution were fitted to the whole spectrum.*

Three HN-functions in addition to a conductivity contribution were fitted to the whole spectrum. The shape of the α-process deviates from a single Debye process ($\alpha=\gamma=1$) and is highly asymmetric toward the high and low-frequency side. The deviation at the high frequency side is caused by the β-process while at the low frequency side by broad wing. This low frequency wing is described by a third HN-function. The parameters of this third HN-function were extracted from lower temperatures and were kept fixed at higher temperatures.

Figure 2-21 shows a representative plot of the imaginary part of the complex dielectric function as a function of frequency for the branched hexaalkyl hexa-*peri*-hexabenzocoronenes, HBC-C$_{14,10}$, at T=323.15 K [1]. A single relaxation process (α-process) exists in addition to the ionic conductivity. Thus, one HN-function in addition to a conductivity contribution were fitted to the whole spectrum.

The results of the DS investigation for the mono-cyano HBC with respect to the β, α, and α'-processes and the process due to the ionic conductivity can better be discussed with respect to the three representations shown in Figure 2-22.
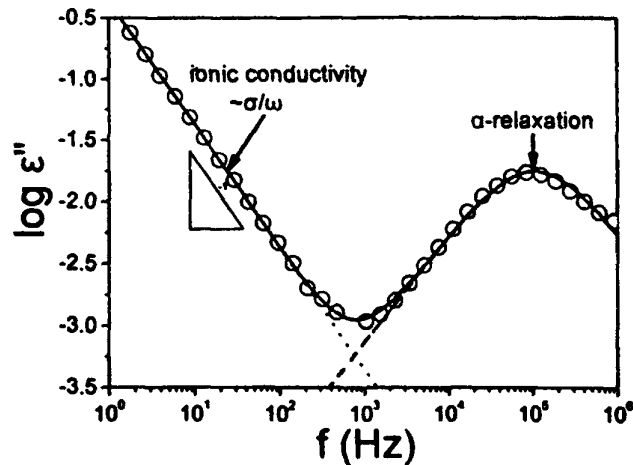
Figure 2-21: *Imaginary part (ε",O) of the complex dielectric function ε*(ω) versus frequency for the branched hexaalkyl hexa-peri-hexabenzocoronenes,HBC-C$_{14,10}$, at T=323.15 K. The α-process appears in the high frequency side in addition to the ionic conductivity (~σ/ω) in the low frequency side. The solid line is the sum of the α-process and the conductivity contribution. One HN-function in addition to the conductivity contribution were fitted to the whole spectrum.*
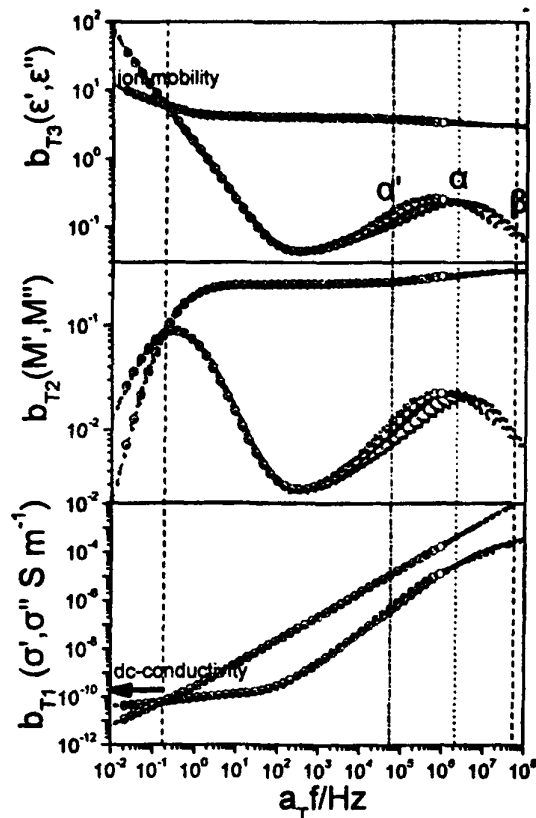
Figure 2-22: *Composite plot of the dielectric function $\varepsilon^* = \varepsilon'-i\varepsilon''$ (top), the electric modulus $M^* = M'+iM''$ (middle), and the ionic conductivity $\sigma^* = \sigma'+i\sigma''$ (bottom) shifted to a reference temperature (388.15 K) in the vicinity of the mono-cyano HBC ionic relaxation. The vertical dashed, dotted, dashed-dotted, and short-dashed lines give the locations of the β, α, α', and ionic mobility, respectively. Note that in all representations the crossing of the real and imaginary parts occurs at the same frequency which signifies the rate of the ion mobility.*

The Figure displays "master curves" of the ε^* (=ε'-$i\varepsilon''$), the electric modulus M^* (=M'+iM'') and the conductivity σ^* (=σ'+$i\sigma''$) that are interrelated through Eqs. (2.32) and (2.43). The superpositions were made around the M'' maximum related to the ionic relaxation and the same horizontal shift factors (a_T) were applied in the ε^* and σ^* representations. Notice that in all representations the crossing of the real and imaginary parts occurs at the same frequency signifying the rate of the process due to the ionic mobility (short-dashed line). In the high frequency side, the α' (dashed-dotted-line), α (dotted line) and the β (dashed line) processes appear. The positions of the β, α, and α'-processes and the process due to the ionic conductivity are approximately the same in the different representations, since the relaxation times from the M^* and ε^* representations are related through Eq. (2.55), and for very weak processes the relaxation times are practically indistinguishable. Lastly, the dc part of the ionic conductivity is low and typically $\approx 10^{-10}$ S m^{-1}.

2.3 References

[1] Elmahdy, M. M.; Floudas, G.; Kastler, M.; Müllen, K. *J. Phys. C* (in press).

[2] Pisula, W.; Tomović, Ž.; Simpson, C.; Kastler, M.; Pakula, T.; Müllen, K. *Chem. Mater.* **17**, 4296 (2005).

[3] Feike, M.; Demco, D. E.; Graf, R.; Gottwald, J.; Hafner, S.; Spiess, H. W. *J. Magn. Reson.* A **122**, 214 (1996).

[4] Schnell, I.; Spiess, H. W. *J. Magn. Res. – Adv. Magn. Reson.* **151**, 153 (2001).

[5] Saalwächter, K.; Schnell, I. *Solid State Nucl.Magn. Res.* **22**, 154 (2002).

[6] Saalwachter, K.; Spiess, H. W. *J. Phys. Chem.* **114**, 5707 (2001).

[7] Langer, B.; Schnell, I.; Spiess, H. W.; Grimmer, A.-R. *J. Magn. Res.* **138**, 182 (1999).

[8] Maricq, M. M.; Waugh, J. S. *J. Chem. Phys.* **70**, 3300 (1979).

[9] Fischbach, I.; Ebert, F.; Spiess, H. W.; Schnell, I. *ChemPhysChem* **5**, 895 (2004).

[10] Dusold, S.; Sebald, A. *Annu. Rep. NMR Spectrosc.* **41**, 185 (2000).

[11] Gullion, T.; Schaefer, J. *Adv. Magn. Reson.* **13**, 57(1989).

[12] De Paul, S. M.; Saalwächter, K., Graf, R.; Spiess, H. W. *J. Magn. Reson.* **146**, 140 (2000).

[13] Mierzwa, M.; Floudas, G.; Neidhöfer, M.; Graf, R.; Spiess, H. W.; Meyer W. H.; Wegner, G. *J. Chem. Phys.* **117**, 6289 (2002).

[14] Schmidt-Rohr, K.; Spiess, H. W. *Multidimensional Solid-State NMR and Polymers*, Wiley, New York, (1994).

[15] Kremer, F.; Schönhals, A., *Broadband Dielectric Spectroscopy*, Springer, Berlin, (2002).

[16] Gedde, U. W., *Polymer Physics*, Chapman & Hall, London, (1995).

[17] McCrum, N. G.; Read, B. E.; Williams, G., *Anelastic and Dielectric Effects in Polymeric Solids*, Dover, New York, (1991).

[18] Onsager, L. *J. Am. Chem. Soc.* **58**, 1486 (1938).

[19] (a) Kohlrausch, R. *Pogg. Ann. Phys.* **12**, 393 (1847). (b) Williams, G.; Watts, D. C. *Trans. Faraday Soc.* **66**, 80 (1970). (c) Williams, G.; Watts, D. C.; Dev, S. B.; North, A. M. *Trans. Faraday Soc.* **67**, 1323 (1971).

[20] Cole, K. S.; Cole, R. H. *J. Chem. Phys.* **9**, 341 (1941).

[21] Davidson, D. W.; Cole, R. H. *J. Chem. Phys.* **19**, 1484 (1951).

[22] Ito, N.; Richert, R. *J. Chem. Phys.* **123**, 106101 (2005).

[23] Richert, R. *Physica A* **287**, 26 (2000).

[24] Dyre, J. C. *J. Appl. Phys.* **64**, 2456 (1988).

[25] Weinert, U.; Mason, E. A. *Phys. Rev. A* **21**, 681 (1980).

[26] Voronel, A.; Veliyulin, E.; Machavariani, V. Sh.; Kisliuk, A.; Quitmann, D. *Phys. Rev. Lett.* **80**, 2630 (1998).

[27] Dyre, J. C.; Schröder, T. B. *Rev. Mod. Phys.* **72**, 873 (2000).

[28] Havriliak, S.; Negami, S. *Polymer* **8**, 161 (1967).

[29] Alvarez, F.; Alegrva, A.; Colmenero, J. *Phys. Rev. B* **44**, 7306 (1991).

[30] Steeman, P. A. M.; van Turnhout, J. *Macromolecules* **27**, 5421 (1994).

[31] Wübbenhorst, M.; van Turnhout, J. *J. Non-Cryst. Solids* **305**, 40 (2002).

[32] Wübbenhorst, M.; van Koten, E.; Jansen, J.; Mijw, M.; van Turnhout, J. *Macromol. Rapid Commun.* **18**, 139 (1997).

[33] Papadopoulos, P.; Floudas, G.; Schnell, I.; Lieberwirth, I.; Nguyen, T. Q.; Klok, H. A. *Biomacromolecules* **7**, 618 (2006).

[34] Elmahdy, M. M.; Floudas, G.; Oldridge, L.; Grimsdale, A. C.; Müllen, K. *ChemPhysChem* **7**, 1431 (2006).

[35] Elmahdy, M. M.; Chrissopoulou, K.; Afratis, A.; Floudas, G.; Anastasiadis, S. H. *Macromolecules* **39**, 5170 (2006).

[36] Elmahdy, M. M.; Floudas, G.; Mondeshki, M. ; Spiess, H. W.; Dou, X.; Müllen, K. *Phys. Rev. Lett.* **100**, 107801 (2008).

Chapter 3

Self-assembly and Dynamics of Branched HBC Derivatives

3.1 Introduction

Among the different discotic LC hexa-*peri*-hexabenzocoronenes (HBCs) are particularly promising because their large aromatic core permits one of the highest values for the intrinsic charge carrier mobility [1-3]. The nonsubstituted HBCs do not reveal any phase behavior or solubility [4], therefore the attachment of flexible aliphatic chains to the HBCs periphery, as depicted in Scheme 3-1, is an elegant tool to introduce solubility and thus processability [5,6]. Three are the major phases found in most discotic HBCs: crystalline, liquid crystalline and isotropic [7]. In the crystalline state, the disc-shaped molecules organize into columns that further assemble into a two-dimensional lattice composed of nanophase separated tilted aromatic cores and more flexible alkyl chains. Within the crystalline state, discs posses some mobility thus this phase is better described as columnar plastic crystalline (Col$_p$). In the columnar liquid crystalline phase, the discs rotate freely around the columnar axis. In the isotropic phase, the columnar structures break into monomeric species, leading to an amorphous melt.

Despite earlier studies on the dynamics of triphenylene discotics, the dynamics of HBCs have not been investigated so far and this despite the record high charge carrier mobilities. Herein, we employ the two HBCs with the highest charge carrier mobilities and investigate the molecular dynamics by dielectric spectroscopy (DS) within the different phases [8]. An ultimate goal of such studies is to understand how the local (and perhaps global) disc dynamics within the columns influence the charge carrier mobility. Because of molecular symmetry, a strong dielectrically active process is not expected in these compounds. Nevertheless, we find a very weak dipolar relaxation with a non-Arrhenius temperature-dependence that freezes at 215 K. The origin of this process is discussed in terms of the freezing of the disc axial motion at the respective glass temperature (T_g).

3.2 Materials

Two branched hexaalky HBC derivatives were synthesized (by Dr. Kastler, MPI-P) for the purpose of this investigation. The two HBC molecules (HBC-$C_{10,6}$ and HBC-$C_{14,10}$, see Scheme 3-1) bear long side chains branched at the close vicinity of the HBC aromatic core. Notice that the molecules bear the same HBC core with different architectures of the alkyl chains. The synthesis of the two compounds has been reported elsewhere [6].
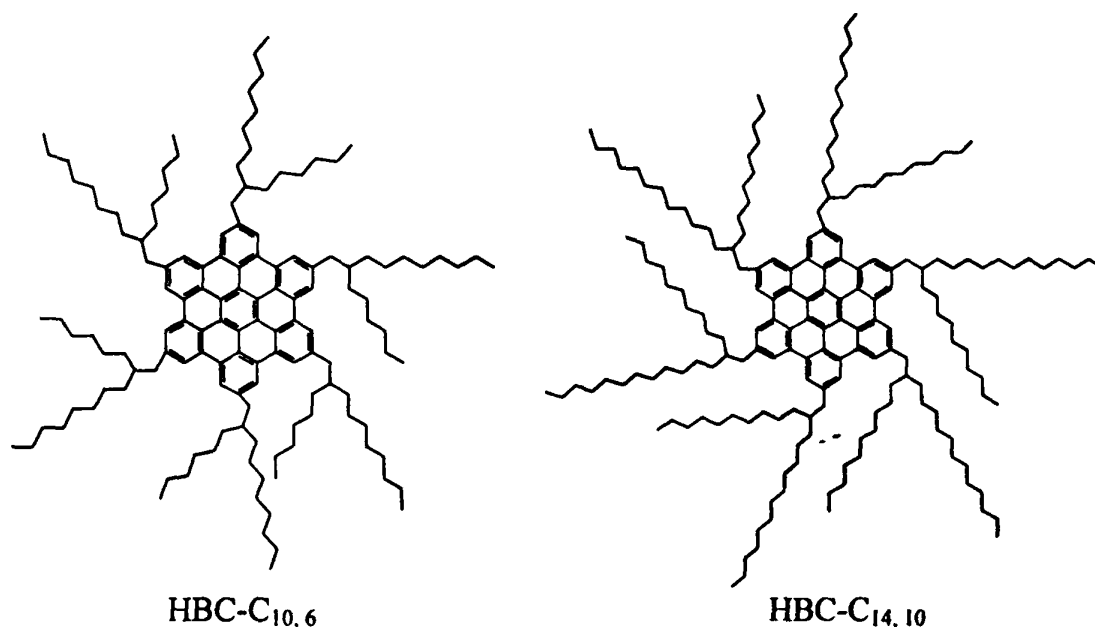
HBC-$C_{10,6}$ HBC-$C_{14,10}$

Scheme 3-1: *Schematic structures of the HBC-$C_{10,6}$ (left) and HBC-$C_{14,10}$ (right).*

3.3 Self-assembly

The phase transformation in the HBC-$C_{14,10}$ and HBC-$C_{10,6}$ at atmospheric pressure were studied by differential scanning calorimetry (DSC) with a heating and cooling rate of 10 K/min. The transition temperatures, heats of fusion and respective phases are compiled in Table 3.1.

Table 3.1. Thermal characterization and phase transitions of the investigated HBCs.

Compound	Transition temperature (K)	Enthalpy (J/g)	Phase transition
HBC-$C_{10,6}$	$220^a/217^b$	-	G^a/G^b
	$290 (258)^c$	9.3	$Col_p \rightarrow Col_d$
	370 (362)	2.5 (2.8)	$Col_d \rightarrow I$
HBC-$C_{14,10}$	321 (300)	35.7 (34.4)	$Col_p \rightarrow I$
	215	-	G^b

G^a: glass transition from DSC - G^b: glass transition from DS
Col_p: columnar plastic crystalline phase - Col_d: columnar disordered LC phase - I : isotropic phase
^{c}: from DS
(parentheses indicate values during cooling)

As shown in the DSC trace of the HBC-$C_{10.6}$ (Figure 3-1) a clear step in the specific heat can be seen in the second heating run at a temperature of about 220 K associated with the liquid-to-glass transition (T_g). T_g is followed by two thermally-induced phase transformations at 290 K and 370 K.
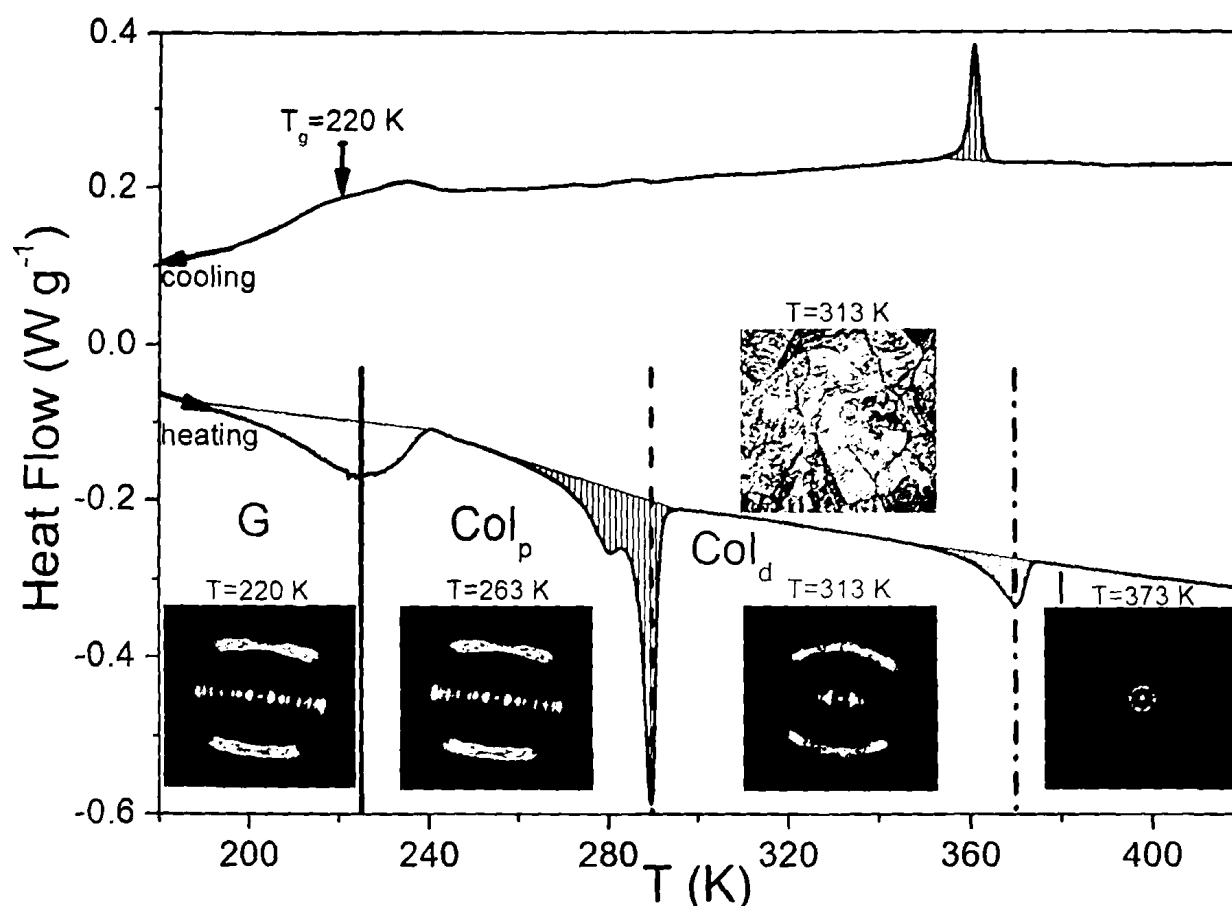
Figure 3-1: *DSC trace of the HBC-$C_{10.6}$ obtained during the second cooling and heating runs with a rate of 10 K/min. The vertical arrow indicates the glass temperature. The vertical solid, dashed and dash-dotted lines give the locations of the transition temperatures from the glassy state (G) to the columnar plastic crystalline phase (Col_p) (solid line) to the columnar disordered LC phase (Col_d) (dashed line) to the isotropic phase (I) (dash-dotted line). 2D-WAXS images obtained from an oriented fiber (T_{extr}=253 K) are shown at four temperatures corresponding to the glassy state (220 K), Col_p phase (263 K), Col_d phase (313 K) and to the I phase (373 K). A POM image of the HBC-$C_{10.6}$ sandwiched between two glass slides and cooled at 0.1 K/min is shown. The image was taken at 313 K (i.e. within the Col_dphase) and suggests a smectic mesophase.*

As we will see below with respect to the structural analysis, the low temperature transition (290 K) is from the columnar plastic crystalline phase (Col_p) to the columnar disordered LC phase (Col_d). The high temperature transition (370 K) reflects the transformation from the Col_d phase to the isotropic phase (I). The Col_p phase is characterized by three-dimensional crystal-like order in oblique lattice (see below), while the discs within the columns are able to rotate about the columnar axis. In addition, they show a plastic deformation at room temperature in comparison to crystalline materials [3]. The Col_d phase is characterized by structural disorder,

such as non-parallel arrangement of the discs, longitudinal and lateral displacements with free rotation around the columnar axis [9]. We mention here that de Gennes suggested that regions of high and low packing density (the pinched regions) are required to mitigate the packing ·frustration imposed by the flexible alkyl chains and the rigid cores [10]. On the other hand the HBC-$C_{14,10}$ (Figure 3-2) undergoes a phase transformation directly from the columnar plastic crystalline to the isotropic state at 321 K (on heating).
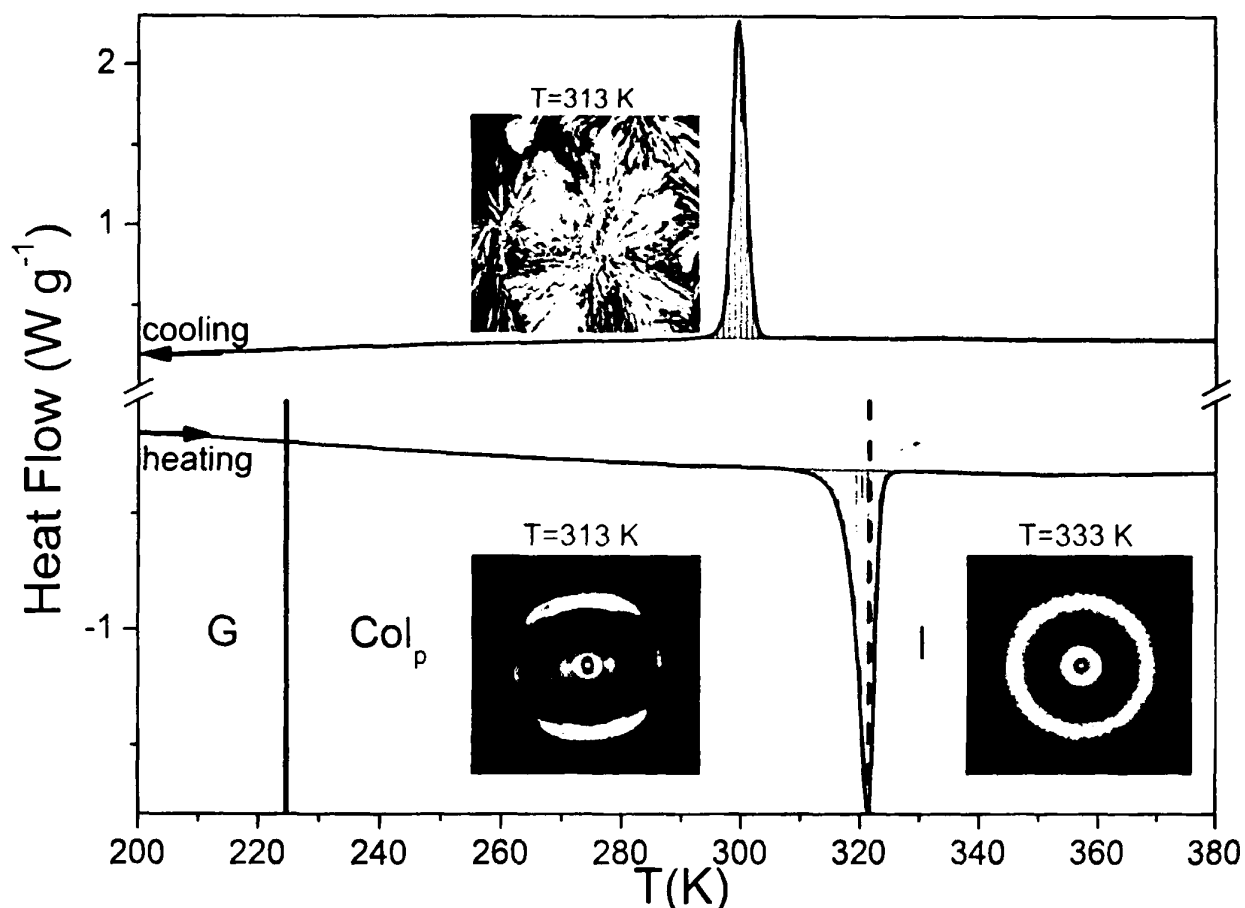
Figure 3-2: *DSC trace of the HBC-$C_{14,10}$ obtained during the second cooling and heating runs with a rate of 10 K/min. Upon heating the HBC-$C_{14,10}$ exhibits one phase transition at 321 K (300 K on cooling) from the columnar plastic crystalline (Col$_p$) to the isotropic phase (I). 2D-WAXS images obtained from an extruded fiber (T_{extr}=298 K) are shown at two temperatures corresponding to the columnar plastic crystalline phase (313 K) and to the isotropic phase (333 K). A POM image of the HBC-$C_{14,10}$ sandwiched between two glass slides cooled at 0.1 K/min is shown at 313 K, i.e. within the Col$_p$ phase. This image shows the formation of regular spherulites.*

Notice that the glass temperatures of the two compounds obtained from DSC are in close proximity and in excellent agreement with the one obtained from the dielectric spectroscopy measurements that will be discussed below. On the other hand, steric demand at the core periphery lowers the temperature to the isotropic phase to 370 K and 321 K for the HBC-$C_{10,6}$ and HBC-$C_{14,10}$, respectively.
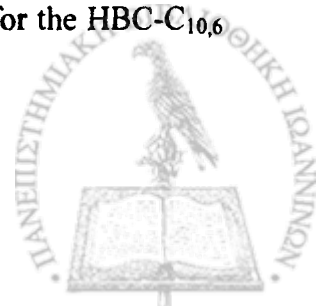
Polarizing optical microscopy (POM) images of the HBC-$C_{14,10}$ in different phases reveal spherulitic domains. Within the spherulites the columnar structures were oriented radially, indicating a high degree of self-organization over long ranges (Figure 3-3a). Contrary to this, the columnar growth of the HBC-$C_{10,6}$ took place around the nucleation center giving rise to a smectic mesophase (Figure 3-3b).
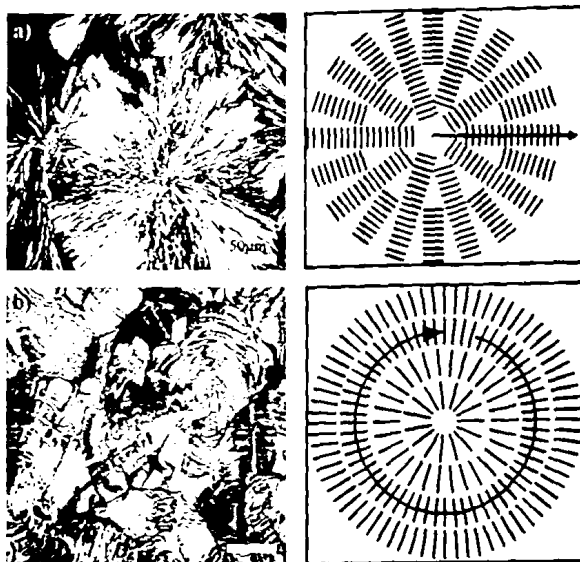
Figure 3-3: *Image from polarizing optical microscopy displaying (a) spherulitic morphologies of the HBC-$C_{14,10}$ with the radial columnar orientation and (b) "scalelike" textures of HBC-$C_{10,6}$ with columnar growth around the nucleation center. Both morphologies were obtained during cooling from the isotropic phase. Schematics of the columnar orientation of a and b are after ref. [11].*

To identify the exact morphologies (and to compare with earlier published data [3]) of HBC-$C_{10,6}$ and HBC-$C_{14,10}$, we investigated the two dimensional wide-angle X-ray scattering patterns obtained from macroscopically oriented samples as a function of temperature (the same samples were subsequently used in the DS study). We first discuss the structure of the HBC-$C_{10,6}$. The WAXS images of the HBC-$C_{10,6}$ (Figure 3-1) within the G and Col_p phases exhibit a set of off-meridional reflections and a set of equatorial reflections. The former reflect intracolumnar distances whereas the latter are of intercolumnar origin. The off-meridional reflections indicate a title of the discotic core with respect to the columnar axis with an intracolumnar period of 0.5 nm leading to a "herringbone" structure (as anticipated from earlier studies [3]). The equatorial reflections correspond to the (10), (01), (11) and (20) reflections of a rectangular lattice (Figure 3-4). The d_{hk} spacings are related to the lattice parameter a through Eq. (1.13) of Chapter 1 and suggest the formation of a columnar rectangular liquid crystal phase (Col_r) [9,12]. Within the Col_d phase, a considerable structural change occurred, accompanied by the fading of the meridional reflections (Figure 3-1). The equatorial

reflections correspond to the (10), (01), (11) and (20) reflections of an oblique unit cell (Figure 3-4). The d_{hk} spacings are related to the lattice parameter a through Eq. (3.1) and suggest the formation of a columnar oblique liquid crystal phase (Col_{ob}) [9,12].

$$d_{hk} = \left[\frac{\left(\frac{h^2}{a^2}\right) + \left(\frac{k^2}{b^2}\right) - \left(\frac{2hk}{ab}\right)\cos\gamma}{\sin^2\gamma} \right]^{-\frac{1}{2}} \tag{3.1}$$

The calculated d-spacings and the lattice parameters within the Col_p phase (at 253 K) and Col_d phase (at 313 K) are shown in Table 3.2.

Table 3.2. XRD data for the HBC-$C_{10,6}$ at two different temperatures; one in the Col_p phase and the other in the Col_d phase on heating.

T (K)	Phase	Lattice parameters (nm)	d_{10} (nm)	d_{intra} (nm)	Unit cell
253	Col_p	a=2.38 b=1.50	2.38	0.52	rectangular
313	Col_d	a=2.19 b=1.64 γ=96°	2.18	0.49	Oblique

The schematics shown in Figure 3-4 below the 2-D WAXS images illustrate the organization within the different phases. Starting from lower temperatures; at T_g=220 K the discs are perfectly ordered reflecting very strong off-meridional reflections and the disc dynamics freeze. Within the Col_p phase (303 K), the discs are well ordered as shown by the strong off-meridional reflections but they can rotate about their columnar axes. Within the Col_d phase the patterns loose their strong off-meridional reflection suggesting some disorder within the columns. At 333 K, the equatorial reflections become nearly isotropic and at 373 K the isotropic phase is reached and the columnar structure break into monomeric species, leading to an amorphous melt.

On the other hand, in the case of HBC-$C_{14,10}$ a direct transition from the columnar plastic crystalline phase (Col_p) to the isotropic phase, without an intermediate LC phase, was observed (Figure 3-5). The equatorial reflections in the Col_p phase (Figure 3-5) correspond to the (10), (01), (11) and (20) reflections of an oblique lattice. The d_{hk} spacings suggest the formation of a columnar oblique liquid crystal phase (Col_{ob}). The calculated d-spacings and the lattice parameters within the Col_p phase are included in Table 3.3.

Table 3.3. XRD data for the HBC-$C_{14,10}$ at two different temperatures within the Col_p phase on heating.

T (K)	Phase	Lattice parameters (nm)	d_{10} (nm)	d_{intra} (nm)	Unit cell
298	Col_p	a=3.27 b=2.75 γ=106°	3.14	0.51	Oblique
313	Col_p	a=3.32 b=2.78 γ=106°	3.19	0.50	Oblique
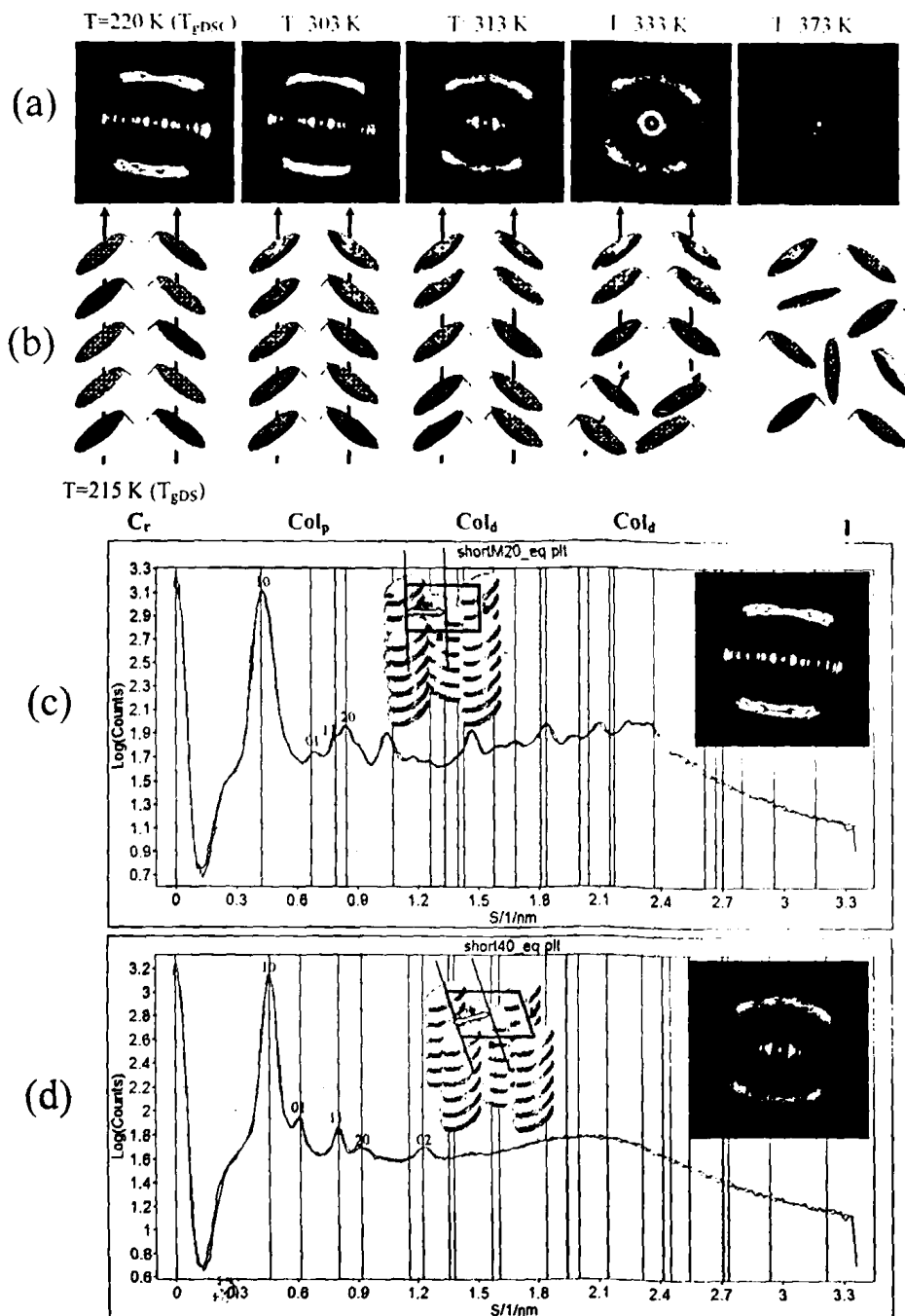
Figure 3-4: *(a) 2D-WAXS images of HBC-$C_{10,6}$ obtained from an oriented fibers (T_{extr}=253 K) at different temperatures.(b) a highly schematic representation of the organization within the different phases. (c) WAXS equatorial reflections at 253 K which correspond to the (10), (01), (11) and (20) reflections of rectangular unit cell. (d) WAXS equatorial reflections at 313 K which correspond to the (10), (01), (11) and (20) reflections which are characteristic of an oblique columnar mesophase (Col_{ob}).*
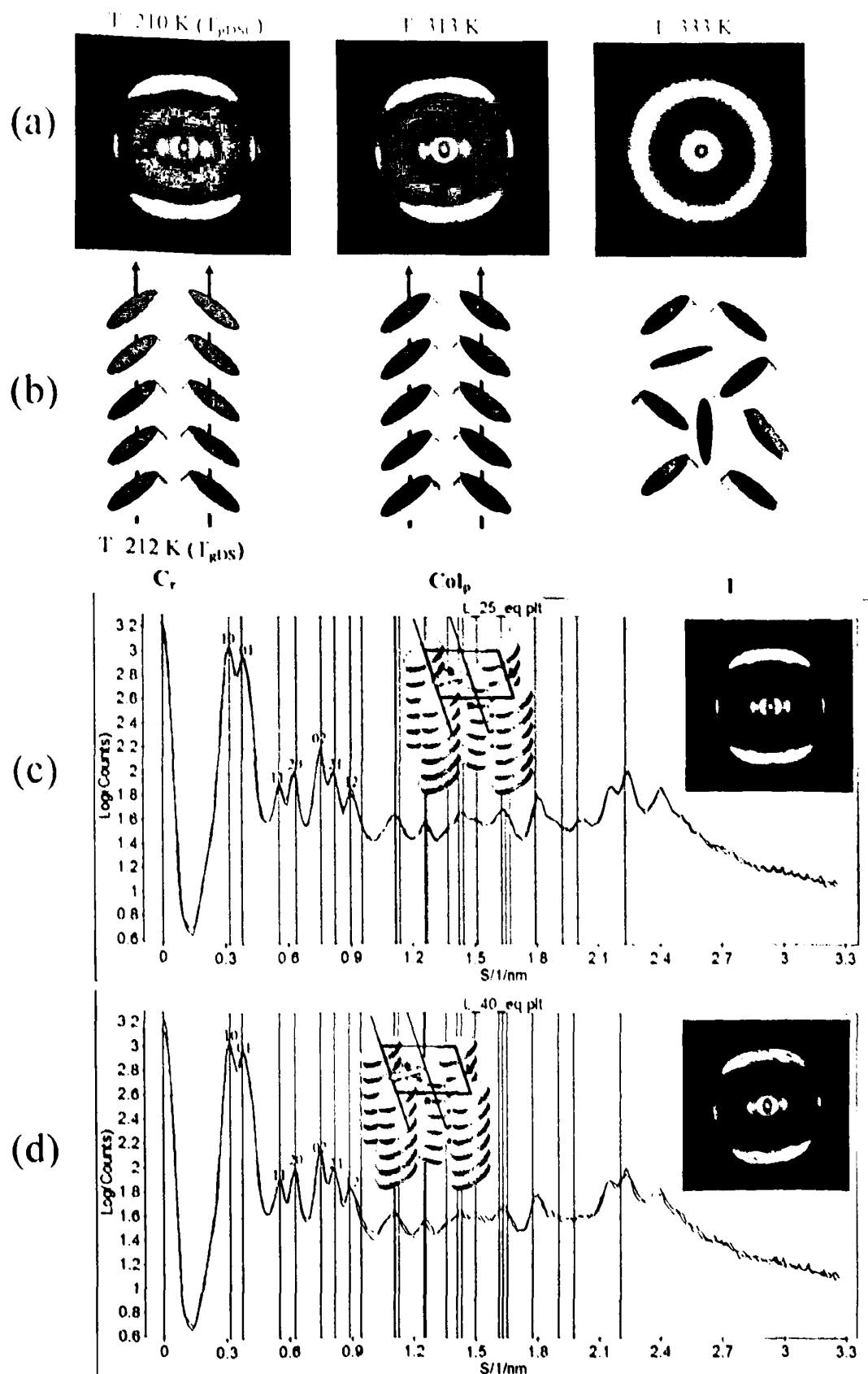
Figure 3-5: *(a) 2D-WAXS images of the HBC-C₁₄,₁₀ obtained from an oriented fiber (T_ext 298 K) at different temperatures. (b) a highly schematic illustration of the arrangement of the aromatic cores in the glassy state, Col_p and in the isotropic phase. WAXS equatorial reflections at 298 K (c) and 313 K (d) correspond to the (10), (01), (11) and (20) reflections which are characteristic of an oblique columnar mesophase (Col_ob).*

Thus the DSC, POM and X-ray studies confirm the phase transformations. In addition, DSC revealed, for the first time, the presence of a glass temperature within the Col_p phase. The origin of the freezing of the dynamics at T_g within the Col_p phase can best be studied by dielectric spectroscopy.

3.4 Molecular dynamics investigation

The molecular dynamics of the HBC-$C_{10,6}$ and HBC-$C_{14,10}$ in the different phases (Col_p, Col_d and I) were investigated by broadband dielectric spectroscopy (DS). Surprisingly, the two compounds display a dipolar relaxation that is faster and more intense in the HBC-$C_{14,10}$ as compared to HBC-$C_{10,6}$ as shown in Figure 3-6.
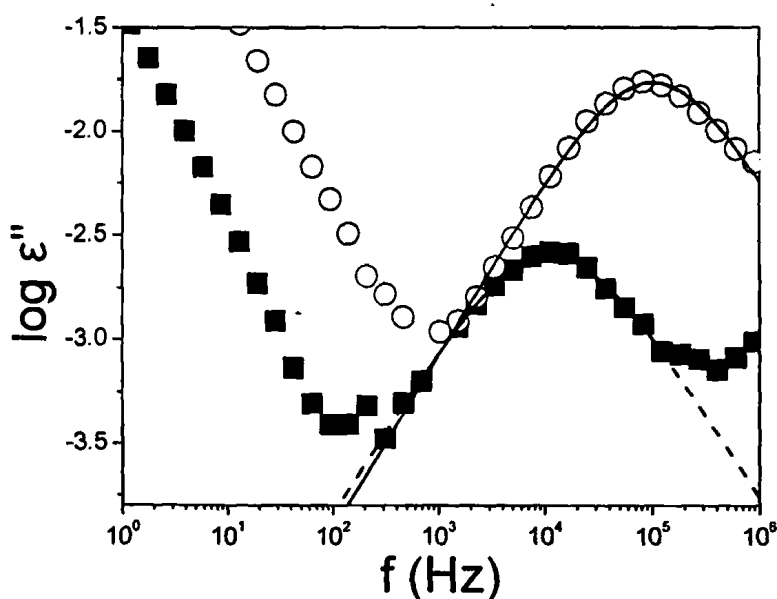
Figure 3-6: *Comparison of the α-process of the HBC-$C_{10,6}$ (■) and HBC-$C_{14,10}$ (O) at 323.15 K. The solid and dashed lines are fits to the HN function given by Eq. (2.47) of Chapter 2.*

The dielectric strength of these processes are very weak ($T\Delta\varepsilon \sim 7$ K for HBC-$C_{10,6}$ and ~12 K for HBC-$C_{14,10}$). This process has a rate similar to the α-process found recently in the dipole-functionalized HBCs [13,14], thus is attributed to the disc axial motion. The effective dipole moment ($\mu_{eff}=(g\mu)^{1/2}$, where μ is the dipole moment and g gives the orientation pair correlations between dipoles) responsible for the α-process can be calculated from the dielectric strength using the Fröhlich equation applicable to spherically symmetric molecules [15]

$$\mu^2 = \frac{3\kappa_B T \Delta \varepsilon}{4\pi g N_0}\left(\frac{3}{\varepsilon_\infty + 2}\right)^2 \frac{2\varepsilon_0 + \varepsilon_\infty}{3\varepsilon_0} \tag{3.2}$$

where $N_0 = \rho N_A / M_0$ is the number of dipoles per unit volume (ρ is the density, N_A is Avogadro's constant, k_B is the Boltzmann constant, M_0 is the molecular weight). As reported from earlier studies [16], the calculated densities of the HBCs are close to 1 g/cm^3. By using this macroscopic density in Eq. (3.2) gives $\mu_{eff} = 0.50 \pm 0.03$ and 0.60 ± 0.08 Debye for the HBC-$C_{10,6}$ and HBC-$C_{14,10}$, respectively. Given the symmetric molecular core of the two compounds, the observation of a dielectrically active process is, at first sight, a surprise. For this reason, controlled oxidation experiments have been made to gain a better understanding of the origin of this relaxation. In these experiments, different samples have been prepared following a variety of experimental conditions. A freshly prepared sample under argon atmosphere was measured by DS and has shown a very weak α-process. Then the same sample was heated to the isotropic phase for different time intervals and then measured by WAXS and DS. We found a stronger dielectric strength (DS) and at the same time, a better organized Col_p phase (WAXS). Clearly, oxidation promotes the π-π stacking of the aromatic cores giving rise to a long-range organization. Different samples prepared under similar conditions confirmed that the strength of the α-process varies with the degree of oxidation.

The dielectric strength ($T\Delta\varepsilon$) as well as the distribution of relaxation times of the Havriliak-Negami (HN) function (see Eq. (2.47) of Chapter 2) associated with the α-process are shown in Figure 3-7. Independent of the degree of oxidation, remarkable changes in the dielectric strength and the shape parameters were found on entering the Col_p and Col_d phases. For the HBC-$C_{14,10}$ the dielectric strength dropped from $T\Delta\varepsilon \sim 12$ K in the I phase to 2 K on entering the Col_p phase. The symmetrical (a) and asymmetrical ($a\gamma$) broadening parameters assumed values of $a = a\gamma = 0.94$ (in the isotropic phase) and $a = a\gamma = 0.7$ (in the Col_p phase). The broadening of the relaxation spectrum suggests increased cooperativity within the Col_p phase. On the other hand, for HBC-$C_{10,6}$ the shape parameters assumed values of $a = a\gamma = 0.94$ (in the I phase), $a = a\gamma = 0.7$ (in the Col_d phase) and $a \sim a\gamma \sim 0.4$ (in the Col_p phase). From the above is evident that the Col_p phase shows by far the more cooperative α-process.

The temperature-dependence of relaxation times, $\tau(T)$, is shown in Figure 3-8 as a function of inverse temperature in the usual Arrhenius representation. The lines are fits to the well-known Vogel-Fulcher-Tammann (VFT) equation [18]

$$\tau_{max} = \tau_0 \exp\left(\frac{B}{T - T_0}\right) \tag{3.3}$$

where B is an activation parameter, T_0 is the "ideal" glass temperature located near but below the T_g and τ_0 is the high temperature intercept. The VFT parameters τ_0, B and T_0 assumed values of 3×10^{-14} s, 5527 ± 440 K and 62 ± 22 K for the HBC-$C_{10,6}$ and 3×10^{-14} s, 4800 ± 400 K and 80 ± 14 K for the HBC-$C_{14,10}$. From the VFT dependence, the glass temperature can be estimated as the temperature where the corresponding α relaxation times are of the order of 10^2 s. The thus obtained glass temperatures are 217 ± 22 K and 215 ± 14 K for the HBC-$C_{10,6}$ and HBC-$C_{14,10}$, respectively, in excellent agreement with the values obtained from DSC.
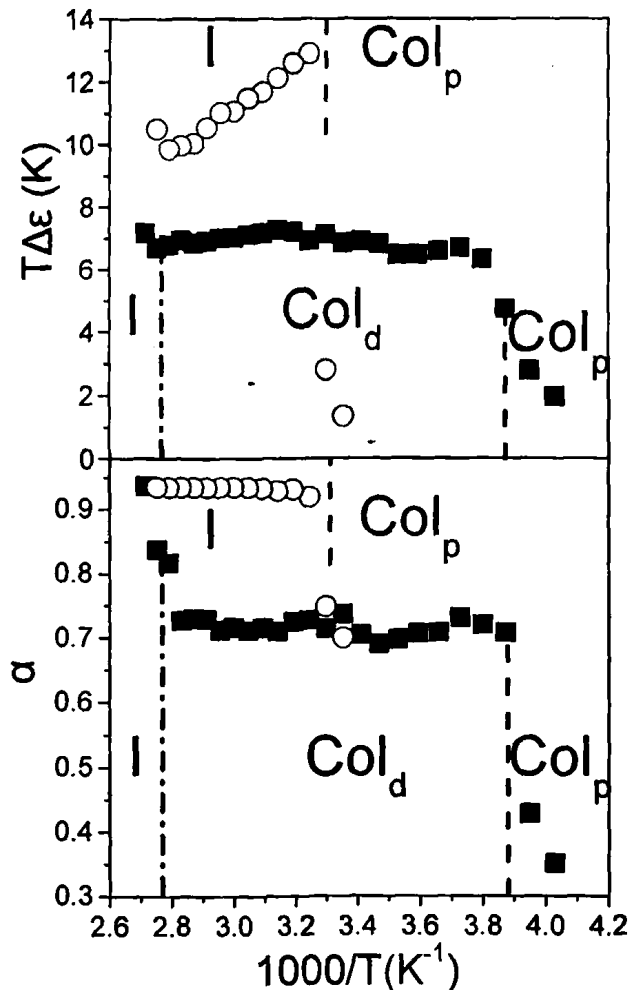
Figure 3-7: *(Top) T-dependence of the dielectric strength (TΔε) corresponding to the α-process of the HBC-$C_{10,6}$ (■) and HBC-$C_{14,10}$ (○). The vertical dashed and dash-dotted lines give the locations of the transition temperatures from DSC on cooling except the one for the HBC-$C_{10,6}$ from Col_p to Col_d phase which is obtained from DS on cooling. (Bottom) T-dependence of the shape parameter (α) of the Havriliak-Negami (HN) function characterizing the distribution of relaxation times of the HBC-$C_{10,6}$ (■) and HBC-$C_{14,10}$ (○).*
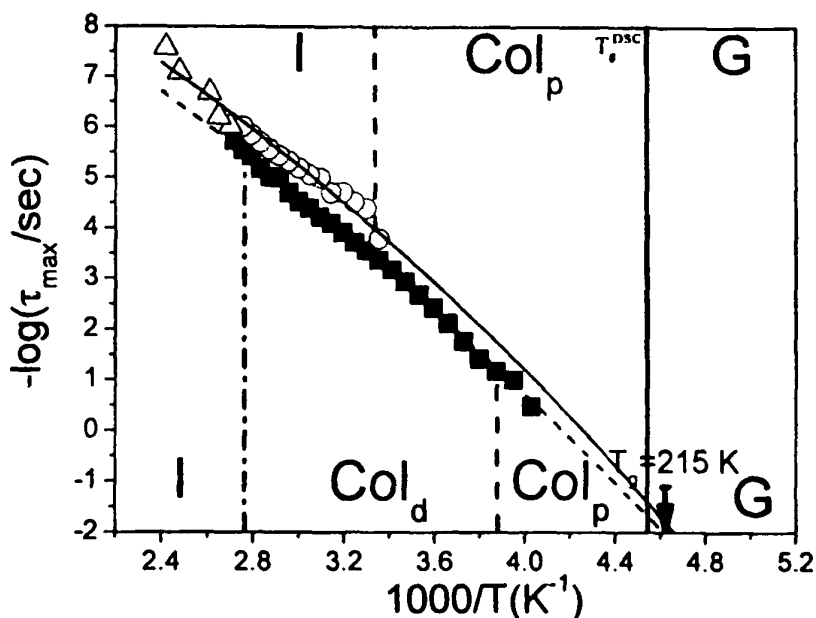
Figure 3-8: *Arrhenius relaxation map for the HBC-$C_{10,6}$ (■) and HBC-$C_{14,10}$ (○). The solid and dashed lines are fits to the VFT equation (see text). The vertical lines correspond to the transition temperatures obtained from DSC on cooling except the one for the HBC-$C_{10,6}$ from Col_p to Col_d phase which is obtained from DS on cooling. NMR data (△) obtained from ref. [17] of the core deuterated molecule (HBC-C_{12}) is included for comparison.*

Interestingly, the $\tau(T)$ dependence is continuous through out the transitions. This probably relates to the very weak dipole moment of the compounds. Nevertheless, we have shown the presence of a glass temperature in both HBCs. Earlier NMR studies on a core-deuterated triphenylene molecules revealed that the glass temperature is associated with a cooperative axial motion of the discs around the columnar axis [19]. To obtain the geometry of the DS α-process in the present compounds we include some recent NMR work on a core-deuterated HBC-C_{12} molecule [17] in Figure 3-8. The NMR times have an apparent activation energy of 114 kJ/mol and are in close proximity with the DS data, suggesting that both techniques are following the same process (disc axial motion). This clearly demonstrates that the glass temperature of the two compounds is associated with cooperative axial rotational motion of the discs around the columnar axis. Thus, T_g in HBCs corresponds to the freezing of the disc axial rotation at ~215 K.

The conductivity, σ, associated with the charge carrier mobility was also extracted from DS. Typical results of the frequency dependence of the real part of the conductivity, σ', for the HBC-$C_{14,10}$ are shown in Figure 3-9. The general behavior, with the conductivity being independent of frequency at low frequencies (dc-conductivity) and becoming frequency

dependent at higher frequencies is very similar to that observed in a broad range of structurally disordered materials [20-24].
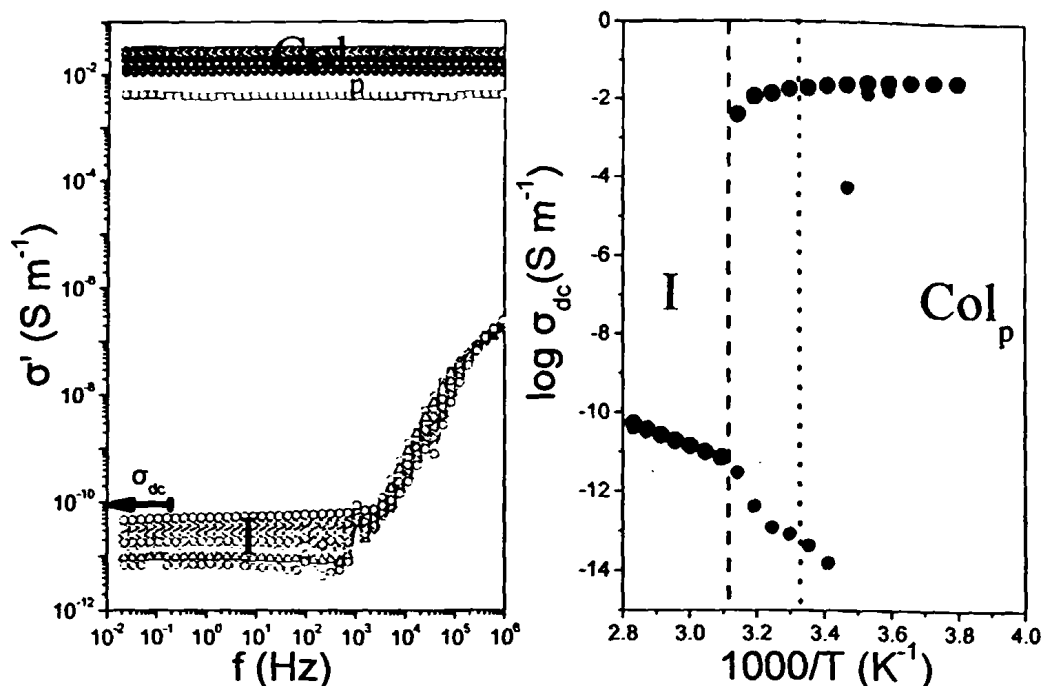
Figure 3-9: *(Left) The frequency dependence of the real part of the conductivity of the HBC-$C_{14,10}$ at different temperatures on cooling: 263.15 K (■), 268.15 K (●), 273.15 K (▲), 278.15 K (▼), 283.15 K (◆), 288.15 K (◄), 293.15 K ( ), 298.15 K (◗), 303.75 K (★), 308.15 K (◆), 313.15 K (●), 318.15 (□), 323.15 ( ), 328.15 (△), 333.15 (▽), 338.15 (◇), 343.15 K (◁), 348.15 (▷), 353.15 (☆). (Right) the temperature dependence of the dc-conductivity of the HBC-$C_{14,10}$ on cooling (●) and subsequent heating (●). The vertical dashed- and dotted-lines give the location of the transition temperatures on cooling and subsequent heating, respectively, obtained from the DSC. Notice the sudden increase in the dc-conductivity of HBC-$C_{14,10}$ on entering the Col_p phase. These results show the possibility of very high conductivity values within the Col_p phase of HBCs. However, the precise conditions for this effect need to be explored in more detail.*

The variation of the dc-conductivity, σ_{dc}, with temperature is shown in Figure 3-9. The dc-conductivity increases by about 8 orders of magnitude from the isotropic to the Col_p phase. An analogous effect was observed previously on doped and macroscopically aligned triphenylene (HAT6) derivatives. For example, doping HAT6 with 1 mol% of $AlCl_3$ converts the discotic hexagonal ordered (D_{ho}) phase into a quasi-one-dimensional semiconductor ($\sigma \sim 10^{-3}$ S/m) with the preferred direction of conductivity being parallel to the columnar axes [25]. Given the low intrinsic charge carrier concentration and large energy gap (of about 4 eV) [26] of HBCs it is likely that the high conductivity values associate with a *homeotropic* alignment [27] of HBC discs between the metal electrodes. The conditions of homeotropic alignment (temperature,

annealing effects, sample thickness, external electric field) have not been explored within this Thesis.

3.5 Summary

The two HBCs investigated by dynamic and structural probes revealed that a slight variation of the side chains affects the packing and gives rise to different organization within the columnar phases. Dielectric spectroscopy revealed a single cooperative VFT-like process freezing at ~215 K, associated with the freezing of the axial disc rotation (α-process). Oxidation increases the dielectric strength of the process and promotes columnar stacking. Although the temperature-dependent relaxation times were continuous through out the phase transformations, the broadening of the relaxation spectra was discontinuous at the respective transitions. Among the different ordered phases, the plastic crystalline phase (Col_p) posses the highest cooperativity for the disc axial rotation. Homeotropic alignment within the Col_p phase can give rise to very high conductivity values; however this effect requires further investigations.

3.6 References

[1] van de Craats, A. M.; Warman, J. M.; Fechtenkötter, A.; Brand, J. D.; Harbison, M.A. and Müllen, K. *Adv. Mater.* **11**, 1469 (1999).

[2] Warman, J. M.; van de Craats, A. M. *Mol. Cryst. Liq. Cryst.* **396**, 41 (2003).

[3] Pisula, W.; Kastler, M.; Wasserfallen, D.; Mondeshki, M.; Piris, J.; Schnell, I.; Müllen, K. *Chem. Mater.* **18**, 3634 (2006).

[4] Stabel, A.; Herwig, P.; Müllen, K.; Rabe, J. P. *Angew. Chem. Int. Ed.* **34**, 1609 (1995).

[5] Wu, J.; Pisula, W.; Müllen, K. *Chem. Rev.* **107**, 718 (2007).

[6] Kastler, M.; Pisula, W.; Wasserfallen, D.; Pakula, T.; Müllen, K. *J. Am. Chem. Soc.* **127**, 4286 (2005).

[7] Fischbach, I.; Pakula, T.; Minkin, P.; Fechtenkötter, A.; Müllen, K.; Spiess, H. W.; Saalwachter, K. *J. Phys. Chem. B* **106**, 6408 (2002).

[8] Elmahdy, M. M.; Floudas, G.; Kastler, M.; Müllen, K. *J. Phys C* (submitted).

[9] Kumar, S. *Chem. Soc. Rev.* **35**, 83 (2006).

[10] de Gennes, P. G. *J. Phys. Lett.* **44**, 657 (1983).

[11] Kastler, M.; Pisula, W.; Laquai, F.; Kumar, A.; Davies, R. J.; Baluschev, S.; García-Gutiérrez, M. C.; Wasserfallen, D.; Butt, H. J.; Riekel, C.; Wegner, G.; Müllen, K. *Adv. Mater.* **18**, 2255 (2006).

[12] Laschat, S.; Baro, A.; Steinke, N.; Giesselmann, F.; Hägele, C.; Scalia, G.; Judele, R.; Kapastina, E.; Sauer, S.; Schreivogel, A.; Tosoni, M. *Angew. Chem. Int. Ed.* **46**, 4832 (2007).

[13] Elmahdy M. M.; Floudas, G.; Mondeshki, M. ; Spiess, H. W.; Dou, X.; Müllen, K. *Phys. Rev. Lett.* (in press, issue March 17, 2008).

[14] Elmahdy, M. M.; Dou, X.; Mondeshki, M.; Floudas, G.; Butt, H. J.; Spiess, H.W.; Müllen, K. *J. Am. Chem. Soc.* (in press, web release March 7, 2008).

[15] McCrum, B. G.; Read, B. E.; Williams, G., *Anelastic and dielectric effects in polymeric solids*, New York: Dover, (1991).

[16] Ito, S.; Wehmeier, M.; Brand, J. D.; Kübel, C.; Epsch, R.; Rabe, J. P.; Müllen, K. *Chem. Eur. J.* **6**, 4327 (2000).

[17] Kayser, C. W., *Ph.D. Thesis*, Mainz, (1999).

[18] Floudas, G. *Prog. Polym. Sci.* **29**, 1143 (2004).

[19] Leisen, J.; Werthg, M.; Boeffel, C.; Spiess, H.W. *J. Chem. Phys.* **97**, 3749 (1992).

[20] Bottger, H.; Bryskin, V. V., *Hopping Conduction in Solids*, VCH, Berlin, (1985).

[21] Mott, N. F.; Davies, E. A., *Electronic Processes in Non-Crystalline Materials*, Clarendon Press, Oxford, (1979).

[22] Pollak, M.; Geballe, T. H. *Phys. Rev.* **122**, 1742 (1961).

[23] Epstein, A. J.; Rommelman, H.; Abkowitz, M.; Gibson, H. W. *Mol. Cryst. Liq. Cryst.* **77**, 81 (1981).

[24] Simon, J.; Andre, J. J., *Molecular Semiconductors*, Springer Verlag, Berlin, (1985).

[25] Boden, N.; Bushby, R. J.; Clements, J. J. *Mater. Sci. Mater. Electron.* **5**, 83 (1994).

[26] Chandrasekhar, S.; Prasad, S. K. *Contemop. Phys.* **40**, 237 (1999).

[27] Bushby, R. J.; Lozman, O. R. *Current Opinion in Colloid & Interface Science* **7**, 343 (2002).

Chapter 4

Self-assembly and Dynamics of Functionalized HBC Derivatives

4.1 Introduction

As we mentioned earlier, a key factor in the design of HBCs for electronic applications is the high one-dimensional charge carrier mobility (above 1 cm^2/Vs) that is approaching the value for the intersheet mobility in graphite (3 cm^2/Vs) [1,2]. The origin of this favorable mobility is the optimized π-π overlap of the aromatic cores. During the process of self-organization, the disc-shaped molecules organize into columns that assemble into two-dimensional arrays, whereas the alkyl chains fill the intercolumnar space [3]. The balance of enthalpic and entropic interactions, is shifted in HBCs towards the former that stabilize two main columnar structures: a hexagonal liquid crystalline phase (Col_h) and a crystalline phase (C_r), at higher and lower temperatures, respectively. Nevertheless, the stability of these phases (i.e., the exact phase state) remains unknown for the majority of the compounds. In view of the high charge carrier mobility of the crystalline phase, the stability of this phase to temperature and pressure variations needs to be explored in detail.

Another, seemingly unrelated issue, is that of the intrinsic disc mobility within the columnar structures. Since the electronic charge carriers are likely to be transported by the stacked HBC cores, knowledge of the intrinsic rotational dynamics of the discs is important for the design of HBCs for particular applications. Already, our earlier investigation of the branched HBCs revealed considerable disc dynamics within the LC phases (Chapter 3). However, in these systems, the structural relaxation (α-process) results from oxidation, hence can be considered as an artifact.

A more systematic investigation of discotic liquid crystals with respect to the nanoscale self-assembly, the molecular dynamics, the thermodynamic phase state and the pathways of structure formation with possible metastable states, requires a combination of model systems

bearing dipoles directly attached to the cores and different microscopic techniques that are sensitive probes of the time-scale and geometry of motion. Furthermore, additional thermodynamic variables are needed (i.e., pressure [4]) for constructing the complete phase diagram. For this purpose we employ a series of dipole functionalized HBCs. First, we study the effect of dipole substitution on the stability of the liquid crystalline phases. Second, we investigate the core dynamics within the columns by combining dielectric spectroscopy with site-specific NMR techniques. These probes provide unambiguously the rate and geometry of motion. Third, we employ pressure and investigate, for the first time, the stability of the liquid crystalline and crystalline phases by providing the thermodynamic phase diagram for dimethoxy substituted HBC. This study delineates the pressure and temperature stability limits of the crystalline phase associated with the highest charge carrier mobility. Lastly, we monitor for the first time, the evolution of structure formation by dielectric means, following a distinct path within the T-P phase diagram. In this study we are interested in the presence or absence of intermediate states, the possible nucleation sites and the existence of long-lived metastability. The latter study provides glimpses of the exact mechanism for structural re-organization and growth.

4.2 Materials

Four dipole functionalized HBC derivatives (with mono-cyano, mono-bromo, dimethoxy and mono-ethynyl substitution, see Scheme 4-1) were synthesized for the purpose of this investigation. The synthesis of two of these compounds (mono-bromo and dimethoxy HBCs) have been reported elsewhere [5,6], whereas the synthesis of the other two (mono-cyano and mono-ethynyl HBCs) is reported here for the first time [7]. Notice that the molecules bear the same HBC core with different functional groups and different architectures of the alkyl chains.

mono-cyano

mono-bromo

dimethoxy
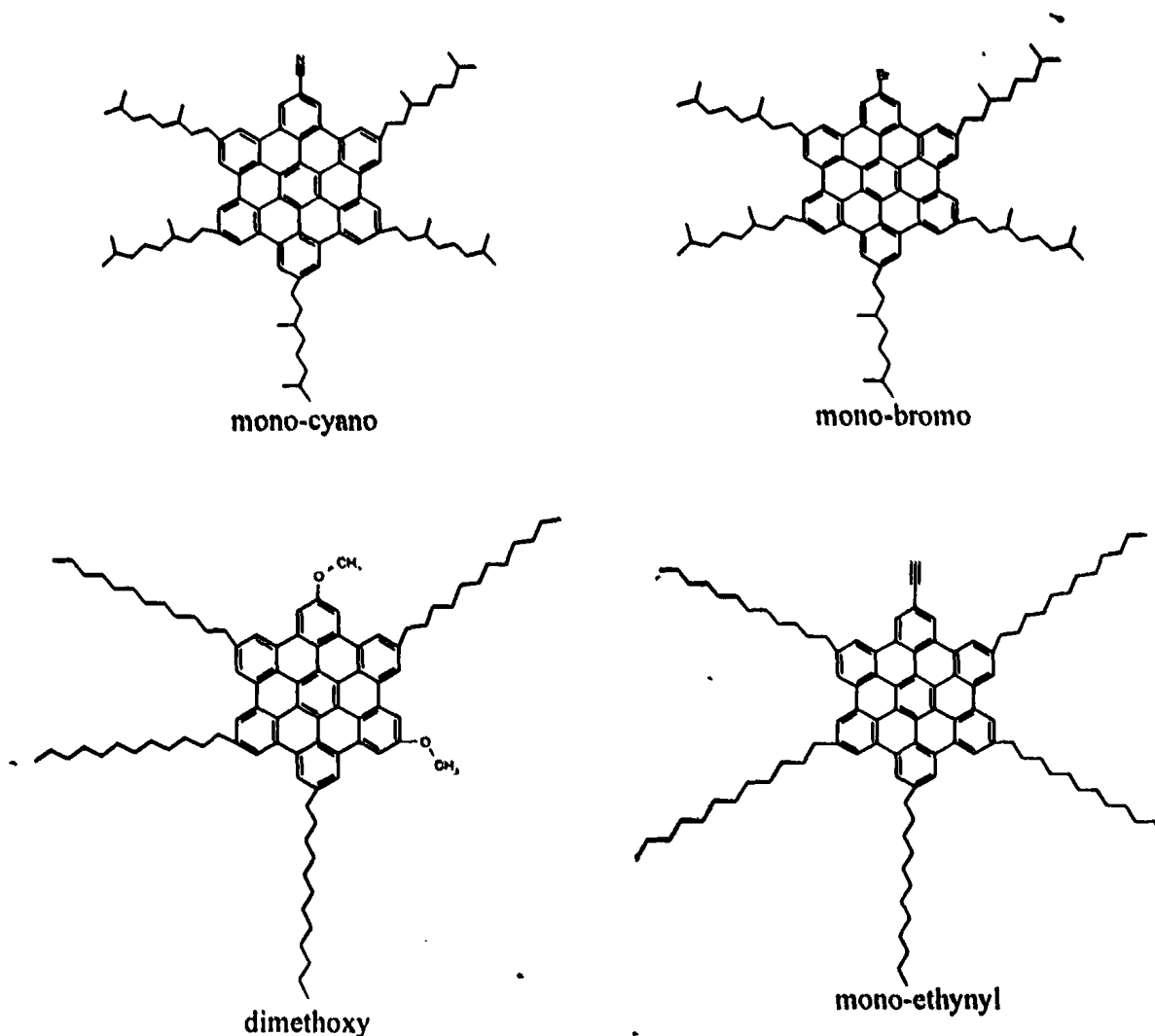
mono-ethynyl

Scheme 4-1: *Schematic structures of the mono-cyano HBC (upper left), mono-bromo HBC (upper right), dimethoxy HBC (bottom left) and mono-ethynyl HBC (bottom right).*

4.3 Thermal properties (DSC)

The thermal behavior was determined by differential scanning calorimetry (DSC) on cooling and subsequent heating (10 K/min) revealing the absence of a phase transformation for the mono-cyano, and mono-bromo HBCs within the investigated T-range (Figure 4-1). However a glass temperature was identified at 236 K with an associated heat capacity step of 0.16 J/gK. The dimethoxy HBC, instead, undergoes a transition at 382 K on heating (344 K on. cooling) with a heat of fusion of 52 J/g (54 J/g on cooling). Similarly, the mono-ethynyl HBC undergoes a transition at 305 K on heating (280 K on cooling) with a heat of fusion of 24 J/g (18 J/g on cooling). The phases and transition temperatures for all samples are summarized in Table 4.1.

Table 4.1. Thermal properties and transition temperatures of the functionalized HBCs.

Sample	Transition temperature (K)	Enthalpy (J/g)	Phase/Phase transition	d_{10} (nm)^d	Lattice parameter a (nm)^d	d_{intra} (nm)^d
mono-cyano HBC	$234^a(228)^b$ 237^c	-	Col$_h$/Glass transition Col$_h$/Glass transition	2.40	2.77	0.360
mono-bromo HBC	$238^a(226)^b$ 237^c	-	Col$_h$/Glass transition	2.48	2.86	0.363
dimethoxy HBC	$382^a(344)^b$ 236^c	$52^a(54)^b$	C$_r$-Col$_h$/ Glass transition	2.51	2.90	0.363
mono-ethynyl HBC	$305^a(280)^b$ 236^c	$24^a(18)^b$	C$_r$-Col$_h$/ Glass transition	2.25	2.60	0.354

^{a} heating (differential scanning calorimetry) ^{b} cooling (differential scanning calorimetry)
^{c} cooling (dielectric spectroscopy) ^{d} at 403 K (Col$_h$ phase)
C$_r$: crystalline phase Col$_h$: columnar hexagonal liquid crystalline phase
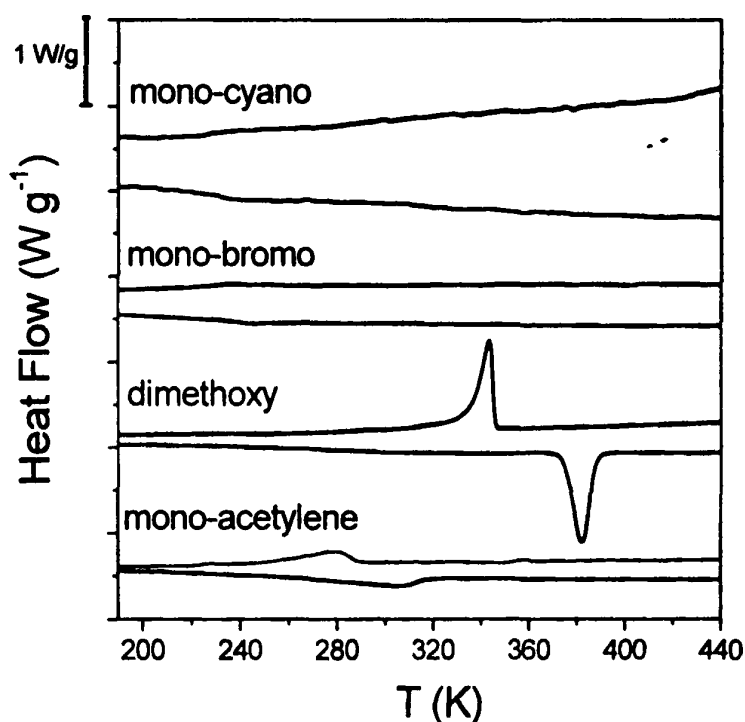
Figure 4-1: *DSC curves for the four dipole functionalized HBCs obtained during the second cooling (in blue) and heating (in red) runs with 10 K/min. Note that crystallization takes place in the dimethoxy- and mono-ethynyl samples which is absent in the mono-cyano and mono-bromo traces.*

4.4 Structure and molecular dynamics of the mono-cyano HBC

4.4.1 Structure investigation

The relation between molecular structure and the supramolecular organization of the mono-cyano HBC has been investigated by temperature-dependent two-dimensional wide-angle X-ray scattering (2D-WAXS). The WAXS images was obtained from an oriented fiber

$(T_{extr}=273$ K) at different temperatures on heating from 253 to 423 K and on cooling from 383 to 303 K. The WAXS images (Figure 4-2) exhibit strong meridional reflections and a set of equatorial reflections with ratios $1:\sqrt{3}:\sqrt{4}$ relative to the primary peak. In addition, a weak reflection at intermediate distances is observed.
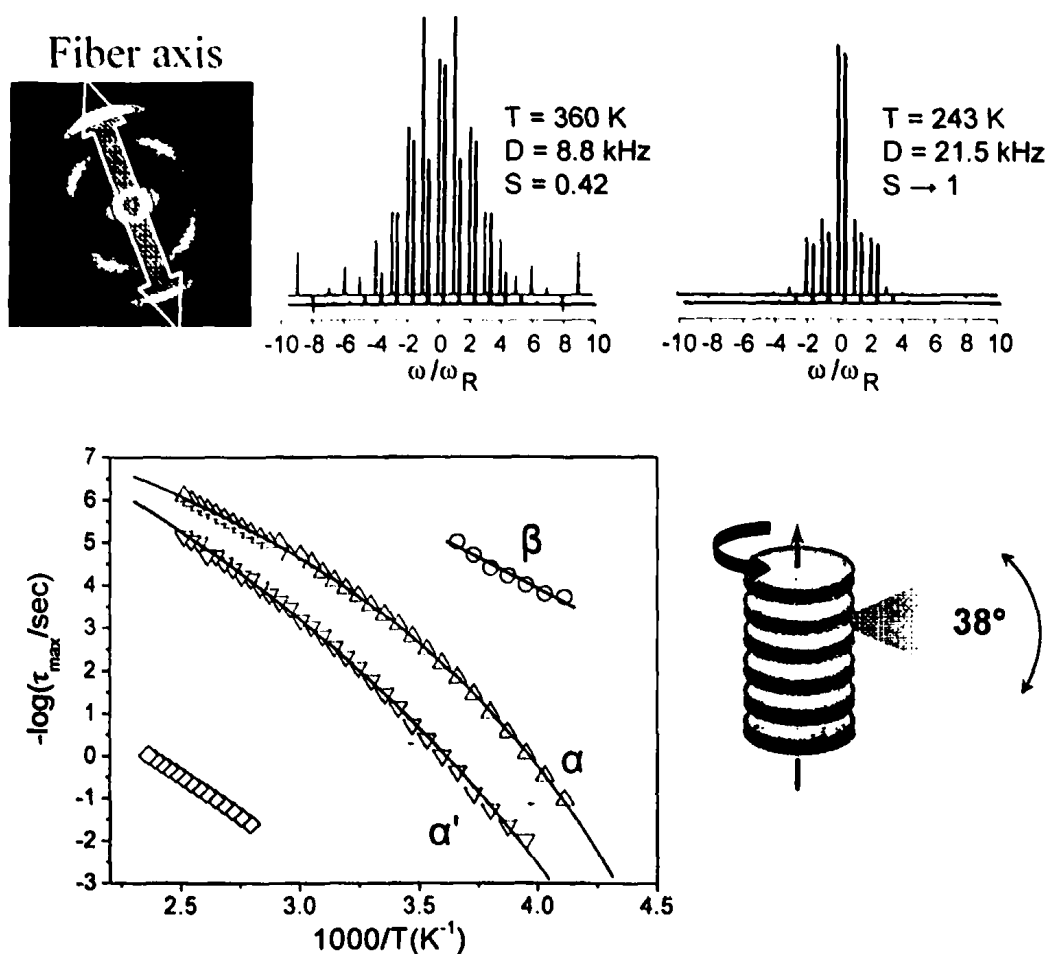
Figure 4-2: *(Top): 2D-WAXS image of the mono-cyano HBC obtained from an oriented fiber ($T_{extr}=273$ K) at 423 K revealing a columnar hexagonal liquid crystalline phase (Col_h) (left). $^{13}C-^{1}H$ REREDOR spinning sideband patterns recorded at 25 kHz spinning at the magic angle and 360 K and 160 μs recoupling time (middle) and at 243 K and 40 μs recoupling time (right) with the simulated patterns (blue) superimposed, resulting in local dynamic order parameters of S=0.42 and 1, respectively. (Bottom): Arrhenius relaxation map (left) for all dielectrically active processes and of the ionic mobility. Notice: (i) the β-process (circles) with an Arrhenius T-dependence, (ii) the α (up triangles) and α' (down triangles) processes with VFT dependence, and (iii) the "slow" process (rhombus) due to the ionic mobility and the columnar structure indicating both in-plane and out-of-plane motions (right).*

The strong meridional reflection reflects intracolumnar distances whereas the equatorial reflections are of intercolumnar origin and correspond to the (10), (11) and (20) reflections of a hexagonal lattice (Figure 4-3). The d_{hk} spacings (where h and k are the Miller indices) are related to the lattice parameter a through Eq. (1.12) of Chapter 1 and suggest the formation of a

columnar hexagonal liquid crystalline phase (Col$_h$). The calculated d-spacings and the lattice parameters are included in Table 4.2.

Table 4.2. XRD data for the mono-cyano HBC at two different temperatures within the Col$_h$ phase on heating.

T (K)	Phase	Lattice parameters (nm)	d_{10} (nm)	d_{intra} (nm)	Unit cell
253	Col$_h$	a=2.64	2.28	0.357	Hexagonal
423	Col$_h$	a=2.71	2.35	0.361	Hexagonal

Figure 4-3: *WAXS equatorial reflections at 253 K (top) and 423 K (bottom) for the mono-cyano HBC (obtained on heating). The equatorial reflections correspond to the (10), (11) and (20) reflections which are characteristic of a hexagonal columnar mesophase.*

118

The weak reflection at intermediate distances indicates dipole-dipole correlations with an angle of about 90° as revealed by the azimut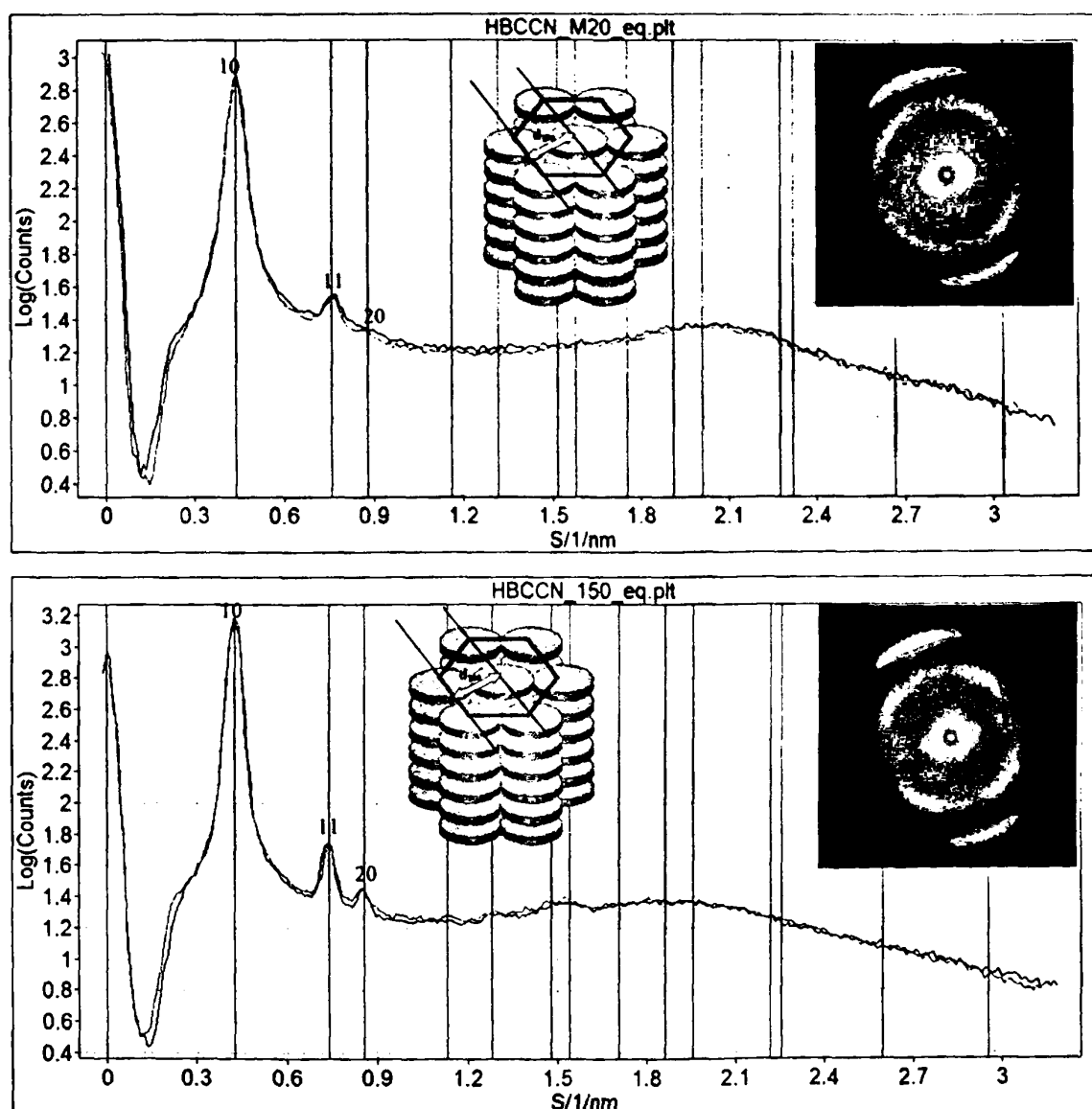hal intensity distribution. From the T-dependence of the corresponding meridional and equatorial reflections the corresponding intra- and inter-columnar thermal expansion coefficients were extracted and found to be different ($\beta_{intra}\sim7.6\times10^{-5}$ K^{-1} and $\beta_{inter}\sim1.35\times10^{-4}$ K^{-1}). The anisotropy in thermal expansivity originates from the anisotropic nature of the system composed from graphene discs and hydrocarbon tails [8]. The inter-columnar thermal expansion is higher reflecting the higher expansion of hydrocarbon tails with increasing temperature.

4.4.2 Molecular dynamics investigation

The analysis of the heteronuclear NMR rotor encoded rotational echo double resonance NMR (REREDOR) spinning sideband patterns provides site-specific information of the molecular motion [9-11] through the effective ^{1}H-^{13}C dipole-dipole coupling constant, D_{CH}, and the associated local dynamic order parameter, S, representing the residual motional anisotropy of a given molecular segment. S is given in the form of the second order Legendre polynomial and is obtained experimentally as the ratio of the measured effective dipole-dipole coupling constant to that of a static pair (see Eq. (1.14) of Chapter 1).

For the mono-cyano HBC derivative a glassy phase is detected at temperatures below ~240 K, where the aromatic core is practically frozen ($D = 21.0$ kHz, $S \rightarrow 1$). This temperature lies in the proximity of the glass temperature identified by DSC and DS (Table 4.1). For the alkyl chains, the ^{1}H-^{13}C dipole-dipole coupling constants of the CH$_2$ groups are reduced but to an average $D=14.5$ kHz, $S=0.69$, apart from the chain ends. In the Col$_h$ mesophase, the ^{1}H-^{13}C dipole-dipole coupling constant of the aromatic CH moiety is reduced to 8.8 kHz due to the fast in-plane rotation [12-14]. Further reduction of the dynamic order parameter of the CH segment to $S = 0.42$ at 360 K is ascribed to out-of-plane disc excursions ($\sigma=38°$). The mean angle (38°) of this motion is obtained by assuming that the local dynamic order parameter S, results from a Gaussian distribution of displacement angles [14]. The correlation times of the Arrhenius plot given in Figure 4-2 suggest that both alpha processes are in the fast limit ($>10^5$ Hz) only above 360 K. Below, NMR signal loss under the pulse sequence and line broadening effects can be expected. To clarify this point we performed ^{13}C cross-polarization NMR measurements for the mono-cyano HBC over the temperature range from 237 to 412 K (Figure 4-4). The spectra are included below and the peak intensity corresponding to the aromatic CH carbon at 119 ppm is plotted in Figure 4-5.
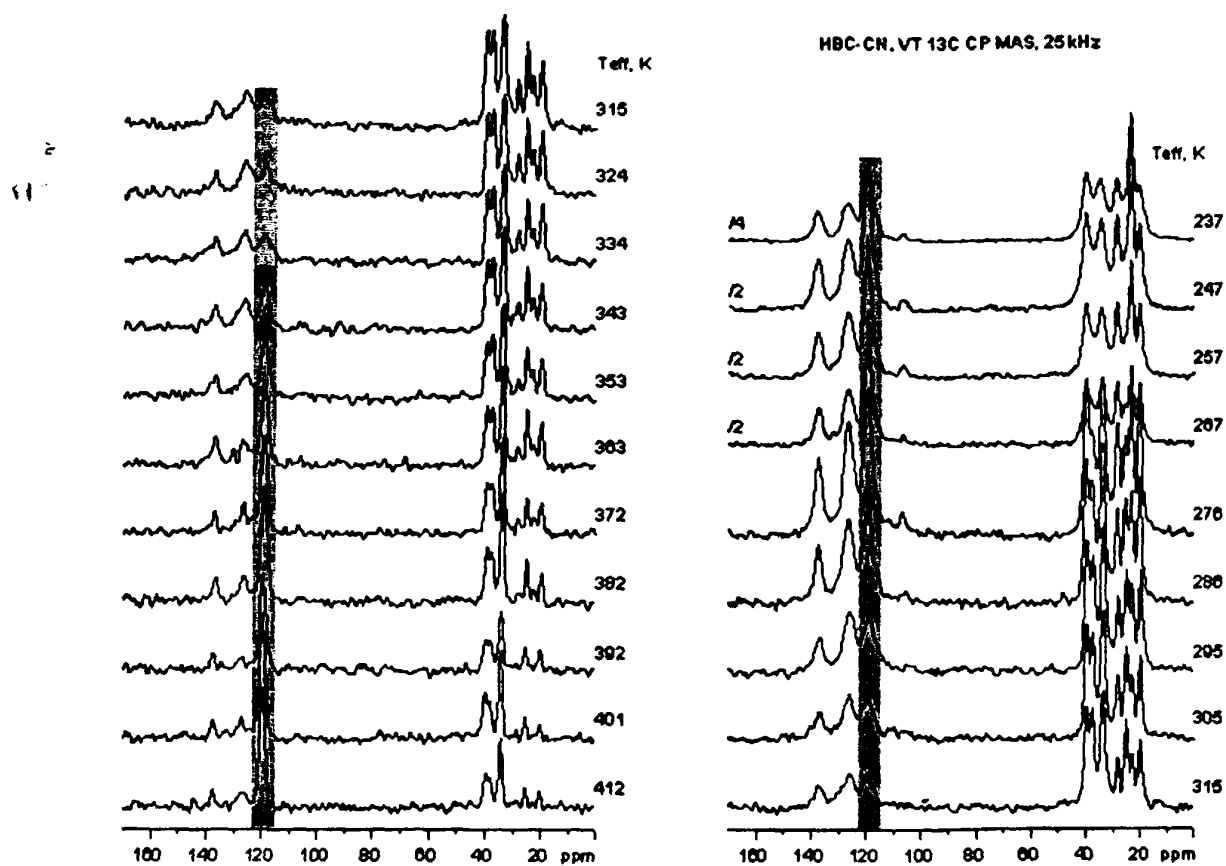
Figure 4-4: *Variable temperature ^{13}C cross-polarization (CP) NMR spectra of the mono-cyano HBC at 1ms CP time, 25 kHz spinning at the magic angle (2s recycle delay and 2 k scans).*
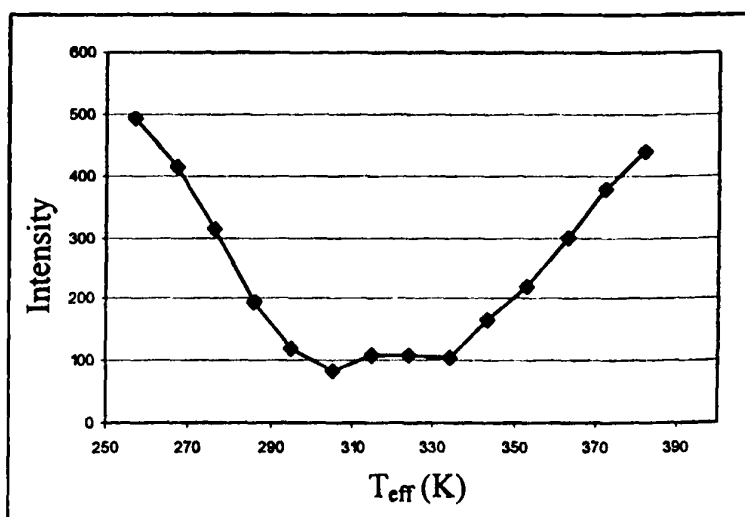
Figure 4-5: *Peak intensity corresponding to the aromatic CH carbon (119 ppm) for the mono-cyano HBC plotted as a function of temperature.*

Evidently, severe signal loss occurs for temperatures in the range 305-343 K corresponding to the α-process (axial motion) that according to the REREDOR experiment comprises both in-plane and out-of plane axial motions. Note that the signal is never lost completely, consistent with a heterogeneous distribution of correlation times. At the glass transition of organic

glasses, the time scale of the molecular dynamics often exhibits a heterogeneous distribution of correlation times [15,16]. Indeed, such behavior is found here by recording ^{13}C-^1H sideband patterns at an intermediate temperature of 267 K. For a short τ_{RC} of 40 μs, spectra of still frozen discs with $S \rightarrow 1$ are observed, whereas the spectrum for τ_{RC} of 160 μs gives $S = 0.42$, due to the fraction of mobile discs performing in and out-of plane motion (see Figure 4-2). For τ_{RC} of 80 μs, the spectrum exhibits both features.

The corresponding time-scales of this complex heterogeneous dynamics can best be studied in the HBCs bearing strong dipole moments through Dielectric Spectroscopy. Three dielectrically active processes (β, α and α') are detected associated with the cyano dipole relaxation as shown in Figure 4-6.
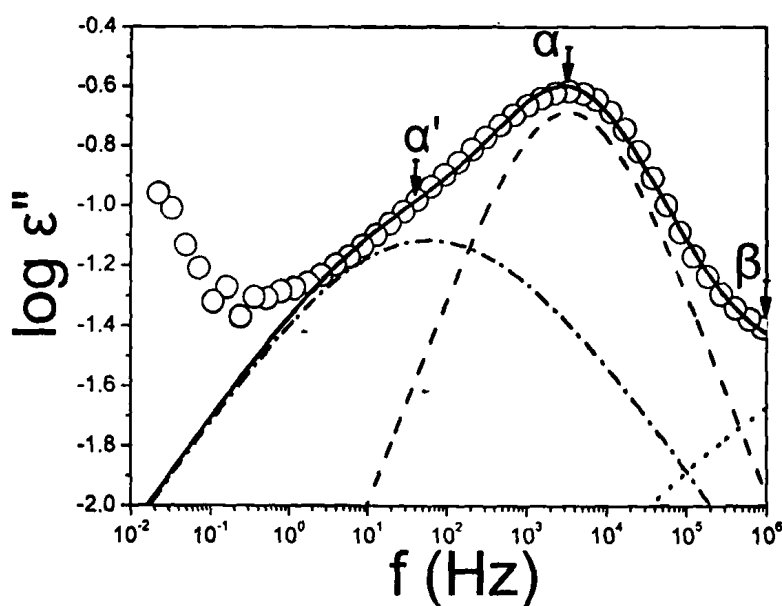
Figure 4-6: *Imaginary part (ε'',O) of the complex dielectric function $\varepsilon^*(\omega)$ versus frequency for the mono-cyano HBC at T=303.15 K. In the high frequency side, the β (dotted-line), α (dashed-line) and the α' (dash-dotted-line) processes appear. The solid line is the sum of the β, α and α' processes. Three HN-functions were fitted to the whole spectrum.*

Three HN-functions (HN function is given by Eq. (2.47) of Chapter 2) were fitted to the whole spectrum. The shape of the α-process deviates from a single Debye process ($\alpha=\gamma=1$) and is highly asymmetric toward the high and low-frequency side. The deviation at the high frequency side is caused by the β-process while at the low frequency side by broad wing. This low frequency wing is described by a third HN-function. The parameters of this third HN function were extracted from lower temperatures and were kept fixed at higher temperatures. The relaxation times of the three processes (β, α and α') and the one process associated with the

ionic conductivity relaxation (obtained from the crossing of the M' and M'') are shown in Figure 4-2, in the usual Arrhenius representation. The low-temperature β-process has an Arrhenius T-dependence [4]

$$\tau = \tau_0 e^{E/RT} \tag{4.1}$$

with a single activation energy $E=55\pm5$ kJ/mol and a $\tau_0=4\times10^{-16}$ s, characteristic of a local process. Thus the β-process is assigned to small-angle vibrational motions of the cyano group induced by the more mobile alkyl chains. At higher temperatures the α and α' processes have steeper temperature dependence that can be described by the Vogel-Fulcher-Tammann (VFT) Equation (3.3) given in Chapter 3. The B, T_0 and T_g parameters assume the following values: 900 ± 23 K, 161 ± 2 K and 237 ± 3 K for the α and 1730 ± 115 K, 128 ± 6 K and 255 ± 6 K for the α' process. The characteristic relaxation times of the ion mobility also display the common VFT dependence. Interestingly, the DSC T_g corresponds to the freezing of the DS α-process (at $\tau\sim10^2$ s). This process is less restricted and less volume demanding (see below with respect to the pressure dependence) and thus freezes at a lower temperature. Both processes are non-Debye with low (α)- and high $(\alpha\gamma)$-frequency HN slopes of $\alpha=\alpha\gamma=0.7$ and $\alpha=\alpha\gamma=0.4$ for the α and α' processes, respectively and intensities of $T\Delta\varepsilon\sim240$ and 150 K. Clearly, the fast axial motion, as seen in NMR, leaves an uncompensated residual dipole moment as the dipole breaks the symmetry of the HBC disc and results in unevenly populated sites for the axial motion. This residual dipole moment then relaxes through the slower (α') process with considerably lower relaxation strength. Consistent with the results of NMR and X-rays, the α-process reflects collective axial motions of the discs, which leaves a residual dipole with a defined average orientation within the column. The orientation correlation of the dipoles within the columns, however, has a limited lifetime and relaxes through highly collective intra- and perhaps inter-columnar rotational dynamics $(\alpha'$ process).

To explore further the origin of the slower process and to construct the phase diagram, we employ pressure as the additional relevant thermodynamic parameter. In these experiments, pressure is applied isothermally at temperatures where α and α' processes are probed within the experimental window as shown in Figure 4-7. The relaxation times of the two processes (α and α') are shown in Figure 4-8, in the usual Arrhenius representation. Increasing pressure results in the slowing-down of both processes, but, remarkably there is a steeper P-dependence for the slower α' process.
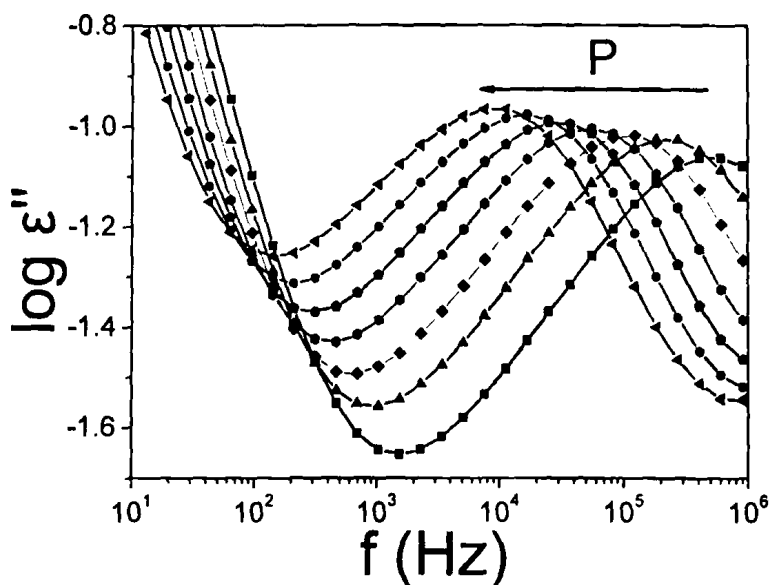
Figure 4-7: *Dielectric loss for the mono-cyano HBC at 393.15 K for different pressures: 1 MPa (■), 40 MPa (▲), 80 MPa (◆), 120 MPa (●), 160 MPa (◆), 200 MPa (●) and 240 MPa (◀).*
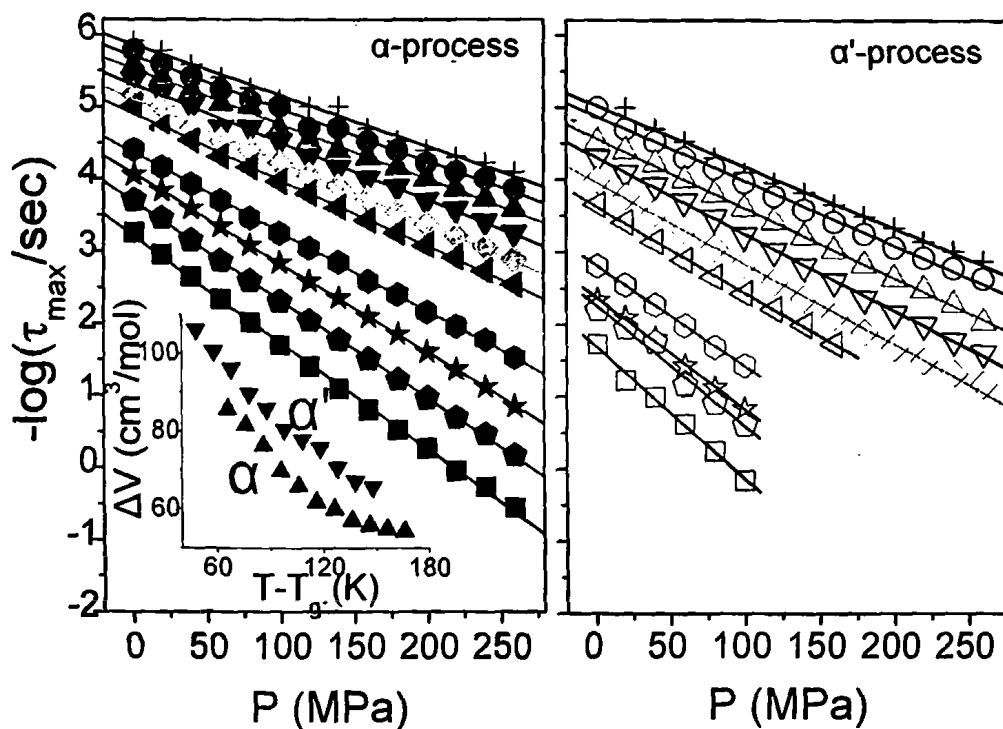
Figure 4-8: *Pressure dependence of the relaxation times at maximum loss corresponding to the α (left) and α' (right) processes of mono-cyano HBC. The symbols indicate temperatures in the range from 303 K (squares) to 403 K (crosses) in steps of 10 K. The lines are the result of the fit giving rise to the apparent activation volume. (Inset) Temperature dependence of the apparent activation volumes (ΔV) plotted as a function of the temperature difference from the respective T_g.*

The linear dependence of $\log \tau$ versus pressure can be used to define an apparent activation volume, ΔV, as [4]

$$\Delta V = 2.303 RT \left(\frac{\partial \log \tau}{\partial P} \right)_T \tag{4.2}$$

This quantity is plotted in the inset to Figure 4-8 as a function of the temperature difference from the respective T_g. Note that the apparent activation volume for the two processes decreases with increasing temperature and that $\Delta V_{\alpha'} > \Delta V_{\alpha}$. The latter indicates that pressure slows down more the highly collective slower process as compared with the less volume demanding axial motion of the discs.

Based on the T- and P-investigations a phase diagram can be constructed for the mono-cyano HBC that is depicted in Figure 4-9.

Figure 4-9: *"Phase diagram" for the mono-cyano HBC showing two "glass" phases and the columnar hexagonal liquid crystalline phase (Col$_h$) at higher temperatures. The lines are the result of the fit to Eq. (4.3).*

The two $T_g(P)$ dependencies corresponding to the freezing of the fast axial (α-process) and of the slower collective re-organization (α'- process) can be described by the empirical Equation [4]:

$$T_g(P) = T_g(0)\left(1 + \frac{b}{c}P\right)^{\frac{1}{b}}$$
(4.3)

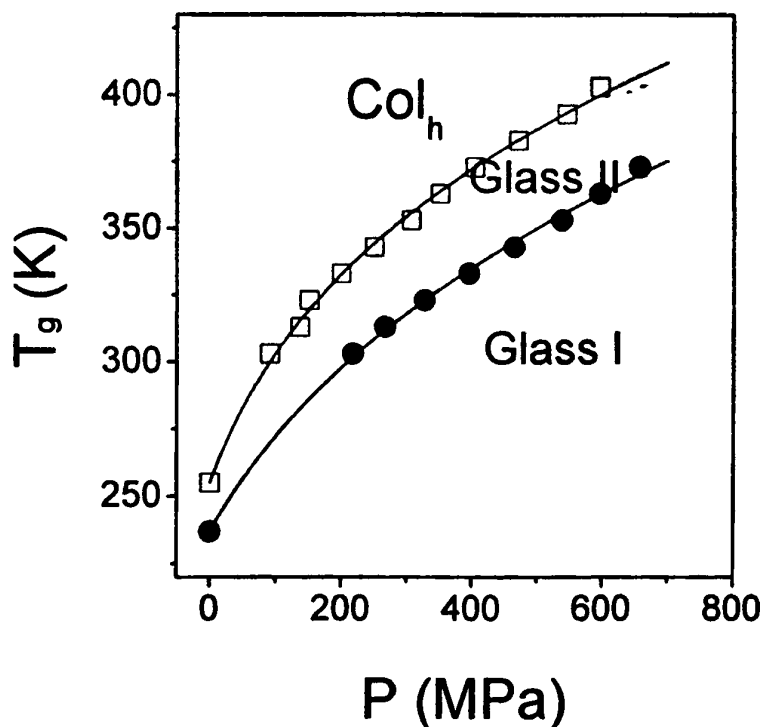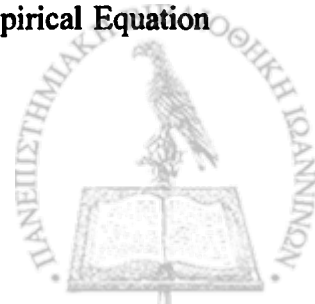where b and c are fitting parameters (b=3.9, c=540 MPa and $(dT/dP)_{P\to 0}$ = 0.44 K/MPa for the α-process and b=4.8, c=370 MPa and $(dT/dP)_{P\to 0}$ = 0.69 K/MPa for the α'-process). These dependencies separate the T-P phase space in three regimes depicted as "glass I", "glass II" and Col_h. As a result of the stronger pressure dependence for the slow collective reorganization, increasing pressure effectively stabilizes the "glass II" phase.

4.5 Structure, molecular dynamics and kinetics of structure formation of the dimethoxy HBC

4.5.1 Structure investigation

The dimethoxy and mono-ethynyl HBCs are of particular important because they undergo a transformation from the LC to the C_r phase. The DSC traces of the dimethoxy HBC revealed a first-order phase transformation at temperature of 382 K on heating (344 K on cooling) as shown in Figure 4-10. 2D-WAXS images of dimethoxy HBC obtained from an oriented fiber at different temperatures on heating and subsequent cooling are shown in Figure 4-11. The high temperature phase in the dimethoxy exhibits a set of strong meridional reflections and a set of equatorial reflections with ratios $1{:}3^{1/2}{:}4^{1/2-}$ relative to the primary peak. The former reflect intracolumnar distances whereas the latter are of intercolumnar origin and correspond to the (10), (11) and (20) reflections of a hexagonal lattice (Figure 4-12). The d_{hk} spacings are related to the lattice parameter a through Eq. (1.12) of Chapter 1 and suggest the formation of a columnar hexagonal liquid crystalline phase (Col_h). The calculated d-spacings and the lattice parameters are included in Tables 4.2 and 4.3. On the other hand, the low temperature phase in the dimethoxy HBC, is crystalline (C_r). As we will see below with respect to the dynamics, despite the strong WAXS reflections within C_r, the discs can still rotate. The off-meridional reflections indicate a tilt of the discotic cores with respect to the columnar axis with an intracolumnar periodicity of ~0.36 nm, giving rise to the known "herringbone" structure. As a result of the elliptic projection of the discs in the plane, the symmetry of the C_r phase deviates from the usual hexagonal lattice. The sequence of equatorial reflections appears now at wave vectors, 2.48, 3.6 and 5 nm^{-1} which correspond to the (10), (01) and (11) reflections of an oblique unit cell [17,18] (Figure 4-13). The d_{hk} spacings are related to the lattice parameter a through Eq. (3.1) of Chapter 3 and suggest the formation of a columnar oblique liquid

crystalline phase (Col_{ob}). The calculated d-spacings and the lattice parameters are included in Table 4.3. Within both phases the side chains are molten as shown by the small values of the local dynamic order parameter deduced from NMR (see below) and from the absence of distinct reflections in X-rays. Their intra- and inter-molecular correlations give rise to a broad "amorphous halo" centered around q~12-14 nm^{-1}.
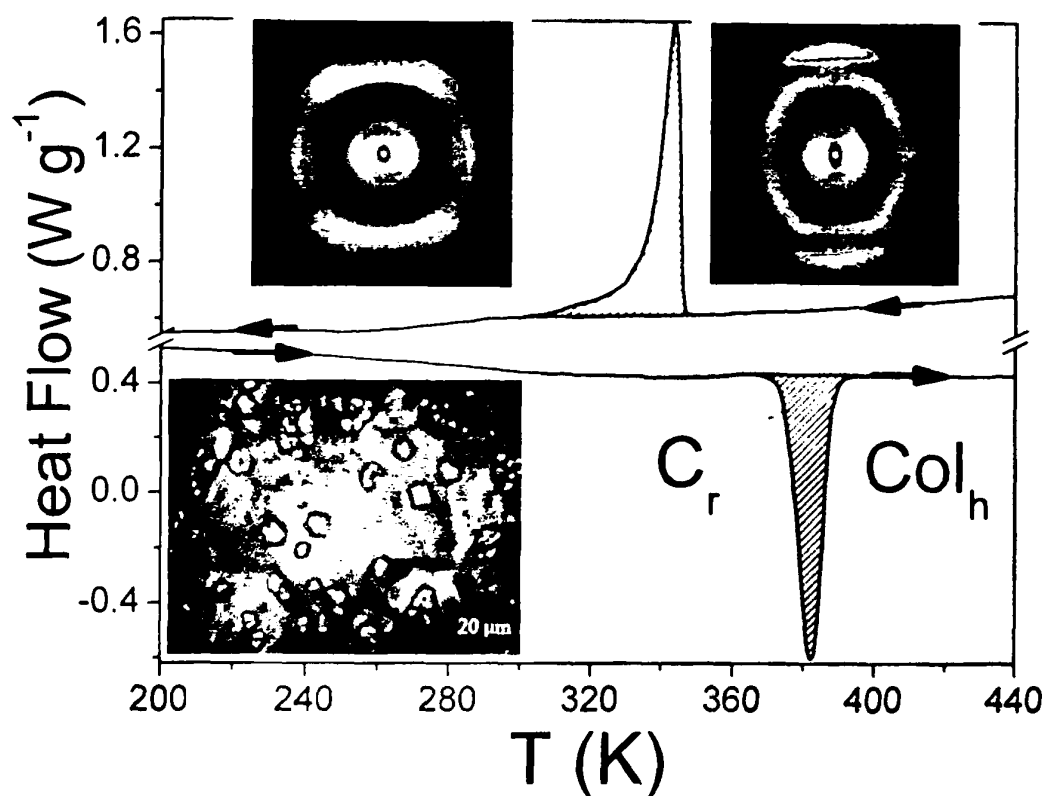
Figure 4-10: *DSC trace of the dimethoxy HBC obtained during the second cooling/heating runs with 10 K/min. 2D WAXS images obtained from an oriented fiber shown at 303 K and 373 K, corresponding to the crystalline (C_r) and columnar hexagonal liquid crystalline phase (Col_h). Image from POM obtained on slow cooling at 303 K showing both spherulites (C_r) with a radial columnar orientation and smaller circular objects with columnar growth around the nucleation centers (Col_h).*

The $Col_h \rightarrow C_r$ transformation revealed a hysteresis. The WAXS images display mixed reflections on cooling to 303 K from the Col_h phase, suggesting a slow phase transformation (Figure 4-11). This is also evident in the POM image of the dimethoxy HBC (Figure 4-10), taken at 303 K on cooling from 500 K. The image displays several circular textures with columnar growth around the multiple nucleation centers (Col_h) and some spherulitic textures with a radial columnar orientation (C_r). Note that the nucleation density of the former features exceeds the latter as well as the absence of any correlation between the nucleation sites of the

Col$_h$ and C$_r$ phases. This phase coexistence reflects the very slow phase transformation kinetics that will be explored in detail below.
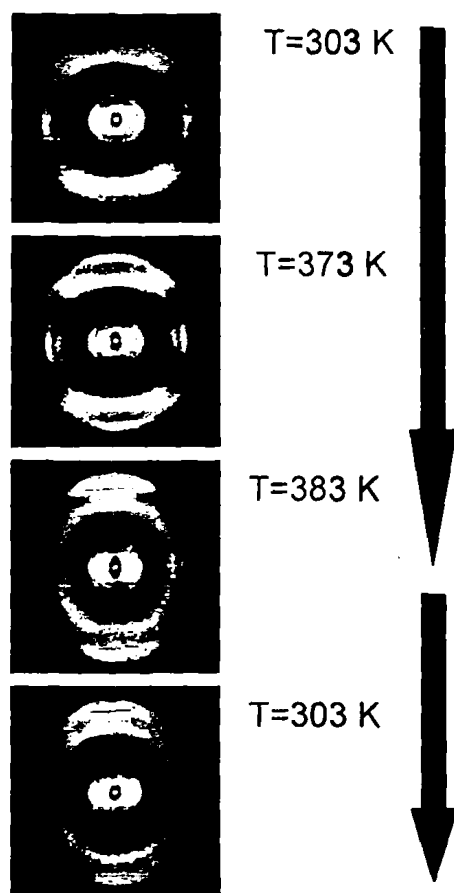
Figure 4-11: *Two-dimensional X-ray images from the dimethoxy HBC obtained on heating and subsequent cooling. The image at 303 K corresponds to the crystalline phase whereas the one at 383 K to the columnar hexagonal liquid crystalline phase. The lower image is obtained at 303 K on cooling from 383 K (taken after 1 hour). Note the slow Col$_h$ to C$_r$ phase transformation kinetics.*
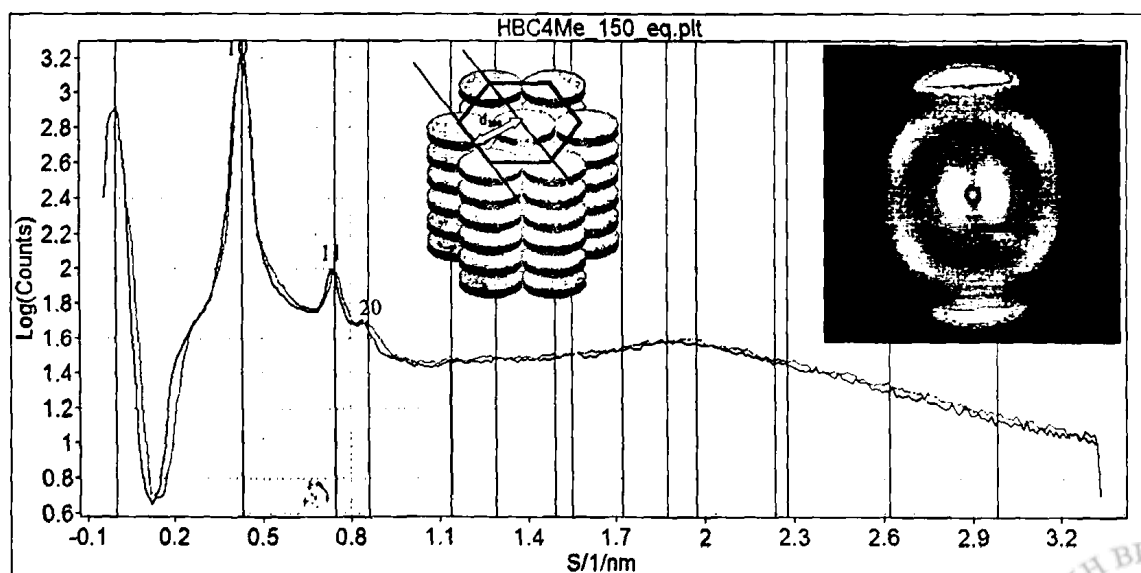
Figure 4-12: *WAXS equatorial reflections at 423 K for the dimethoxy HBC (obtained on heating). The equatorial reflections correspond to the (10), (11) and (20) reflections which are characteristic of a hexagonal columnar mesophase.*
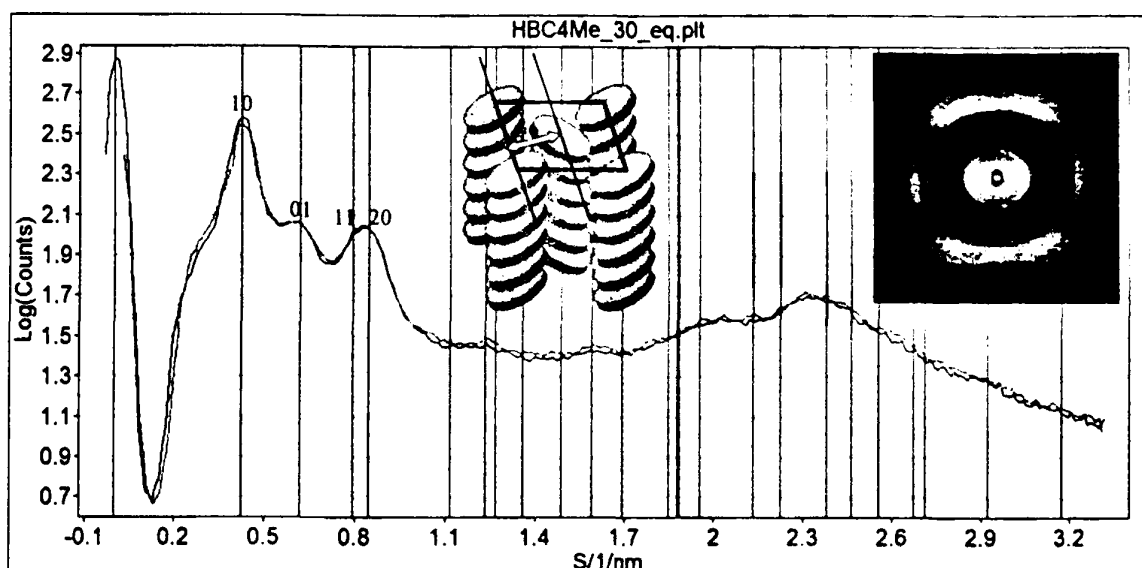
Figure 4-13: *WAXS equatorial reflections at 303 K for the dimethoxy HBC (obtained on heating). The equatorial reflections correspond to the (10), (01), (11) and (20) reflections which are characteristic of oblique columnar mesophase (Col$_{ob}$).*

Table 4.3. XRD data for the dimethoxy HBC at two different temperatures; one in the C$_r$ phase and the other in the Col$_h$ phase on heating.

T (K)	Phase	Lattice parameters (nm)	d$_{10}$ (nm)	d$_{intra}$ (nm)	Unit cell
303	C$_r$	a=2.39 b=1.64 γ=98°	2.37	0.44	Oblique
423	Col$_h$	a=2.68	2.32	0.36	Hexagonal

In addition to the above scattering experiments, NMR can also be employed to identify the type of columnar packing. Recently, the comparison of quantum chemical *ab* initio calculations with experimental ^{1}H solid-state NMR spectra allowed the assignment of the specific molecular packing [19,20]. This approach takes advantage of the marked sensitivity of the ^{1}H chemical shift to intermolecular interactions. ^{1}H magic-angle spinning (MAS) and ^{1}H-^{1}H two-dimensional double quantum (DQ) MAS NMR experiments were performed on the dimethoxy HBC within the C$_r$ and Col$_h$ phases. The ^{1}H-^{1}H DQ MAS spectrum (Figure 4-14) reveals a pattern characteristic of a tilted arrangement of HBC discs (i.e., with the "herringbone" structure [20]). Three aromatic resonances within the C$_r$ phase that could be explained by the different degrees to which the aromatic protons experience the ring current of adjacent layers are observed. These resonances merge into a single peak on heating to the Col$_h$ phase, where the aromatic protons in the planar disc arrangement experience identical average ring currents [20].
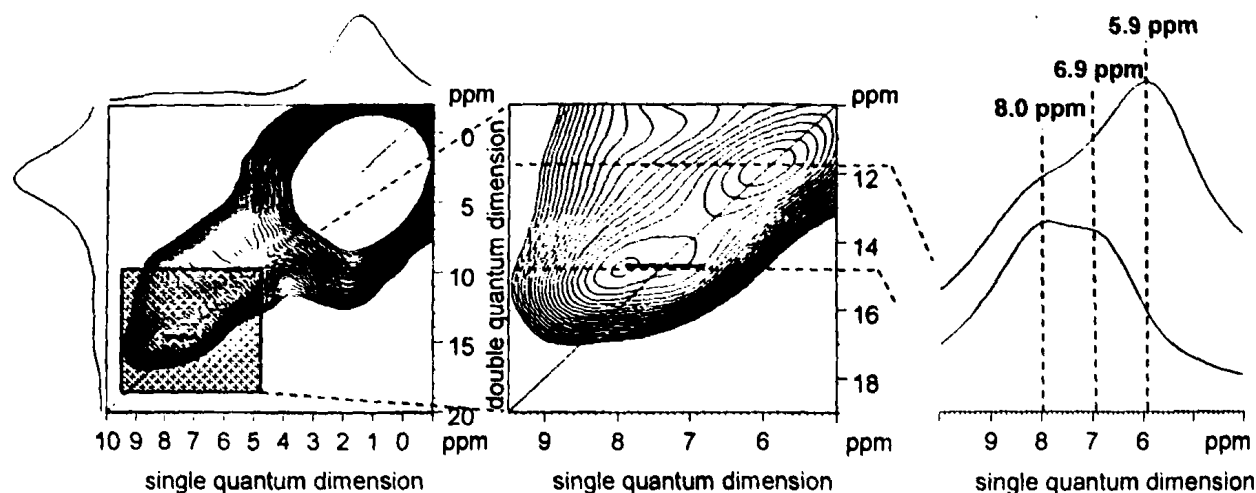
Figure 4-14: *(Left) Two-dimensional solid-state ^1H-^1H DQ MAS NMR spectrum of the dimethoxy HBC recorded at 310 K (effective sample temperature), 40 μs used to excite and reconvert the DQ coherences and 25 kHz MAS, (middle) the aromatic region magnified and (right) two one-dimensional slices at 11.8 and 14.9 ppm with the aromatic proton chemical shifts assigned.*

4.5.2 Molecular dynamics investigation

The analysis of the heteronuclear REREDOR NMR spinning sideband patterns provides site-specific information of the molecular mobility [9-11]. Different experiments were performed for the dimethoxy HBC derivative, corresponding to the C_r and Col_h phases. For quantitative analysis the recorded REREDOR spinning sideband patterns are compared with calculated ones for different dipole-dipole coupling constants. The fit has an estimated accuracy of 10%. The intensity of the center-band, being sensitive to multi-spin effects, is typically not included in the analysis. In the crystalline state (Figure 4-15), the measured ^1H-^{13}C dipole-dipole coupling constant for the aromatic CH pairs is *ca.* 19 kHz ($S = 0.90$) showing that the aromatic core is essentially rigid at 310 K. The slight reduction of the ^1H-^{13}C dipole-dipole coupling constant from the rigid state value (i.e., $S=1$) can be due to in-plane fluctuations as well as to out-of-plane disc excursions. On the contrary, the C12 alkyl chains retain significant mobility within the crystalline state. The effective dipole-dipole coupling constants measured for the chain CH_2 groups ($D = 8.5$ kHz, $S = 0.40$) and at the chain ends (D ~5.9 kHz, S ~0.28) clearly show that on average the C12 chains remain flexible and amorphous. Therefore within the crystalline phase, discs are not completely frozen but are able to perform small-angle motions whereas the alkyl chains retain significant mobility.

Figure 4-15: *REREDOR spinning sideband patterns for the dimethoxy HBC recorded at 25 kHz spinning at the magic angle, 80 µs recoupling time and 310 K effective sample temperature in the crystalline state (C_r), with the calculated patterns (in blue) superimposed. The derived ^1H-^{13}C dipole-dipole coupling constants for the respective CHn (n=1,2) moieties are presented together with the related local dynamics order parameters, respectively, for the HBC core S=0.90 (top, left), the alkyl chains S=0.40 and the more mobile chain ends S~0.28 (middle). The typical herringbone structure is also shown (top, right).*

In the Col_h mesophase, the ^1H-^{13}C dipole-dipole coupling constant for the aromatic CH moiety of the dimethoxy HBC first of all, is reduced by a factor of two due to the fast in-plane rotation of the discotic molecules similar to ^2H-NMR, where the same bond direction is probed [9,12,13,21-23]. Further reduction of the dynamic order parameter of the core CH segment ($S = 0.45$) is attributed to out-of-plane disc excursions. The mean angle (24°) of this motion (Figure 4-16) is determined by assuming that the local dynamic order parameter S, results from a Gaussian orientation distribution of displacement angles [14]. In the Col_h mesophase the alkyl chain dynamics exhibits a mobility gradient from the spatially most restricted C_α CH_2 group ($D = 6.0$ kHz, $S = 0.29$) to the more distant alkyl groups ($D = 3.0$ kHz, $S = 0.14$).
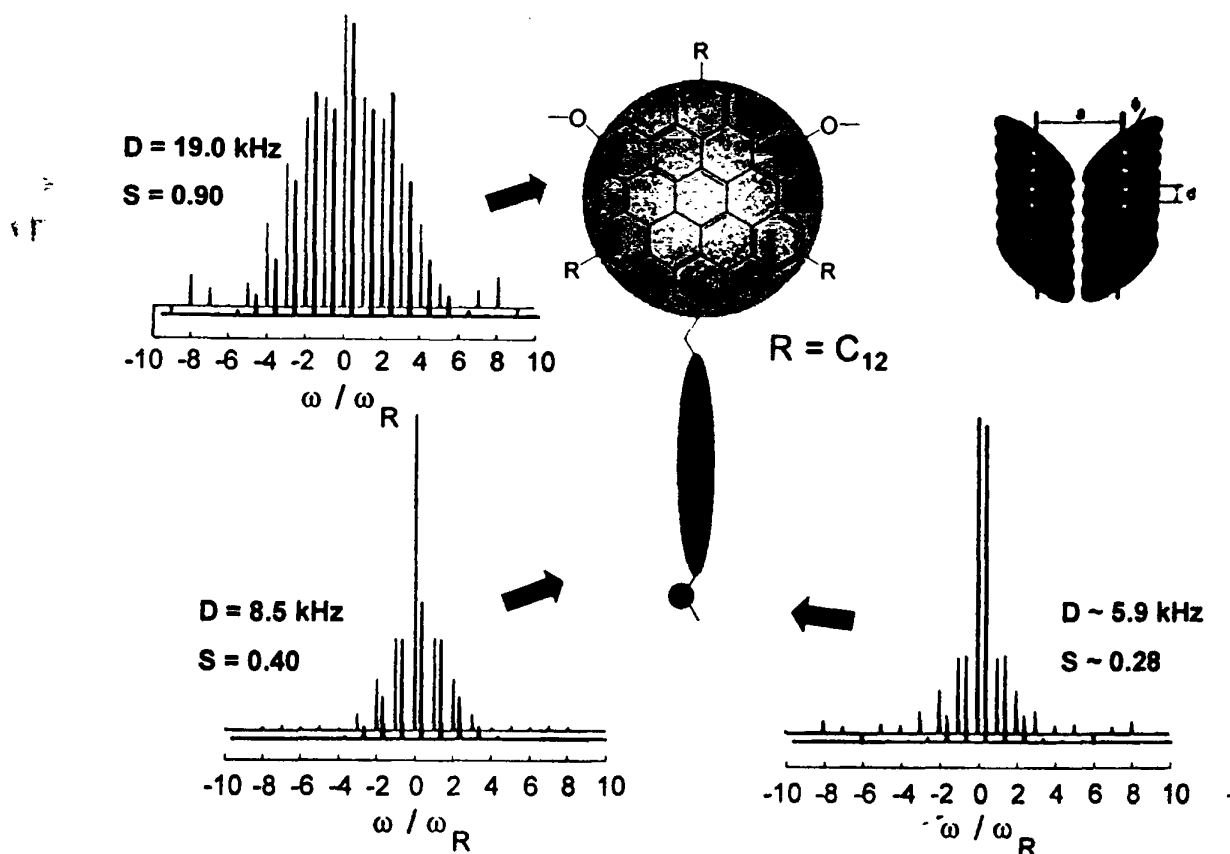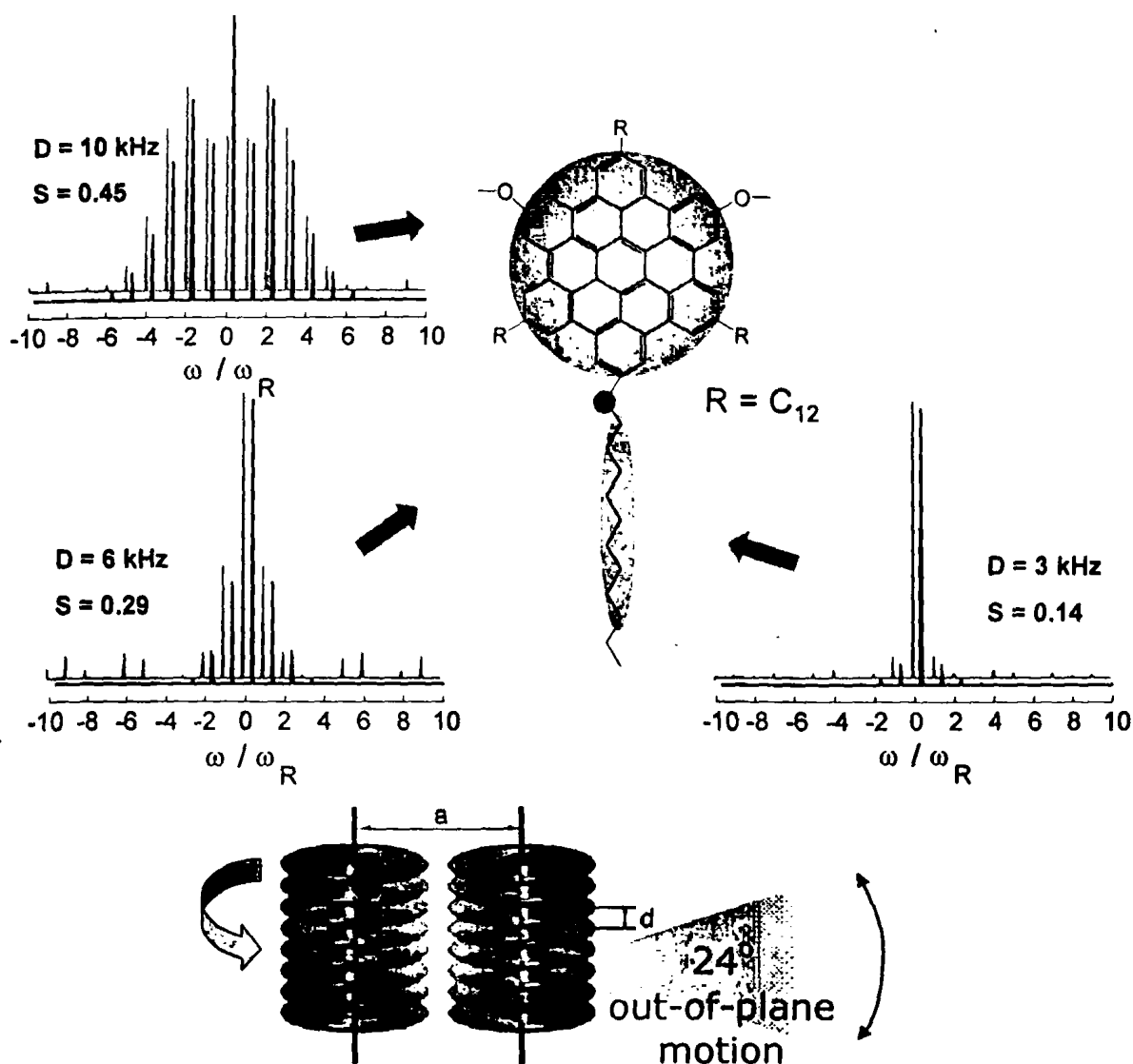
Figure 4-16: *REREDOR spinning sideband patterns for the dimethoxy HBC recorded at 25 kHz spinning at the magic angle, 160 μs recoupling time and 400 K effective sample temperature in the liquid-crystalline state (Col$_h$), with the calculated patterns (in blue) superimposed. The derived ^1H-^{13}C dipole-dipole coupling constants for the respective CHn (n=1,2) moieties are presented together with the related local dynamics order parameters S. Note that the aromatic core S-value is reduced to 0.45 suggesting both in-plane rotation and out-of-plane excursions, while the higher degree of motional freedom for the alkyl chains results in S values in the range of 0.29 to 0.14. The columnar disc organization within the Col$_h$ phase is shown in the bottom.*

In the dimethoxy HBC the dipoles are directly attached to the core, therefore the disc dynamics can be probed by Dielectric Spectroscopy and compared directly with the core dynamics obtained by NMR. Figure 4-17 depicts a series of dielectric loss curves measured at different temperatures, both below and above the transition, reflecting the in-plane disc rotation (α-process). The curves show increasing broadening and a reduction in the dielectric strength in going from the high temperature Col$_h$ phase to the C$_r$ phase. Note that the DSC

crystallization temperature (at 343 K) is substantially higher than the one assigned by DS (at 303 K; based on the broadening of the loss curves) reflecting a strong rate dependence of the critical temperature T_c. The Figure also depicts some faster process (β- process).
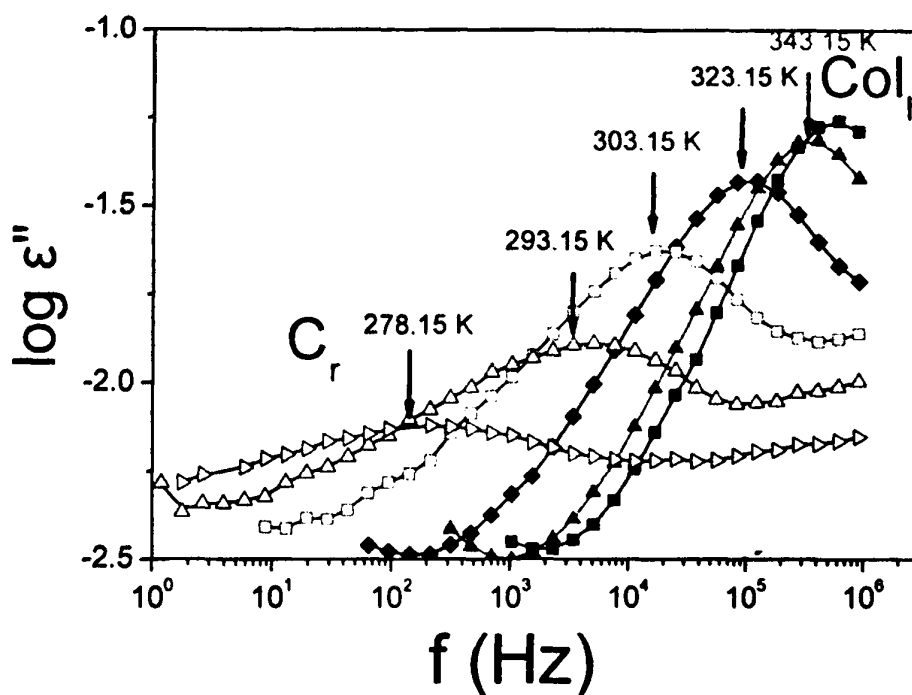
Figure 4-17: *Dielectric loss for the dimethoxy HBC obtained on cooling at 0.1 MPa, shown at different temperatures: (filled squares): 353.15 K, (filled up triangles): 343.15 K, (filled rhombus): 323.15 K, (open squares): 303.15 K, (open up triangles): 293.15 K and (open right triangles): 278.15 K. Notice the loss in dielectric strength and the broadening of the relaxation spectrum on entering the C_r phase. The spectrum at 343.15 K corresponds to the DSC exotherm and the one at 303.15 K is the critical temperature suggested by DS.*

The relaxation times of the different processes in the dimethoxy HBC are shown in Figure 4-18, in the usual Arrhenius representation. The low-temperature β-process has an Arrhenius $\tau(T)$ dependence (Eq. (4.1)) with a single activation energy $E=50\pm4$ kJ/mol and a $\tau_0=4\times10^{-14}$ s, characteristic of a local process associated with small amplitude vibrations (dielectric strength of only $T\Delta\varepsilon\sim7$ K) within the C_r phase. A broad distribution of relaxation times is evident by the values of the HN shape parameters ($\alpha=\alpha\gamma=0.3$). The mere presence of this process does not contradict the NMR result ($S=1$, within C_r) because averaging of the ^{13}C-^1H dipole-dipole couplings requires motions on the time scale below 10^{-5} s.

Two-dimensional exchange NMR, is able however, to unravel the geometry of motions on longer time-scales [12,14]. Based on the combined information from NMR (geometry of
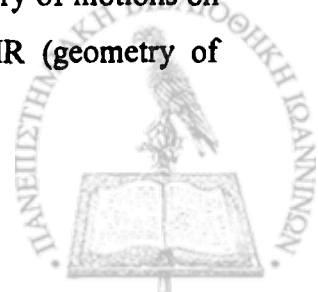
motion) and DS (rates of motion), the α-process reflects collective axial disc motions around the columnar axes.
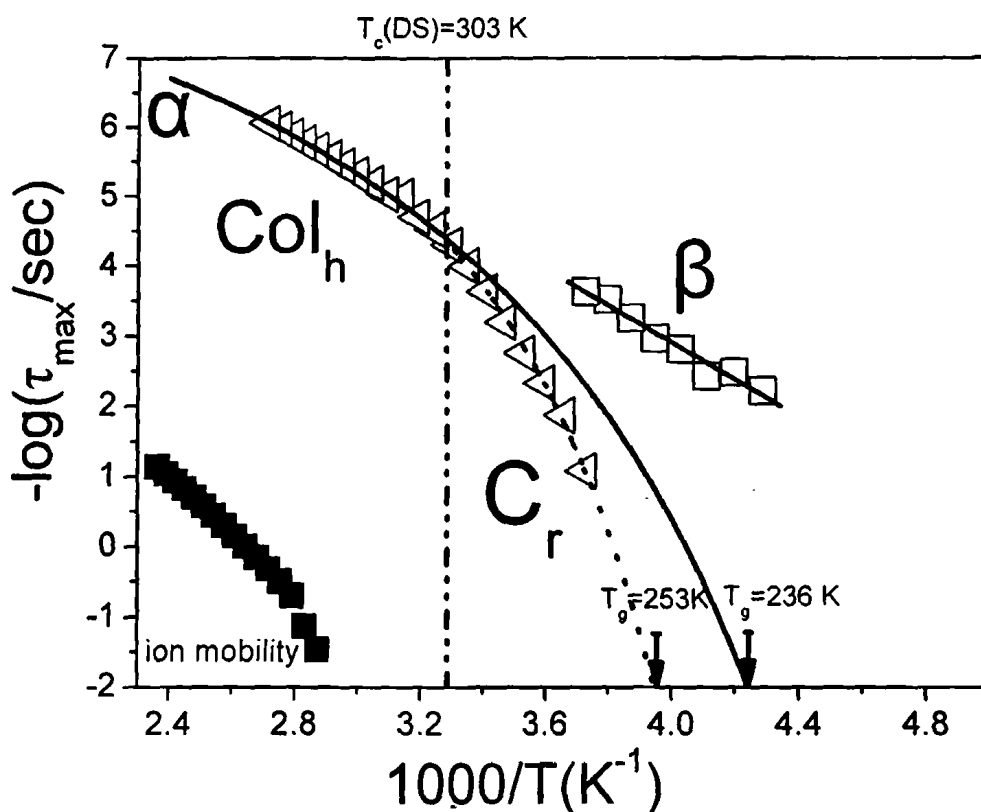
Figure 4-18: *Temperature dependence of the relaxation times (obtained on cooling) for all dielectrically active processes and of the ionic mobility in the dimethoxy HBC. (filled squares): ionic mobility, (open squares): β-process, (left triangles): α-process. Notice the change in the α-process dynamics in going from the high temperature Col_h to the C_r phase (vertical dashed-dotted line). Full and dotted lines extrapolate to the glass temperature (defined at $\tau \sim 10^2$ s) of the Col_h (hypothetical) and C_r phases, respectively.*

The α-process displays unique characteristics in going from the C_r to the Col_h phase. Within the Col_h phase, the $\tau(T)$ dependence can be described by the Vogel-Fulcher-Tammann (VFT) equation (see Eq. (3.3) of Chapter 3). The τ_0, B, T_0 and T_g (the glass temperature is identified as the temperature where the corresponding structural relaxation time is at 10^2 s) parameters assume the following values: 6×10^{-6} s (within the Col_h phase), 1345 ± 50 K, 185 ± 7 K and 236 ± 7 K, respectively. On entering the C_r phase, the α-process displays a steeper T-dependence with B, T_0 and T_g parameters assuming values of 1013 ± 2 K, 214 ± 4 K and 253 ± 4 K, respectively. Notice that the crystalline phase has a higher effective glass temperature (corresponding to the freezing of the axial disc rotation) as compared to the (hypothetical) T_g of the Col_h phase. The Figure contains also a process due to the ionic mobility extracted from the electric modulus

representation. This process is about 7 orders of magnitude slower from the α-process dynamics but bears a similar VFT temperature dependence. This suggests that the dynamics of ionic impurities, present in all HBCs, are affected by the disc rotational dynamics.

The HN shape parameters for the α-process are also sensitive indicators for the phase transformation (i.e., Figure 4-17). Figure 4-19 depicts the low- (α) and high- ($\alpha\gamma$) frequency slopes of the α-process as a function of temperature.
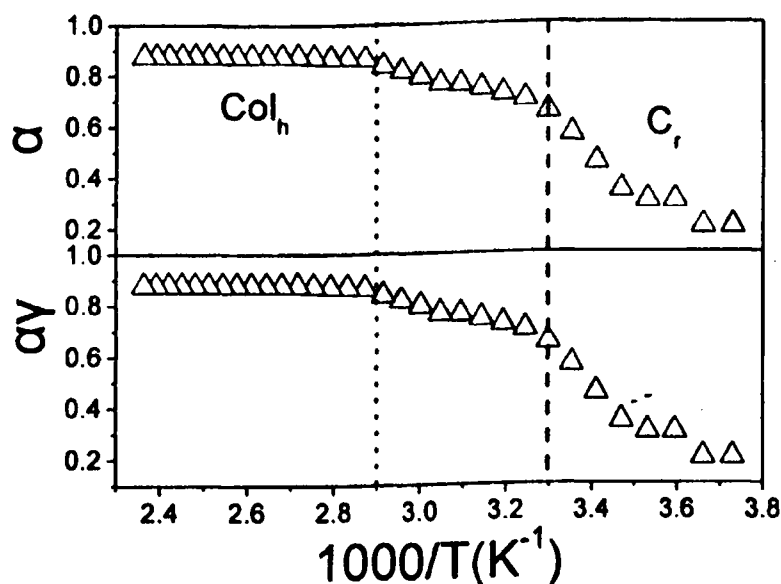
Figure 4-19: *Temperature dependence of the low- (α) and high- (αγ) frequency slopes characterizing the distribution of relaxation time spectrum of the α-process. Dotted and dashed lines give the critical temperatures of the Col$_h$ to C$_r$ transformation as seen from DSC and DS, respectively.*

The plot shows a narrow, albeit non-Debye process ($\alpha=\alpha\gamma=0.9$) within the Col$_h$ phase, and a much broader ($\alpha=\alpha\gamma\sim0.3$) distribution within the C$_r$ phase. Therefore, the axial disc motion within the crystalline state is a collective process characterized by a heterogeneous environment, which gives rise to the broad distribution of relaxation times [9]. The onset of the broadening coincides with the DSC transition on cooling, however the transition, as seen from DS (assigned to the temperature where the width of the α-process doubles its high T value), appears at even lower temperatures ($T_c^{DS}\sim303$ K), implying kinetic effects.

Applications of HBCs as advanced electronic materials require knowledge of the thermodynamic temperature and pressure boundaries (spinodals) and stability (and metastability) of the different phases. We aim at constructing the complete phase diagram (P-T) for the dimethoxy HBC that comprises different phases (Col$_h$, C$_r$, "glassy"). Hence, pressure is employed as the additional thermodynamic parameter. In these experiments, pressure is

applied isothermally at temperatures corresponding to the Col_h phase where the α-process is probed within the experimental window (Figure 4-20).
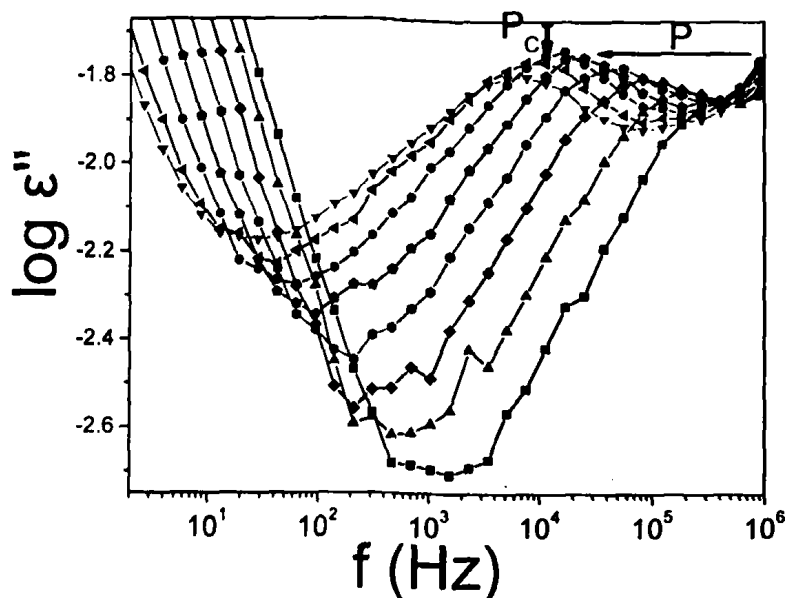
Figure 4-20: *Dielectric loss for the dimethoxy HBC at 343.15 K for different pressures: 1 MPa (■), 40 MPa (▲), 80 MPa (◆), 120 MPa (●), 160 MPa (◆), 200 MPa (●), 240 MPa (◄) and 260 MPa (▼). The vertical arrow gives the critical pressure (P_c) for the Col_h-C_r transformation.*

Increasing pressure first slows-down the α-process (as anticipated by densification), and subsequently induces the transformation to the C_r phase. The transformation is evident by the steeper $\tau(P)$ dependence within C_r, and from the increased broadening of the α-process (Figure 4-21). The low-frequency HN parameter is included in Figure 4-21 and depicts a dramatic pressure-induced broadening under isothermal conditions. Thus the critical pressure, P_c, required for the transformation, can be obtained either from the change in the $\tau(P)$ dependence or from the $\alpha(P)$ dependence and is depicted by the thick line (in Figure 4-21).

Under the assumption that the α-process is purely activated, the linear dependence of $\log \tau$ vs. P can be used to extract the apparent activation volume, ΔV, given by Eq. (4.2). According to this picture, ΔV represents the difference between the molar volumes of the initial and final (activated) states. Nevertheless, certain similarities of this quantity with the molecular volume were found in a series of studies [4, 24-31]. This quantity, within the Col_h and C_r phases, is plotted in Figure 4-22 as a function of temperature and reveals a higher apparent activation volume for the α-process within the C_r phase. This is also the case in crystallizing polymers [32-34] and suggests a more cooperative disc rotation within the C_r phase.
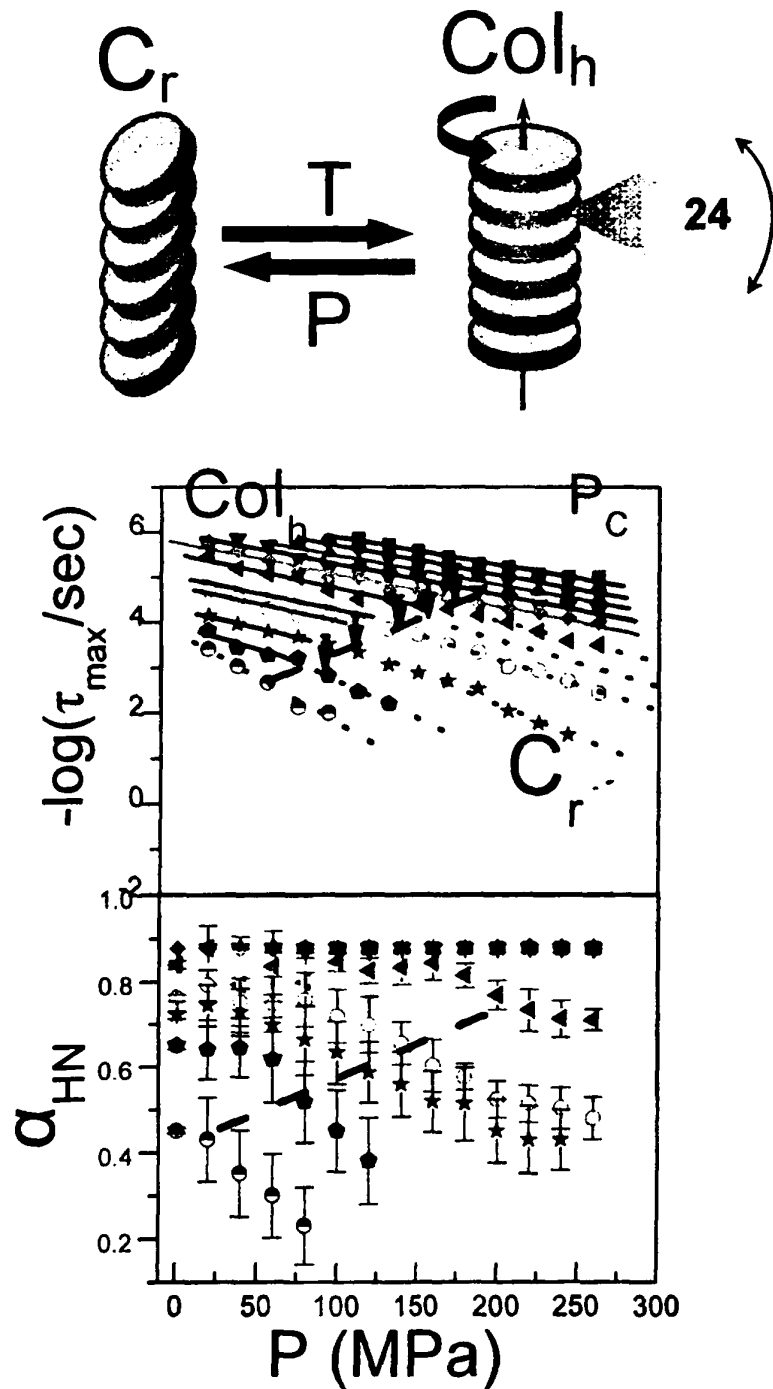
Figure 4-21: *(Top): Schematic of the transformations between the crystalline and columnar liquid crystal phases induced by temperature and pressure. (Middle): α-process relaxation times as a function of pressure for the following "isotherms": (filled squares): 393.15 K, (filled circles): 383.15 K, (filled up triangles): 373.15 K, (filled down triangles): 363.15 K, (filled rhombus): 353.15 K, (filled left triangles): 343.15 K, (filled right triangles): 333.15 K, (open circles) 323.15 K, (stars): 313.15 K, (filled polygons): 303.15 K and (half-filled circles): 293.15 K. Lines represent linear fits to the respective regimes. The dashed black line gives the critical pressure (P_c) for the Col_h - C_r transformation. (Bottom): HN low frequency parameter of the α-process as a function of pressure for the different isotherms (as above). The black dashed line gives again the critical pressure P_c.*
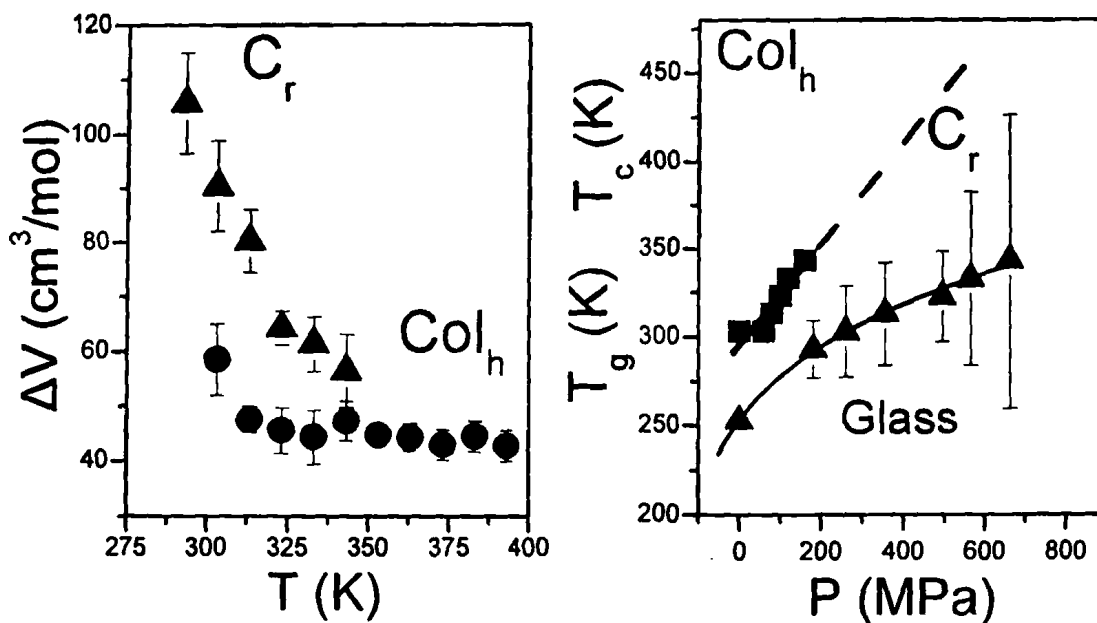
Figure 4-22: *(Left) Temperature dependence of the apparent activation volume corresponding to the crystalline (C_r) and columnar hexagonal liquid crystalline (Col_h) phases of the dimethoxy HBC. (Right): phase diagram for the dimethoxy HBC depicting the pressure dependence of the Col_h-C_r transition temperature (squares) and of the glass temperature (up triangles) the latter defined as the temperature where the α-relaxation times are at ~1 s. The lines represent fits to Eqs. (4.3) and (4.4), respectively.*

The apparent activation volume at 303 K (i.e., at T_g+50 K) within the crystalline phase is about half the molecular volume (250 cm^3/g obtained from X-rays [35]).

Based on the T- and P-investigations the phase diagram can be constructed for the dimethoxy HBC and is depicted in Figure 4-22. The Figure contains the pressure dependence of the glass temperature corresponding to the freezing of the disc axial motion within the crystalline phase and the pressure dependence of the critical temperature, T_c, for the Col_h to C_r transformation obtained from the data of Figure 4-21. The former can be described by the empirical Eq. (4.3), where $T_g(0)$=253 K, b and c are fitting parameters (b=6±1, c=810±90 MPa and $(dT/dP)_{P \to 0}$ = 0.3 K/MPa). The latter is described by Clausius-Clapeyron equation for 1st order transitions as [36]:

$$\frac{dP}{dT} = \frac{\Delta H_f}{T \Delta V} \tag{4.4}$$

where ΔH_f is the heat of fusion associated with the C_r to Col_h phase transformation, T is the transition temperature at atmospheric pressure and ΔV is the associated change of specific volume. From the slope of the $T(P)$ dependence, dP/dT=3.6 MPa/K, and the DSC heat of

fusion (54 J/g) the change of specific volume at the transition can be estimated. The thus estimated change of specific volume (0.047 cm^3/g) suggests a substantial volume reduction on entering the crystalline phase. These dependencies separate the *T-P* phase space in three regimes depicted as "glass", "C_r" and "Col_h". As a result of the stronger pressure dependence of the first order C_r to Col_h phase transformation, as opposed to the weaker $T_g(P)$, increasing pressure effectively stabilizes the C_r phase. For example, the crystalline phase can be stabilized to 450 K at 600 MPa, i.e., about 150 K above its atmospheric pressure limit. This stabilization of the crystalline phase to higher temperatures can have consequences in applications in view of the higher charge carrier mobility found in this phase.

The pressure coefficients of the transition temperature, dT/dP, for some calamitic and discotic liquid crystals in comparison with the present HBCs are compiled in Table 4.4.

Table 4.4. The dT/dP values for some calamitic and discotic liquid crystals in comparison with the present work.

Compound	Phase transition	dT/dP (K/MPa)	Used technique
dimethoxy HBC (present work)	$C_r \rightarrow Col_h$	0.278	High-pressure DS [7]
rufigallol-HOE	II→III III→II	0.042 0.175	High-pressure NMR [37]
benzene hexa-n-octanoate	$C_r \rightarrow$Mesophase Mesophase→I	0.086 0.068	High-pressure optical set-up [38]
p,p'-bis(heptyloxy)azoxybenzene	$C_r \rightarrow$SmC SmC→N N→I	0.167 0.117 0.233	High-pressure optical set-up [39]
cholesteryl myristate	$C_r \rightarrow$SmA SmA→C C→I	0.154 0.227 0.435	High-pressure optical set-up [40]

C_r: crystal - Col_h: columnar hexagonal - I and III: having the same columnar hexagonal packing
SmC: smectic C phase - SmA: smectic A phase - N: nematic phase - C: cholesteric phase
I: isotropic phase

4.5.3 Kinetics of phase transformation

In general, the two main mechanisms of structural evolution following a *T*- or *P*- jump from an initial state favoring phase I to a final state favoring phase II are spinodal decomposition and nucleation and growth. Below we discuss these two possibilities.

4.5.3.1 Spinodal decomposition versus nucleation and growth (NG)

Spinodal decomposition is a method by which a mixture of two or more materials can separate into distinct regions with different material concentrations [41]. This method differs
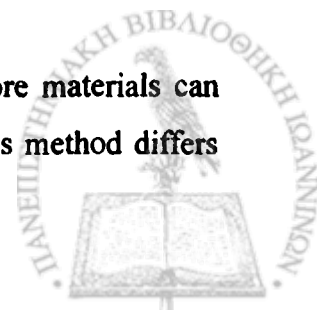
from nucleation and growth (NG), in that, phase separation occurs throughout the material, and not just at nucleation sites [42,43]. To observe spinodal decomposition, a very fast change of T or P, often called a quench, is required to move from the stable to the spinodally unstable region of the phase diagram (Figure 4-23) [44]. Although spinodal decomposition refers to the spontaneous formation of a phase separated state in two component systems, we could think of an analogous mechanism in the present case. Following a quench, the oblique phase is formed immediately (Figure 4-23) and at later times further adjustment of the disc spacing along the meridional direction gives rise to the C_r phase. We could define a pair-correlation function, $g(t)$, along the column axis that becomes more sharp with time.
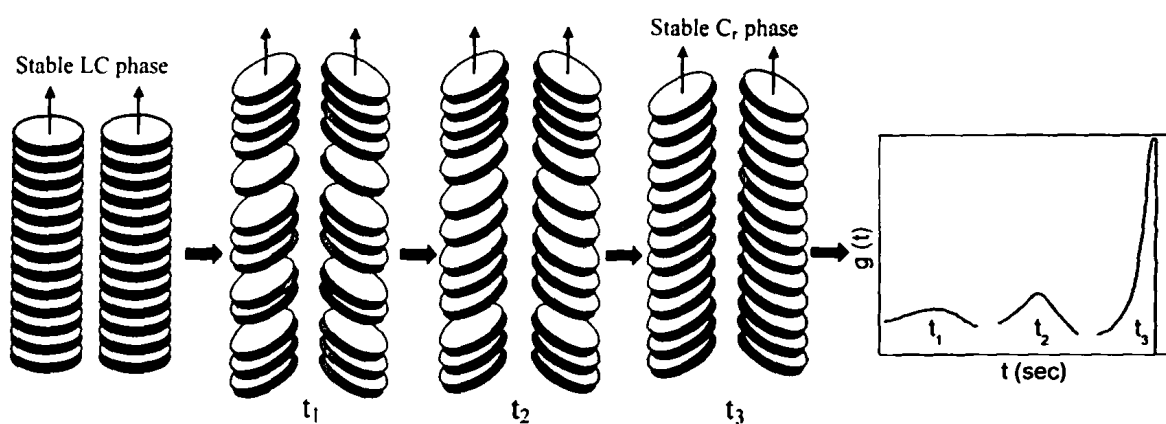
Figure 4-23: *Schematic illustration of a spinodal decomposition-like mechanism following a quench from the LC to the C_r phase. The graph gives the meridional disc pair correlation function for the different times t_1, t_2 and t_3.*

Figure 4-24 illustrates a nucleation and growth mechanism within the columnar mesophase. Nucleation of the oblique phase initiates at some initial time t_1 with concentration φ_{obl}, and then grows along the columnar axis, leading to the final C_r phase.
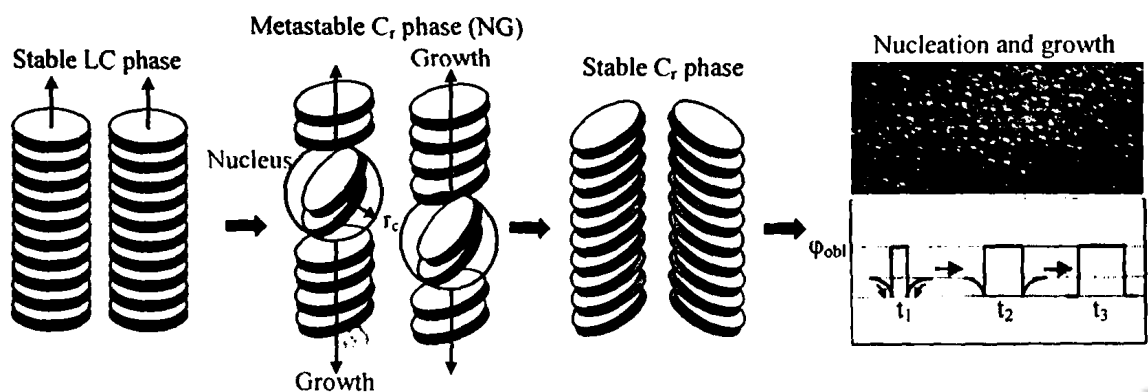
Figure 4-24: *Schematic illustration of the nucleation and growth (NG) mechanism following a quench from the LC to the C_r phase within the columnar mesophase.*

The latter mechanism (NG) requires crossing an energy barrier for the formation of a stable nucleus with a radius $r>r_c$, where r_c refers to the formation of a critical radius. The dependence of the change of free energy, ΔG, (ΔG is due to the formation of a nucleus of the newly evolving phase) on the nucleus radius r is shown in Figure 4-25.
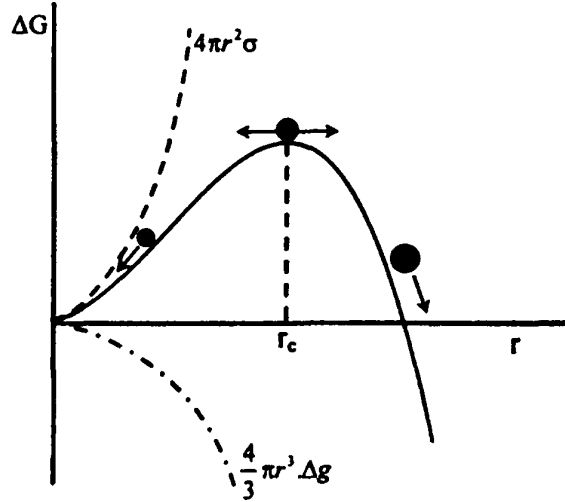
Figure 4-25: *Schematic illustration of the change of the ΔG in the course of formation of a nucleus of the new evolving phase. The variable state parameter of the nucleus (its size) are specified here by the radius, r.*

The increase in the ΔG is due to the positive contribution from the surface energies ($\sigma_i A_i$, where σ_i is the specific surface energy of surface i and A is the surface area) which, at temperatures below the equilibrium melting point, opposes the negative contribution from the crystallization free energy ($\Delta g V_{crystal}$, where Δg is the specific change in free energy and $V_{crystal}$ is the volume of the nucleus) [45]:

$$\Delta G = \Delta g V_{crystal} + \sum_i A_i \sigma_i \qquad (4.5)$$

For a spherical crystal, the change of free energy, ΔG, on crystallization is then given by:

$$\Delta G = \frac{4}{3}\pi r^3 \Delta g + 4\pi r^2 \sigma \qquad (4.6)$$

where r is the radius of the spherical crystal and σ is the specific free energy of the surface (the surface tension). The critical radius, r_c, (the radius of the sphere associated with the free energy barrier), can be obtained by setting the first derivative of ΔG with respect to r equal to zero [45]:

$$\frac{\partial \Delta G}{\partial r} = 4\pi r_c^2 \Delta g^* + 8\pi r_c \sigma = 0$$

$$r_c = -\frac{2\sigma}{\Delta g^*} \qquad (4.7)$$

For a nucleus with a radius $r<r_c$, the thermodynamic evolution criteria lead to the conclusion that the respective aggregates will dissolve as a rule, again. In contrast, a nucleus with a size $r>r_c$ will grow, in general, up to macroscopic dimensions.

4.5.3.2 The effect of pressure on inducing the $Col_h \rightarrow C_r$ transformation

The WAXS and POM investigations provided evidences for long-time Col_h-C_r coexistence on cooling from the Col_h phase. Important issues involved in phase transformation kinetics [46] include the existence of intermediate states, the identification of nucleation sites, and the presence of long-lived metastability. With respect to the nucleation sites, POM (Figure 4-10) revealed a lower nucleation density for the crystalline phase and the absence of any correlation between the nucleation sites of the two phases. In this section we explore the effect of pressure on inducing the Col_h-C_r transformation under "isothermal" conditions. Such pressure-jump experiments are more efficient than the corresponding temperature experiments since the application and equilibration of pressure is faster. Figure 4-26 gives the dielectric loss of the dimethoxy HBC at 313.15 K following a pressure jump from 0.1 to 110 MPa.
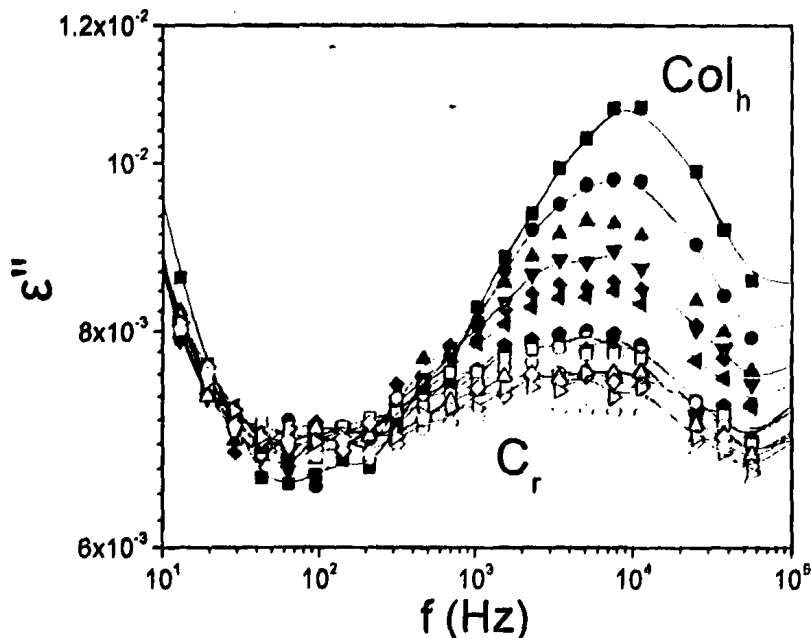
Figure 4-26: *Kinetics of the Col_h - C_r transition for the dimethoxy HBC at 313.15 K, following a pressure jump from 0.1 to 110 MPa. The different symbols correspond to different dielectric loss curves obtained at the following times: (filled squares): 64 s, (filled circles): 118 s, (filled up triangles): 240 s, (filled down triangles): 346 s, (filled rhombus): 459 s, (filled left triangles): 570 s, (filled polygon): 1102 s, (half-filled circle): 1214 s, (open square): 1335 s; (open circle): 1803 s; (open up triangle): 1988 s; (open rhombus): 2433 s; (open right triangle): 3065 s; (open polygon): 4397 s. Notice the long time required for the transformation at this pressure.*

The Figure depicts the evolution of the α-process associated with the disc axial motion during the Col$_h$-C$_r$ phase transformation. During the phase transformation the α-process broadens and looses dielectric strength reflecting the restricted amplitude of the in-plane and out-of-plane angular excursions within the crystalline phase (from S=0.45 to S=0.9). Note that the complete phase transformation requires several hours at this pressure. To explore the phase transformation kinetics, different pressure jumps have been performed starting from 0.1 MPa to different final pressures of 80, 110 160 and 200 MPa at 313.15 K. In all cases the evolution of the integrated intensity can be represented by the well-known Kohlrausch-Williams-Watts (KWW) equation [47]

$$\int \varepsilon'' df = A \exp\left[-\left(\frac{t - t_0}{\tau^*} \right)^\beta \right] + d \qquad (4.8)$$

where A is the amplitude, t_0 is an initial time required for temperature equilibration following the pressure jump, τ^* is the characteristic time associated with the Col$_h$ to C$_r$ transformation, β is the KWW exponent and d is a constant. The evolution of the integrated intensity is shown in Figure 4-27 for the different final pressures (P_f).

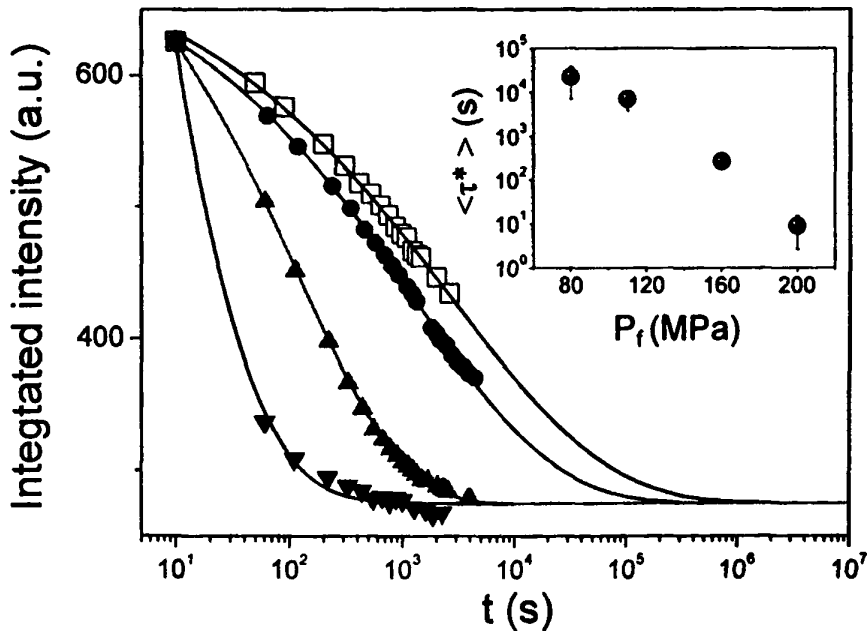**Figure 4-27:** *Evolution of the normalized integrated intensity of the α-process at 313.15 K following pressure jumps from 0.1 MPa to different final pressures: 80 MPa (open squares), 110 MPa (filled circles), 160 MPa (up triangles) and 200 MPa (down triangles). The lines are fits to Eq. (4.8). In the inset the average relaxation times are plotted as a function of final pressure (P_f).*

The average characteristic times associated with the phase transformation ($<\tau^*>=(\tau^*//\beta)\Gamma(1//\beta)$, where Γ is the gamma function) are shown in the inset and reveal that the deeper the pressure jump the faster the transformation to the C_r phase [33]. This was anticipated in crossing the Col_h-C_r spinodal, since the driving force for nucleating the new phase is expected to scale with the dimensionless parameter $\delta\sim(P\text{-}P_c)/P_c$, where P_c is the critical pressure (~60 MPa at 313.15 K). Furthermore, according to a simple nucleation and growth theory, the nucleation barrier $\Delta F/k_B T$ should scale as δ^{-2} (δ^{-1}) for homogeneous (heterogeneous) nucleation. What was not anticipated, however, is the stretched exponential relaxation (β=0.31, 0.34, 0.46 and 0.3 for final pressures of 80, 110, 160 and 200 MPa) typical for melt relaxation dynamics. Typical nucleation and growth, proceeds via the well-known Avrami equation [48], i.e., similar to Eq. (4.8), but with exponent $\beta \geq 1$ that characterizes the type of nucleation process and the dimensionality of growth (herein the expected value of β was 1 or 2 based on one-dimensional growth from athermal or thermal nuclei, respectively). In addition, a linear dependence of $\ln\tau$ vs. δ^{-2} or δ^{-1} could not be obtained (Figure 4-28).
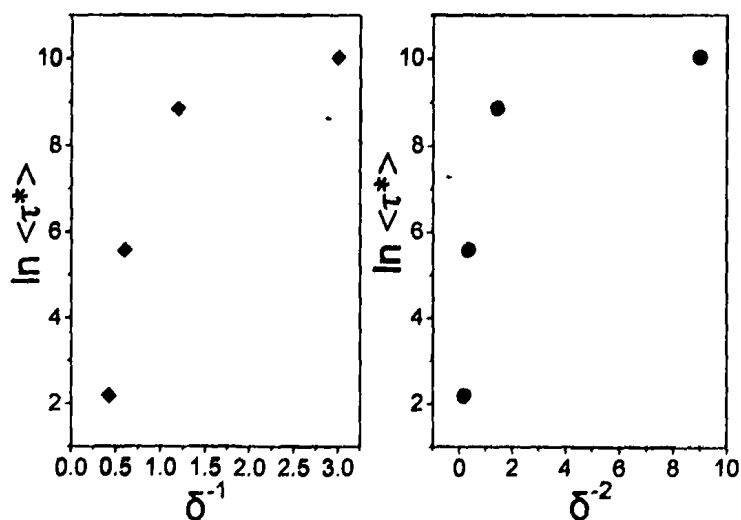
Figure 4-28: *The average characteristic time associated with the phase transformation versus the dimensionless parameter δ for two cases: (i) heterogeneous (δ^{-1}) and (ii) homogeneous nucleation (δ^{-2}).*

These deviations from typical nucleation and growth kinetics need to be explored in more detail, both by DS and NMR, and may reflect a more complicated scenario (e.g., fractal type process). Nevertheless, these experiments reveal slow kinetics of phase transformation that could be important in the design of HBCs for particular applications. For example, a metastable crystalline phase can be induced for several hours by suitable pressure (or temperature) variations.

4.6 Comparison of the structure and the α-dynamics for the four dipole functionalized HBCs

4.6.1 Comparison of the structure

The main effect of dipole substitution is to destabilize the C_r phase: in the HBCs bearing the stronger dipoles ($\mu_{mono\text{-}cyano}$=4.55 D, $\mu_{mono\text{-}bromo}$=1.62 D) the C_r phase is completely unstable whereas in the HBCs with the weaker dipoles ($\mu_{dimethoxy}$=0.64 D, $\mu_{mono\text{-}ethynyl}$=0.25 D) the C_r phase appears at low temperatures. These results on the dipole functionalized HBCs are in agreement with earlier studies on HBCs [5,35] and triphenylene [49-52] discotic liquid crystals. For example, mono-substituted triphenylenes with similar polar functionalities exhibited increased stability of the liquid crystalline mesophase [49]; the C_r phase was destabilized and the range corresponding to the liquid crystalline phase was increased by some 122 K. Another study [52] explored the effect of electron-withdrawing and electron-donating groups. It was found that the former had greater propensity of forming columnar phases as compared to the latter that were essential non-mesogenic. The type of side-chains (linear vs. branched) may also affect the width of the C_r and Col_h phases [5]. There are two earlier studies on bromo-functionalized HBCs in the ortho and para positions bearing either linear [35] or branched [5] chains. In both cases, i.e., independent of the type of alkyl side chain, the effect of dipole substitution in the ortho position was to shift the C_r to Col_h transition to lower temperatures. In the case of para-substitution, the net dipole is zero and thus the transition temperature was unaffected. This suggests that when comparing the effects of dipole substitution and type of alkyl chains it is the former that exerts the stronger influence on the phase state of the HBC compounds investigated herein. In conclusion, NMR and WAXS experiments allowed the complete identification of the two columnar phases; columnar hexagonal liquid crystalline (Col_h) and crystalline (C_r) phases at higher and lower temperatures respectively.

4.6.2 Comparison of the α-dynamics

In Figure 4-29, the axial disc dynamics (comprising both in- and out-of plane motions) are compared for the four dipole functionalized HBCs. Within the Col_h phase, the $\tau(T)$ dependencies are nearly indistinguishable. In addition, there is no remarkable change in the distribution of relaxation times, reflecting that the phase state (Col_h) largely controls both the $\tau(T)$ and the distribution of relaxation times.
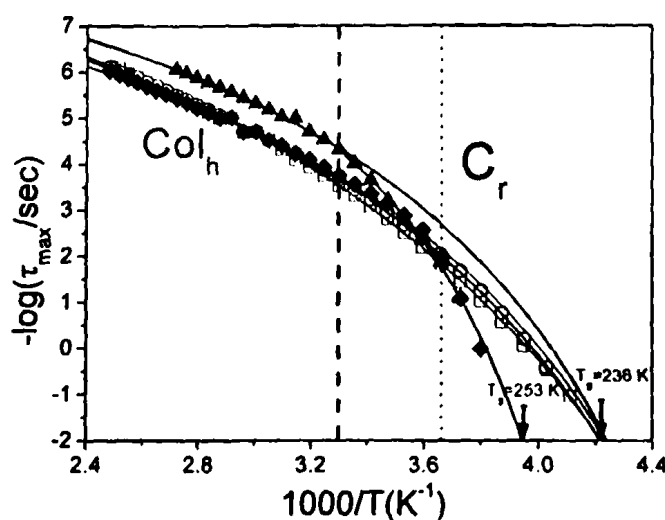
Figure 4-29: *Comparison of the α-process relaxation times for the different dipole functionalized discotics: (open squares): mono-cyano HBC, (open circles): mono-bromo HBC, (filled rhombus): mono-ethynyl HBC, and (filled up triangles): dimethoxy HBC. Notice the similarity in the $\tau(T)$ dependence within the Col_h phase and the steeper $\tau(T)$ within the C_r phase for the dimethoxy- (thick vertical line) and mono-ethynyl HBC (dotted vertical line).*

From the VFT dependence of the α-process, the glass temperature assume similar values for the three HBCs, in the range 235-237 K. The nearly indistinguishable $\tau(T)$ dependencies for the three samples within the same phase (Col_h) suggest that the time-scale of the collective axial disc motion depends on T, P and only weakly on alkyl chain branching. On the other hand, for the dimethoxy- and mono-ethynyl HBCs undergoing a transition to the crystalline state, the temperature dependence $\tau(T)$ becomes much stronger on entering the C_r phase. This again suggests that the dynamics are controlled - to a large extend - by the thermodynamic state. Last, we mention that a slower than the α-process has been identified in the same dipole functionalized HBCs bearing the stronger dipoles (mono-cyano and mono-bromo). The origin of this slower process has been assigned to collective re-organization of the columns, necessary to completely relax the dipole moment and pertinent, e.g., to the alignment of the columns on surfaces [9].

4.7 Summary

The self-assembly and the disc dynamics within the columnar phases were studied in a series of dipole-functionalized HBCs. The effect of functionalization with strong dipoles is to destabilize the columnar crystalline phase (C_r). On the other hand, substitution by weaker dipoles (dimethoxy- and mono-ethynyl HBCs) gives rise to the crystalline phase on cooling.

The disc dynamics and geometry of motion were studied by dielectric spectroscopy and site-specific NMR techniques. It was shown that the strongly temperature dependent α-process reflects the collective axial disc rotational dynamics. The glass temperature, associated with the freezing of the collective axial disc motion, was around 236 K for the discotics within the liquid crystalline phase and at 253 K for the dimethoxy-functionalized HBC within the crystalline phase. Hence, the phase state controls the dynamic response. The relaxation times and breadth of the α-process have distinctly different temperature- and pressure- dependencies on entering the crystalline state. These features enabled the construction of the complete phase diagram (T-P) for the dimethoxy functionalized HBC. The main outcome from this study is the increased stability of the crystalline phase at elevated pressures. As a result, this phase is stabilized up to 450 K when pressurized to 600 MPa, with possible consequences with respect to charge carrier mobilities.

The transformation of the Col_h to the C_r phase, studied by pressure jumps, revealed long-lived metastability and fractional exponents that strongly depend on the quench depth. These results on the slow Col_h to C_r transformation and the stabilized C_r phase at elevated pressures suggest new thermodynamic and kinetic pathways of stabilizing the phase with the high charge carrier mobility.

4.8 References

[1] Pisula, W.; Menon, A.; Stepputat, M.; Lieberwirth, I.; Kolb, U.; Tracz, A.; Sirringhaus, H.; Pakula, T.; Müllen, K. *Adv. Mater.* **17**, 684 (2005).

[2] van de Craats, A. M.; Warman, J. M.; Fechtenkötter, A.; Brand, J. D.; Harbison, M.A. and Müllen, K. *Adv. Mater.* **11**, 1469 (1999).

[3] Demus, D.; Goodby, J.; Gray, G. W.; Spiess, H. W.; Vill, V., *Handbook of Liquid Crystals, Vol. 2B: Low Molecular Weight Liquid Crystals II,* Wiley-VCH, (1998).

[4] Floudas, G. *Progr. Polym. Sci.* **29**, 1143 (2004)..

[5] Fechtenkötter, A. ; Tchebotareva, N. ; Watson, M.; Müllen, K. *Tetrahedron* **57**, 3769 (2001).

[6] Dou, X.; Yang, X.; Bodwell, G.J. ; Wagner, M.; Enkelmann, V.; Müllen, K. *Org. Lett.* **9**, 2485 (2007).

[7] Elmahdy, M. M.; Dou, X.; Mondeshki, M.; Floudas, G.; Butt, H. J.; Spiess, H.W.; Müllen, K. *J. Am. Chem. Soc.* (in press, web release March 7, 2008).

[8] Glüsen, B.; Kettner, A.; Kopitzke, J.; Wendorff, J. H. *J. Non-Cryst. Solids* **241**, 113 (1998).
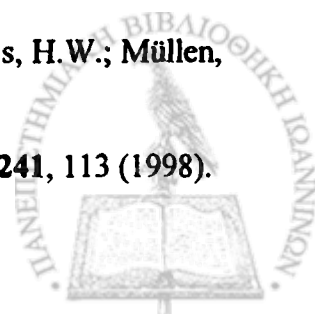
[9] Elmahdy M. M.; Floudas, G.; Mondeshki, M. ; Spiess, H. W.; Dou, X.; Müllen, K. *Phys. Rev. Lett.* (in press, issue March 17, 2008).

[10] Saalwächter, K.; Schnell, I. *Solid State Nucl. Magn. Res.* **22**, 154 (2002).

[11] Saalwachter, K.; Spiess, H.W. *J. Phys. Chem.* **114**, 5707 (2001).

[12] Leisen, J.; Werthg, M.; Boeffel, C.; Spiess, H.W. *J. Chem. Phys.* **97**, 3749 (1992).

[13] Herwig, P.; Kayser, C.W.; Müllen, K.; Spiess, H.W. *Adv. Mater.* **8**, 510 (1996).

[14] Schmidt-Rohr, K.; Spiess, H.W., *Multidimensional Solid State NMR and Polymer*, Academic Press, New York, (1994).

[15] Schmidt-Rohr, K.; Spiess, H.W. *Phys. Rev. Lett.* **66**, 3020 (1991).

[16] Tracht, U.; Wilhelm, M.; Heuer, A.; Feng, H.; Schmidt-Rohr, K.; Spiess, H.W. *Phys. Rev. Lett.* **81**, 2727 (1998).

[17] Kumar, S. *Chem. Soc. Rev.* **35**, 83 (2006).

[18] Laschat, S.; Baro, A.; Steinke, N.; Giesselmann, F.; Hägele, C.; Scalia, G.; Judele, R.; Kapàstina, E.; Sauer, S.; Schreivogel, A.; Tosoni, M. *Angew. Chem. Int. Ed.* **46**, 4832 (2007).

[19] Ochsenfeld, C.; Brown, S. P.; Schnell, I.; Gauss, J.; Spiess, H. W. *J. Am. Chem. Soc.* **123**, 2597 (2001).

[20] Brown, S.; Schnell, I.; Brand, J., D.; Müllen, K.; Spiess, H. W., *J. Am. Chem. Soc.* **121**, 6712 (1999).

[21] Fischbach, I.; Pakula, T.; Minken, P.; Fechtenkötter, A.; Müllen, K.; Spiess, H. W. Saalwächter, K. *J. Phys. Chem. B* **106**, 6408 (2002).

[22] Vallerien, S. U.; Werth, M.; Kremer, F.; Spiess, H. W. *Liq. Cryst.* **8**, 889 (1990).

[23] Werth, M.; Vallerien, S. U.; Spiess, H. W. *Liq. Cryst.* **10**, 759 (1991).

[24] Mpoukouvalas, K.; Floudas, G. *Macromolecules*, **41**, 1552 (2008).

[25] Mpoukouvalas, M. ; Gomopoulos, N. ; Floudas, G. ; Herrmann, K. ; Hanewald, A. ; Best, A. *Polymer* **47**, 7170 (2006).

[26] Mpoukouvalas, K ; Floudas, G.; Verdonck, B.; Du Prez, F. E. *Phys. Rev. E* **72**, 011802 (2005).

[27] Floudas, G.; Reisinger, T. *J. Chem. Phys.* **111**, 5201 (1999).

[28] Floudas, G.; Cravalides, C.; Reisinger, T.; Wegner, G. *J. Chem. Phys.* **111**, 9847 (1999).

[29] Gitsas, A.; Floudas, G.; Wegner, G. *Phys. Rev. E* **69**, 041802 (2004).

[30] Mpoukouvalas, M.; Floudas, G.; Zhang, S. H.; Runt, J. *Macromolecules* **38**, 552 (2005).

[31] Papadopoulos, P.; Floudas, G.; Schnell, I.; Klok, H. A.; Aliferis, T.; Iatrou, H. ; Hadjichristidis, N. *J. Chem. Phys.* **122**, 224906 (2005).

[32] Mierzwa, M.; Floudas, G.; Wegner, G. *Dielectrics Newsletters* (2000).

[33] Mierzwa, M.; Floudas, G. *IEEE Transactions on Dielectrics and Electrical Insulation* **8**, 359 (2001).

[34] Mierzwa, M.; Floudas, G.; Štepánek, P.; Wegner, G. *Phys. Rev. B* **62**, 14012 (2000).

[35] Ito, S.; Wehmeier, M.; Brand, J.D.; Kübel, C.; Epsch, R.; Rabe, J.R.; Müllen, K. *Chem. Eur. J.* **6**, 4327 (2000).

[36] McKenna, G. B. in *Polymer Properties, Vol. 2 of Comprehensive Polymer Science*, edited by C. Booth and C. Price, Pergamon, Oxford, (1989).

[37] Hollander, A.; Hommels, J.; Prins, K.O.; Spiess, H.W.; Werth, M. *J. Phys. II France* **6**, 1727 (1996).

[38] Chandrasekhar, S.; Sadashiva, B. K.; Suresh, K. A.; Madhusudana, N. V.; Kumar, S.; Shashidhar, R.; Venkatesh, G. *J. Phys. Colloques*, **40**, C3-120 (1979).

[39] Kelker, H.; Hatz, R., *Handbook of Liquid Crystals*, Verlag Chemie GmbH, D-6940 Weinheim, (1980).

[40] Shashidhar, R. *Mol. Cryst. Liq. Cryst.* **43**, 71 (1977).

[41] Schmelzer, J.W.P *Mater. Phys. Mech.* **6**, 21 (2003).

[42] Langer, J. S.; Bar-on, M.; Miller, H. D. *Phys. Rev. A* **11**, 1417 (1975).

[43] Binder, K. in *Materials Science and Technology: A comprehensive treatment: Phase Transformations in Materials*, edited by P. Haasen, Vol. 5, Weinheim: VCH Verlag, (1990).

[44] Jones, R. A. L., *Soft Condensed Matter*, Oxford University Press, Oxford, (2002).

[45] Gedde, U. W., *Polymer Physics,* Chapman & Hall, London, (1995).

[46] Hadjichristidis, N.; Pispas, S.; Floudas, G., *Block Copolymers: Synthetic Strategies, Physical Properties and Applications*, Wiley & Sons Inc., Hoboken, NJ, (2002).

[47] *Broadband Dielectric Spectroscopy*; Kremer, F.; Schönhals, A. Eds.; Springer: Berlin, (2002).

[48] Avrami, M. J. *J. Chem. Phys.* **7**, 1103 (1939) ; **8**, 212 (1940); **9**, 177 (1941).

[49] Rego, J. A.; Kumar, S.; Ringsdorf, H. *Chem. Mater.* **8**, 1402 (1996).

[50] Boden, N.; Bushby, R. J.; Cammidge, A. N.; Duckworth, S.; Headdock, G. J. *Mater. Chem.* **7**, 601 (1997).

[51] Boden, N.; Bushby, R. J.; Lu, Z. B.; Cammidge, A. N. *Liq. Cryst.* **26**, 495 (1999).

[52] Foster, E. J.; Jones, R. B.; Lavigueur, C.; Williams, V. E. *J. Am. Chem. Soc.* **128**, 8569 (2006).

Chapter 5

Self-assembly and Dynamics of Calamitic Liquid Crystals:
The Oligoindenofluorenes Case

5.1 Introduction

In the past decades an enormous research as well as commercial interest has focused on the new field of conjugated organic electronics materials [1-5]. This interest, which was rejuvenated thanks to the Nobel Prize in chemistry (Shirakawa, MacDiarmid and Heeger [6-8]), is due to the fact that conjugated organic materials are able to transport charges, i.e., they can be conductors or semiconductors [9-11]. In this context these materials are often described as synthetic metals [12]. On the other hand these materials are organic molecules or polymers and thus offer unique processability [13]. Owing to their mechanical stability these materials can even be deposited on flexible substrates. These features provide the possibility of producing "plastic organic electronics" at very low costs [7,12]. Potential applications for polymeric materials include fully printed polymer field effect transistors (PFETs) [14,15], conjugated polymer photovoltaic cells [16], organic light emitting diodes (OLED) [17] and lasers [18] as well as polymer sensors, actuators, batteries and components for fuel cells [19]. Low molecular weight compounds can be used in vapour-deposited thin-film transistors [20], and as charge transporting or emitting molecular glasses in OLEDs [21], photovoltaic cells, photo copiers and laser printers [22]. Moreover, small conjugated molecules or oligomers can be designed in order to mimic the functionality of single electronic units like transistors, diodes, resistors and switches on a molecular scale [23]. It is thus possible to further reduce the dimensions of these electronic components to the nanometre level.

As mentioned above, óhe key application for conducting polymers, oligomers and conjugated small molecules is their use in OLEDs. Such light emitting devices, with poly(para-phenylenevinylene) (PPV) as the emissive material, have first been described in 1990 by Friend et al. [17] and are of the general structure depicted in Figure 5-1a.
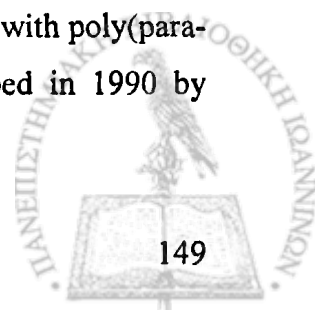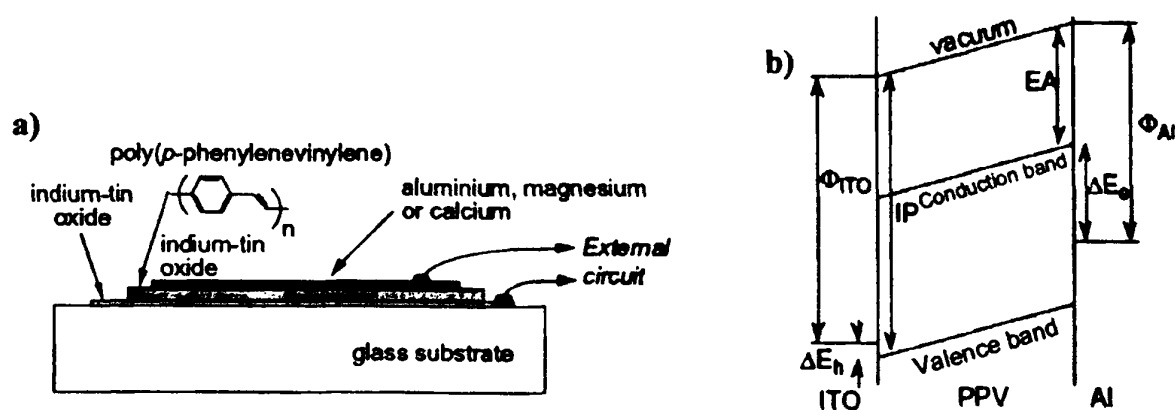
Figure 5-1: *Structure and schematic energy-level diagram of a single-layer polymer electroluminescent diode by Friend. a) Device structure. b) Schematic energy level diagram for an ITO/PPV/Al LED, showing the ionization potential (IP) and electron affinity (EA) of PPV, the work functions of ITO and Al (Φ_{ITO} and Φ_{Al}), and the barriers to injection of electrons and holes (ΔE_e and ΔE_h). There is a small barrier for hole injection from the ITO electrode into the valence band states, and, with aluminium as cathode, a considerably larger barrier for electron injection into the PPV conduction band states. After ref. [4].*

A simple one-layer OLED consists of an emitter material which is sandwiched between a transparent bottom electrode (anode) and a metal electrode (cathode) on top. Usually an indium tin oxide (ITO) coated glass substrate serves as a transparent anode for hole-injection (ITO has a relatively high work function and is therefore suitable for use as hole-injecting electrodes) whereas the cathode normally consists of metals with low work functions (Al, Mg, Ca). The emitter material can either be a polymer like PPV [4], polyfluorene (PF) [10,24], polyindenofluorenes (PIFs) [25-27] or a low molecular weight compound such as tris(8-hydroxyquinolinato)-aluminium (Alq_3) [4] (Figure 5-2).
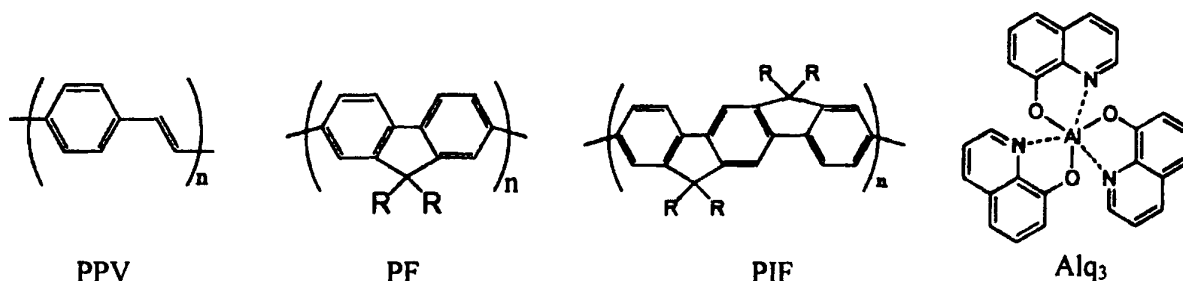
Figure 5-2: *The chemical structure of some organic light emitting materials used in the OLEDS.*

If an external field is applied between the two electrodes, positive (holes) and negative (electrons) charges are injected at the anode and cathode, respectively (Figure 5-3). These charges recombine within the emission layer by formation of localized excited states (excitons) which can then decay radiatively [4]. During the charge-recombination process, the spin
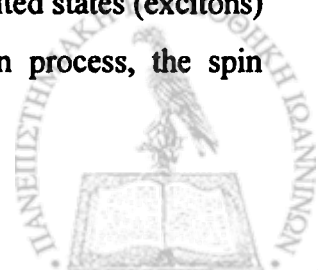
directions of the electrons involved can orient themselves into four possible combinations, each with an equal probability.

These orientations form excitons in two different patterns. The first pattern, known as a "singlet", can have only one of the four possible combinations. The other, known as a "triplet", can have three different combinations. For example, in the case of butadiene, as represented in Figure 5-4, the two lowest molecular orbitals, π_1 and π_2, contain four electrons [1]. The ground state is a singlet state because the electrons are of the opposite spin on each orbital.
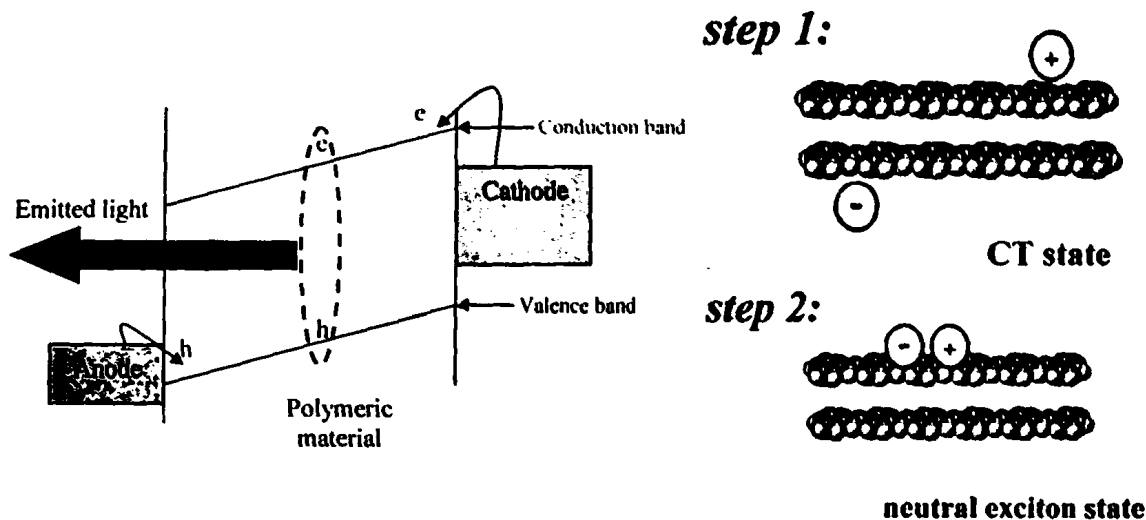
Figure 5-3: *(Left) Light-emission process in OLEDs. (Right) Two-step charge recombination process begins when two initially separated charges combine to form a loosely-bound charge-transfer (CT) state. That then decays down to a lower singlet or triplet neutral exciton state. Modified after ref. [1].*

An excited state is obtained when an electron jumps from the π_2 orbital to the higher energy antibonding orbital π_3^*. During that transition, the electron can keep the same spin orientation as in the ground state and a singlet excited state is obtained. It can undergo a spin flip, the excited state being then a triplet state.
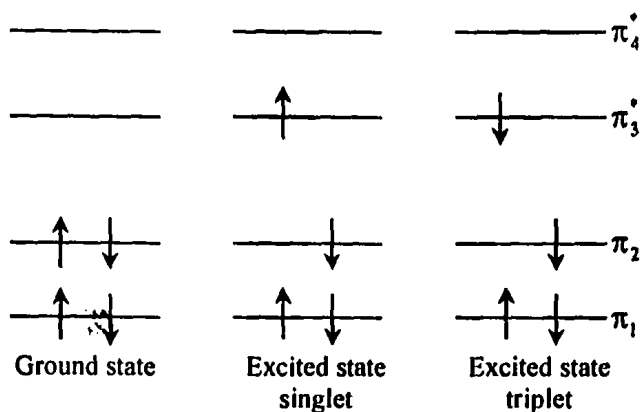
Figure 5-4: *Energy diagram of the molecular orbital for butadiene. After ref. [1].*

Though the formation of singlet and triplet excitons both result in neutralization of the charges, only the singlets-which according to spin statistics should be created in just 25 percent of the recombinations-produce light in π-conjugated polymers. Theoretically, that means 75 percent of the charge recombinations are wasted. To go beyond 25 percent for the devices to be more efficient, Brédas and his colleagues [28-30] showed theoretically that systems built from long polymer chains should be able to boost the percentage of light-emitting singlets to as high as 50 percent because in long chains, triplets were believed to take much longer to convert into neutral excitons after they initially meet to form a loosely-bound "charge transfer state".

OLED displays have certain advantages compared to liquid crystal displays (LCD) and other display technologies [31]. For example, they possess rather high power efficiencies because they are emissive displays and do not need an additional backplane illumination. Further advantages are fast response times (up to 104 times faster than LCD), high luminance at relatively low voltages, wide view angle and high contrast. Flexible and large area displays are also possible. Another interesting finding is that, some organic light emitting polymers, (such as PFs and PIFs) exhibit liquid crystalline character. This is not surprising, giving that PFs and PIFs are calamitic liquid crystals (different classes of calamitic liquid crystals are discussed in Chapter 1) and in principle, many different phases can be expected from these materials. Therefore, PFs and PIFs combine both characters: liquid crystallinity and light emission making them good candidates for electronic applications.

Despite these advantages the conventional one-layer OLED displays still have some drawbacks. One major problem is the unbalanced charge flow through the devices which leads to higher operating voltages and reduced lifetimes [13]. The difference between the amount of positive (holes) and negative (electrons) charge carriers injected into the device is mainly caused by a mismatch between the valence band and the conduction band levels of the emitter material with respect to the Fermi level of the adjacent electrode (Figure 5-5a).
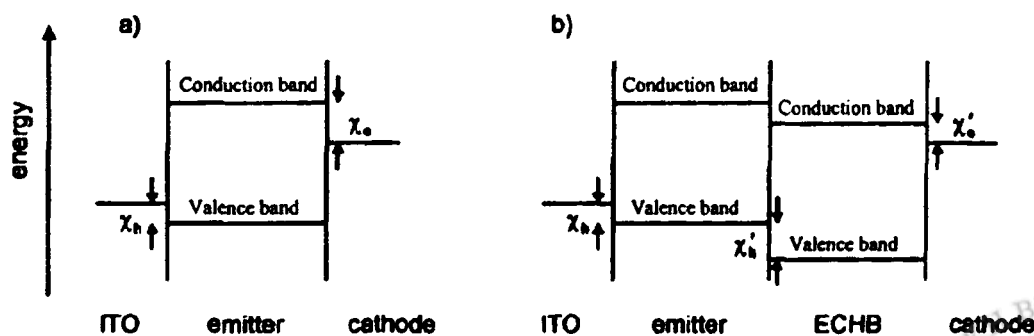

Figure 5-5: *Energy level diagram of an a) single-layer OLED and b) OLED with additional electron-conducting/hole-blocking layer (ECHB). The energy barriers for the injection of holes and electrons are denoted as χ_h and χ_e, respectively. Modified after ref. [32].*

Moreover, in many emitter materials holes possess a higher mobility than electrons which leads to non-radiative neutralization of the positive charges at the cathode [33,34]. To circumvent this problem additional charge-injection layers between the emission layer and the corresponding electrodes have be introduced. Especially, the insertion of a so-called electron-conducting/hole-blocking (ECHB) layer has proved to effectively inhibit the quenching of holes at the cathode (Figure 5-5b) [13]*.

5.2 Oligoindenofluorenes: Towards new blue light-emitting polymers

Conjugated oligomers are used as model systems for studying the effect of the monomer structure and overall morphology on the optical properties [39]. One particular advantage of oligomers is that they can be synthesized free from "defects". It is known that defects play an important role in determining the emissive properties of conjugated polymers; in particular, the presence or formation of emissive ketone defects are thought to be responsible for the color instability in PFs [10] and PIFs [27]. Oligofluorenes have been prepared and their optical properties studied by several groups [40-47]. In a recent investigation, the dynamics of a series of oligofluorenes up to the polymer, which form a nematic mesophase were reported [48]. The dynamics were investigated with dielectric spectroscopy (DS) and revealed two processes (called α- and β-) associated with the liquid-to-glass transition and the glassy state, respectively. The α-process had a non-Arrhenius temperature-dependent relaxation times $\tau(T)$ and a temperature- and molecular-weight-dependent spectral broadening of intramolecular origin.

On the other hand, oligoindenofluorenes have only been obtained in very small amounts from preparative gel-permeation chromatography (which separates mixtures of oligomers obtained from polymerization). The absorption and emission maxima of these materials were used to estimate the effective conjugation length for the polymer (the effective conjugation length of PIFs has been determined to be equal to 5-6 monomer units [25]), but the properties of such oligomers have not been studied further due to insufficient material.

(*) Materials with good electron transport properties are molecules or polymers with low-lying conduction band levels such as oxadiazoles (PBD), triazines, benzothiadiazoles, etc. [35,36]. For the improved injection of holes, materials with high-lying valence band levels are needed. Typical hole transporting materials (HTM) are aromatic amines like triaryldiamines or electron rich polymers like poly(ethylenedioxythiophene) (PEDOT) [5,37,38].

Herein, we report the optical properties, self-assembly mechanism, and associated molecular dynamics of a series of oligoindenofluorenes up to the polymer [49] synthesized by Dr. A. C. Grimsdale in the group of Prof. K. Müllen at MPI-P in Mainz. This work is aiming at:

(i)   probing the keton defects which are responsible for the color instability in PIFs LEDs by using two techniques; photoluminescence and DS. For this purpose, an indenofluorene monoketon (IFK) was synthesized for comparison with those of the defect-free IF oligomers.

(ii)   identifying the type of mesophase (nematic/smectic) by using POM technique.

(iii)   understanding the origin of the intrinsic dynamics associated with the liquid-to-glass transition and within the mesophase that are important for the design of polymer light emitting diodes.

Finally, these results are compared to the corresponding properties of oligofluorene samples [48]. We find that oligoindenofluorenes have several similarities to the corresponding oligofluorenes, but also some distinct differences with respect to the mesoscopic order and glass temperatures that make them attractive materials for electronic applications.

5.2.1 Materials

A series of oligoindenofluorenes up to the polymer have been synthesized for the purpose of this investigation [49]. Keton defects are thought to be responsible for the color instability in PIFs LEDs. For this purpose an indenofluorene monoketon (IFK) was synthesized as well for comparison with those of the defect-free IF oligomers. Schematic structures of the IF monomer, IFK, IF dimmer, IF trimer, and IF polymer are shown in Scheme 5-1.
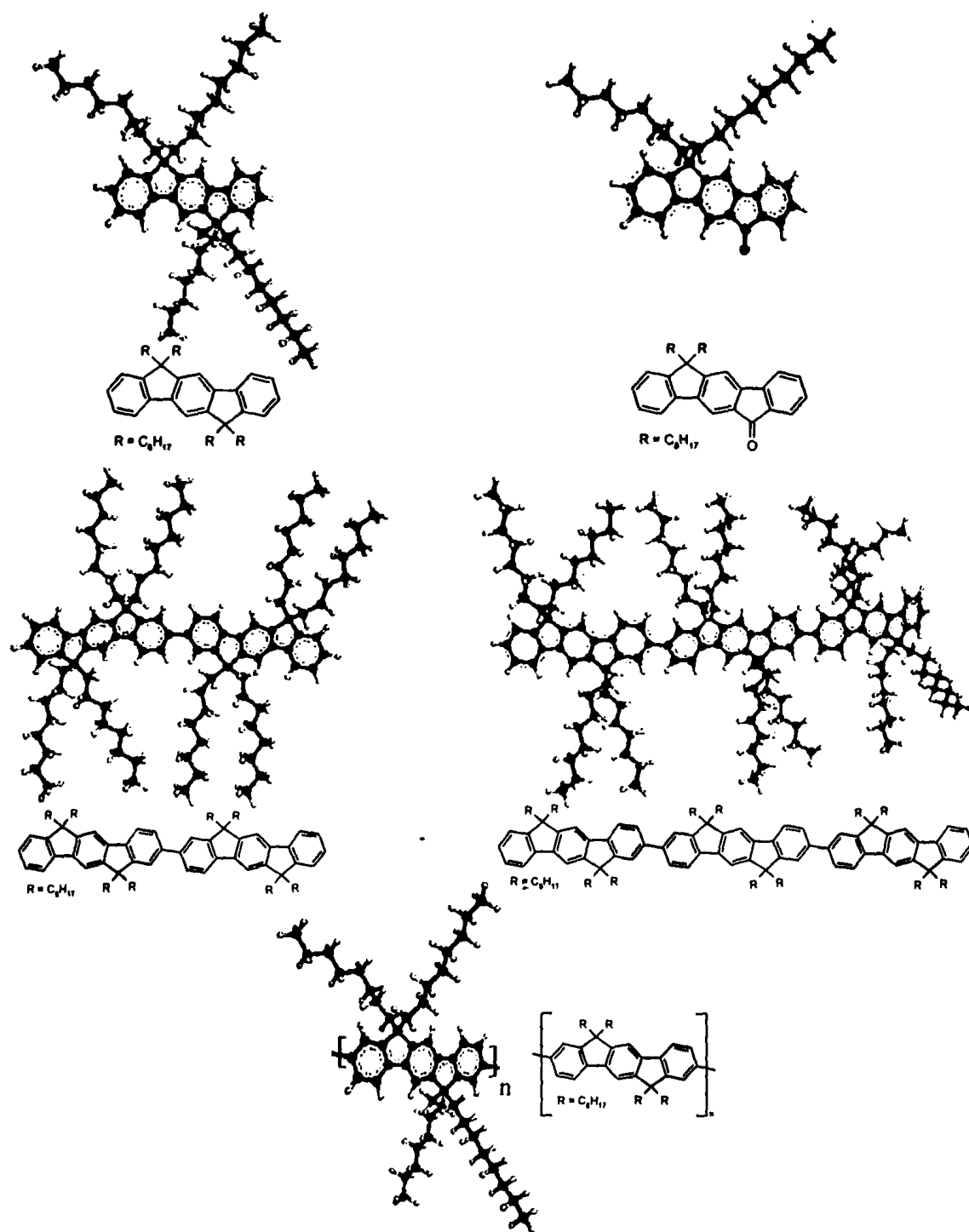
Scheme 5-1: *Schematic structures of the IF monomer (top left), IFK (top right), IF dimmer (middle left), IF trimer (middle right), and IF polymer (bottom).*

5.2.2 Spectral characteristics

The UV/Vis absorption spectra of the IF dimer and trimer in solution (Figure 5-6) show broad absorption peaks with maxima at 371 and 383 nm, respectively. The emission spectrum of the IF dimer in solution exhibits vibronic fine structure, with a maximum emission at 406 nm and a shoulder at 430 nm. Likewise, the emission spectrum of the IF trimer in solution,

possesses the same spectral shape, bathochromically shifted by 15 nm with a maximum emission at 421 nm.
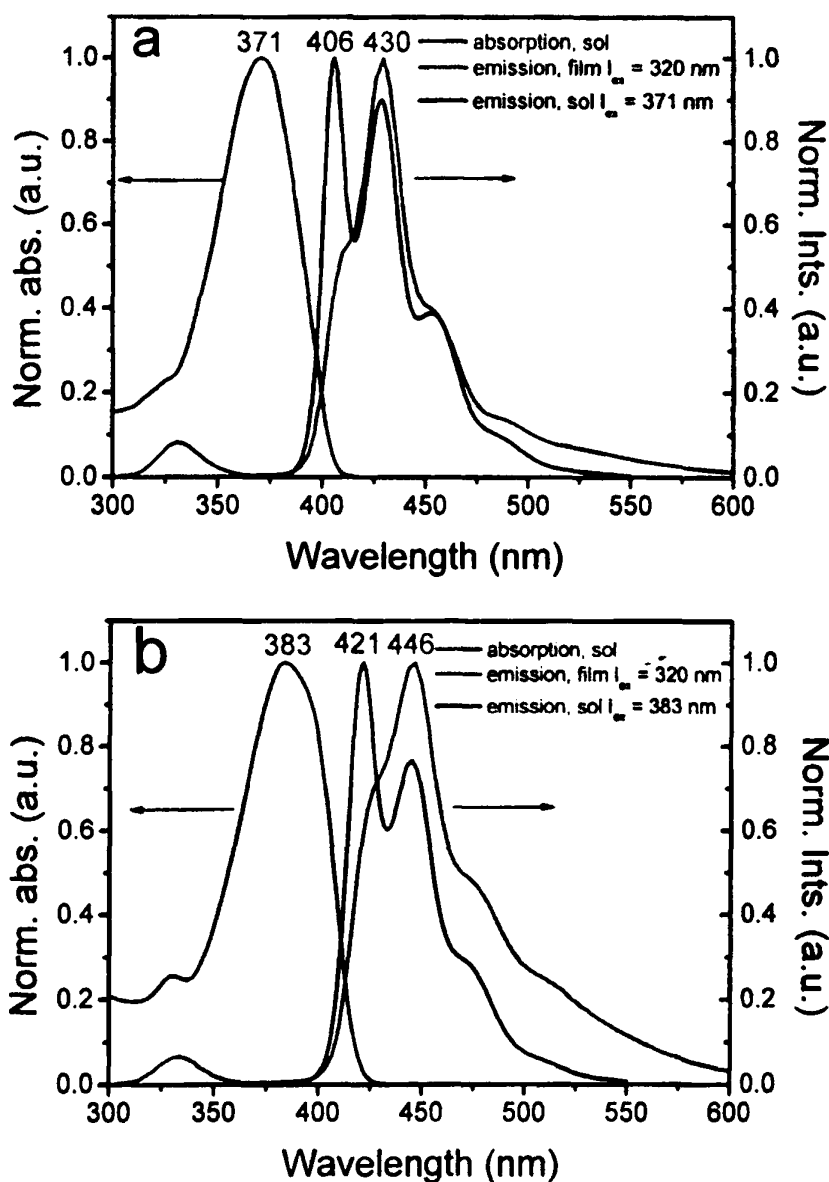
Figure 5-6: *(a) Solution UV/Vis absorption (red line) and photoluminescence emission solution (blue line) and film (magenta line) spectra of IF dimer. (b) Solution UV/Vis absorption (red line) and photoluminescence emission solution (blue line) and film (magenta line) spectra of IF trimer.*

The thin-film emission spectra of the IF dimer and trimer exhibit a maximum emission which is at the same wavelength as the shoulder of the solution emission. We attribute this change in spectral shape to the self-absorption of the material and to the different vibronic contributions of the two states. The peak broadening and tailing in the trimer film emission spectrum indicate some degree of aggregation. The presence of defect structures on the IF oligomers would result
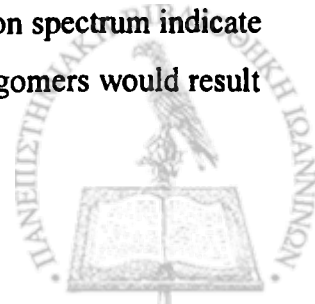
in a strong, broad emission band in the range of 550 nm, which is absent in the spectra of Figure 5-6 [25-27]. This result suggests that the IF oligomers are free from structural defects.

5.2.3 Structure investigation

The differential scanning calorimetry (DSC) and polarizing optical microscopy (POM) results (Figures 5-7 and 5-8) reveal that the oligomers form ordered mesophases at intermediate temperatures, followed by a glassy state at lower temperatures. For IFK, POM revealed the absence of any mesophase.
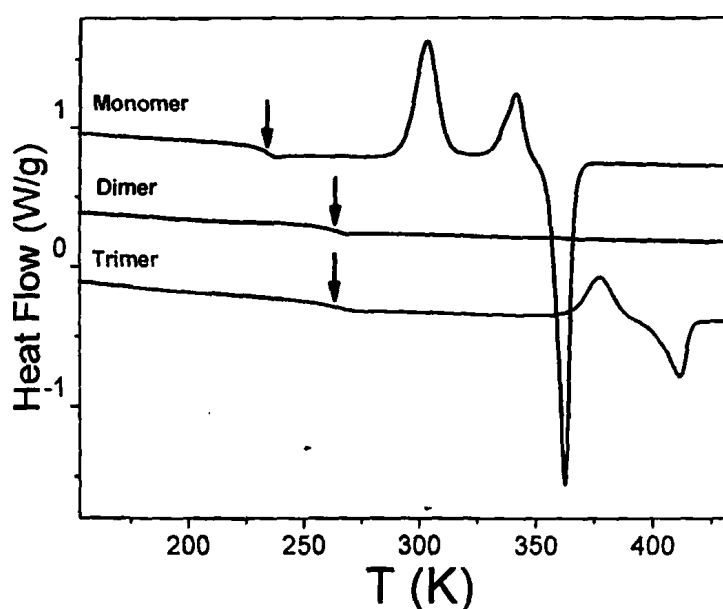
Figure 5-7: *DSC traces obtained during the second heating run with a rate of 10 K/min. The vertical arrows indicate the respective glass temperatures. The traces have been shifted vertically for clarity.*

To identify the exact morphologies in the remaining samples, we investigated the wide-angle X-ray scattering (WAXS) patterns of macroscopically oriented samples. The WAXS patterns from the oriented trimer (Figure 5-9) and dimer (Figure 5-10) fibers display some similarities but also some differences. The trimer pattern consists of intense meridional low-angle reflections and some less intense equatorial reflections. The periodicity along the extrusion direction (the vertical arrow in Figure 5-9 gives the fiber axis) corresponds to the intramolecular repeat distance (d_{me}). This periodicity is attributed to the main-chain repeat unit (monomer) with a characteristic length of d_{me}=1.17 nm at 403 K, in good agreement with the calculated monomer length. The first intense equatorial reflection (at q=7.2 nm^{-1}) gives the lateral periodicity between the supramolecular assemblies with an interlayer period of d_{eq} ≈

0.88 nm. The latter suggests that the spacing between the self-assembled backbone layers is controlled by the length of the side chains (see Scheme 5-1). The remaining equatorial reflections at q values of 12.1, 14.3, and 19 nm^{-1} with relative positions $1{:}3^{1/2}{:}4^{1/2}{:}7^{1/2}$ with respect to the low-angle reflection (at $q=7.2$ nm^{-1}) suggest a hexagonal packing of the side chains.

Figure 5-8: *POM images of the monomer (left; T=313 K), the dimer (middle; T=373 K), and the trimer (right; T=423 K). All the images suggest smectic mesophases.*

These findings for the structure in the trimer are summarized in a schematic way in Figure 5-11a, which depicts a 3D arrangement of the trimer in the oriented fiber state. The rigid parts of the trimer stack on each other, to form layers aligned parallel to the fiber axis. The flexible aliphatic side chains fill the space between the backbones and effectively control the lateral distance.

The WAXS pattern for the dimer has similar reflections with respect to their positions but rotated by 90°. The intense equatorial low-angle reflection ($d_{eq}=1.2$ nm) has the same periodicity as the intense trimer meridional reflection, which suggests that the backbone repeat unit is now along the equator (i.e. in the horizontal direction) and thus perpendicular to the fiber axis. This turn in the orientation of the dimer structure results from the similarity in the lengths of the backbone and side chains in their fully extended conformation (Scheme 5-1). During fiber formation, there is competition for orientation along the extrusion direction, with the longer length found preferentially along the fiber axis. For the trimer, the longer length is clearly the backbone, which orients along the extrusion direction (Figure 5-11a). For the dimer, the dominating length dimension is that of the side chains, which gives rise to the observed rotation of the whole structure (Figure 5-11b). We should mention here that annealing up to 343 K does not change the pattern, which suggests that this is the equilibrium orientation. As expected, the WAXS pattern of the monomer (not shown) has exactly the same orientation as the dimer.

Figure 5-9: *Top: WAXS pattern from a trimer fiber taken at T=403 K (the fiber was extruded at 333 K). The vertical arrow gives the orientation of the fiber axis and the horizontal and vertical arrows the equatorial and meridional directions, respectively. Bottom: equatorial (red line) and meridional (blue dashed-line) scattered intensity distributions.*
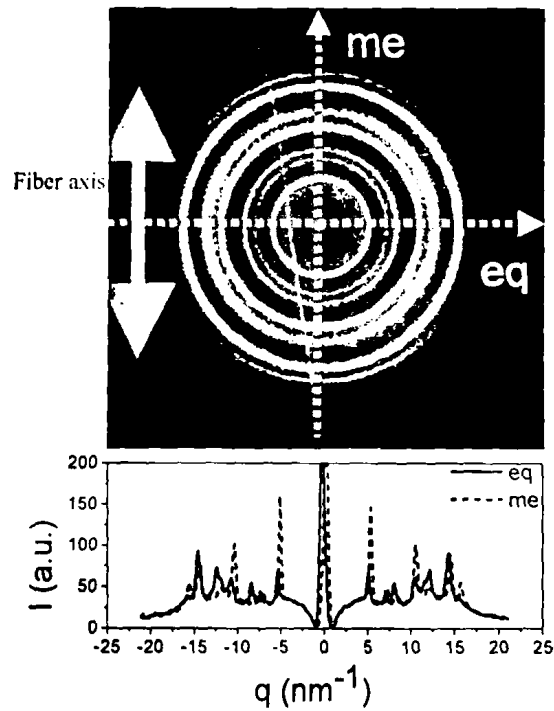

Figure 5-10: *Top: WAXS pattern from a dimer fiber taken at T=298 K (the fiber was extruded at 298 K). The vertical arrow gives the orientation of the fiber axis and the horizontal and vertical arrows the equatorial and meridional directions, respectively. Bottom: equatorial (red line) and meridional (blue dashed-line) scattered intensity distributions.*
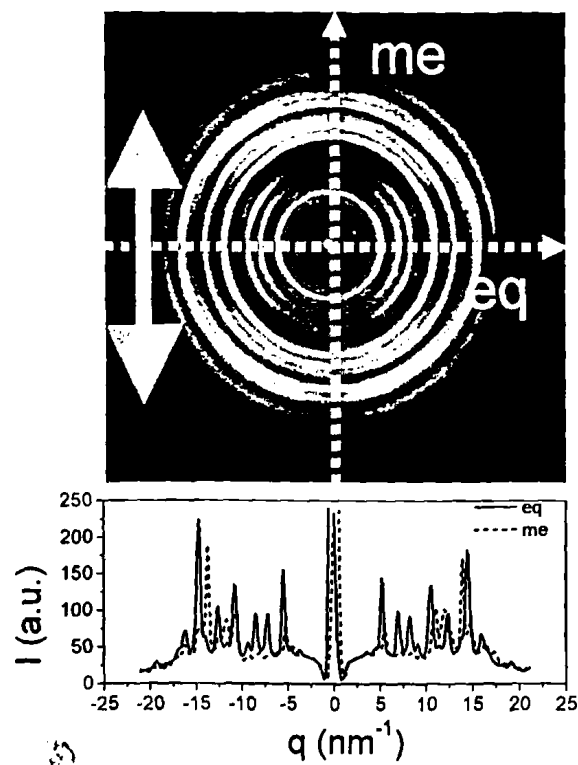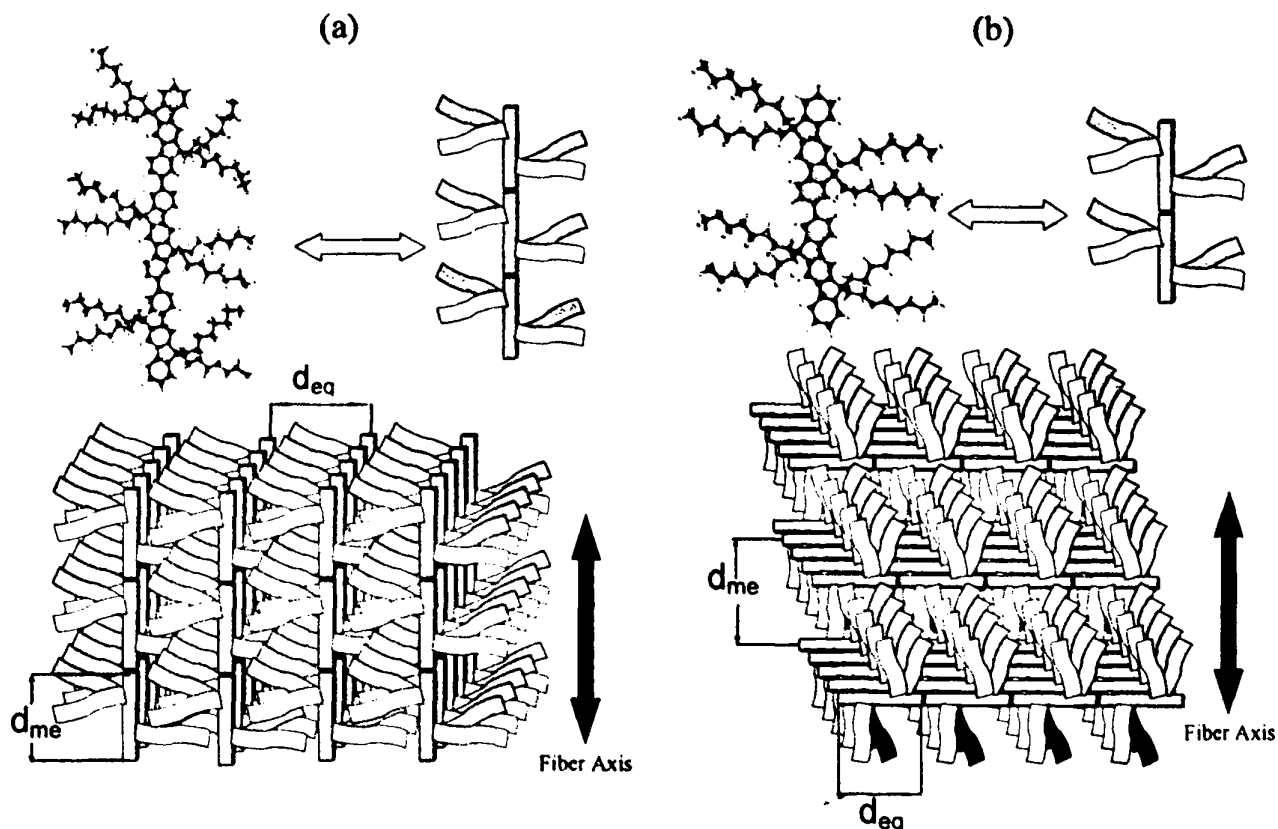
Figure 5-11: *Schematics of the structures of a) trimer and b) dimer extruded fibers.*

Overall, the observed WAXS patterns reflect the spatial segregation of the immiscible aromatic and aliphatic parts of the oligomers, driven by the intermolecular cohesive forces favoring π stacking of the aromatic segments and the entropically driven conformations of the flexible side chains. Likewise, the orientation of these structures with respect to the extrusion direction results from a competition between the backbone and side-chain lengths.

5.2.4 Molecular dynamics investigation

Earlier studies of the dynamics in shape-persistent macromolecules [50] (including polymer liquid crystals, hairy-rod polymer, and synthetic polypeptides) reveal the existence of dynamic processes usually found in amorphous polymers and glass-forming liquids. Accordingly, the DS results from the IFs reveal multiple dynamic processes: i) the main (α) process freezing at the DSC glass temperature, ii) a faster process within the glassy phase (β process) with very low intensity attributed to side-chain relaxation, and iii) a process due to the ionic conductivity at higher temperatures. Because of the low intensity of the glassy process, which makes the deconvolution a difficult task, we only discuss here the primary α-process together with the process due to the ionic mobility.

Figure 5-12 gives the result of the attempted time-temperature superposition (*tTs*) with respect to the dielectric loss data in the vicinity of the α-process. At each temperature, a single frequency-scale shift factor a_T and a singl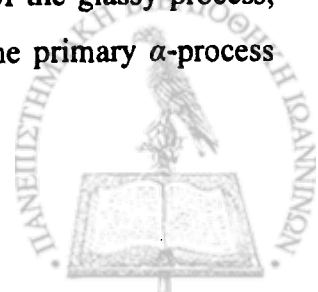e (but very small) loss-scale shift factor b_T allow the superposition of the different curves with the data at the reference temperature. This procedure gives rise to the shown "master curve" with an extended frequency axis. Note that *tTs* is only approximately valid near the peak position. The solid line in Figure 5-12 gives the result of a representative fit of the dielectric loss peak to a single HN function (see Eq. (2.47) of Chapter 2). Note the deviations from the line at higher and lower frequencies. The lower-frequency deviations are caused by the ionic conductivity, whereas the deviations at higher frequencies are caused by the presence of a very weak secondary process well within the glassy phase. The shape of the loss peak deviates from a single Debye process (α=γ=1) and is highly asymmetric toward the high-frequency side. This finding agrees with the shape of the α-process in oligofluorenes [48]; however, in the latter systems *tTs* was clearly violated. The temperature dependence of the shift factors is shown in the inset to Figure 5-12. The $a_T(T)$ dependence conforms to the Williams-Landel-Ferry (WLF) equation [Eq. (5.1)] [51]:

$$\log a_T = -\frac{c_1^r \left(T - T_r\right)}{c_2^r + \left(T - T_r\right)}$$

(5.1)

where c_1^r (=7.2) and c_2^r (=91.3 K) are the corresponding WLF parameters at the reference temperature T_r (=298.15 K). These parameters at the dimer glass temperature are recalculated as c_1^g =12.4 and c_2^g =53 K and will be discussed subsequently. In the same Figure the corresponding data (constructed by applying frequency a_{T^*} and loss-scale b_{T^*} shift factors) from the IFK are compared with respect to the curve at a reference temperature (*T*=283.15 K). Notice i) the much higher dielectric loss and ii) the failure of *tTs* for the α-process.

DS is very sensitive to the presence of the carbonyl group (ketone defects) due to the large dipole moment, as suggested by the comparison in Figure 5-12. The primary relaxation process (α-process) in all IF oligomers displays a low dielectric strength (typically $T\Delta\varepsilon \approx 5$ K) as compared to $T\Delta\varepsilon \approx 1430$ K for the IFK. The effective dipole moment ($\mu_{eff}=(g\mu)^{1/2}$, where μ is the dipole moment and g gives the orientation pair correlations between dipoles) responsible for the α-process can be calculated from the dielectric strength using the Fröhlich equation applicable to spherically symmetric molecules [52] (see Eq. (3.2) of Chapter 3). Using a macroscopic density of 1 g/cm^3 gives μ_{eff}=0.27±0.06 and 3.0±0.1 D for the IF oligomers and IFK, respectively. Again, these results suggest the absence of ketone defects in the IF

oligomers. In accord with the low dipole moment, the oligomer photoluminescence (PL) shows stable blue emission both in solution and in films (Figure 5-6). In solution, a blue emission is documented from the PL maxima at 406 and 430 nm for the dimer and 421 and 446 nm for the trimer. In the solid state, the main emission maxima are at 430 and 446 nm for the dimer and trimer, respectively, again suggesting the absence of defects in agreement with the results from the DS investigation.
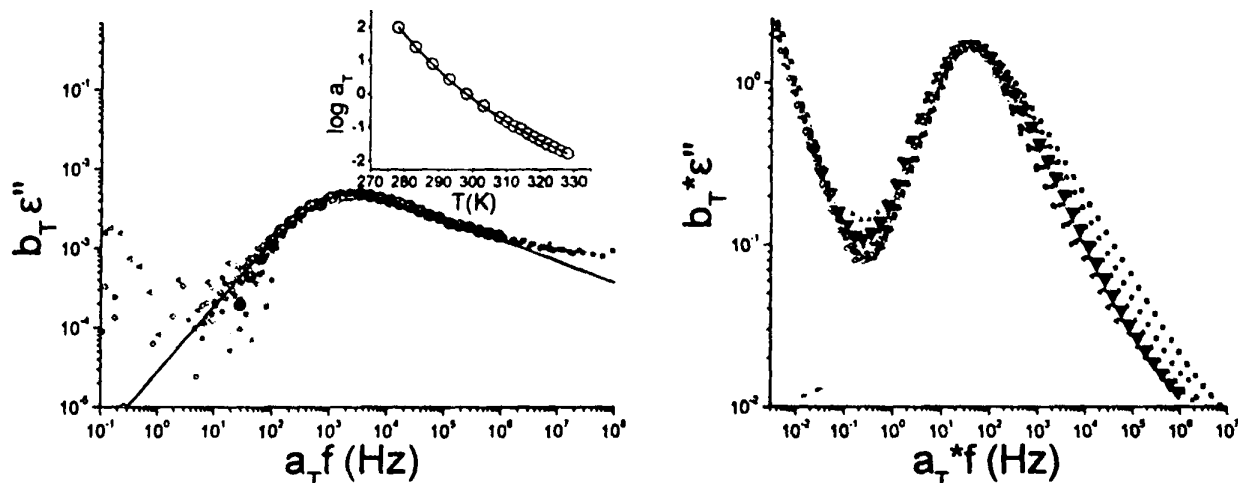

Figure 5-12: *Left: attempted time-temperature superposition (tTs) of the dielectric loss for the dimer α process. The data points shown correspond to measurements within the T range 278.15 to 328.15 K. The reference temperature (●) is at 298.15 K. Dielectric loss data fit (—) to the HN equation (see Eq. (2.47) of Chapter 2). The deviations at higher frequencies are due to the presence of a weak β process. Inset: logarithm of the shift factors a_T plotted as a function of temperature. The line is the result of a fit to the WLF equation (see text). Right: attempted tTs for the IFK α process. The data correspond to measurements within the T range 268.15 to 343.15 K. The reference temperature (▼) is at 283.15 K. The maximum loss value is some 350 times higher than in the sample without the ketone group; tTs clearly fails for the α process.*

The results of the DS investigation with respect to the α-process and the process due to the ionic conductivity are better discussed with respect to the three representations shown in Figure 5-13. The Figure displays "master curves" of the $\varepsilon^*=\varepsilon'-i\varepsilon''$, the electric modulus $M^*=M'+iM''$, and the conductivity $\sigma^*=\sigma'+i\sigma''$ that are interrelated through Eqs. (2.33) and (2.43) of Chapter 2 and emphasize different aspects of the same processes. The superpositions were made around the M'' maximum and the same horizontal shift factors (a_T) were used for the ε^* and σ^* representations. Note that in all representations the crossing of the real and imaginary parts occurs at the same frequency, which signifies the rate of the process due to the ionic mobility (dashed-line). Below the M' and M'' crossings the moduli have respective slopes of 2 and 1, as found for the mechanical moduli in the flow regime [51]. The deviations from these

dependencies at the lowest measured frequencies are caused by the electrode polarization (notice also the upturn of ε' at low frequencies) [52]. The α-process also appears as a peak but in the high frequency side (dotted-line). The position of the α-peak is approximately the same in the different representations, since the relaxation times from the M^* and ε^* representations are related through $\tau_{M^*}/\tau_{\varepsilon^*} \approx \varepsilon_\infty/\varepsilon_0$, and for very weak processes the relaxation times are practically indistinguishable.
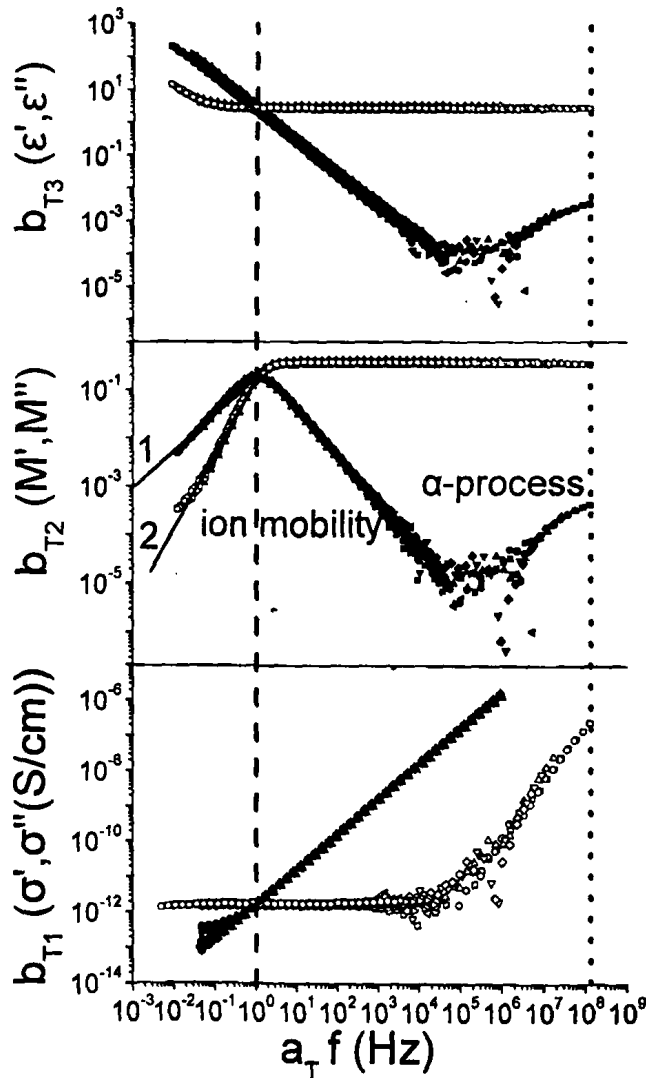
Figure 5-13: *Composite plot of the dielectric function $\varepsilon^* = \varepsilon' - i\varepsilon''$(top), the electric modulus $M^* = M' + iM''$ (middle), and the ionic conductivity $\sigma^* = \sigma' + i\sigma''$ (bottom) shifted to a reference temperature (433.15 K) in the vicinity of the IF dimer ionic relaxation. The real (imaginary) parts are shown with open (filled) symbols. The vertical dashed (dotted) lines give the location of the ionic mobility (α process) rates at the reference temperature.*

Lastly, the dc part of the ionic conductivity is typically $\approx 10^{-12}$ S cm^{-1} (dimer at T=433 K), that is, typical of insulators and revealing the absence of impurities in the present systems. More
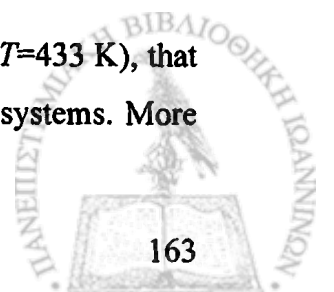
information on the structural relaxation can be obtained from the T-dependence of the respective times.

The dependence of the relaxation times on T at maximum loss corresponding to the α-process for the oligoindenofluorenes and the polymer are shown in Figure 5-14 as a function of temperature in the usual Arrhenius representation. The solid lines are fits to the well-known Vogel-Fulcher-Tammann (VFT) equation (see Eq. (3.3) of Chapter 3). For the polymer, the strong conductivity contribution precludes measurements over a broader T range. For that reason a fixed "primitive" time τ_0 $(=2.7 \times 10^{-11}$ s) is used based on the dimer data that span a broader T range.
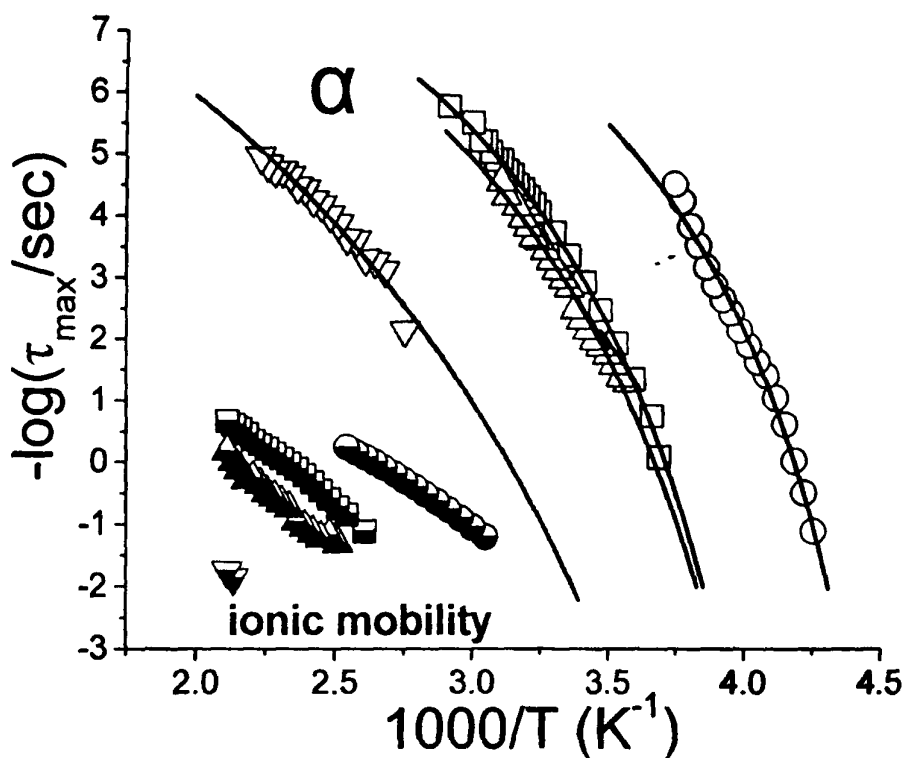
Figure 5-14: *Arrhenius relaxation map for the different processes in the IF monomer (circles), dimer (squares), trimer (up triangles), and polymer (down triangles). The different symbols correspond to the α process (open symbols) and the process due to the ionic mobility (half-filled symbols). The lines are fits to the VFT equation. The corresponding data for IFK are omitted for clarity but the VFT parameters are included in Table 5-1.*

The above parameters for the α-process are summarized for the different samples in Table 5.1, which also includes the corresponding values from the monomer with fluorenone for comparison. Notice that the latter results in a higher "ideal" glass temperature by some 26 K, which suggests a more rigid backbone structure. The data for the ionic mobility, obtained from the crossing of the M'' with M' (Figure 5-13), are also plotted in Figure 5-14 for comparison.

Clearly, ions are relaxing at characteristic times about eight decades slower than the segmental α-process, nevertheless with similar activation parameters B (related to the WLF parameters through $B = c_1^g c_2^g$) as for the α-process.

From the VFT dependence, the glass temperature can be defined from DS as the temperature with a corresponding α-relaxation time of $\tau \approx 10^2$ s, and is compared with the corresponding value from DSC (rate of 10 K/min) in Figure 5-15 as a function of the degree of polymerization n.

Table 5.1. Vogel-Fulcher-Tammann (VFT) parameters and glass temperatures of the indenofluorene (monomer, dimer, trimer and polymer) and the indenofluorene monoketone.

Sample	τ_0 (s)	B (K)	T_0 (K)	T_g (K) (at $\tau = 10^2$ s)
Monomer	2.7×10^{-11} [a]	458±12	196±1	232±2
Dimer	2.7×10^{-11}	650±70	208±4	260±1
Trimer	2.7×10^{-11} [a]	750±20	-	261±2
Polymer	2.7×10^{-11} [a]	1500±60	178±10	297±10
IFK	1.8×10^{-11}	560±20	222±1	266±1
[a] Held fixed to the corresponding dimer value.				

There is excellent agreement between the values of T_g from DSC and DS and both can be fitted according to the Fox equation [Eq. (5.2)]:

$$T_g = T_g^\infty - \frac{A}{n} \tag{5.2}$$

where T_g^∞ is the glass temperature at infinite molecular weight and A (=62±12) is a constant. We should mention here that the T_g point of PIF in Figure 5-15 has a larger uncertainty due to the higher extrapolation used in the VFT dependence (as a result of the higher conductivity in this sample). The corresponding DS data for the oligofluorenes and the polymer are included (as a line) in the same figure. Despite the higher uncertainty for the PIF T_g, even the IF oligomers display a distinctly different $T_g(n)$ dependence that gives rise to a lower T_g^∞ ($\approx 291 \pm 9$ K) for the PIF, as compared to the PF (with $T_g^\infty \approx 332$ K) [48], which suggests a higher backbone flexibility in the former. At first, this is surprising given the more rigid monomer structure. This situation may arise from competition for a more rigid monomer structure favoring an increase in T_g and a higher number of side chains (PIFs have twice as many as

PFs), which can increase the main-chain mobility and could lead to a lower T_g in PIFs as compared to PFs. According to this proposition, the monomer and dimer IF samples display a higher T_g as compared to the corresponding oligofluorenes. However, by increasing the molecular weight, the backbone becomes less rigid than the PF analogy. In addition, IFK has a more rigid backbone, as revealed by the increase in T_g by 34 K compared to that of the IF monomer.

Based on the above, IF oligomers can be synthesized defect free as stable blue-emitting materials. Their self-assembly mechanism is influenced not only by the spatial segregation of the aromatic and aliphatic parts but also by the competition between the backbone and side-chain lengths, thus forming more ordered mesophases (smectic) than the corresponding oligofluorenes (nematic).
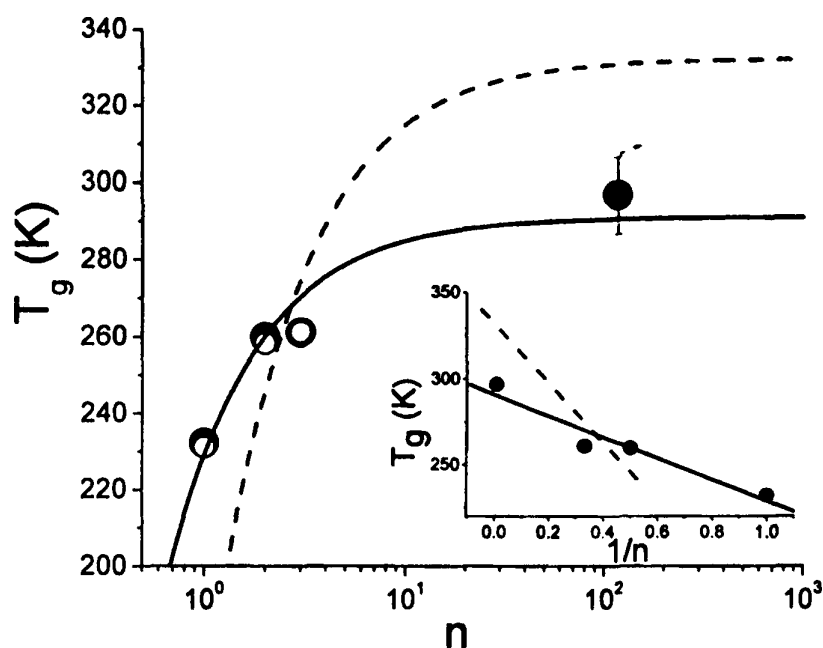
Figure 5-15: *Dependence of T_g on the number of IF repeat units (n) obtained from DS (●; at $\tau=10^2$ s) and DSC (○; heating rate of 10 K/min). The corresponding data from the oligofluorenes (-----) are also included for comparison [48]. The lines are fits according to the Fox equation (see text). Inset: T_g values from DS as a function of 1/n.*

Despite the stiff backbone, these materials exhibit dynamic characteristics known from amorphous polymers and glass-forming liquids: a glass temperature, α and β (albeit weak) processes, non-Arrhenius T dependence of relaxation times, and non-Debye distribution of relaxation times.

5.3 Summary

Wide angle X-ray scattering, photoluminescence, polarizing optical microscopy, differential scanning calorimetry, and dielectric spectroscopy have been used to study the optical properties of a new class of blue-light emitting organic compounds. The mechanism of the self-assembly of these oligoindenofluorenes up to the polymer, their thermal properties, and associated molecular dynamics also reveal important clues about their behaviour and potential for applications in organic light-emitting diodes (OLEDS) and other devices.

The results on the structure and associated dynamics revealed several similarities between the oligoindenofluorenes and the corresponding oligofluorenes. For instance, both classes of material show low dielectric loss and low ionic conductivity, which facilitates stable blue emission in both. However, there are some important differences too. The oligoindenofluorenes are more highly ordered and form smectic mesophases rather than nematic mesophases. Smectic mesophases are more amenable to device applications because they are more ordered. The oligoindenofluorenes also have a lower glass transition temperature than their oligofluorene counterparts and so can be switched between the ordered and disordered phases more easily. These are major advantages of PIF as compared to PF that are critical for device fabrication.

5.4 References

[1] Nalwa, H. S., *Handbook of Advanced Electronic and Photonic Materials and Devices: Light-Emitting Diodes, Lithium Batteries and Polymer Devices*, Vol. 10, Academic Press, San Diego, (2001).

[2] Nalwa, H. S., *Handbook of Organic Conductive Molecules and Polymers*, Vol. 4, Wiley, Chichester, (1997).

[3] Kiess, H. G., *Conjugated Conducting Polymers*, Springer Verlag, Berlin, (1992).

[4] Friend, R. H.; Gymer, R. W.; Holmes, A. B.; Burroughes, J. H.; Marks, R. N.; Taliani, C.; Bradley, D. D. C.; Dos Santos, D. A.; Brédas, J. L.; Lögdlund, M.; Salaneck, W. R. *Nature (London)* **397**, 121 (1999).

[5] Friend, R. H. *Pure Appl. Chem.* **73**, 425 (2001).

[6] Shirakawa, H. *Angew. Chem.* **113**, 2642 (2001).

[7] MacDiarmid, A. G. *Angew. Chem.* **113**, 2649 (2001).

[8] Heeger, A. J. *Angew. Chem.* **113**, 2660 (2001).

[9] Carroll, R. L.; Gorman, C. B. *Angew. Chem. Int. Ed.* **41**, 4379 (2002).

[10] Scherf, U.; List, E. J. W. *Adv. Mater.* **14**, 477 (2002).

[11] Braun, D.; Heeger, A. J. *Appl. Phys. Lett.* **58**, 1982 (1991).

[12] Rehahn, M. *Chem. Unserer Zeit* **37**, 18 (2003).

[13] Kraft, A.; Grimsdale, A. C.; Holmes, A. B. *Angew. Chem.* **110**, 416 (1998).

[14] Ficker, J.; Ullmann, A.; Fix, W.; Rost, H.; Clemens, W. *J. Appl. Phys.* **94**, 2638 (2003).

[15] Rost, H.; Ficker, J.; Alonso, J. S.; Leenders, L.; McCulloch, I. *Synth. Met.* **145**, 83 (2004).

[16] Cravino, A.; Sariciftci, S. N. *J. Mater. Chem.* **12**, 1934 (2002).

[17] Burroughes, J. H.; Bradley, D. D. C.; Brown, A. R.; Marks, R. N.; Mackay, K.; Friend, R. H.; Burns, P. L.; Holmes, A. B. *Nature (London)* **347**, 539 (1990).

[18] McGehee, M. D.; Heeger, A. J. *Adv. Mater.* **12**, 1655 (2000).

[19] Roth, H.-K, Schrödner, M. *Materialwissenschaft Und Werkstofftechnik* **34**, 254 (2003).

[20] Kelley, T. W.; Baude, P. F.; Gerlach, C.; Ender, D. E.; Muyres, D.; Haase, M. A.; Vogel, D. E.; Theiss, S. D. *Chem. Mater.* **16**, 4413 (2004).

[21] Mitschke, U.; Bäuerle, P. *J. Mater. Chem.* **10**, 1471 (2000).

[22] Strohriegl, P.; Grazulevicius, J. V. *Adv. Mater.* **14**, 1439 (2002).

[23] Carroll, R. L.; Gorman, C. B. *Angew. Chem. Int. Ed.* **41**, 4379 (2002).

[24] Bernius, M. T.; Inbasekaran, M.; O'Brien, J.; Wu, W. *Adv. Mater.* **12**, 1737 (2000).

[25] Setayesh, S.; Marsitzky, D.; Müllen, K. *Macromolecules* **33**, 2016 (2000).
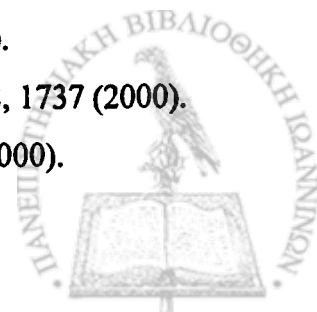
[26] Grimsdale, A. C.; Leclere, P.; Lazzaroni, R.; Mackenzie, J. P.; Murphy, C.; Setayesh, S.; Silva, C.; Fried, R. H.; Müllen, K. *Adv. Funct. Mater.* **12**, 729 (2002).

[27] Keivanidis, P. E.; Jacob, J.; Oldridge, L.; Sonar, P.; Carbonnier, B.; Baluschev, S.; Grimsdale, A. C.; Müllen, K.; Wegner, G. *ChemPhysChem* **6**, 1650 (2005).

[28] Wiesenhofer, H.; Beljonne, D.; Scholes, G. D.; Hennebicq, E.; Brédas, J. L. E.; Zojer, E. *Adv. Funct. Mater.* **15**, 155 (2005).

[29] Brédas, J. L. *Abstracts of Papers of the American Chemical Society* 227: U424-U424 395-POLY Part 2, MAR 28 (2004).

[30] Hennebicq, E.; Pourtois, G.; Scholes, G. D.; Herz, L. M.; Russell, D. M.; Silva, C.; Setayesh, S.; Grimsdale, A. C.; Müllen, K.; Bredas, J. L.; Beljonne, D. *J. Am. Chem. Soc.* **127**, 4744 (2005).

[31] Holmes, A. *Nature (London)* **421**, 800 (2003).

[32] Stahl, R., *Electroactive Conjugated Polymers as Charge-Transport Materials for Optoelectronic Thin-Film Devices*, PhD thesis, Würzburg (2005).

[33] Sheats, J. R.; Antoniadis, H.; Hueschen, M.; Leonard, W.; Miller, J.; Moon, R.; Roitman, D.; Stocking, A. *Science* **273**, 884 (1996).

[34] Greenham, N. C.; Friend, R. H. *Solid State Physics* **49**, 1 (1995).

[35] Hughes, G.; Bryce, M. R.; *J. Mater. Chem.* **15**, 94 (2005).

[36] Kulkarni, A. P.; Tonzola, C. J.; Babel, A.; Jenekhe, S. A. *Chem. Mater.* **16**, 4556 (2004).

[37] O'Brien, D. F.; Burrows, P. E.; Forrest, S. R.; Koene, B. E.; Loy, D. E.; Thompson, M. E. *Adv. Mater.* **10**, 1108 (1998).

[38] Koene, B. E.; Loy, D. E.; Thompson, M. E. *Chem. Mater.* **10**, 2235 (1998).

[39] Müllen, K.; Wegner, G., *Electronic Materials: The Oligomer Approach*, Wiley-VCH, Weinhem (1998).

[40] Jo, J. H.; Chi, C. Y.; Hoger, S.; Wegner, G.; Yoon, D. Y. *Chem. Eur. J.* **10**, 2681 (2004).

[41] Klärner, G.; Miller, R. D. *Macromolecules* **31**, 2007 (1998).

[42] Lee, S. H.; Tsutsai, T. *Thin Sold Films* **363**, 76 (2000).

[43] Anemian, R.; Mulatier, J.-C.; Andraud, C.; Stephan, O.; Vial, J.-C. *Chem. Commun.* **15**, 1608 (2002).

[44] Geng, Y.; Trajkovska, A.; Katsis, D.; Ou, J. J.; Culligan, S. W.; Chen, S. H. *J. Am. Chem. Soc.* **124**, 8337 (2002).

[45] Katsis, D.; Geng, Y. H.; Ou, J. J.; Culligan, S. W.; Trajkovska, A.; Chen, S. H.; Rothberg, L. J. *Chem. Mater.* **14**, 1332 (2002).

[46] Li, Z. H.; Wong, M. S.; Tao, Y.; Lu, J. P. *Chem. Eur. J.* **11**, 3285 (2005).

[47] Chi, C. Y.; Im, C.; Enkelmann, V.; Ziegler, A.; Liesser, G.; Wegner, G. *Chem. Eur. J.* **11**, 6833 (2005).

[48] Papadopoulos, P.; Floudas, G.; Chi, C.; Wegner, G. *J. Chem. Phys.* **120**, 2368 (2004).

[49] Elmahdy, M. M.; Floudas, G.; Oldridge, L.; Grimsdale, A. C.; Müllen, K. *ChemPhysChem* **7**, 1431 (2006).

[50] Floudas, G. *Progr. Polym. Sci.* **29**, 1143 (2004).

[51] Ferry, J. D., *Viscoelastic Properties of Polymers*, John Wiley and Sons, (1970).

[52] McCrum, B. G.; Read, B. E.; Williams, G., *Anelastic and Dielectric Effects in Polymeric Solids*, Dover, New York, (1991).

Chapter 6

Conclusions

In the present Thesis the self-assembly and dynamics of a series of discotic and calamitic liquid crystals has been studied aiming at answering some open questions.

With respect to the discotic liquid crystals, a series of un-functionalized and dipole functionalized HBCs were studied with dielectric spectroscopy (DS) and site-specific NMR techniques. Despite the symmetric shape, the un-functionalized HBCs displayed a very weak dipolar relaxation with a non-Arrhenius temperature dependence that freezes at ~215 K. DS and NMR revealed that the origin of this process was the freezing of the disc axial motion at the respective glass temperature (T_g). For the latter, four dipole functionalized HBC derivatives were studied bearing strong (mono-cyano and mono-bromo HBCs) to moderate (dimethoxy and mono-ethynyl HBCs) dipole moments. This facilitated a systematic study of the strength of dipole substitution on the phase state and dynamics. The effect of dipole substitution with strong dipoles on the phase state was to destabilize the columnar crystalline phase at low temperatures. On the other hand, substitution with weaker dipoles gave rise to a crystalline phase on cooling. Since the crystalline state is the one associated with high values of the charge carrier mobility, this result suggested that substitution with strong dipoles should be avoided for electronic applications. Nevertheless, this facilitated the study of the intrinsic disc dynamics by DS and site-specific NMR techniques.

In all cases, it was shown that the strongly temperature dependent α-process reflects the collective axial disc rotational dynamics. The freezing of the axial disc motion occurred at about 236 K for the discotics within the liquid crystalline phase (bearing stronger dipoles) and at 253 K for the discotics within the crystalline phase (bearing moderate dipoles). The important conclusion was that the phase state completely controls the dynamic response.

Another finding was that the relaxation times and breadth of α-process have distinctly different temperature- and pressure-dependencies on entering the crystalline state. These features enabled the construction of the first phase diagram $(T\text{-}P)$ for HBCs. The main outcome

171

from this study was the increased stability of the crystalline phase at elevated pressures. Thus, the C_r phase is stabilized up to 450 K when pressurized to 600 MPa. This can have consequences with respect to charge carrier mobilities, since a broader C_r phase is a major requirement for charge transport.

The transformation of the liquid crystalline to the crystalline phase was studied by pressure-jumps aiming at identifying possible intermediate states, nucleation sites and the existence of long-lived metastability. The results of the kinetic investigation revealed the absence of intermediate states but have shown long-lived metastability and fractional exponents that strongly depend on the quench depth. Although most of these finding support nucleation and growth as the main mechanism of structural formation, the dependence of the kinetic times on the driving force (δ) was not typical for a nucleation and growth forces. This point is interesting and requires further investigation. Nevertheless, these results on the slow transformation from the liquid crystalline to the crystalline phase at elevated pressures suggest new thermodynamic and kinetic pathways of stabilizing the phase with the highest charge carrier mobility.

The results on the purity, the self-assembly and the associated dynamics of the oligoindenofluorenes, that are model systems of calamitic liquid crystals with applications as OLEDs, revealed several similarities with the corresponding oligofluorenes. For instance, both classes of materials showed low dielectric loss and low ionic conductivity, that facilitates stable blue emission in both. However, there were some important differences too. The oligoindenofluorenes are more highly ordered and form smectic mesophases rather than nematic mesophases. Smectic mesophases are more amenable to device applications because they are more ordered. The oligoindenofluorenes also have a lower glass transition temperature than their oligofluorene counterparts and so can be switched between the ordered and disordered phases more easily. These are major advantages of oligoindenofluorenes (and PIF) as compared to oligofluorenes (and PF) that are critical for device fabrication.

Appendix 1

Theory of Higher Order Phase Transitions

The critical temperature and the critical pressure corresponding to the critical point introduced by Landau's theory are T_{cr} and P_{cr}, respectively [1]. No ordered phase is stable if P, T exceed P_{cr} or T_{cr}. If one of the critical parameters is chosen arbitrarily (e.g. $P<P_{cr}$) a certain temperature $T_0\sim T_{cr}$ will exist, where the degree of order vanishes for $T\rightarrow T_0$. Such a transition may be of the first or of higher order. A first order transition is represented by a curve like b and d in Figure 1-19 of Chapter 1, and a second order transition can be described by adjusting the term so that it vanishes for $T\rightarrow T_0$ [1]:

$$\alpha = a\left(T - T_0\right) = a\Delta T \tag{A1.1}$$

Then we get

$$F = F_0 + a\Delta T\xi + \beta\xi^2 + \frac{1}{3}\gamma\xi^3 \tag{A1.2}$$

which becomes for $T\rightarrow T_0$:

$$F = F_0 + \beta\xi^2 + \frac{1}{3}\xi^3 \tag{A1.3}$$

with a real solution $\xi=0$, as demanded. On the other hand, the state $\xi=0$, $T\rightarrow T_0$ is approached steadily, but $\partial^2 F/\partial\xi^2\neq0$ under the stability conditions:

$$F = F_{min}; \quad \partial F/\partial \xi = 0 \quad for \quad T \neq T_0$$

$$\frac{\partial F}{\partial \xi} = \alpha \Delta T + 2\beta \xi + \gamma \xi^2 = 0$$

$$\frac{\partial^2 F}{\partial \xi^2} = 2(\beta + \gamma \xi) > 0 \tag{A1.4}$$

$$\xi_{min} = \frac{-\beta + \sqrt{\beta^2 - \alpha \gamma \Delta T}}{\gamma}$$

The entropy is determined by the fundamental expression:

$$S = -(dF/dT)_V \tag{A1.5}$$

From Eqs. (A1.2) and (A1.5) with neglecting the temperature dependence of β and γ, the entropy will given by

$$S = -(dF/dT)_V = -a\xi \tag{A1.6}$$

This relation shows clearly the direct relation between the entropy and the degree of order. Subsequently, the specific heat is derived as

$$c_p = T\left(\frac{\partial S}{\partial T}\right)_P = -aT\left(\frac{\partial \xi}{\partial T}\right)_P = \frac{a^2 T}{2\sqrt{\beta^2 - a\gamma \Delta T}} \cong \frac{a^2 T_0}{2\sqrt{\beta^2 - a\gamma \Delta T}} \tag{A1.7}$$

If $\Delta T = 0$, the specific heat is

$$c_p = \frac{a^2 T_0}{2\beta} \tag{A1.8}$$

The behavior of the specific heat, c_p, as a function of temperature exhibits the following features. In the crystalline phase, C_r, c_p first increases linearly with temperature and then rises at an increasingly faster rate upon approaching the melting point. Similarly, c_p generally rises with increasing temperature, and this rise is linear in some ranges. The pretransition ranges are characterized by a sharp increase in c_p below, and a sharp decrease in c_p above the transition temperature when observed in the direction of increasing temperature. After the transition to the isotropic liquid, c_p first decreases sharply, passes through a minimum, and a gain rises slightly and linearly with temperature. If the nearly linear behavior of c_p is extrapolated from the isotropic region into the nematic and vice versa, a usually markedly larger specific heat is
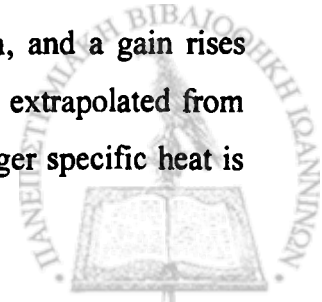
found in the liquid crystal. However, this experience cannot be generalized or applied to all smectic phases as shown in Figure A1-1.
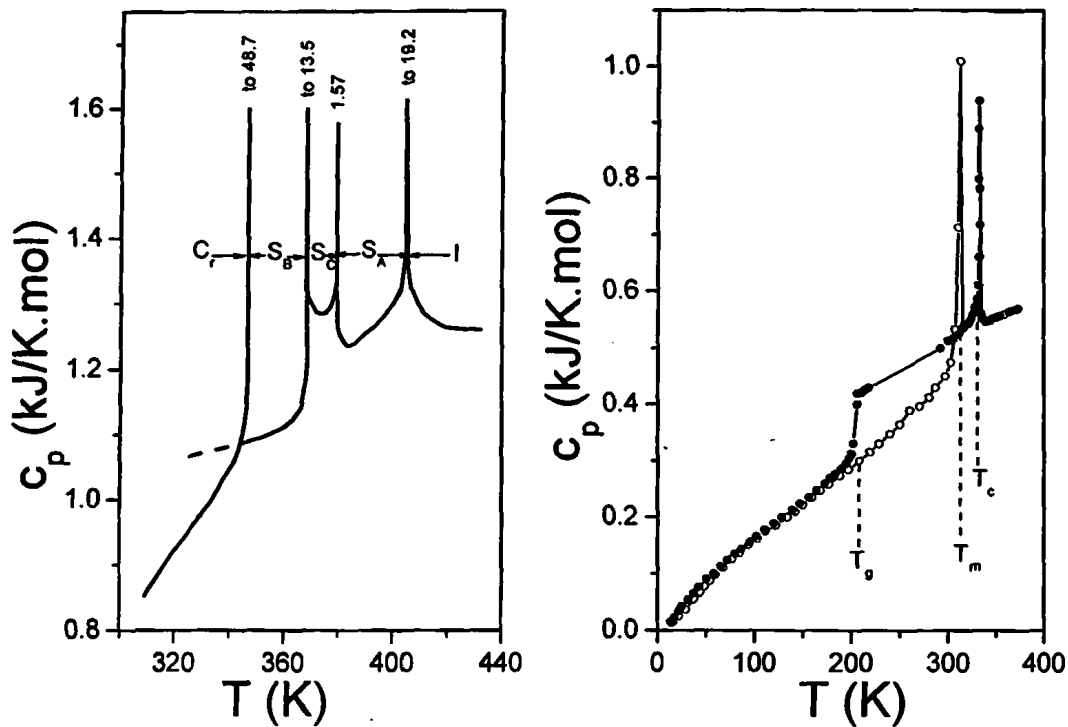

Figure A1-1: *(Left) Specific heat, c_p, vs. temperature for n-amyl 4-n-dodecyloxybenzylidene-4-aminocinnamate undergoing several (Crystal→SmB→SmC→SmA→isotropic) transitions. (right) Corresponding plot for the N-(o-hydroxy-p-methoxybenzylidene)-p-butylaniline. O: crystal, nematic, and isotropic liquid; ●: glassy and supercooled liquid crystal. After ref. [1].*

A1.1 References

[1] Kelker, H.; Hatz, R., *Handbook of Liquid Crystals*, Verlag Chemie GmbH, D-6940 Weinheim, (1980).

Appendix 2

Defects in Columnar Mesophases

The symmetry elements in the hexagonal structure composed of liquid-like columns are shown in Figure A2-1. The director $\hat{n}$ is parallel to the column axis; a (or equivalently a' or a'') is the lattice vector of the two-dimensional hexagonal lattice; L_2, T_2 and θ_2 are two-fold axes of symmetry; L_3 is a three-fold axis and L_6 a six-fold axis. Any point on L_2 or L_6 is a center of symmetry. Any plane normal to $\hat{n}$, and the planes (L_6, T_2) and (L_6, θ_2) are planes of symmetry.
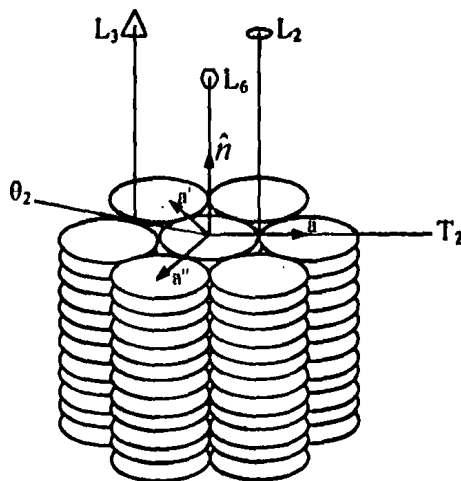

Figure A2-1: *The hexagonal columnar phase with the symmetry elements in the structure. After ref. [1].*

The most general defects that can occur in the columnar mesophases are dislocations and disclinations [1-4].

A2.1 Dislocations

dislocations are "defects" which break translational symmetries in liquid crystals. The Burgers vector b of a dislocation in the columnar structure is normal to the columnar axis. In general [1,2],

$$b = la + ma'$$

<div align="right">(A2.1)</div>

where l and m are positive or negative integers. Dislocations are of two basic types, edge and screw. For edge dislocations, b is perpendicular to the dislocation line L. Two types of edge dislocations are possible: longitudinal edge dislocations (L parallel to $\hat{n}$, Figures A2-2a,b) and transverse edge dislocations (L perpendicular to $\hat{n}$, Figures A2-2c,d). For screw dislocations b is parallel to L (Figures A2-2e,f). A hybrid composed of screw and edge dislocations is shown in Figure A2-2g.
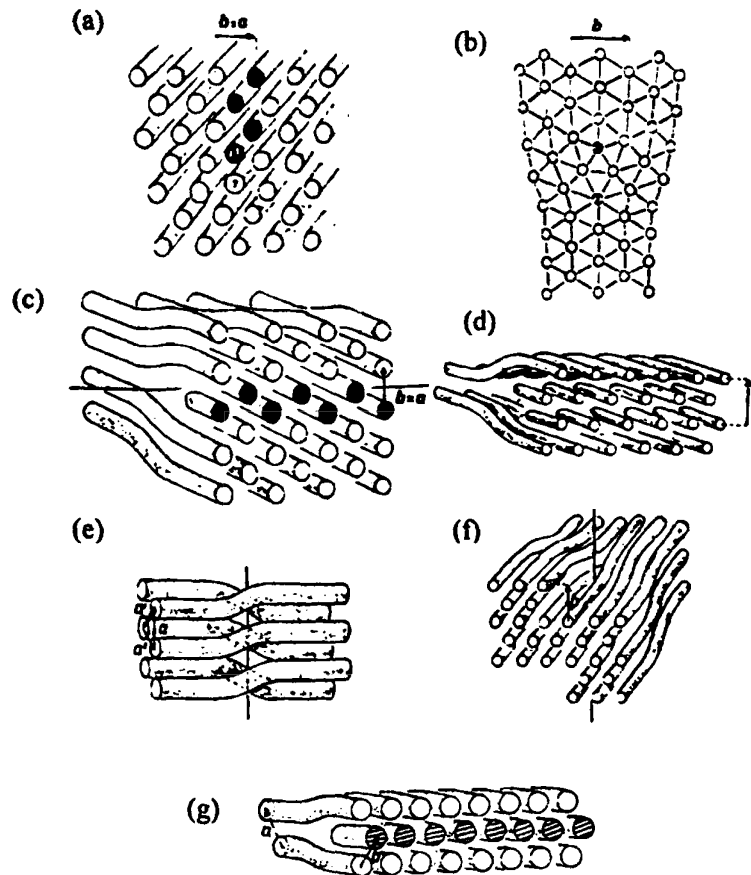

Figure A2-2: *Dislocations in the columnar phase:(a, b) longitudinal edge dislocations; (c, d) transverse edge dislocations; (e, f) screw dislocations; (g) a hybrid of screw and edge dislocations. After ref. [1].*

A2.2 Disclinations

Disclinations are "defects" which break rotational symmetries in liquid crystals. Longitudinal wedge disclinations are the standard crystal disclinations in a hexagonal lattice. The rotation vector is L_6 or L_3 or L_2, parallel to the columns. Two examples of such defects are shown in Figures A2-3a,b.
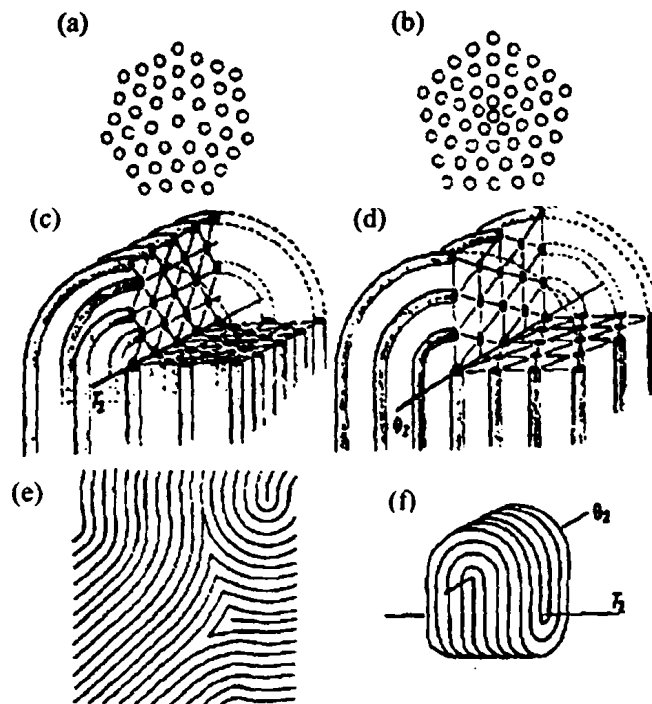
Figure A2-3: *Disclinations in the columnar phase: (a, b) -π/3 and π/3 longitudinal wedge disclinations about the six-fold axis L₆; (c, d) π transverse wedge disclinations about the binary axes T₂ and θ₂, respectively; (e) -π transverse wedge disclination leading to the formation of walls; (f) two π disclinations at right angles to each other, one about T₂ and the other about θ₂. After ref. [1].*

The lattice becomes compressed near a positive disclination and stretched near a negative one. In general, most of these disclinations have prohibitively large energies, and hence they occur as unlike pairs at the core of a disclination. In transverse wedge disclinations the rotation vector is θ_2 or T_2, normal to $\hat{n}$. Examples of $\pm\pi$ disclinations are shown in Figures A2-3c,d,e. Two transverse wedge disclinations may occur in association, as shown in Figure A2-3f. The angle between the rotation axes may be 90°, 60° or 30°. Such defects have been observed experimentally. The symmetry of the columnar phase also permits the occurrence of twist disclinations in the hexagonal lattice and of hybrids consisting of a twist disclination in the hexagonal lattice and a wedge disclination in the director field. These defects are not likely to exist. Examples of the disclinations defects are shown in Figure A2-4.
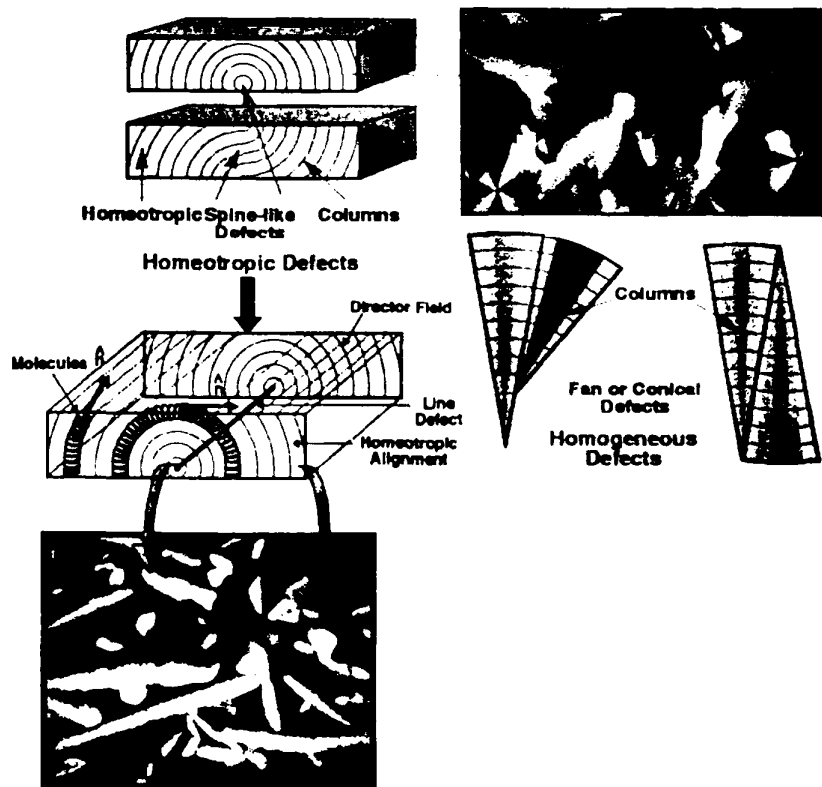
Figure A2-4: *(left) Spine-like defects formed in homeotropic textures of columnar mesophases. (right) Fan or conical-like defects formed in homogeneous textures of columnar mesophases. After ref. [5].*

A2.3 References

[1] Demus, D.; Goodby, J.; Gray, G. W.; Spiess, H. W.; Vill, V., *Handbook of Liquid Crystals, Vol. 2B: Low Molecular Weight Liquid Crystals II*, Wiley-VCH, (1998).

[2] Chandrasekhar, S.; Ranganath, G. S. *Rep. Prog. Phys.* **53**, 57 (1990).

[3] Lavrentovich, O. D., *Patterns of Symmetry Breaking*, edited by H. Arodz et al., Kluwer Academic Publishers, Netherlands, (2003).

[4] Kléman, M. *Rep. Prog. Phys.* **52**, 555 (1989).

[5] http://www.yorklc.com/docs/pdf/LCM.pdf

Appendix 3

Mobility Measurements

For studying charge transport in discotic liquid crystals, the Pulse Radiolysis Time-Resolved Microwave Conductivity (PR-TRMC) and the Time-of-Flight (TOF) techniques are most widely used. The two techniques are described briefly below.

A3.1 Pulse-radiolysis time-resolved microwave conductivity (PR-TRMC)

In the PR-TRMC approach the material of interest is ionized by pulsed irradiation with 3 MeV electrons from a Van de Graaff accelerator using pulse widths of 20-50 ns [1]. This results in the creation of charge carriers (electrons and holes) with a uniform and known concentration of the order of micromolar (Figure A3-1).

charge separation

intracolumnar
charge transport

intercolumnar
charge recombination

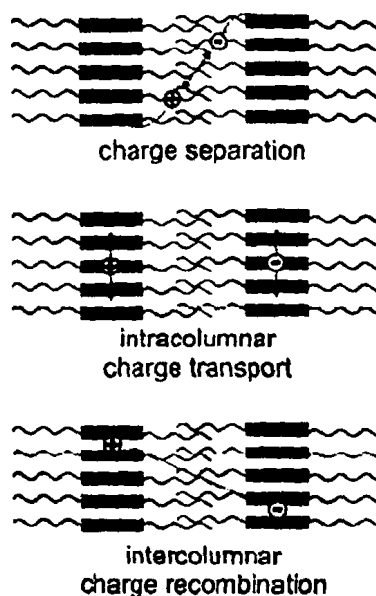**Figure A3-1:** _Schematic representations of the charge separation process following pulsed ionization, which leads to the formation of long-lived, mobile charge carriers on separate columns in discotic materials. After ref. [2]._

The created pairs of electrons and holes formed within the saturated hydrocarbon mantle can diffuse to different columnar stacks in competition with their geminate recombination within

the mantle. In this way the electron and hole of a pair can become localized on separate stacks with a barrier towards recombination provided by the intervening saturated hydrocarbon medium. If the charge carriers formed in the columnar stacks are mobile this results in an increase in the conductivity of the sample which is monitored with nanosecond time-resolution as a transient decrease in the power of microwaves which propagate through the irradiated medium. The recombination of the mobile charge carriers occurs mainly via intercolumnar electron tunnelling through the intervening hydrocarbon mantle [2]. This is evidenced as a dramatic increase in the time-scale of the decay of the radiation-induced conductivity from a few hundred nanoseconds to close to a millisecond as the peripheral alkyl substituents increase in size [3]. The decay time was found to obey an exponential dependence on the intercolumnar distance [2]. A PR-TRMC conductivity transient has two characteristics; the magnitude at the end of the pulse ($\Delta\sigma_{eop}$), which is proportional to the product of the concentration of carriers formed (n), and their mobility ($\Sigma\mu_{1D}$), and the decay after the pulse, which provides information on the subsequent recombination and/or trapping of the mobile charge carriers. The PR-TRMC method has the advantage that (i) it does not require homeotropic alignment of the sample and even polycrystalline materials can be studied; (ii) ohmic electrode contacts are not required and (iii) because of the ultrahigh frequency used (26.5-37.5 GHz), problems arising from medium polarization and field-induced drift to domain boundaries are absent. A disadvantage is that only the sum of the charge carrier mobilities, $\Sigma\mu_{1D}$, is measured; the sign of the major carrier cannot therefore be determined. For a pair of charge carriers with mobilities $\mu(-)$ and $\mu(+)$, the conductivity change at the end of a pulse, $\Delta\sigma_{eop}$, is related to the concentration of charge carrier pairs formed, n, and the sum of their mobilities, $\Sigma\mu_{1D}=$ $[\mu(+)+\mu(-)]$, by [1]

$$\Delta\sigma_{eop} = en\sum\mu_{1D} \qquad (A3.1)$$

where e is the value of the elementary charge (1.6×10^{-19} coulomb).

A detailed description of the apparatus used and the method of data analysis of PR-TRMC is given in ref. [1].

A3.2 Time-of-flight (TOF)

Photoconductivity in the columnar phase is of much interest because of its practical importance and several studies have been reported in recent years [4-6]. The photocurrent transients were studied by a time-of-flight (TOF) method.
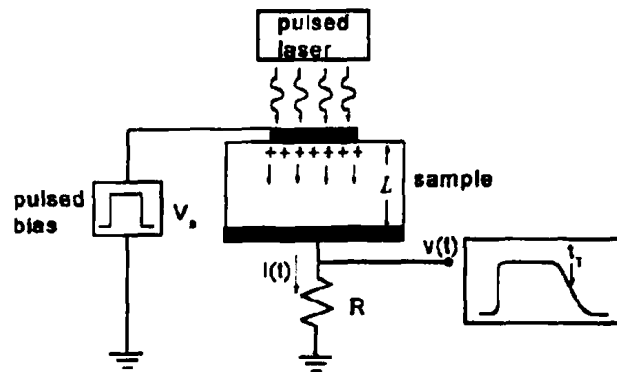
Figure A3-2: *Schematic representation of the TOF set-up. After ref. [7].*

For TOF measurement, which is schematically depicted in Figure A3-2, the sample is sandwiched between two glass plates coated with semi-transparent aluminium electrodes that are blocking for carrier injection into the sample. A pulsed (10 ns) N_2 laser generates electron-hole pairs in the electrically biased cell. Depending on the polarity of the electric field applied across the sample, either electrons or holes will then be drifted through the sample cell producing a displacement current $I(t)$, which is recorded by using an oscilloscope. The transit time, t_T, i.e., the time needed for the charge carriers to cross the sample, is related to the average drift velocity $v_d = L/t_T$ which, in turn, is linearly related to the electric field E via the drift mobility μ_d, $v_d = \mu_d E$, provided Ohm's law holds. The effective drift mobility, μ_d, is therefore given by [7]

$$\mu_d = \frac{L}{E \cdot t_T} = \frac{L^2}{V \cdot t_T}$$

(A3.2)

where $E = V/L$ is the applied electric field, L the sample thickness and V the applied voltage. The transit time can be measured directly on the current trace, in which case it is variously defined as the time at which the current has dropped by values going from 10 to 50% (the latter one being most commonly used), or it can be obtained by integrating the current and using the time at which the collected charge saturates or it can be approximated by two linear components with different slopes at short and long times. An important advantages of the TOF method is that (i) the contributions of positive and negative carriers can be measured separately, simply by inverting the polarity of the applied electric DC field; (ii) electron and hole recombination can routinely be neglected since only one type of carrier drifts through the sample; and (iii) it provides a direct measurement of mobility and requires no knowledge of the concentration of charge carriers.

A3.3 References

[1] Warman, J. M.; van de Craats, A. M. *Mol. Cryst. Liq. Cryst.* **396**, 41 (2003).

[2] Warman, J. M.; Piris, J.; Pisula, W.; Kastler, M.; Wasserfallen, D.; Müllen, K. *J. Am. Chem. Soc.* **127**, 14257 (2005).

[3] Schouten, P. G.; Warman, J. M.; Gelinck, G. H.; Copyn, M. J. *J. Phys. Chem.* **99**, 11780 (1995).

[4] Adam, D.; Closs, F.; Frey, T.; Funhoff, D.; Haarer, D.; Ringsdorf, H.; Schuhmacher, P.; Siemensmeyer, K. *Phys. Rev. Lett.* **70**, 457 (1993).

[5] van de Craats, A. M.; Siebbeles, L. D. A.; Bleyl, I.; Haarer, D.; Berlin, Y. A.; Zharikov, A. A.; Warman, J. M. *J. Phys. Chem. B* **102**, 9625 (1998).

[6] Boden, N.; Bushby, R. J.; Clements, J.; Donovan, K. J.; Movaghar, B.; Kreouzis, T. *Phys. Rev. B* **58**, 3063 (1998).

[7] Brinza, M.; Willekens, J; Benkhedir, M. L.; Emelianova, E. V.; Adriaenssens, G. J. *J. Mater. Sci.:Mater. Electron.* **16**, 703 (2005).

CURRICULUM VITAE

MAHDY M. ELMAHDY

University of Ioannina
Department of Physics
P.O. Box 1186
451 10 Ioannina, Greece
E-mail: me01641@cc.uoi.gr
Tel: +30-2651-098561
Fax: +30-2651-098693

PERSONAL

- Date of birth: 22/04/1974
- Place of birth: Mansoura, Egypt
- Marital status: Married, one child

EDUCATION

- Dec. 2003-present: Postgraduate Student, Physics Department, University of Ioannina, Greece (Thesis advisor: Prof. G. Floudas)
- Jan. 1998-April 2002: M.Sc. in Physics, University of Mansoura, Mansoura, Egypt
- Sept. 1996-Sept. 1997: M.Sc. courses, University of Mansoura, Mansoura, Egypt
- Sept. 1992-May 1996: B.Sc. in Physics, University of Mansoura, Mansoura, Egypt

ACADEMIC APPOINTMENTS

- Dec. 1997-June 2002: Demonstrator at Physics Department, Mansoura University, Mansoura, Egypt.
- June 2002-today: Assistant lecturer at Physics Department, Mansoura University, Mansoura, Egypt.

RESEARCH INTERESTS

Dielectric Spectroscopy (as a function of temperature and pressure) to study:
- (i) Dynamics of discotic liquid crystals
- (ii) Local and global polymer dynamics in restricted geometries

(iii)   Self-assembly, phase state, molecular dynamics and kinetic of structure formation

Fellowships

1. Recipient of Greek National Foundation Scholarships (IKY) awards (Dec. 2003-Dec. 2007)

PAPERS IN REFEREED JOURNALS

[1] **M.M. Elmahdy**, X. Dou, M. Mondeshki, G. Floudas, H.J. Butt, H.W. Spiess, K. Müllen
"Self-assembly, molecular dynamics and kinetics of structure formation in dipole functionalized discotic liquid crystals"
J. Am. Chem. Soc. (in press, web release March 7, 2008).

[2] **M.M. Elmahdy**, G. Floudas, M. Mondeshki, H.W. Spiess, X. Dou, K. Müllen
"Origin of the complex molecular dynamics in functionalized discotic liquid crystals"
Phys. Rev. Lett. 100, 107801, 2008.

[3] **M.M. Elmahdy**, G. Floudas, M. Kastler, K. Müllen
"Molecular dynamics of branched hexaalkyl hexa-*peri*-hexabenzocoronenes"
J. Phys. C (in press)

[4] K. Chrissopoulou, A. Aftaris, S.H. Anastasiadis, **M.M. Elmahdy**, G. Floudas, B. Frick
"Structure and dynamics in PEO nanocomposites"
Eur. Phys. J. Special Topics 141, 267, 2007.

[5] **M.M. Elmahdy**, G. Floudas, L. Oldridge, A.C. Grimsdale, K. Müllen
"Self-assembly and molecular dynamics of oligo-indenofluorenes"
Chem. Phys. Chem. 7, 1431, 2006.

[6] **M.M. Elmahdy**, K. Chrissopoulou, A. Aftaris, G. Floudas, S.H. Anastasiadis
"Effect of confinement on polymer segmental motion and ion mobility in PEO/layered-silicate nanocomposites"
Macromolecules (Communication), 39, 5170, 2006.

[7] **M.M. Elmahdy**, G. Floudas, C.G. Clark, K. Müllen
"Self-assembly and dynamics of a fluorous biphasic hexaphenylbenzene"
In preparation

[8] F.M. Reicha, A.M. Elabsy, A.A. Atta, **M.M. Elmahdy**
"Structure of Electropolymerized Polyacrylonitrile"
J. Polym. Matter 21, 445, 2004.

PRESENTATIONS IN SCIENTIFIC CONFERENCES

[1] "Glass Transition in Discotic Liquids Crystals - Effects of Pressure" (Oral presentation, G. Floudas)
European Science Foundation Exploratory Workshop on "Glassy Liquids under Pressure: Fundamentals and Applications", Ustron, Poland (October 10-14, 2007).

186
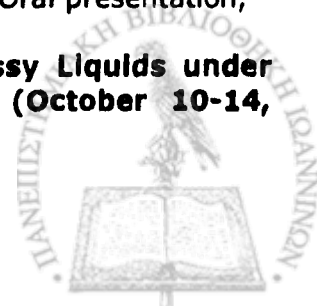
[2] "Structure and Dynamics of Branched Hexaalkyl and Functionalized Hexa-*peri*-hexabenzocoronenes"
XXIII Hellenic Solid State Physics and Materials Science Conference, Athens, Greece (September 23-26, 2007).

[3] a. "Self-assembly and molecular dynamics of oligoindenofluorenes"
b. "Self-assembly and molecular dynamics of hexa (3'-(1H, 1H-perfluorododecyloxy)-5'-Dodecyloxyphenyl) benzene"
c. "Effect of confinement on polymer segmental motion and ion mobility in PEO/layered –silicate nanocomposites"
6th Hellenic Conference on Polymers, Patras, Greece (November 3-5, 2006).

[4] a. "Self-assembly and molecular dynamics of oligoindenofluorenes"
b. "Effect of confinement on polymer segmental motion and ion mobility in PEO/layered-silicate nanocomposites"
XXII Hellenic Solid State Physics and Materials Science Conference, Patras, Greece (September 24-27, 2006).

[5] "Structure and dynamics in polymer/layered silicates"
3rd Workshop on Nanosciences & Nanotechnologies (NN06), Thessaloniki, Greece (July 10-12, 2006).

[6] "Effect of confinement on the polymer segmental motion and on ion mobility in PEO/layered-silicate nanocomposites"
American Physical Society, March Meeting, Baltimore, MD, USA (March 13-17, 2006).

[7] "Structure and dynamics in PEO nanocomposites"
3rd International Workshop on Dynamics in Confinement, Grenoble, France (March 23-26, 2006).